

Dissertation in Astronomy
submitted to the
Combined Faculties of the Natural Sciences and Mathematics
of the Ruperto-Carola-University of Heidelberg, Germany,
for the degree of
Doctor of Natural Sciences

Put forward by
M.Sc. *Mario Gennaro*
born in **Campi Salentina (LE), Italy**

Oral examination: 30.11.11

Massive clusters revealed in the near infrared

Constraining the early stages of stellar evolution

Mario Gennaro

Max-Planck-Institut für Astronomie

**Referees: Prof. Dr. Thomas Henning
Prof. Dr. Ralf S. Klessen**

Zusammenfassung

Sternhaufen können als Bausteine von Galaxien angesehen werden. Untersuchungen der Entstehung und Entwicklung von Sternhaufen ist daher eine Kernfrage für das Verständnis der Entwicklung ihrer Heimatgalaxien. Speziell junge massereiche Sternhaufen nehmen eine Schlüsselrolle ein bei der Spezifizierung der Physik der Sternentstehung und -entwicklung. Die Sternpopulation innerhalb dieser extrem massereichen Objekte umspannt den kompletten Bereich von Sternmassen von den sehr massearmen Braunen Zwergen bis zu den massereichsten, heute bekannten, stellaren Objekten. Eines der wichtigsten Werkzeuge für die Untersuchung der Sternhaufen sind stellare Entwicklungsmodelle, d.h. Entwicklungswege und Isochronen, mit deren Hilfe sich Massen und das Alter ableiten lassen. Aufgelöste Sternpopulationen in Sternhaufen können wiederum genutzt werden um diese theoretischen Modelle zu testen und zu kalibrieren.

In dieser Dissertation präsentiere ich zuerst eine Studie der aktuellen Generation der Vorhauptreihenmodelle und deren sorgfältige Anwendung zur Bestimmung stellarer Eigenschaften. Darauf folgend nutze ich diese Sternmodelle um Westerlund 1, den massereichsten jungen Sternhaufen der Milchstrasse, zu untersuchen. Der letzte Teil dieser Arbeit beschäftigt sich mit der ersten Multiwellenlängenuntersuchung der kürzlich entdeckten Sternentstehungsregion CN15/16/17. Diese Region wurde im Rahmen einer ausgedehnten Suche nach Sternhaufen beobachtet. Ich nutze Nahinfrarotbeobachtungen, um nach bisher unentdeckten Sternhaufen in unserer Galaxis zu suchen, mit dem Ziel das Mysterium der Sternentstehung in den inneren Regionen der Milchstrasse zu enthüllen.

Abstract

Stellar clusters can be considered as the building blocks of galaxies. Studying how clusters form and evolve is crucial in understanding the evolution of their host galaxies. Young massive stellar clusters, in particular, play a key role in placing constraints on the physics of star formation and evolution. The stellar population inside these extremely massive objects spans the full range of stellar masses from very low mass brown dwarfs to the most massive stellar objects currently known. One of the most important tools to study stellar clusters are stellar evolutionary models, i.e. tracks and isochrones from which masses and ages can be derived. Resolved stellar populations in clusters can in turn be used to test and calibrate these theoretical models.

In this work I first present a study of the current generation of pre-main sequence models and their thorough use for assessing stellar properties. I then continue using stellar models to study the most massive young cluster in the Milky Way: Westerlund 1. The last part of this work deals with the first multiple wavelength investigation of a recently discovered star forming region: the CN15/16/17 complex. This region was observed in the framework of an extended cluster search. I used near infrared observations to look for the missing cluster that are yet to be found in our Galaxy in order to unveil the mysteries of star formation in the inner parts of the Milky Way.

A Totó e Gregorio ...

CONTENTS

INTRODUCTION	1
OUTLINE OF THE THESIS	4
PRE MAIN SEQUENCE MODELS	4
WESTERLUND 1	5
CLUSTERS SEARCH	5
1 TESTING PRE-MAIN SEQUENCE MODELS: THE POWER OF A BAYESIAN APPROACH	9
1.1 INTRODUCTION	9
1.2 THE BAYESIAN METHOD	11
1.2.1 DEFINITION	12
1.2.2 THE LIKELIHOOD FUNCTION AND THE 2-VARIABLES COVARIANCE MATRIX	13
1.2.3 THE VALUE OF THE COVARIANCE BETWEEN LUMINOSITY AND TEMPERATURE	13
1.2.4 PRIOR DISTRIBUTIONS	14
1.2.5 MARGINAL DISTRIBUTIONS, BEST VALUES, UNCERTAINTIES AND RELATIVE PRECISION	15
1.2.6 COMPARISON OF DIFFERENT CLASSES OF MODELS	17

1.3	THE SET OF MODELS	18
1.4	SYNTHETIC DATA SETS: TESTING THE METHOD	20
1.5	THE DATA SET	26
1.6	THEORETICAL VS. DYNAMICAL MASSES – THE STANDARD SET OF MODELS	31
1.7	ANALYSIS OF THE DATA USING DIFFERENT CLASSES OF MODELS	34
1.8	APPLICATION TO BINARIES	40
1.8.1	RS CHA	44
1.8.2	RXJ 0529.4+0041 A	44
1.8.3	V1174 ORI	45
1.8.4	EK CEP	46
1.8.5	TY CRA	47
1.8.6	ASAS J052821+0338.5	48
1.8.7	HD 113449	49
1.8.8	NTT 045251+3016	50
1.8.9	HD 98800 B	51
1.9	THE STARS IN TAURUS-AURIGA	51
1.10	SUMMARY AND CONCLUSIONS	53
1.A	TABLES OF BAYES FACTORS	56
1.B	MASS AND AGE MARGINAL DISTRIBUTIONS	61
2	MASS SEGREGATION AND ELONGATION OF THE STARBURST CLUSTER WESTERLUND 1	69
2.1	INTRODUCTION	69
2.2	THE DATA	71
2.3	2D COMPLETENESS MAPS	71
2.4	PHOTOMETRIC ERRORS	75

2.5	SUBTRACTION OF THE FIELD STARS	75
2.6	THE STELLAR MODELS	80
2.7	FUNDAMENTAL PARAMETERS OF WESTERLUND 1	80
2.7.1	REDDENING AND EXTINCTION	81
2.7.2	DISTANCE AND AGE	83
2.8	THE IMF OF WESTERLUND 1	85
2.8.1	THE MASS OF THE SINGLE STARS	85
2.8.2	IMF SLOPE AND TOTAL MASS DETERMINATION	85
2.8.3	SPATIAL VARIABILITY OF THE IMF	89
2.9	MORPHOLOGY OF WESTERLUND 1	93
2.9.1	RESULTS OF THE GEFF FIT	95
2.9.2	POSSIBLE SOURCES OF ELONGATION	96
2.9.3	THE EFFECTIVE CUMULATIVE RADIUS	98
2.9.4	THE ORIGIN OF MASS SEGREGATION FOR WESTERLUND 1	99
2.10	CONCLUSIONS	102
2.A	COMPLETENESS MAPS	103
2.A.1	ADDING AND DETECTING ARTIFICIAL STARS	103
2.A.2	BUILDING THE 2D MAPS	104
2.A.3	INTERPOLATION IN MAGNITUDE	105
2.A.4	COMPLETENESS FOR THE CONTROL FIELD	105
2.B	EVALUATING THE PHOTOMETRIC ERRORS AND THEIR CORRELATIONS	106
2.B.1	ASSIGNING PROPER PHOTOMETRIC ERRORS AND THEIR CORRELATION TO EACH DETECTED STAR	108
2.B.2	PHOTOMETRIC ERRORS FOR THE CONTROL FIELD	108

2.C	σ - CLIPPING	110
2.D	BOOTSTRAP ESTIMATE OF THE IMF PARAMETERS AND THEIR ERRORS	111
3	MULTIPLE EPISODES OF STAR FORMATION IN THE CN15/16/17 MOLECULAR COMPLEX	115
3.1	INTRODUCTION	115
3.2	JHK_S PHOTOMETRY	116
3.3	IRAC MID-INFRARED PHOTOMETRY	119
3.4	SUB-MM CONTINUUM EMISSION	122
3.5	K-BAND SPECTROSCOPY	124
3.6	SPECTRAL CLASSIFICATION	126
3.7	NEBULAR EMISSION	131
3.8	INTEGRATED RADIO CONTINUUM FLUX	132
3.9	DB10 AND DB11 CLUSTERS	134
3.10	CONCLUSIONS	138
	SUMMARY AND FUTURE WORK	139
	BIBLIOGRAPHY	141

INTRODUCTION

Stellar clusters are the best available laboratories for studying many important aspects of star formation and evolution. Understanding the interplay between gravity, gas and stellar dynamics, stellar evolution and feedback from massive stars is the ultimate question of stellar cluster research.

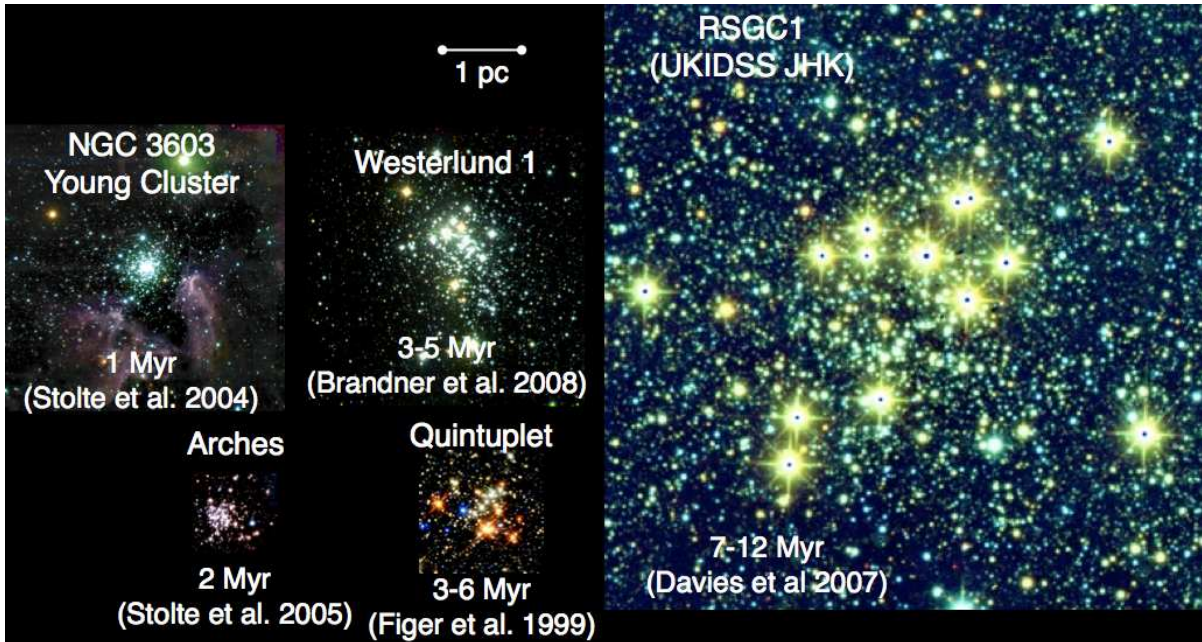
With the help of stellar evolutionary models it is possible to study properties such as the stellar ages and masses and from these infer, e.g. the star formation history and the initial mass function of the clusters (Hillenbrand et al. 2009; Bastian et al. 2010). Hydro-dynamical and n-body simulations allow a study of the evolution of a cluster as a dynamical system in which stars are considered as single particles interacting with each other and with the intra-cluster gas (Bonnell et al. 2011; Gieles et al. 2011).

On a Galactic scale clusters can be used to trace star formation and understand how it proceeds as a function of environment. External radiation field, turbulence amount and metallicity of the environment might affect the outcome of the star formation process (see e.g. Mac Low & Klessen 2004; Mac Low et al. 2005; Jappsen et al. 2009; Peters et al. 2011 and references therein). These quantities change as a function of position in the Galaxy. For example, higher cloud temperatures are expected in the proximity of the Galactic Center, possibly resulting in a change of the characteristic Jeans length and consequently of the initial mass function.

Observations of resolved cluster populations can place strong constraints on stellar evolution theory. Among stellar clusters, young and massive systems are very interesting because:

- at their young ages they preserve traces of the star formation process
- their most massive members are still present, while they have evolved and disappeared in

Figure 1: A sample of Galactic starburst clusters displayed on the same physical scale.



older systems

- given the large range in mass, stars in very different evolutionary phases are simultaneously observable
- given the large number of stars they can be studied using a statistical approach, obtaining robust results

We will refer to the most massive clusters ($M \gtrsim 10^4 M_\odot$) as starburst clusters. This term indicates that a large amount of gas mass is converted into stars on a very small spatial scale (~ 1 pc) and on a very short time scale (~ 1 Myr), i.e. a burst of star formation. Very massive starburst clusters ($M \gtrsim 10^5 M_\odot$), also called Super Star Clusters, are studied almost exclusively in other galaxies, but in this case the low mass stellar population can not be resolved.

Several clusters in the Milky Way deserve the status of starburst, according to our definition. These can in turn be divided into clusters in the spiral arms and clusters in the Galactic Center region. A sample of known Galactic starburst clusters is shown in Fig. 1.

The most massive young cluster in our Galaxy is Westerland 1 ($\tau \sim 4$ Myr, $M \sim 5 \times 10^4 M_\odot$, see Brandner et al. 2008; Gennaro et al. 2011a), located in the Scutum-Crux arm at a distance of ~ 4 kpc from our Sun. An other spiral-arm starburst cluster is NGC 3603 Young Cluster (YC), younger ($\tau \sim 1 - 2$ Myr) and less massive ($M \sim 1.5 \times 10^4 M_\odot$) than Westerland 1 (see Stolte et al. 2004; Rochau et al. 2010) and located in the Carina arm at ~ 6.7 kpc from us.

Four older clusters have been discovered recently, which also are thought to be more massive than $10^4 M_{\odot}$. All these clusters are characterized by a rich population of red supergiants, i.e. massive stars in their post main sequence evolution, with an age between 10 and 20 Myr. The first three in order of discovery are named Red Super-Giant Clusters (RSGC) 1, 2 and 3 (Figer et al. 2006; Davies et al. 2007; Clark et al. 2009) while the most recently discovered cluster is Alicante 8 (also named RSGC 4, see Negueruela et al. 2010b). These four clusters are located in a relatively small area at Galactic latitudes $l \sim 24^{\circ} - 28^{\circ}$ and are believed to be at a distance of ~ 6.5 kpc. This concentration of high mass clusters is thought to be related to the proximity of the tip of the Galactic Bar, at the base of the Scutum arm ($l \sim 27^{\circ}$). Within this picture, the dynamical interaction between the Disk and the Bar can explain such a massive star forming region in our Galaxy. The unevolved population of the RSGCs is not visible though. This is due to the strong contamination from the foreground and background population and also because the red supergiants outshine the underlying fainter population. Consequently, the distance of these regions is still quite uncertain. An alternative scenario to the Bar-enhanced star formation is that these clusters are spread on a larger region along a similar line of sight. The clusters line of sight actually cuts the giant Molecular Ring in our Galaxy. This structure, observed in the radio, starts at the end of the Bar and is located at ~ 4.5 kpc from the Galactic Center. The base of the Scutum-Crux arm may also be considered as part of this molecular ring.

Three additional starburst clusters are detected in the Galactic Center region: Arches, Quintuplet and the Young Nuclear Cluster (see Figer et al. 1999; Gerhard 2001; Stolte et al. 2005b; Pau-mard et al. 2006; Hußmann et al. 2011). These object formed in a very different environment, compared to the spiral arms. The strong tidal forces, high radiation and magnetic field and high temperature of the molecular clouds in the Galactic Center region provide a particularly interesting laboratory for studying very extreme star formation as observable in extragalactic cases. For example it has been suggested that these exceptional conditions might favor the formation of more massive stars when compared to the milder spiral arms environment (Morris 1993; Morris & Serabyn 1996).

The Large Magellanic Cloud hosts an other very massive starburst cluster: R136 in the 30 Doradus region (Tarantula Nebula). This object is probably the most massive young compact cluster in the Local Group with a total mass of $\sim 10^5 M_{\odot}$ and an age of ~ 3 Myr (Andersen et al. 2009).

The most massive clusters in our Galaxy and in the nearby Magellanic Clouds can be studied and used as templates for extra-galactic star clusters. The information that is extracted from the former, resolved objects can then be extrapolated to the latter, unresolved systems, for which only integrated properties are observed. In this way star formation can ultimately be studied in a cosmological framework.

OUTLINE OF THE THESIS

The aim of my past three years of work has been to have a critical approach to the study of stellar clusters, taking into account the uncertainties on both the theoretical and the observational side. An introductory background to the three main parts of the Thesis is given below.

PRE MAIN SEQUENCE MODELS

Stellar evolution is one of the better understood branches of astrophysics. Stellar modeling still presents several problems though, and several aspects of the micro- and macro-physics have not yet been fully explored. I focused my attention on the pre-main sequence (PMS) phase, i.e. the initial phase of evolution for low- and intermediate-mass stars ($M \lesssim 8.0M_{\odot}$). These stars reach the full equilibration of the hydrogen nuclear burning cycles (pp or CNO depending on their mass) after their main accretion phase has terminated. Hence they evolve towards the main sequence (MS) being fully formed but still not fully supported by nuclear reactions. Most of the energy radiated during the PMS phase comes from the heat released by the structure's contraction (Hayashi & Nakano 1965). More massive stars are thought to ignite hydrogen fusion when they are still accreting, hence they do not experience a PMS phase in the traditional sense.

The contraction phase is much faster than the MS phase. In clusters where PMS stars can be observed, these objects can be used as chronometers to infer the clusters' ages. Calibration of PMS models is therefore very important to obtain reliable age estimates.

In Chap. 1 I present an analysis aiming to perform such calibration using an up-to-date database of stellar models, computed with the FRANEC evolutionary code (Tognelli et al. 2011). In addition to stellar clusters, detached binaries are another powerful observational tool that astronomers can use to constrain stellar evolution theory. For eclipsing binaries and astrometric binaries the masses of the components can be measured in a distance-independent fashion. I use the available dynamical mass measurements for PMS stars and a Bayesian approach to examine the ability of the current generation of models in correctly reproducing the observations.

One of the open questions of PMS modeling concerns the role played by accretion in affecting the observable properties of very young stars, i.e. their effective temperatures and luminosities. Depending on the properties of the accretion flow -basically the amount of entropy deposited into the star- the stellar structure might or might not be able to re-adjust in sufficient time when strong episodic accretion occurs. Therefore different stellar radii might be observed in case the star is experiencing strong accretion. Different authors disagree on the impact accretion can have on the stellar ages which are inferred using non-accreting models. For accreting models with

$M \lesssim 1M_{\odot}$ and an age of ~ 1 Myr Baraffe et al. (2009) claim that an age up to 10 Myr might be erroneously derived. On the other hand, with a different accretion prescription, Hosokawa et al. (2011) found no systematic mismatch between accreting and non-accreting models.

However, in starburst clusters the problem of accretion for low-mass stars is less severe. The presence of many massive stars with their strong winds and radiation fields clears the cluster environment from most of the gas that is left after the initial formation phase. Hence, already at an age of ~ 1 Myr, accretion has been quenched by massive stars feedback. This is clearly shown in Rochau et al. (2010) where standard (non-accreting) PMS models nicely fit the observed low-mass PMS stars sequence.

WESTERLUND 1

In Chap. 2 I use a combination of FRANEC PMS models and PADOVA MS models (Marigo et al. 2008) to study the properties of the most massive starburst cluster in our Galaxy: Westerlund 1 (Westerlund 1961). The stellar masses are used to build the cluster's mass function. The spatial distribution of stars as a function of mass is also studied. I investigate the morphological properties of the cluster and observed that Westerlund 1 is strongly elongated and also shows signs of mass segregation. Interpretations of these findings are given.

As already mentioned, Galactic starburst clusters are templates for extragalactic Super Star Clusters. The latter are thought to be massive enough to retain a large fraction of their stellar population throughout their evolution, ultimately forming Globular Clusters. Westerlund 1 might be the only example of such proto-globular clusters in our Galaxy.

CLUSTERS SEARCH

According to the current understanding, up to 90% of the stars that are born in the present-day Milky Way are formed in clusters (Lada & Lada 2003). However, it is still uncertain how the formation scenario, the cluster long-term survival and the stellar feeding to the field population depend on the environment and galactocentric distance.

Due to the high degree of interstellar extinction, very few young clusters are known in the Galactic Plane at distances from the Sun larger than 2 kpc. Moreover, if we look towards the center of our Galaxy, the identification of clusters is even harder due to the severe crowding by fore/background stars. Spurious cluster detections are also possible because of the patchy nature of the interstellar medium, which may cause strongly spatially varying foreground extinction and consequently variations in the star counts.

Due to the strong extinction for lines of sight in the Galactic Plane, the detection of distant clusters at optical wavelengths is challenging, even for the most massive clusters located towards the center of the Milky Way. The best way to identify new clusters in the inner region of the Galaxy is therefore the use of infrared wavelengths.

Over the past decade the search for new clusters has gained new and fresh interest thanks to the development of infrared instrumentation, which resulted in surveys such as the Two Micron All Sky Survey (2MASS, Skrutskie et al. 2006) and DENIS (Epchtein et al. 1999).

Using images from 2MASS Dutra et al. (2003a) and Bica et al. (2003) discovered a total of 346 new infrared clusters, stellar groups and candidates, of which 58 are located towards the Galactic Center (see also Dutra & Bica 2000). Even though 2MASS is suitable for the identification of cluster candidates, both through visual inspection and automated searches (Ivanov et al. 2002; Koposov et al. 2008), the limited angular resolution ($\sim 2''$) and photometric depth ($K_S \lesssim 13.5$ mag in the Galactic Plane) make a detailed study of the stellar content and the determination of age and mass for these objects almost impossible.

More recently the UKIRT Infrared Deep Sky Survey – Galactic Plane Survey (UKIDSS – GPS, Lucas et al. 2008) is being carried out, with deeper ($K_S \lesssim 18$ mag) and better angular resolution ($\sim 0.8''$) data than 2MASS, but limited to the part of the Milky Way's Disk with Galactic longitude larger than -2° . The VISTA Variables in the Via Lactea survey (VVV) is scanning the Milky Way bulge and an adjacent section of the disk in the $YZJHK_S$ (Arnaboldi et al. 2007; Minniti et al. 2010). Recently, Borissova et al. (2011) reported the discovery of 96 new cluster candidates using the VVV data.

In parallel to the near infrared ground based surveys, mid-infrared surveys of the whole Galactic Plane have been carried out using the IRAC camera on board the Spitzer Space Telescope, i.e. the GLIMPSE and GLIMPSE II surveys (Benjamin et al. 2003; Churchwell et al. 2009). These surveys have revealed an unprecedented richness in star forming sites in our Galaxy. Churchwell et al. (2006) and Churchwell et al. (2007) investigated the 4 IRAC channel composite images obtained by the GLIMPSE I and II surveys looking for molecular bubbles; they found almost 600 of these objects. Part of these objects are associated with the presence of young massive stars.

Within the sample of molecular bubbles identified in the GLIMPSE II survey ($|l| < 10^\circ$, $|b| < 1^\circ$), 29 are associated with H II regions. This means that they very likely host massive stars which ionize the atomic hydrogen (Alvarez et al. 2004). The soft UV component of the stellar radiation excites the polycyclic aromatic hydrocarbons (PAHs) just outside the H II regions, making the bubbles very bright in the $8 \mu\text{m}$ IRAC channel. The presence of massive stars, in turn, indicates the presence of an underlying stellar cluster.

However, to confirm the nature of these objects, and assess the presence of a cluster inside each bubble, additional observations are needed. The combination of a spectroscopic classification of the high-mass stars and deep, high-resolution imaging of the intermediate- and low-mass members results in an unambiguous determination of the basic properties of the clusters whose presence is confirmed (extinction, distance, age and mass).

I started an observational campaign to study the sub-sample of 29 bubbles associated with known H II regions. I obtained time at the NTT telescope (La Silla, Chile), using the SofI instrument to target the bubbles in both JHK_S imaging mode and K_S -band spectroscopy. In Chap. 3 I present the results of these observations for one of the cluster candidates. The importance of a multiple-wavelength observational approach is shown (see Feldt et al. 1999; Henning et al. 2001 for similar examples). I use a combination of spectroscopy, radio and sub-millimeter fluxes, mid- and near-infrared imaging to obtain a clear picture of the young star forming region CN15/16/17 (using the Churchwell et al. (2007) nomenclature).

TESTING PRE-MAIN SEQUENCE MODELS: THE POWER OF A BAYESIAN APPROACH*

1.1 INTRODUCTION

The current understanding of star formation processes largely relies on the ability of assigning ages and masses to young stars using pre-main sequence (PMS) models. The observed luminosity and effective temperature of stars in their early evolutionary stages can be translated into mass and age only by the comparison with PMS stellar tracks. Unfortunately the early evolutionary stages of the stellar life are among those less tightly constrained by observations and most uncertain from the theoretical point of view. This situation becomes progressively worse for stellar mass below $\approx 1.2 M_{\odot}$. This is mainly a consequence of the poor treatment of superadiabatic convection. Moreover there are still large uncertainties on the main input physics describing the cold and dense matter typical of low-mass stars interiors adopted in modern evolutionary codes. This theoretical uncertainty is testified by the large discrepancy still present between different sets of low-mass PMS models (see e.g. Siess et al. 2000; Baraffe et al. 2002; Tognelli et al. 2011).

An ever growing amount of detailed information is becoming available for both star-forming regions in the Milky Way (see Reipurth 2008a,b) and in the Magellanic Clouds (Cignoni et al. 2009, 2010; Gouliermis et al. 2010), prompted by the remarkable improvement in the observational techniques over the last decade. The aforementioned theoretical uncertainties imply that many of the properties inferred for these regions, such as the initial mass function and the star formation history, strongly depend on the adopted PMS models, particularly for stars less massive than $\approx 1.2 M_{\odot}$.

*This chapter is adapted from the paper Gennaro et al. (2011b)

The importance of these kind of studies urges an empirical calibration of PMS tracks and isochrones based on a statistically significant sample of young stars with precisely determined parameters (mass, temperature, radius, luminosity and chemical abundances). Most useful in this respect are the detached, double lined, eclipsing systems which directly provide stellar masses, temperatures and radii, yielding also a distance independent luminosity through the Stephan law. Unfortunately, the currently available sample of PMS stars in eclipsing binaries amounts only to 10 objects in 6 systems (see Sect.1.5 and Table 1.3). Other important observational constraints to PMS models are provided by astrometric measurement of binary systems that can be resolved thanks to interferometric observations. For these systems the radii can not be determined though. Three binary systems with both stars in the PMS phase are currently known and studied (Table 1.3). A third technique providing mass values for young stars is based on spectroscopic observations of circumstellar disks. From the keplerian velocities masses are inferred, although these measurements require an independent estimate of the distance to determine the linear value of the radius at which velocities are measured. Also the sample of known objects in this category is quite small with only 9 stars (see again Table 1.3)

As already shown in the early attempts to test PMS stellar tracks against observations of eclipsing binaries (see e.g. Palla & Stahler 2001; Hillenbrand & White 2004; Stassun et al. 2004; Alecian et al. 2007a; Boden et al. 2007; Mathieu et al. 2007), the mass values inferred from theoretical models are in reasonable agreement with the dynamical ones for intermediate mass stars, whereas for low-mass stars theoretical values tend to underestimate the stellar mass (see Fig. 3 in Mathieu et al. 2007).

From these studies it is also clear that the usefulness of such tests in constraining the theoretical PMS models is severely limited by the still scarce accuracy of the current empirical measurements of the other stellar parameters, i.e. the luminosity, the chemical abundances and above all the effective temperature (see e.g. Hillenbrand & White 2004; Mathieu et al. 2007). In the next future both the size and the quality of the observed sample of test objects to calibrate PMS stellar tracks and isochrones are bound to increase.

We apply an objective Bayesian method to compare theoretical predictions with observations, obtaining robust uncertainties for the output values and assessing the overall quality of the comparison. Since the method, which is detailed in Sect.1.2, allows for the use of stellar tracks for a large and very fine grid of metallicity, mass and age values, we tested only the Pisa-PMS models. These are calculated using the newest version of the FRANEV evolutionary code (see e.g. Tognelli et al. 2011). The main characteristics of the models are described in Sect.1.3. In Sect.1.4 we assess the ability of the method to retrieve the stellar properties by means of synthetic tests. In Sect.1.5 we describe the observational data set, which includes all the currently available low-mass PMS data. The complete data set is analysed in Sect.1.6, where theoretical masses derived from our standard set of models are compared to the dynamical measurements. In Sect.1.7 we

compare the results for multiple sets of models. Section 1.8 is dedicated to detailed study of each binary system while the stars in the Taurus-Auriga association are analysed in Sect.1.9. A summary with concluding remarks is presented in Sect.1.10.

1.2 THE BAYESIAN METHOD

The general question we try to answer can be described as the problem of determining certain parameters (the age and mass of a star) by comparing models' predictions with empirical evidence (effective temperatures, luminosities, radii, dynamical masses of stars in binary systems). In order to do so we used a Bayesian approach, which allows to fully exploit the data.

One of the main advantages of the Bayesian approach over the frequentist one is the possibility of using the available information about the model parameters –the *prior probability*. Thanks to Bayes' Theorem this information is naturally included in the calculation of the new parameters' probability after additional evidence is collected – the *posterior probability*. In this way it is possible to further constrain the models' parameter space in an iterative process of refinement. On the other hand the main disadvantage is that often the whole space of possible models is not accessible. This means that the normalizing factor appearing on the r.h.s of Bayes' Theorem –q. (1.1) below–, can not always be evaluated. In such cases it is impossible to rigorously compute the normalized probability for a model to be correct given the empirical evidence. Nevertheless it is still possible to compare and choose between two different models, by taking the ratio of the posterior probabilities thus removing the normalization factor.

The notation we will adopt is the same as in Jørgensen & Lindegren (2005) –hereafter JL05. The method described in JL05 has been successfully used to provide stellar ages and masses for the stars in the Geneva-Copenhagen survey (see Nordström et al. 2004; Holmberg et al. 2007, 2009). It is a general method that can be applied to many other astrophysical cases, such ours.

Let \mathbf{q} be a set of observational quantities (or any combination of them), for example temperature and luminosity or gravity and temperature. Let \mathbf{p} be a set of model parameters and Ξ a set of meta-parameters identifying a class of models. We introduce this distinction between \mathbf{p} and Ξ for practical reasons. The parameters \mathbf{p} are the triple (τ, μ, ζ) , i.e. age, mass and metallicity of the model. The meta-parameters Ξ are instead the mixing-length parameter, α , the primordial helium abundance, Y_p , and the helium-to-metals enrichment ratio $\Delta Y/\Delta Z$. These three meta-parameters are chosen on the basis of some considerations and can be regarded as fixed inputs for the evolutionary models library as a whole, which gives them a different status compared to the \mathbf{p} set. The α parameter is usually calibrated on a solar model (see Basu & Antia 2008 and references therein). The Y_p value is constrained by big bang nucleosynthesis and observation of

metal poor H II regions (Izotov et al. 2007; Peimbert et al. 2007; Dunkley et al. 2009; Steigman 2010). $\Delta Y/\Delta Z$ is constrained by chemical evolution models of the Galaxy (Romano et al. 2005; Carigi & Peimbert 2008) or by comparing the absolute magnitude of unevolved nearby dwarf stars with stellar models (Jimenez et al. 2003; Casagrande et al. 2007; Gennaro et al. 2010).

The Ξ triple is usually fixed for any set of stellar tracks or isochrones available in the literature. Nevertheless there is no strong reason to assume that the solar calibration of α has to be suitable also for PMS stars of any mass (see e.g. the discussion in Montalbán et al. 2004; Tognelli et al. 2011). Also Y_p and $\Delta Y/\Delta Z$ are known with some uncertainty, which is quite large specially for the latter. Hence, having the opportunity to calculate our own stellar models, we allowed for variations of the meta-parameters, calculating stellar models libraries for a total of nine combinations of them (see Sect.1.3 for a detailed description). In principle other meta-parameters exist, like the relative distribution of metals (the mixture), the opacity tables, the equation of state. Indeed any *choice* of physical inputs identifies a class of models, but we will not explore the effects of changes in the microphysics.

In the following we will drop the Ξ term and, if not explicitly stated, we will refer only to one particular class of models, i.e. one fixed choice of $\Xi_j = (\alpha_j, Y_{pj}, \Delta Y/\Delta Z_j)$. We will come back to the comparison of different classes in Sects. 1.2.6 and 1.7.

1.2.1 DEFINITION

Bayes' Theorem states that the posterior probability of the parameters \mathbf{p} given the observations \mathbf{q} is:

$$f(\mathbf{p}|\mathbf{q}) = \frac{f(\mathbf{q}|\mathbf{p})f(\mathbf{p})}{f(\mathbf{q})} \quad (1.1)$$

The probability $f(\mathbf{q}|\mathbf{p})$ of observing the quantities \mathbf{q} given the parameters \mathbf{p} is proportional to $\mathcal{L}(\mathbf{p}|\mathbf{q})$, the *Likelihood* of the parameters \mathbf{p} given the evidence \mathbf{q} . The quantity $f(\mathbf{p})$ is the prior distribution of the parameters, which incorporates the information already available about them. The normalizing factor, $f(\mathbf{q}) = \int f(\mathbf{q}|\mathbf{p})f(\mathbf{p}) d\mathbf{p}$ is called marginal distribution; it represents the probability of observing new evidence \mathbf{q} under a complete set of mutually exclusive hypothesis, i.e. under all possible values for \mathbf{p} .

To calculate the integral, we should have access to all possible models, for all possible sets of parameters (and meta-parameters), or at least the subset of all plausible models, i.e. models for which $f(\mathbf{p})$ is not negligible. Even though the integration is not possible here, this is not a problem. As long as we are interested only in comparing different classes of models or estimating the most probable set of parameters within a single class, this can be accomplished by taking proba-

bility ratios, hence removing the normalization. Having considered that, we can then rewrite the posterior probability as:

$$f(\mathbf{p}|\mathbf{q}) \propto \mathcal{L}(\mathbf{p}|\mathbf{q})f(\mathbf{p}). \quad (1.2)$$

1.2.2 THE LIKELIHOOD FUNCTION AND THE 2-VARIABLES COVARIANCE MATRIX

Equation (1.2) is identical to eq. (3) in JL05, but in our work we extend the definition of Likelihood to the case of pairs of observables with non-zero covariance. This is particularly important –and often neglected– when the observables used to determine the stellar parameters are luminosity and temperature of stars in eclipsing binaries. Because of the way the two quantities are derived, they are strongly correlated (see Mathieu et al. 2007). Let the vector of observables be a 2D vector: $\mathbf{q} = (x, y)$; the definition of Likelihood in the general case is:

$$\begin{aligned} \mathcal{L}(\mathbf{p}|\mathbf{q}) = & \frac{1}{2\pi\sigma_x\sigma_y\sqrt{1-\rho^2}} \times \exp \left\{ -\frac{1}{2(1-\rho^2)} \times \right. \\ & \left. \times \left[\frac{[x(\mathbf{p}) - \hat{x}]^2}{\sigma_x^2} + \frac{[y(\mathbf{p}) - \hat{y}]^2}{\sigma_y^2} - \frac{2\rho[x(\mathbf{p}) - \hat{x}][y(\mathbf{p}) - \hat{y}]}{\sigma_x\sigma_y} \right] \right\} \end{aligned} \quad (1.3)$$

Here \hat{x} and σ_x are the measured value for the observable x and its uncertainty, respectively (the same for \hat{y} and σ_y). The quantity $\rho = \frac{\text{Cov}(x,y)}{\sigma_x\sigma_y}$ is the *correlation coefficient* of x and y . The quantities $x(\mathbf{p})$ and $y(\mathbf{p})$ are the values predicted by the model for the parameter values \mathbf{p} .

1.2.3 THE VALUE OF THE COVARIANCE BETWEEN LUMINOSITY AND TEMPERATURE

In the case of EBs the quantities that can be determined from the light curve are the effective temperatures ratio between the primary and secondary, $T_{\text{eff},1}/T_{\text{eff},2}$, and the radii, R_1 and R_2 . The temperature of the primary has to be inferred by other indicators such as some temperature-sensitive lines in the spectrum and a subsequent Spectral Type - Temperature conversion. Luminosities are not directly measured, but derived using Stephan's Law: $L = 4\pi\sigma_{\text{SB}}R^2T_{\text{eff}}^4$.

On the other hand, since the most used tool of stellar evolution is the Hertzsprung-Russel diagram (HR diagram), where $\log L$ and $\log T_{\text{eff}}$ are displayed, most of the analysis of binary systems is done in the HR diagram. So it is useful to have a proper treatment of the covariance matrix for

luminosity and temperature. Given Stephan's law, the standard deviation of $\log L$ is calculated as:

$$\sigma_{\log L} = \sqrt{\frac{1}{\ln 10} \left(2 \frac{\sigma_R}{R} + 4 \frac{\sigma_{T_{\text{eff}}}}{T_{\text{eff}}} \right)} \quad (1.4)$$

where σ_R and $\sigma_{T_{\text{eff}}}$ are the uncertainties on radius and temperature¹. The covariance between $\log L$ and $\log T_{\text{eff}}$ is given by:

$$\begin{aligned} \text{Cov}(\log L, \log T_{\text{eff}}) &= 2 \text{Cov}(\log R, \log T_{\text{eff}}) + 4 \text{Var}(\log T_{\text{eff}}) \\ &\approx 4 \text{Var}(\log T_{\text{eff}}) \end{aligned} \quad (1.5)$$

where $\text{Var}(\log T_{\text{eff}}) \equiv \sigma_{\log T_{\text{eff}}}^2$.

In both eqs. (1.4) and (1.5) we assume that temperatures and radii have vanishing covariance. This is not necessarily true for EBs, for which they are derived from the same light curve using fitting algorithms. However we are forced to neglect the corresponding term in the total luminosity-temperature covariance since we do not have access to the covariance matrix for radii and temperatures. Nevertheless we expect this covariance to be small specially when radii and temperatures are derived by multiple fitting of light-curves obtained independently in several photometric bands.

1.2.4 PRIOR DISTRIBUTIONS

We will make use of different types of prior distributions for the parameters. Here is a brief description of each of them:

Mass: for most of the systems in our sample the dynamical mass is the observable that is known with the best precision. For this reason we will often use a Gaussian mass prior $f(\mathbf{p}) \propto \exp\left\{-\frac{1}{2} \left[\frac{(\mu - m_{\text{ob}})}{\sigma_{m_{\text{ob}}}} \right]^2\right\}$. Apart from better constraining the mass values, this particular kind of prior is very informative and helps constraining also the stellar ages (see e.g. Sect.1.4).

Metallicity: for most of the systems measurements of $[\text{Fe}/\text{H}]$ are available, too. These can also be included as priors after converting $[\text{Fe}/\text{H}]_{\text{ob}}$ into the corresponding Z_{ob} value. The value of Z_{ob} depends on $[\text{Fe}/\text{H}]_{\text{ob}}$ but also on $\Delta Y/\Delta Z$, Y_P and $(Z/X)_{\odot}$ (for details see equations

¹Note that \ln is the base-e logarithm and \log the base-10

(1) and (2) in Gennaro et al. 2010). As a consequence we use different Z_{ob} values for a given $[\text{Fe}/\text{H}]_{\text{ob}}$ when we compare actual data to different classes of models Ξ_j .

If we assume that $[\text{Fe}/\text{H}]$ errors are distributed as Gaussians, the corresponding error distribution in Z is calculated as:

$$f_{\text{prior}}(Z) = \mathcal{G}(\phi(Z)) \frac{d\phi(Z)}{dZ}, \quad (1.6)$$

where we introduced $\phi(Z) \equiv [\text{Fe}/\text{H}]$ and $[\text{Fe}/\text{H}]$ is regarded as a function of Z ; \mathcal{G} is a Gaussian function. In the general case, the derived $f_{\text{prior}}(Z)$ can be asymmetric and, in particular, very different from a Gaussian. Nevertheless, given the typical errors in our data set (i.e. $\sigma([\text{Fe}/\text{H}]) \sim 0.1$ dex), the departure from Gaussianity is very small and can be neglected as can be seen in Fig. 1.1, where the Gaussian distribution in Z and that obtained as in Eq. (1.6) are shown. In both cases, we start from an observed $[\text{Fe}/\text{H}]$ distributed as a Gaussian and with $\mu = 0.1$ dex and $\sigma = 0.1$ dex. The mean value and variance of the $\mathcal{G}(Z)$ are determined using eq. (1) and (2) of Gennaro et al. (2010) and simple error propagation rules.

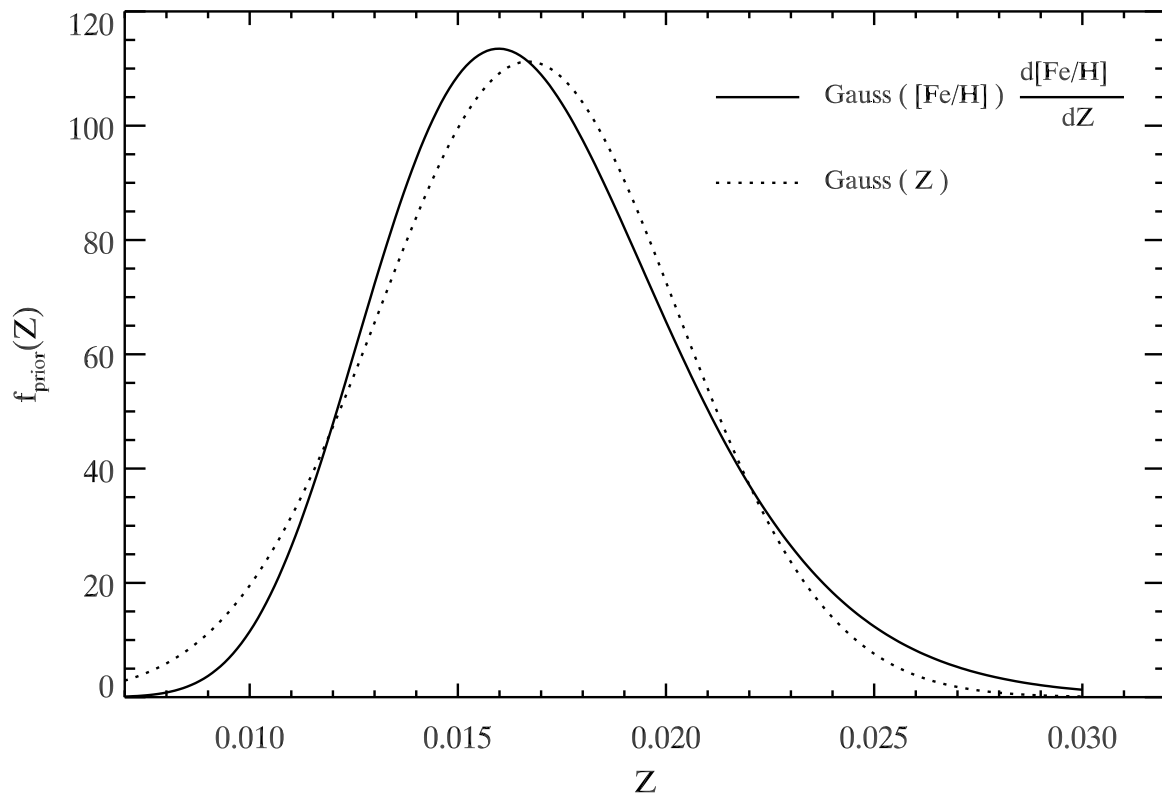
Moreover we can not always be sure that the error distribution on $[\text{Fe}/\text{H}]$ is itself Gaussian. $[\text{Fe}/\text{H}]$ errors certainly have a random, Gaussian component that can, however, be smaller than the overall uncertainty due to the poorly constrained systematics. With this in mind, we opted for a Gaussian functional form for the prior in Z .

Age: in the case of two stars in the same system, coevality might be considered as an additional prior, assuming that these two stars formed at the same time. In this case, we simply impose that both stars are coeval by multiplying their age marginal distributions (see below) hence getting a system age distribution.

1.2.5 MARGINAL DISTRIBUTIONS, BEST VALUES, UNCERTAINTIES AND RELATIVE PRECISION

As in JL05, the integration of eq.(1.2) with respect to all parameters but one, p_i , yields the marginal distribution for p_i . From this distribution it is possible to determine the most probable value for p_i and its confidence interval. The two parameters we are interested to determine are the stellar age τ , and mass μ . We will use the same symbol as in JL05 for the age marginal distribution, $G(\tau)$, and analogously define the mass marginal distribution, $H(\mu)$. By writing

Figure 1.1: Comparison between a Gaussian prior in Z and the prior that is derived as in eq. (1.6). The assumed starting $[\text{Fe}/\text{H}]$ distribution is a Gaussian with $\mu = 0.1$ dex and $\sigma = 0.1$ dex.



explicitly the triple of parameters, we define:

$$G(\tau) = \int \mathcal{L}(\tau, \mu, \zeta | \mathbf{q}) f(\tau, \mu, \zeta) d\mu d\zeta \quad (1.7a)$$

$$H(\mu) = \int \mathcal{L}(\tau, \mu, \zeta | \mathbf{q}) f(\tau, \mu, \zeta) d\tau d\zeta \quad (1.7b)$$

JL05 demonstrated that the mode of the marginal distribution is a more robust indicator than the mean for estimating stellar ages. This is particularly true for strongly asymmetric distributions or distributions showing multiple peaks. We also adopted the mode as the best value estimator but changed the definition of the uncertainty interval with respect to JL05. If \mathcal{A} is the total area under the distribution curve, $F(x)$, we define the confidence interval $[x_{\min}, x_{\max}]$:

$$\int_{x_1}^{x_{\min}} F(x) dx = \int_{x_{\max}}^{x_u} F(x) dx = 0.16\mathcal{A} \quad (1.8)$$

where we assume that the variable x is defined in the interval $[x_1, x_u]$. In this way 16% of the total probability is rejected on each side of the confidence interval. This definition coincides with that of a 1σ interval in the case of a Gaussian distribution. We follow again JL05 in the definition of the relative precision, ϵ :

$$\epsilon = \sqrt{x_{\max}/x_{\min}} - 1 \quad (1.9)$$

Using this definition it is possible to compare the *quality* of different age and mass determinations. The worst relative precision is attained when the marginal distribution is flat. In this case, assuming again $x \in [x_1, x_u]$ we have:

$$\frac{x_{\max}}{x_{\min}} = \frac{x_u - \frac{16}{100}(x_u - x_1)}{x_1 + \frac{16}{100}(x_u - x_1)}$$

We calculated models in the age interval $[0.5, 100]$ Myr and mass interval $[0.2, 3.6] M_{\odot}$, hence the worst relative precisions attainable are $\epsilon(\tau) \approx 1.26$ and $\epsilon(\mu) \approx 1.03$.

1.2.6 COMPARISON OF DIFFERENT CLASSES OF MODELS

Comparison of two classes of models is possible by calculating the Bayes Factor, i.e. the ratio of the *evidences* for the two classes. The evidence itself is defined as the integral of the likelihood

marginalized over the model parameters prior distributions. Hence the Bayes Factor for the i -th and j -th class of models is:

$$BF_{ij} = \frac{f(\mathbf{q}|\Xi_i)}{f(\mathbf{q}|\Xi_j)}, \quad (1.10)$$

where the evidence for each class is defined as:

$$\begin{aligned} f(\mathbf{q}|\Xi) &= \int f(\mathbf{q}, \mathbf{p}|\Xi) d\mathbf{p} \\ &= \int f(\mathbf{q}|\mathbf{p}, \Xi) f(\mathbf{p}|\Xi) d\mathbf{p} \end{aligned} \quad (1.11)$$

The Bayes Factor tells us nothing about the best values of the parameters \mathbf{p} , but it can be used to estimate which class of models –which set of meta-parameters Ξ – gives an overall best-fit to the data. Strong deviations of BF_{ij} from unity indicate that one class of models is a significantly better choice than the others.

1.3 THE SET OF MODELS

In the present analysis we used the very recent PMS tracks from the Pisa database² which contains a very fine grid of models for 19 metallicity values between $Z = 0.0002$ and $Z = 0.03$, three different initial helium abundances and three values of the mixing-length parameter for each metallicity. The models have been computed using an updated version of the FRANEC evolutionary code which takes into account the state-of-art of all the input physics (see Tognelli et al. 2011 for a detailed description). Here we briefly summarize the main characteristics of the code which are relevant for the present work and deeply affect both the morphology and the position of the PMS tracks in the HR diagram.

We adopted the equation of state (EOS) released in 2006 by the OPAL group (see e.g., Rogers & Nayfonov 2002), the OPAL high-temperature radiative opacity released by the same group in 2005 (see e.g., Iglesias & Rogers 1996) for $\log T[\text{K}] > 4.5$, and the Ferguson et al. (2005) low-temperature radiative opacities for $\log T[\text{K}] \leq 4.5$. The radiative opacity tables, both for low and high temperatures, are computed assuming the solar-scaled heavy-element mixture by Asplund et al. (2005).

The outer boundary conditions, required to integrate the stellar structure equations, have been taken from the atmosphere models computed by Brott & Hauschildt (2005) for $T_{\text{eff}} \leq 10\,000$ K, and by Castelli & Kurucz (2003) for higher temperatures.

²The database is available at the URL: <http://astro.df.unipi.it/stellar-models/>

Convection is treated according to the Mixing Length Theory (Böhm-Vitense 1958), following the formalism described in Cox & Giuli (1968). We used the classical Schwarzschild criterion to evaluate the borders of convectively unstable regions.

The hydrogen burning reaction rates are from the NACRE compilation (Angulo et al. 1999), with the exception of the $^{14}\text{N}(p,\gamma)^{15}\text{O}$ from the LUNA collaboration (Imbriani et al. 2005). The code explicitly follows the chemical evolution of the light elements (D, ^3He , Li, Be and B) from the early phases at the beginning of the Hayashi track. The models are evolved starting from a completely formed and fully convective structure, neglecting accretion.

We extracted from the Pisa PMS database tracks for 12 metallicities, namely $Z = 0.007, 0.008, 0.009, 0.01, 0.0125, 0.015, 0.0175, 0.02, 0.0225, 0.025, 0.0275, 0.03$. The purpose was to cover the full range of metallicities for the observed sample of stars. For models in this range of metallicities we adopted an initial deuterium abundance $X_{\text{D}} = 2 \cdot 10^{-5}$, suitable for pop. I stars (see e.g., Vidal-Madjar et al. 1998; Linsky et al. 2006; Steigman et al. 2007).

For each value of Z the initial helium abundance, Y , has been obtained by the linear relation,

$$Y = Y_{\text{p}} + Z \frac{\Delta Y}{\Delta Z} \quad (1.12)$$

where Y_{p} is the primordial helium abundance, and $\Delta Y/\Delta Z$ is the helium-to-metals enrichment ratio. For Y_{p} we adopted both the recent WMAP estimation $Y_{\text{p}} = 0.2485$ (see e.g., Cyburt et al. 2004; Steigman 2006) and a lower value $Y_{\text{p}} = 0.230$ (Lequeux et al. 1979; Pagel & Simonson 1989; Olive et al. 1991). In the first case we used both $\Delta Y/\Delta Z = 2$ as commonly adopted in literature (see e.g., Pagel & Portinari 1998; Jimenez et al. 2003; Flynn 2004; Casagrande et al. 2007) and $\Delta Y/\Delta Z = 5$ which is the extreme value suggested by recent analysis (see e.g., Gennaro et al. 2010 and references therein), while for $Y_{\text{p}} = 0.230$ we fixed $\Delta Y/\Delta Z = 2$. Hence, for each value of Z , we computed models with three initial helium abundances.

The efficiency of superadiabatic convection is parametrized by the α parameter where the mixing length ℓ is given by $\ell = \alpha H_{\text{p}}$ and H_{p} is the pressure scale-height. Following the usual procedure of calibrating the mixing length efficiency using the Solar observables, we obtained $\alpha = 1.68$ for our reference set of models. However there is no strong reason to adopt this value for stars in different evolutionary phases compared to the Sun. Recent analysis of PMS stars in binary systems (see e.g., Simon et al. 2000; Steffen et al. 2001; Stassun et al. 2004) and studies of lithium depletion in young clusters (Ventura et al. 1998; D'Antona & Montalbán 2003) suggest a sub-solar efficiency of the superadiabatic convection in low-mass PMS stars. Therefore we decided to adopt tracks for three α values, i.e. $\alpha = 1.2$ (low efficiency), $\alpha = 1.68$ (our solar calibrated), $\alpha = 1.9$ (high efficiency).

Taking into account the three Y values and the three α values, we computed models for each metallicity using a total of nine combinations of the Ξ triples of meta-parameters.

The tracks have been computed for a very fine grid of masses, with a spacing of $0.05 M_{\odot}$ in the range $M = 0.2 - 1.0 M_{\odot}$, of $0.1 M_{\odot}$ for the range $M = 1.0 - 2.0 M_{\odot}$ and of $0.2 M_{\odot}$ for the range $M = 2.0 - 3.0 M_{\odot}$. The tracks have been further interpolated on a finer mass-grid with a spacing of $0.01 M_{\odot}$ and in age with a spacing of 0.05 Myr in the full mass range. This was done in order to achieve a very high precision in the determination of both the mass and age for the observed stars.

1.4 SYNTHETIC DATA SETS: TESTING THE METHOD

In order to check the accuracy of our method we first tested it against simulated data. As already demonstrated by JL05, the precision of inferred ages and masses is related to the detailed morphology of isochrones and tracks in the HR diagram. Depending on the mass and the age of a star, its evolution might be faster in some parts of the diagram than in others. The *evolutionary speed* of a star along its track together with the positional uncertainty in the HR diagram determine the absolute precision of the method. Although the PMS is globally a very fast evolutionary phase compared to the MS, there are some stages –i.e. the descent of the Hayashi tracks– slower than others –i.e. the approach towards MS along Heyney tracks when radiative cores are developed. Another general rule is that more massive stars evolve faster, leading to progressively larger spacing between isochrones, and consequently a better relative precision in age determinations for a given evolutionary phase, as the mass increases.

The evolutionary speed is inversely proportional to the age-gradient calculated along one evolutionary track. In the regions of the HR diagram where the evolutionary speed is large, the age-gradient is small and the precision in estimating stellar ages is good. To explain let us define an effective temperature-luminosity error box, as given by observational uncertainties. If we move it across the HR diagram, in regions with small age-gradient we will encircle models with similar ages, leading to a precise age determination, while in regions of large age-gradient (slow evolutionary speed) within the same box there will be models with very different ages, leading to a less precise age estimate. In Fig. 1.2 (upper panel) we show the evolutionary speed. Moving from blue-purple towards red-orange regions the evolutionary speed increases allowing for progressively more precise age determinations.

In analogy to the age-gradient along a track we can calculate the mass-gradient along an isochrone. In this case, regions of small mass-gradient are regions where the stellar masses can be estimated with better precision. The mass gradient along isochrones is shown in Fig. 1.2, lower panel. In this case regions with larger mass-gradient (better precision) are in red.

To explore how the position in the HR diagram affects age and mass determinations, we generated

Figure 1.2: *Top:* evolutionary speed along stellar tracks in the HR diagram. Age-gradient is inversely proportional to this quantity. The colour coding is a scale from red-orange (fast evolution, small age-gradient, good age determination) to blue-purple (slow evolution, large age-gradient, less precise age determination). *Bottom:* mass-gradient calculated along isochrones. Red-orange regions are regions of low gradient (high precision in mass determination), blue-purple regions are regions of high mass gradient where masses are determined with worse precision. Symbols indicate the positions of the simulated stars before the random errors are added. Superimposed in white are some reference tracks and isochrones.

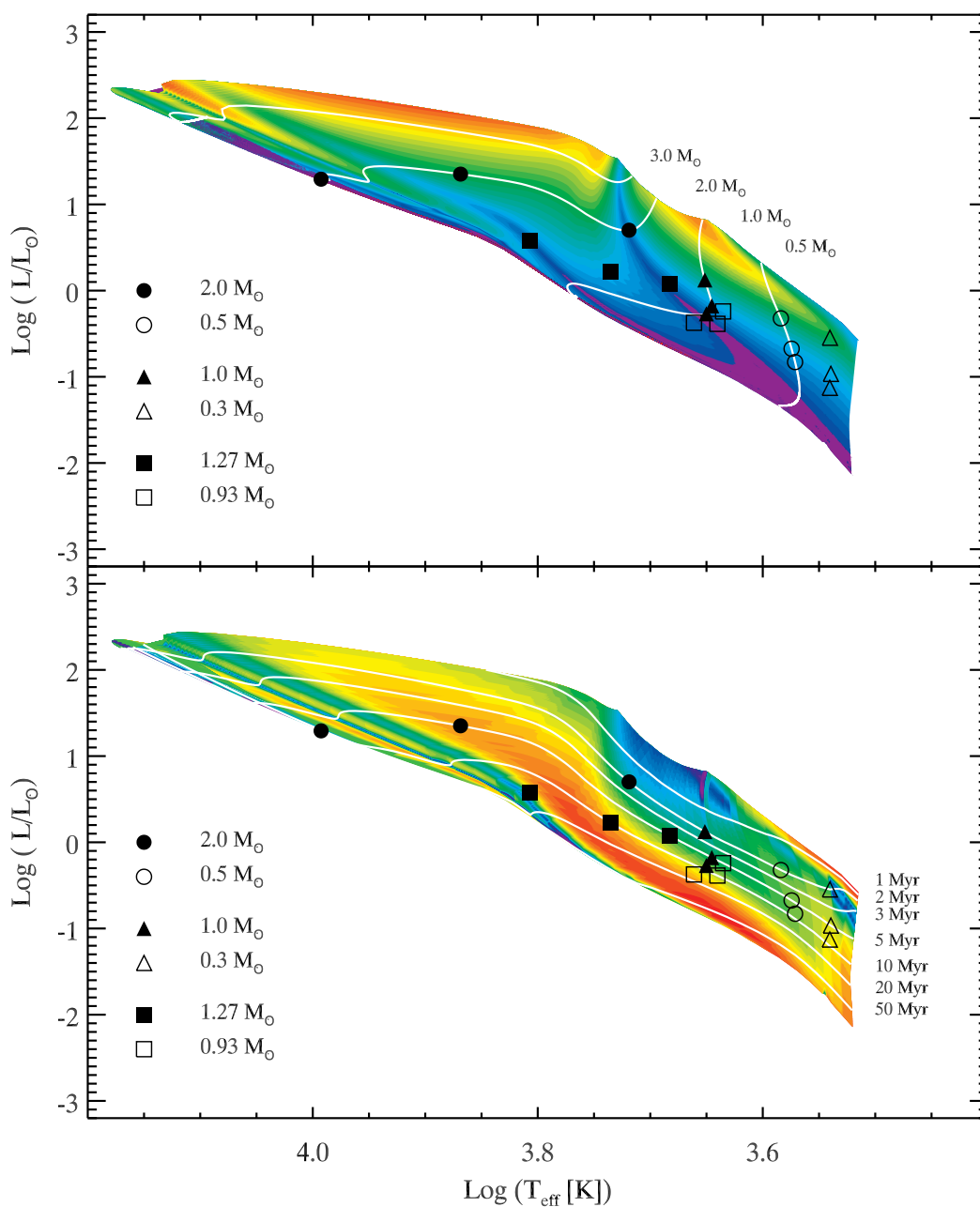


Table 1.1: Mass and ages combination for the simulated EBs. Systems C.x have the same masses of the binary system RXJ 0529.4+0041 A.

System	Primary Mass [M_{\odot}]	Secondary Mass $M[M_{\odot}]$	Age [Myr]
A.2	2.0	0.5	2
A.5	2.0	0.5	5
A.8	2.0	0.5	8
B.2	1.0	0.3	2
B.5	1.0	0.3	5
B.8	1.0	0.3	8
C.5	1.27	0.93	5
C.10	1.27	0.93	10
C.15	1.27	0.93	15

a sample of synthetic EBs for different masses and ages (see Table 1.1).

The simulations of EBs have been done by selecting models from the stellar library with $\alpha = 1.68$, $Y_p = 0.2485$ and $\Delta Y/\Delta Z = 2$. We fixed the Z value to $Z = 0.0125$, similar to our solar model ($Z_{\odot} = 0.0137$). For each combination of masses and ages we generated 100 systems. We added random Gaussian uncertainties to the quantities predicted by the models using standard deviation values equal to the typical errors in our data set ($\sigma_M = 0.015 - 0.020 M_{\odot}$, $\sigma_{\log T_{\text{eff}}} = 0.015$ dex, $\sigma_R = 0.05 R_{\odot}$ and $\sigma_{\log L} = 0.1$ dex). To simulate the observed errors behaviour of EBs, we allowed for random errors in the primary star temperature, $T_{\text{eff},1}$, keeping the ratio of primary-to-secondary effective temperatures, $T_{\text{eff},1}/T_{\text{eff},2}$, fixed. We allowed for independent errors in the radii, R_1 and R_2 . Luminosities are calculated from the temperatures and radii after the errors have been added.

For each simulated system, we applied our Bayesian method to recover the best ages and masses. Since we have chosen to fix $Z = 0.0125$, we fixed it also in the recovery method, which is equivalent to using a prior $f(\zeta) = \delta(\zeta - 0.0125)$ in equations (1.7a) and (1.7b), where δ is Dirac's delta function equal to 1 for $\zeta = 0.0125$ and equal to 0 elsewhere. We ran the method both with a flat prior defined over the whole mass interval and applying a Gaussian prior to the simulated mass. The Gaussian prior is centred on the simulated value of the mass and its σ is of the order of the typical error for the dynamical masses available in the literature (few %). We calculated stellar ages for the single stars and also for the systems. In this last case coevality is imposed by considering $G_C(\tau) = G_P(\tau) \times G_S(\tau)$, i.e. the product of primary and secondary marginal age distributions.

The results for the complete set of simulations are shown in Table 1.2 where we report the percentage of cases in which the simulated age and mass fall within the confidence interval. From the table it is clear that the method is very successful in recovering the simulated values. When no systematic errors are present (in both the model and the data) and if the random error estimates are reliable, we can expect the results of the method for real data to be very robust. Unfortunately this ideal situation is seldom realized in reality, but it is worth noticing that the method is intrinsically able to give a good fit for almost all the regions of the HR diagram.

The fraction of *good recoveries* or *success rate* can be related to the position of the stars in Fig. 1.2. For example the secondary star of the B.x systems –a $0.3 M_{\odot}$ star– is moving towards slower phases of its Hayashi tracks and consequently the fraction of good age recoveries is decreasing with increasing age. Several other things are worth noticing about the recovery fractions in Table 1.2:

- Firstly we want to emphasize the power of the Gaussian mass prior, i.e. its large informative value. In almost all cases where the Gaussian mass prior is imposed, the recovery fraction raises to 100%. This might look obvious but we have to recall that dynamical masses are usually the most reliable data available for a binary system. Moreover it is important to notice that the inclusion of the Gaussian prior leads to a strong improvement also for the age estimates.
- Secondly we want to mention the power of the coevality prior. Fig. 1.3 shows on the left the distribution of the difference between the logarithm of the best fit age and the logarithm of the simulated age for each star. The standard deviation of this distribution is $\sigma = 0.185$ dex. The inset plot shows the recovered ages for those stars giving a bad fit, meaning that the simulated age is outside the 68% confidence interval. The fraction of these bad-fit cases is 19% of the total simulated stars.

In the central panel the stars in each system are paired together and the age of the system is evaluated from the composite age distribution $G_C(\tau)$. The differences between the resulting best ages and the simulated ages show a much narrower distribution, with $\sigma = 0.062$, almost 3 times smaller than the σ for the single stellar ages. Hence using the coevality prior strongly reduces the error in the best age estimate.

The rightmost panel of Fig. 1.3 shows the difference between the logarithms of the primary and secondary components' ages for each pair. This distribution has a $\sigma = 0.257$, which is a factor $\sqrt{2}$ larger than the σ computed for the single stars' ages. Hence the intra-system age-difference distribution is consistent with the two stellar ages being randomly drawn from the single star age distribution. We note that in 13% of the cases the two components are found to be non coeval, meaning that the two uncertainty intervals do not overlap; these systems are shown in the inset diagram. Nevertheless, for all the non coeval cases, using the

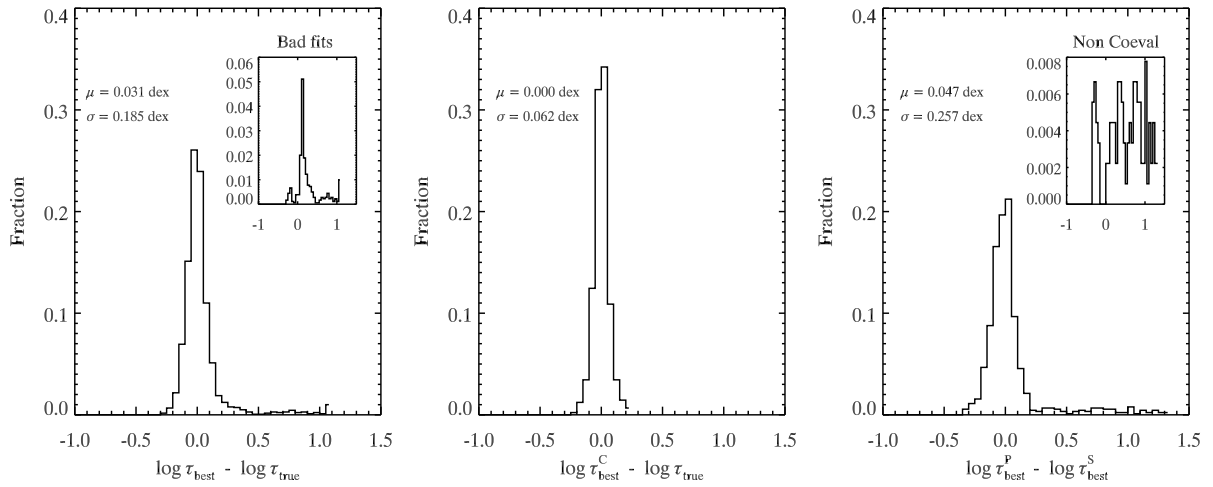
composite age distribution allows to find a system age that is in very good agreement with the simulated one. It is clear that the tail of non coeval systems disappears in the central diagram. This is due to the fact that only the age of one star is poorly determined, while the other component still has a very informative $G(\tau)$, which then drives the composite distribution towards the simulated value.

This is a remarkable result on its own. It is sometimes noted in the literature that evolutionary models are not able to fit binary data for the same age and ad hoc solutions are invoked to reconcile the models and the observation. Here, we demonstrated that not being able to reproduce both components in a binary system with the same isochrone does not necessarily imply that the stars are not coeval or that they are coeval but the models are not able to reproduce this coevality. On the contrary, an age difference or even an age mismatch can simply be a consequence of the observational errors in the HR diagram. It is indeed possible that the random scatter of the positions of coeval stars acts in opposite directions for the two components, making one look older and the other younger, to the point that they might be considered as non-coeval. The actual expected artificial age difference depends on the region of the HR diagram where the two stars are located, and on their errors.

As an example we consider the work by Kraus & Hillenbrand (2009) who analyse the binary population in the Taurus-Auriga association. They found that, in general, stars in physical pairs are more coeval than the association as a whole, with significantly smaller intra-binary age spread than for randomly paired stars selected among the association's members. Nevertheless the authors also find that some of the binaries show an intrinsic age spread larger than what observed for the bulk of the pairs and not consistent -within the errors- with the hypothesis of coeval pairs. They suggest that these outliers can be multiple system with unrecognized companions or stars seen in scattered light or also stars with disk contamination. While this can certainly be the case, we want to point out that the observational errors themselves –even when one might think that they are completely under control as in our simulations– can be partially responsible for an artificially large age-spread (or non-coevality) within a binary system.

- Third, we note that the actual number of good recoveries is a complex function of the stellar position. Is it true that the mass- and age-gradient visualization of Fig. 1.2 can help understanding this function, but we have to warn the reader that those gradients are calculated along isochrones and tracks respectively. The real gradients are 2D functions defined not only along curves. In particular there are regions of the HR diagram where the gradient along tracks and isochrones is quite different from the gradient in the perpendicular direction. Hence in these regions the recovery fraction can be different than what expected by looking at Fig. 1.2 alone. For example, the mass recovery fraction of the primary star of the B.8 case is lower than the B.5 case, even though the B.8 case is in a zone of lower mass gradient (better mass resolution).

Figure 1.3: *Left:* distribution of the difference between the logarithm of the recovered age for the single stars and the logarithm of the simulated age. The inset shows the distribution of age differences only for the stars for which the simulated age is outside of the 68% confidence interval. *Center:* same as left, but the recovered age is obtained from the composite age distribution for each simulated binary system. *Right:* Distribution of the differences between the logarithm of the primary's recovered age and the logarithm of the secondary's recovered age for each system. The inset shows the distribution of age differences for those systems whose primary and secondary components have disjoint 68% age confidence interval and are considered as non coeval.



- As a final remark about Table 1.2 we point out that in some of the cases in which the Gaussian mass prior is imposed the number of good ages recoveries slightly decreases. We investigated this behaviour and observed that it depends on the detailed morphology of the 2D posterior probability in the $\mu - \tau$ space. As an example, consider the primary star for the C.10 case. The success-ratio in the age recovery decreases from 83% to 72% for this star when the Gaussian mass prior is applied.

We show in Fig. 1.4 one of these drop-out cases. The reason why the age for this particular star is not recovered anymore when the prior is included can be easily understood. The Gaussian prior is causing an increase in the relative precision for the marginal distribution, $G_{\text{Gauss}}(\tau)$. This can be seen in the right panel of the figure where the $G_{\text{Gauss}}(\tau)$ distribution has a clearly larger mode and is narrower than $G_{\text{Flat}}(\tau)$. One can notice that the right border of the confidence interval for $G_{\text{Flat}}(\tau)$ is already quite close to the simulated age value of 10 Myr, which is barely within the 68% confidence interval. Hence it is the shrinking of the confidence interval –when the Gaussian prior is applied– that causes the simulated age value to drop out of the 68% confidence interval. Also the actual number of dropouts is related to the detailed structure of the 2D mass and age gradients.

Nevertheless, given that in the vast majority of the cases the mass prior is leading to an improvement of the fit, we consider these drop-out cases of minor importance and will make use of the Gaussian mass prior when dealing with real systems.

1.5 THE DATA SET

The number of PMS stars with direct mass measurements amounts nowadays to about 30 objects. The sample we used consists of 25 PMS and 2 MS stars, whose properties are summarized in Table 1.3.

Among the 27 objects 10 are PMS stars found in eclipsing binary systems (EB). We included the MS $3.1 M_{\odot}$ star TYCrA A and $2.1 M_{\odot}$ star EK Cep A in our sample as well, since their companions are PMS stars in EB systems and we tried to fit both components of binary systems when possible (see Sect.1.8). For EBs the masses, radii, and effective temperature ratios of the two components can be accurately inferred. However the absolute values of the effective temperatures, which rely on the determination of the primary’s Spectral Type and some Spectral Type- T_{eff} relationship, can be affected by systematic errors and constitute a severe source of uncertainty. As an example Hillenbrand & White (2004) pointed out that the main sequence empirical scales used for deriving temperatures from the spectral types might cause systematic temperature offsets when applied to PMS stars, due to the different values of surface gravity for a given spectral type (see also Luhman et al. 1997).

Figure 1.4: A particular realization for the primary star of the C.10 system. In this particular case the age is well recovered in the flat mass prior case and not recovered when the Gaussian mass prior is imposed. *Left:* the HR diagram position for the star with superimposed some reference isochrones (9,10,11 Myr) and tracks (1.17,1.27 and 1.37 M_{\odot}). The cross indicates the position after errors are added, the filled circle represents the original position of a 1.27 M_{\odot} , 10 Myr star. *Center:* 2D posterior probability contours. Dotted line is for the case with flat mass prior and solid line for the case with Gaussian mass prior. *Right:* Marginal age distributions. Vertical lines indicate the confidence interval. Dotted and solid line as for the central panel.

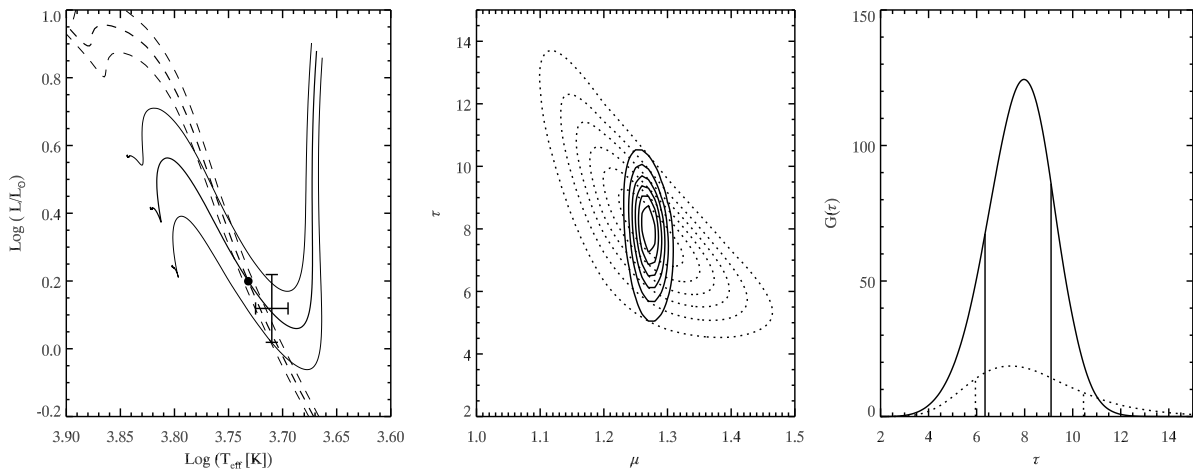
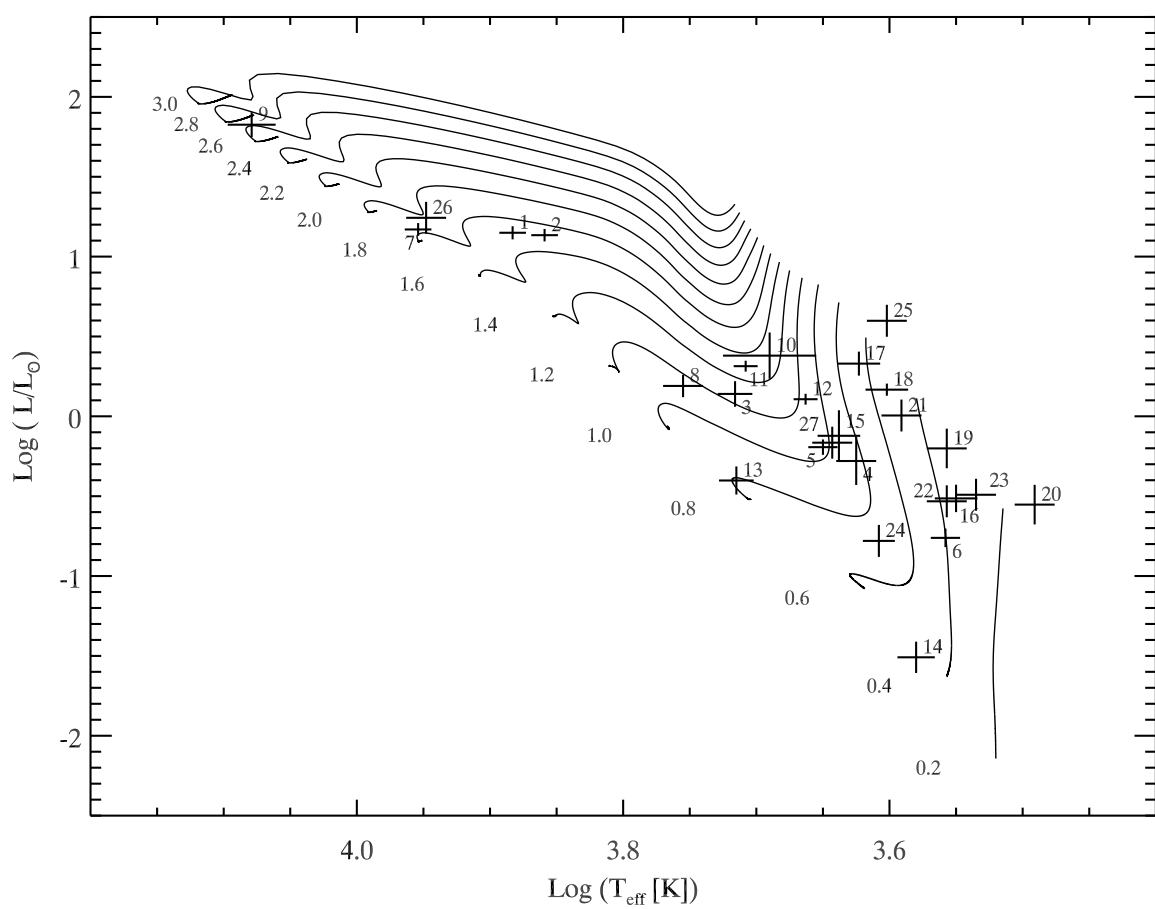


Table 1.2: Percentage of cases in which simulated ages and masses are recovered within the 68% uncertainty interval. P indicates the primary stars in the systems, S the secondary, C stands for Coeval, indicating the cases in which the product of the marginal age distributions of the primary and secondary star $G_P(\tau) \times G_S(\tau)$ is used to infer the age of the whole system. Flat and Gaussian are the adopted mass priors.

System	A.2			A.5			A.8		
	P	S	C	P	S	C	P	S	C
Flat									
Ages	87	92	83	100	74	100	0	79	54
Masses	91	68	-	98	72	-	78	79	-
Gaussian									
Ages	83	98	100	97	94	97	0	82	77
Masses	100	100	-	100	100	-	100	100	-
System	B.2			B.5			B.8		
	P	S	C	P	S	C	P	S	C
Flat									
Ages	94	98	97	96	72	84	95	62	81
Masses	77	76	-	77	71	-	68	73	-
Gaussian									
Ages	100	100	100	94	94	96	92	83	83
Masses	100	100	-	100	100	-	100	100	-
System	C.5			C.10			C.15		
	P	S	C	P	S	C	P	S	C
Flat									
Ages	95	98	89	83	93	78	87	86	94
Masses	82	74	-	100	68	-	86	84	-
Gaussian									
Ages	89	94	93	72	88	58	71	77	78
Masses	100	100	-	100	98	-	100	100	-

Figure 1.5: The HR diagram for our data set. The labels correspond to the ID column in Table 1.3. Superimposed are stellar tracks calculated with $\alpha = 1.68$, $\Delta Y/\Delta Z = 2$ and $Y_p = 0.2485$ and $Z = 0.0125$. The values of the mass –in solar units– are displayed on the left of the corresponding track.



Of the 27 stars in the sample, 6 are found in astrometric/spectroscopic systems (AS), i.e. systems in which the components can be resolved as separate point sources using interferometry. Combining astrometry and line-of-sight velocity measurements the masses of the components are determined in a distance-independent way. With this technique the radii of the components are not measurable, though.

The last 9 objects have masses measured using their circumstellar disks keplerian velocities obtained by means of spectroscopy. The mass for the central star can be determined only if the linear value of the orbital radius at which the velocity is measured is known. Hence stellar masses are in this case distance-dependent. The two stars in the UZ Tau E system form a binary, and their masses are separated using combined spectroscopic measurements for the circumstellar disk and the stellar velocities (DKS).

A very similar sample was already studied in Mathieu et al. (2007) and Stassun (2008) and we refer the reader to the first of these papers for a detailed description of the different observational techniques and the different kind of uncertainties affecting them. Compared to Mathieu et al. (2007) there are some distinct objects in our sample though. The 2M0535-5 brown dwarf EB (Stassun et al. 2006) was excluded because the stellar dynamical masses are smaller than those currently present in the Pisa database. The recently discovered PMS EB ASAS J052821+0338.5 (Stempels et al. 2008) has been added to the sample. We also included the AS binary HD 113449 (Cusano et al. 2010) for which we have slightly different parameters from an updated analysis (Cusano, *private communication*).

The luminosities and effective temperatures for our complete data set are displayed in Fig. 1.5. Overplotted are stellar tracks for $\alpha = 1.68$, $\Delta Y/\Delta Z = 2$ and $Y_P = 0.2485$. We will refer to this set of parameters Ξ as our standard or reference set. In the case of Fig. 1.5 the tracks are calculated for a value of $Z = 0.0125$, similar to the metallicity of our standard solar model (i.e., $Z_\odot = 0.0137$).

For several systems, [Fe/H] values are available from direct spectroscopic measurements. We used the [Fe/H] determinations by D’Orazi et al. (2009) and by D’Orazi et al. (2011) for the systems in Orion and Taurus-Auriga, respectively. Only 4 stars are left without a [Fe/H] measurement. In order to convert the observed [Fe/H] into the global metallicity Z_{ob} , we followed eq. (2) in Gennaro et al. (2010), adopting $(Z/X)_\odot = 0.0181$ by Asplund et al. (2009). Although the Pisa PMS models have been computed adopting the Asplund et al. (2005) heavy elements solar mixture, the seeming inconsistency is inconsequential since models computed with Asplund et al. (2005) and Asplund et al. (2009) but with the same total metallicity Z are essentially indistinguishable (see detailed discussion in Tognelli et al. 2011).

A point worth mentioning is that among the objects listed in Table 1.3 there are a few cases that appear peculiar. Their location in the HR diagram is indeed incompatible with that of stars of

similar mass. By looking at the available dynamical masses, luminosities and temperatures we identified four of these peculiar objects, namely NTT 045251 A, UZ Tau Ea, BP Tau, and MWC 480 (see Table 1.3).

- NTT 045251 A is close to RXJ 0529.4 Ab and V1174 Ori A in the HR diagram, with approximately the same luminosity and T_{eff} . However NTT 045251 A is more massive than the other two stars by 0.4-0.5 M_{\odot} . We checked that this discrepancy can not be reconciled even by assuming that the metallicity of NTT 045251 A is 0.4 dex larger than that of RXJ 0529.4 Ab or V1174 Ori A.
- UZ Tau Ea, $M = 1.016M_{\odot}$, has a T_{eff} similar to V1174 Ori B, DM Tau, CY Tau, and NTT 045251 B which have lower masses, between 0.55 - 0.8 M_{\odot} . Moreover the star is colder than RXJ 0529.4 Ab and V1174 Ori A by about 850 K in spite of their similar masses, luminosities, and [Fe/H].
- BP Tau, $M = 1.320M_{\odot}$, is significantly colder ($\Delta T_{\text{eff}} \gtrsim 1000$ K) and fainter ($\Delta \log L/L_{\odot} \approx 0.9$) than RXJ 0529.4 Aa and EK Cep B, although it is slightly more massive and the metallicities are similar. In addition this star is fainter and colder than the 0.96 M_{\odot} HD 113449, which has a similar metallicity. This is not easy to explain because the minimum luminosity of a 1.3 M_{\odot} model is always larger than that achieved by a 0.9-1.0 M_{\odot} star approaching the ZAMS, as in the case of HD 113449 A.
- MWC 480 ($M = 1.65M_{\odot}$ and [Fe/H] = -0.01 dex) is located in the HR diagram between EK Cep A ($M = 2.02M_{\odot}$ and [Fe/H] = 0.07 dex) and the RS Cha system ($M = 1.87, 1.89M_{\odot}$ and [Fe/H] = 0.17 dex). We checked with our models that the difference in [Fe/H] can justify neither the similar luminosities of MWC 480 and EK Cep nor the higher luminosity of MCW 480 with respect to the RS Cha stars.

1.6 THEORETICAL VS. DYNAMICAL MASSES – THE STANDARD SET OF MODELS

In this section we show the comparison of the whole data set with our evolutionary models. We limited the analysis only to the standard set of models, i.e the Ξ class with $\alpha = 1.68$, $\Delta Y/\Delta Z = 2$ and $Y_p = 0.2485$. Section 1.7 is dedicated to the comparison of models with different meta-parameters, Ξ . Since radii are not available for each star in the data set, the comparison was done in the HR diagram. With the notation of Sect. 1.2, this means $\mathbf{q} = (\log T_{\text{eff}}, \log L/L_{\odot})$. In the

Table 1.3: List of stellar properties.

ID	Name	Type	Mass [M_{\odot}]	Radius [R_{\odot}]	$\log T_{\text{eff}}$ [K]	$\log L$ [L_{\odot}]	[Fe/H]	Ref.
01	RS Cha A	EB	1.890 ± 0.010	2.150 ± 0.060	3.883 ± 0.010	1.149 ± 0.041	0.17 ± 0.01	And91, Rib00, Ale05
02	RS Cha B	EB	1.870 ± 0.010	2.360 ± 0.060	3.859 ± 0.010	1.136 ± 0.039	0.17 ± 0.01	And91, Rib00, Ale05
03	RXJ 0529.4 ¹ Aa	EB	1.270 ± 0.010	1.440 ± 0.050	3.716 ± 0.013	0.140 ± 0.080	-0.01 ± 0.04	Cov04, Dor09
04	RXJ 0529.4 ¹ Ab	EB	0.930 ± 0.010	1.350 ± 0.050	3.625 ± 0.015	-0.280 ± 0.150	-0.01 ± 0.04	Cov04, Dor09
05	V1174 Ori A	EB	1.009 ± 0.015	1.339 ± 0.015	3.650 ± 0.011	-0.193 ± 0.048	-0.01 ± 0.04	Sta04, Dor09
06	V1174 Ori B	EB	0.731 ± 0.008	1.065 ± 0.011	3.558 ± 0.011	-0.761 ± 0.058	-0.01 ± 0.04	Sta04, Dor09
07	EK Cep A	EB	2.020 ± 0.010	1.580 ± 0.015	3.954 ± 0.010	1.170 ± 0.040	0.07 ± 0.05	Pop87, Mar93
08	EK Cep B	EB	1.124 ± 0.012	1.320 ± 0.015	3.755 ± 0.015	0.190 ± 0.070	0.07 ± 0.05	Pop87, Mar93
09	TY CrA A	EB	3.160 ± 0.020	1.800 ± 0.100	4.079 ± 0.018	1.826 ± 0.078	-	Cas98
10	TY CrA B	EB	1.640 ± 0.010	2.080 ± 0.140	3.690 ± 0.035	0.380 ± 0.145	-	Cas98
11	ASAS 052821 ² A	EB	1.387 ± 0.017	1.840 ± 0.010	3.708 ± 0.009	0.314 ± 0.034	-0.15 ± 0.20	Ste08
12	ASAS 052821 ² B	EB	1.331 ± 0.011	1.780 ± 0.010	3.663 ± 0.009	0.107 ± 0.034	-0.15 ± 0.20	Ste08
13	HD 113449 A	AS	0.960 ± 0.087	-	3.715 ± 0.013	-0.402 ± 0.088	-0.03 ± 0.10	Pau06, Cus10
14	HD 113449 B	AS	0.557 ± 0.050	-	3.580 ± 0.014	-1.509 ± 0.098	-0.03 ± 0.10	Pau06, Cus10
15	NTT 045251 ³ A	AS	1.450 ± 0.190	-	3.638 ± 0.016	-0.122 ± 0.160	-	Ste01
16	NTT 045251 ³ B	AS	0.810 ± 0.090	-	3.550 ± 0.016	-0.514 ± 0.086	-	Ste01
17	HD 98800 Ba	AS	0.699 ± 0.064	-	3.623 ± 0.016	0.330 ± 0.075	-0.20 ± 0.10	Bod05, Las09
18	HD 98800 Bb	AS	0.582 ± 0.051	-	3.602 ± 0.016	0.167 ± 0.038	-0.20 ± 0.10	Bod05, Las09
19	UZ Tau Ea ^a	DKS	1.016 ± 0.065	-	3.557 ± 0.015	-0.201 ± 0.124	-0.01 ± 0.05	Pra02, Dor11
20	UZ Tau Eb ^a	DKS	0.294 ± 0.027	-	3.491 ± 0.015	-0.553 ± 0.124	-0.01 ± 0.05	Pra02, Dor11
21	DL Tau ^a	DK	0.720 ± 0.110	-	3.591 ± 0.015	0.005 ± 0.100	-0.01 ± 0.05	Sim00, HW04, Dor11
22	DM Tau ^a	DK	0.550 ± 0.030	-	3.557 ± 0.015	-0.532 ± 0.100	-0.01 ± 0.05	Sim00, HW04, Dor11
23	CY Tau ^a	DK	0.550 ± 0.330	-	3.535 ± 0.015	-0.491 ± 0.100	-0.01 ± 0.05	Sim00, HW04, Dor11
24	BP Tau ^a	DK	1.320 ± 0.200	-	3.608 ± 0.012	-0.780 ± 0.100	-0.01 ± 0.05	Joh99, Dut03, Dor11
25	GM Aur ^a	DK	0.840 ± 0.050	-	3.602 ± 0.015	0.598 ± 0.100	-0.01 ± 0.05	Sim00, HW04, Dor11
26	MWC 480	DK	1.650 ± 0.070	-	3.948 ± 0.015	1.243 ± 0.100	-0.01 ± 0.05	Sim00, HW04, Dor11
27	LkCa 15 ^a	DK	0.970 ± 0.030	-	3.643 ± 0.015	-0.165 ± 0.100	-0.01 ± 0.05	Sim00, HW04, Dor11

And91 = Andersen (1991); Rib00 = Ribas et al. (2000); Ale05 = Alecian et al. (2005); Cov04 = Covino et al. (2004); Dor09 = D’Orazi et al. (2009) Sta04 = Stassun et al. (2004); Pop87 = Popper (1987); Mar93 = Martin & Rebolo (1993); Cas98 = Casey et al. (1998); Ste08 = Stempels et al. (2008); Pau06 = Paulson & Yelda (2006); Cus10 = Cusano et al. (2010); Ste01 = Steffen et al. (2001); Bod05 = Boden et al. (2005); Las09 = Laskar et al. (2009); Pra02 = Prato et al. (2002); Sim00 = Simon et al. (2000); HW04 = Hillenbrand & White (2004); Dor11 = D’Orazi et al. (2011); Joh99 = Johns-Krull et al. (1999); Dut03 = Dutrey et al. (2003)

¹ Short form for RXJ 0529.4+0041

² Short form for ASAS J052821+0338.5

³ Short form for NTT 045251+3016

^a The error on the mass does not include the uncertainty on the distance.

case of stars with available [Fe/H] measurements, a Gaussian prior on the metallicity was applied after converting the [Fe/H] values and their errors into Z values with corresponding errors σ_Z :

$$f(\zeta) = \frac{1}{\sqrt{2\pi\sigma_Z^2}} \times \exp\left[-\frac{(\zeta - Z)^2}{2\sigma_Z^2}\right].$$

In the other cases a flat prior for $Z \in [0.007, 0.03]$ was used.

The outcomes of the full data set comparison are summarized in Fig. 1.6. The stars have been divided into subgroups: eclipsing binaries (EB), astrometric/spectroscopic binaries (AS) or disk kinematic stars (DK). The stars in the UZ Tau E system (DKS, i.e. disk kinematics plus spectroscopy to disentangle the components) are included in the DK sample for simplicity. The three subgroups are displayed from left to right. Each panel shows a comparison of the relative difference between model-inferred mass $-M_{\text{mod}}$ and measured dynamical mass $-M_{\text{dyn}}$. In the upper panels M_{mod} is derived by applying the Gaussian metallicity prior, when available. The lower panels show a comparison between the Gaussian Z prior case (empty symbols) and the flat Z prior case (full symbols). The symbols indicate the mode of the posterior probability; the asymmetric error bars indicate the 68% confidence interval as described in Sect.1.2. In the figure the dynamical mass errors are not added to the error budget. This is meant to purely show the precision of the masses estimated from the models given the observational uncertainties. However this is not a bad approximation for the total mass error budget, given that the quoted errors are of the order of 1% for most of the dynamical masses and up to 10% only in very few cases (see Table 1.3).

By looking at the figure, it is clear that EB masses are well recovered in almost every case but for V1174 Ori B. We will discuss this particular object more in detail in Sect.1.8.3. The general agreement becomes progressively worse for AS binaries and DK stars. For this last subgroup the inferred masses are systematically lower than the dynamical ones. We have to point out that for the latter class of objects the uncertainty on the distance is not included in the dynamical mass error estimate. This uncertainty propagates linearly in the mass uncertainty and quadratically in the luminosity uncertainty. The DK stars in our sample stars are part of the Taurus-Auriga star-forming complex which is located at about 150 pc from the Sun and has a radius of about 15 pc (see e.g Torres et al. 2009). Using an average distance to each star instead of its real distance may then cause a systematic error on the mass estimate of about 10% and on the luminosity of up to 20%. Part of the disagreement might also arise from the fact that the DK objects are T-Tauri stars, intrinsically variable. The temperatures and luminosities we adopt for them are all derived by Hillenbrand & White (2004). The authors try to minimize the effects of accretion luminosity using the I_C band to estimate the stellar luminosity. Nevertheless the estimated stellar luminosities might still be offset from their real values. An other problem might affect the temperature determination. Temperatures are determined from spectral types

using relations calibrated on dwarfs. As Hillenbrand & White (2004) point out, there might be a systematic temperature underestimate due to the fact that PMS stars of a given spectral type are generally warmer than dwarf counterparts. If the real stellar temperatures would be higher part of the discrepancy in our mass estimates would be removed, since larger masses would be needed to reproduce the observed stellar properties.

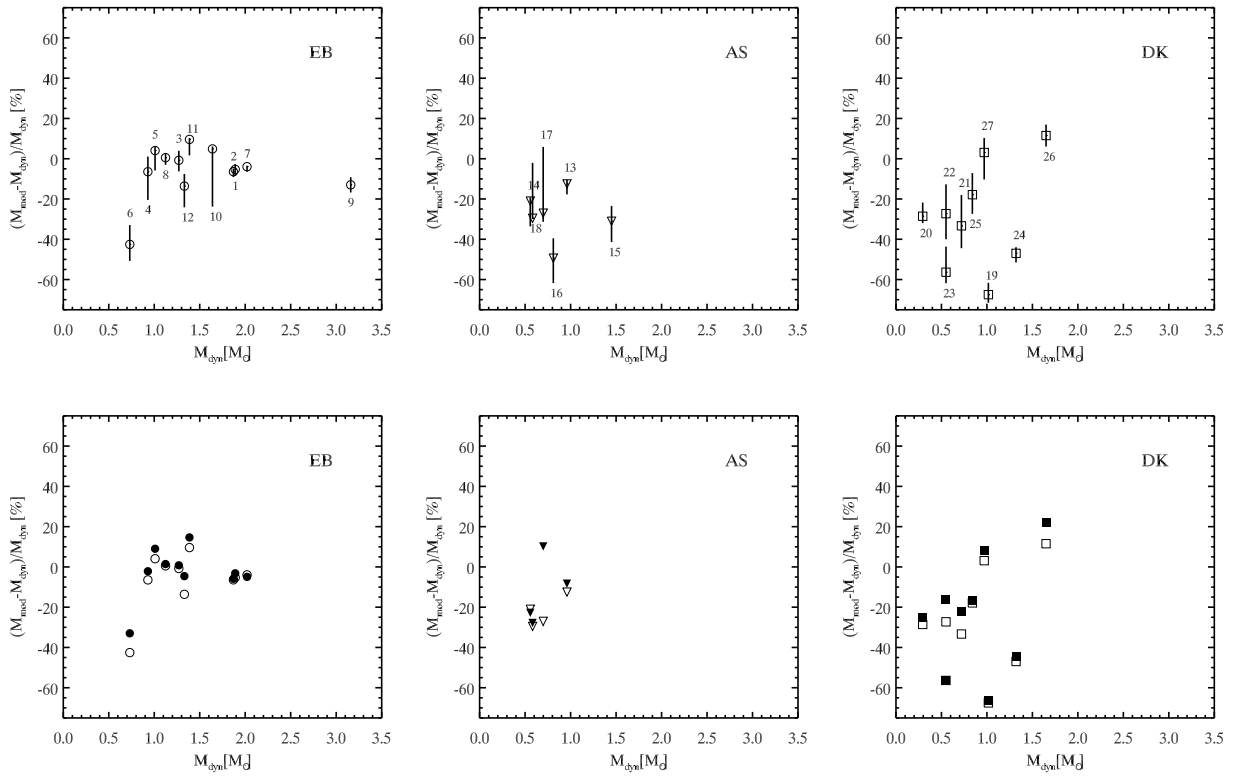
The lower panels of Fig. 1.6 show a quite surprising result. In the cases where we applied the Gaussian prior on the metallicity the final results for M_{mod} are usually in worse agreement with the M_{dyn} values when compared to the flat-prior case. It appears that applying the metallicity Gaussian priors we obtain, in general, lower masses values. This behaviour suggests that the Z_{ob} values used here might be too low. If we force the metallicity to assume systematically lower values than the real values by means of the Gaussian prior, then we naturally obtain lower values for the best masses. This is due to the fact that the lower the metallicity used in a stellar model, the hotter and more luminous the model is for a given mass.

We speculate here that part of the problem with the metallicity prior might reside in the low value of $(Z/X)_{\odot}$ used in the present work to convert the observed $[\text{Fe}/\text{H}]$ into Z . In the recent years this value has undergone a drastic change, specially after the introduction of non-LTE and 3D hydrodynamical atmospheric models for the analysis of Solar abundances (see Asplund et al. 2009 for a review about the topic). The traditional value of $Z_{\odot} \sim 0.02$ has been strongly revised towards much lower values, down to $Z_{\odot} 0.013 \div 0.014$ (see e.g., Serenelli et al. 2009 and references therein). There is still ongoing debate regarding solar heavy elements relative abundances and total metallicity, and the uncertainty on the absolute values is still large. Nevertheless the most recent results are going in the increasing direction for $(Z/X)_{\odot}$, thus reducing the difference with the traditional estimates. A change in $(Z/X)_{\odot}$ will be reflected directly into Z_{ob} since $(Z/X)_{\text{ob}} = (Z/X)_{\odot} \times 10^{[\text{Fe}/\text{H}]}$ and an increase in this quantity would naturally lead to a systematically larger M_{mod} .

1.7 ANALYSIS OF THE DATA USING DIFFERENT CLASSES OF MODELS

As described in Sect. 1.2.6, the ratio of the evidences for two classes of models –the Bayes Factor, BF – can be used to quantify which class of model is better in reproducing the data. Significantly better evidence of a model over an other is claimed when $BF < 0.1$ or $BF > 10$, i.e. when the two evidences differ by one order of magnitude or more (Kass & Raftery 1995). Since the evidence is calculated by marginalizing the *posterior* distribution over all the parameters of the model, the *prior* distribution of the parameters has to be considered as part of the model as well (see e.g. Bailer-Jones 2011 for an application of the Bayes Factor to discriminate between distinct models in a different astrophysical context).

Figure 1.6: Inferred masses from our standard set of isochrones compared with the dynamical masses from literature. Numbers correspond to the ID column of Table 1.3. *From left to right:* stars are divided in subset of eclipsing binaries (EB), astrometric/spectroscopic binaries (AS) and stars with masses inferred from disk kinematics (DK). *Upper panels:* best values are indicated by empty symbols. The asymmetric error bars represent the 68% confidence interval, as defined in Sect. 1.2. In these cases a Gaussian metallicity prior was applied when $[\text{Fe}/\text{H}]$ measurements were available. *Lower panels:* Comparison of the best masses inferred when the metallicity Gaussian prior is imposed (empty symbols, same as upper panels) and when we use a flat prior even for stars with $[\text{Fe}/\text{H}]$ measurements (filled symbols).



We calculated the evidence for each star in the 9 different meta-parameters cases and for each set Ξ we considered 4 different combinations of the prior distributions for the masses and the metallicities. The four combinations are: 1) flat mass prior - flat metallicity prior, 2) Gaussian mass prior - flat metallicity prior, 3) flat mass prior - Gaussian metallicity prior, 4) Gaussian mass prior - Gaussian metallicity prior. Hence we actually have $9 \times 4 = 36$ classes of models. After evidences have been calculated in the 36 cases for each of the 27 stars of the sample, the BFs have all been calculated by dividing each evidence value for a given star by the evidence value for that same star obtained using our standard class of models. The latter is identified by $Y_p = 0.2485$, $\Delta Y/\Delta Z = 2$ and $\alpha = 1.68$ for the 1) case.

The numerical values of the BFs are reported in Appendix 1.A. The Tables 1.7, 1.8, 1.9, and 1.10 display the BF values for the 1), 2), 3), and 4) prior cases respectively. Looking at each table, it is possible to see the change in the evidence among the different Ξ_j sets, within one of the 4 prior cases. From one table to the other, the corresponding entries are calculated for the same Ξ set but in the 4 different prior cases; by looking at these corresponding entries it is possible to see the role played by the prior choice and, actually, understand whether this choice is leading to an improvement of the overall fit or not.

The best way to compare different classes using the whole data set is to calculate the composite evidence for the full set of data. The natural extension of equation (1.11) is that the evidence for the whole data set –represented here by the set of observables $\{\mathbf{q}\}$ – can be written as:

$$\begin{aligned}
 f(\{\mathbf{q}\}|\Xi) &= \prod_k f(\mathbf{q}_k|\Xi) \\
 &= \prod_k \int f(\mathbf{q}_k, \mathbf{p}_k|\Xi) d\mathbf{p}_k \\
 &= \prod_k \int f(\mathbf{q}_k|\mathbf{p}, \Xi) f_k(\mathbf{p}|\Xi) d\mathbf{p}
 \end{aligned} \tag{1.13}$$

The index k runs over the stars in the sample and f_k indicates the specific prior distribution applied for k -th star.

We multiplied the evidences of the 27 stars of the sample to understand which class of model gives the best general result. In addition we restricted the product to stars belonging only to one type of system (EB, AS, DK). When using the whole data set we can compare only the 1) and 2) cases because the Gaussian metallicity prior can not be applied to the 4 stars for which $[\text{Fe}/\text{H}]$ measurements are not available. To compare also the 3) and 4) cases we additionally restricted the sub-samples to only stars with $[\text{Fe}/\text{H}]$ estimates. The classes with the largest composite evidence are listed in Table 1.4. The columns correspond to the different sub-samples. In the first block of the table all the possible cases are compared, i.e. cases 1) and 2) for all the objects –

with and without [Fe/H] measurements– and cases 1), 2), 3), and 4) using only object with [Fe/H] measurements. The other four blocks give the results when each of the prior cases is analysed separately. Again, in cases 3) and 4) we excluded objects without [Fe/H] measurements.

We point out that when a single star is considered the value of the evidence for different classes of models are mostly of the same order of magnitude (see the Tables in Appendix 1.A). Hence these global results are more sensitive to the few objects for which we observe major changes in the evidence between different classes. Nevertheless a general analysis is still important to understand the overall behaviour of stellar models in comparison to available data.

Looking at the first block of entries of Table 1.4 we notice that, for the whole sample, as for any subset of stars, the largest value of the evidence is reached in cases 2) or 4), i.e. when the Gaussian mass prior is imposed. This is expected because the prior on the dynamical mass is a much more informative prior than a flat one defined across the entire mass range of simulated models (i.e. $0.2\text{-}3.6 M_{\odot}$). We already pointed out in Sect.1.4 that, imposing the dynamical mass constraint improves indeed the quality of the fit for both the stellar mass, as expected, and the stellar ages. Here we have another way to look at this, as the evidence is a quantitative measure of the aforementioned fit improvement. The inclusion of the metallicity prior has a similar effect of increasing the evidence for the whole sample and for the sub-sample of EB stars (both restricted only to stars with [Fe/H] measurements). Nevertheless, it does not make a big difference for the AS and DK subgroups for which the best evidence is still reached in case 2) even when restricting only to stars for which [Fe/H] measurements are available. It is worth reminding that for most of the DK stars the [Fe/H] values we used are the average values for the Taurus-Auriga star-forming complex.

An other finding from Table 1.4 is that in almost all the cases, the class of models with $\Delta Y/\Delta Z = 2$, $Y_p = 0.23$ and $\alpha = 1.2$ meta-parameters is the one with the largest evidence. The only exception is the case of AS subset when only stars with known [Fe/H] are considered. For this subset the largest evidence is attained for the $\Delta Y/\Delta Z = 2$, $Y_p = 0.23$ and $\alpha = 1.9$ meta-parameters values. We have to point out that in this particular case only 4 stars are part of the subset and the evidence is only 1.13 times larger than in the $\Delta Y/\Delta Z = 2$, $Y_p = 0.23$, $\alpha = 1.2$ case.

These results are the counterpart of what we have already observed in Sect.1.6 regarding the mass underestimation by standard models. It was clear –specially by looking at the upper panels of Fig. 1.6– that the general trend for the standard set of models is to predict too low masses compared to M_{dyn} . A similar trend can be observed in Fig.3 of Mathieu et al. (2007); here all the considered sets of models show the same kind of behaviour in predicting too low stellar masses, with a mean difference that can be of the order of 20% or more. This suggests that the standard tracks are too hot and luminous when displayed in the HR diagram compared to the observed temperatures and luminosities for the given dynamical masses. A natural way to get a better

agreement with observations is to use colder and fainter set of models by adopting both a lower helium initial abundance and mixing length parameter α value.

This explains why the best overall evidence is achieved by the set with $\alpha = 1.2$, $Y_p = 0.230$, and $\Delta Y/\Delta Z = 2$. Similar low helium content for a given metallicity Z could be obtained also adopting the currently accepted primordial helium value, $Y_p = 0.2485$, together with a very small helium-to-metals enrichment ratio ($\Delta Y/\Delta Z \lesssim 1$, for $Z \approx 0.01 \div 0.02$). However, both choices are quite unlikely. In the former case the $Y_p = 0.23$ value is significantly lower than the recent independent results from extragalactic H II regions and Big Bang Nucleosynthesis theory (Izotov et al. 2007; Peimbert et al. 2007; Dunkley et al. 2009; Steigman 2010). Regarding the latter case, a $\Delta Y/\Delta Z \lesssim 1$ is smaller than the value suggested by Galactic chemical evolution models (Romano et al. 2005; Carigi & Peimbert 2008) or by nearby dwarf stars analysis (Jimenez et al. 2003; Casagrande et al. 2007; Gennaro et al. 2010).

The above analysis suggests that there are still some problems with the current generation of standard PMS models. However the significance of the disagreement between theory and observations is different depending on the subset of objects considered. Moreover, as it is clear from the tables of Appendix 1.A, for many of the objects of the sample the single-star evidence may be the largest for other values of the Ξ meta-parameters. Nevertheless this global test and the analysis of Sect. 1.6 both hint to the fact that a threefold effort is probably needed to a) improve the quality of the data specially assessing the systematic errors, b) better constrain the $\Delta Y/\Delta Z$, and $(Z/X)_\odot$ values and c) improve the physics of stellar models.

Table 1.4: Classes that provide the largest value for the composite evidence (see text).

	All data	EB	AS	DK
All cases				
With & without [Fe/H]	$\Delta Y/\Delta Z = 2, Y_p = 0.23$ $\alpha = 1.2, \text{ case 2}$	$\Delta Y/\Delta Z = 2, Y_p = 0.23$ $\alpha = 1.2, \text{ case 2}$	$\Delta Y/\Delta Z = 2, Y_p = 0.23$ $\alpha = 1.2, \text{ case 2}$	$\Delta Y/\Delta Z = 2, Y_p = 0.23$ $\alpha = 1.2, \text{ case 2}$
Only with [Fe/H]	$\Delta Y/\Delta Z = 2, Y_p = 0.23$ $\alpha = 1.2, \text{ case 4}$	$\Delta Y/\Delta Z = 2, Y_p = 0.23$ $\alpha = 1.2, \text{ case 4}$	$\Delta Y/\Delta Z = 2, Y_p = 0.23$ $\alpha = 1.9, \text{ case 2}$	$\Delta Y/\Delta Z = 2, Y_p = 0.23$ $\alpha = 1.2, \text{ case 2}$
Case 1)				
With & without [Fe/H]	$\Delta Y/\Delta Z = 2, Y_p = 0.23$ $\alpha = 1.2$	$\Delta Y/\Delta Z = 2, Y_p = 0.23$ $\alpha = 1.2$	$\Delta Y/\Delta Z = 2, Y_p = 0.23$ $\alpha = 1.2$	$\Delta Y/\Delta Z = 2, Y_p = 0.23$ $\alpha = 1.2$
Case 2)				
With & without [Fe/H]	$\Delta Y/\Delta Z = 2, Y_p = 0.23$ $\alpha = 1.2$	$\Delta Y/\Delta Z = 2, Y_p = 0.23$ $\alpha = 1.2$	$\Delta Y/\Delta Z = 2, Y_p = 0.23$ $\alpha = 1.2$	$\Delta Y/\Delta Z = 2, Y_p = 0.23$ $\alpha = 1.2$
Case 3)				
Only with [Fe/H]	$\Delta Y/\Delta Z = 2, Y_p = 0.23$ $\alpha = 1.2$	$\Delta Y/\Delta Z = 2, Y_p = 0.23$ $\alpha = 1.2$	$\Delta Y/\Delta Z = 2, Y_p = 0.23$ $\alpha = 1.2$	$\Delta Y/\Delta Z = 2, Y_p = 0.23$ $\alpha = 1.2$
Case 4)				
Only with [Fe/H]	$\Delta Y/\Delta Z = 2, Y_p = 0.23$ $\alpha = 1.2$	$\Delta Y/\Delta Z = 2, Y_p = 0.23$ $\alpha = 1.2$	$\Delta Y/\Delta Z = 2, Y_p = 0.23$ $\alpha = 1.2$	$\Delta Y/\Delta Z = 2, Y_p = 0.23$ $\alpha = 1.2$

1.8 APPLICATION TO BINARIES

In this section we will analyse the binary systems in our data set. For each of them we will check whether the models are able to reproduce the coevolution of the two stars. In all the cases where [Fe/H] measurements are available, we will implicitly use the corresponding Gaussian prior on Z in the marginalization of the probability distributions. In the four remaining cases a flat prior will be used in the available range of metallicities for our models set: $Z \in [0.007, 0.03]$.

We will mainly make use of the standard Ξ -set previously introduced. In the case of severe disagreement between the standard models and the observations, we will explore the possibility that non-standard Ξ -set might give a better agreement with the data.

Figures 1.7 and 1.8 show the HR diagrams with the data for each of the 6 EB and 3 AS systems with the best fitting tracks and isochrones for the standard set of models superimposed. The results are also summarized in Table 1.5. Some entries are missing in the table, corresponding to the cases in which the confidence intervals are poorly defined. This happens when the posterior probability is a very flat function and its mode falls outside the confidence interval. The best fit masses and ages are obtained by applying two different priors in mass, namely a flat and a Gaussian one in Figs. 1.7 and 1.8, respectively. In the case of EBs, for which stellar radii are measured, we have used the surface gravity vs. effective temperature diagram to compare the models with the data. This diagram has the advantage of combining the three measured quantities –mass, radius and temperature– hence representing the most stringent test for the models. For the AS systems we used the HR diagram. We display all the best fit models in the HR diagram for homogeneity.

The best values are obtained after marginalization in Z using a Gaussian prior. For displaying purposes only, we used isochrones and tracks with a specific Z value. The values for each system are obtained after transforming the observed [Fe/H] into Z_{obs} using $\Delta Y/\Delta Z = 2$, $Y_{\text{p}} = 0.2485$ and $(Z/X)_{\odot} = 0.0181$. We then took the closest Z available in our models database. In the case where [Fe/H] is not available we used $Z = 0.0125$, the closest to our solar-calibrated Z value. The overplotted isochrones correspond to the best system composite age, i.e. that obtained by maximizing $G_{\text{C}}(\tau) = G_{\text{p}}(\tau) \times G_{\text{s}}(\tau)$.

Given the large number and size, the figures relative to the each system’s subsection are presented in Appendix 1.B. The upper panels show the marginalized mass distributions and the lower ones the age distributions. The left and right panels show the results obtained using a flat and a Gaussian prior on the mass distribution respectively.

Table 1.5: Results from the comparison with the standard set of models. For the missing entries the confidence interval is poorly defined.

Name	M_{dyn} [M_{\odot}]	M_{mod} [M_{\odot}]	Flat Mass Prior		Gaussian Mass Prior		
			Age (stars) [Myr]	Age (system) [Myr]	M_{mod} [M_{\odot}]	Age (stars) [Myr]	Age (system) [Myr]
RS Cha A	1.890 ± 0.010	$1.79^{+0.07}_{-0.07}$	$8.40^{+0.65}_{-0.60}$	$8.50^{+0.50}_{-0.45}$	$1.85^{+0.02}_{-0.02}$	$8.00^{+0.25}_{-0.30}$	$8.00^{+0.15}_{-0.25}$
RS Cha B	1.870 ± 0.010	$1.74^{+0.06}_{-0.07}$	$8.70^{+0.75}_{-0.75}$		$1.82^{+0.01}_{-0.03}$	$7.95^{+0.30}_{-0.40}$	
RXJ 0529.4 A	1.270 ± 0.010	$1.25^{+0.09}_{-0.09}$	$8.35^{+3.45}_{-1.35}$	$6.25^{+1.20}_{-0.70}$	$1.27^{+0.01}_{-0.02}$	$8.70^{+1.20}_{-1.25}$	$6.90^{+1.15}_{-0.85}$
RXJ 0529.4 B	0.930 ± 0.010	$0.87^{+0.10}_{-0.12}$	$5.25^{+1.35}_{-0.70}$		$0.93^{+0.01}_{-0.02}$	$5.20^{+1.30}_{-0.70}$	
V1174 Ori A	1.009 ± 0.015	$1.04^{+0.06}_{-0.08}$	$5.85^{+0.50}_{-0.40}$	$7.90^{+0.45}_{-0.45}$	$1.01^{+0.01}_{-0.02}$	$5.85^{+0.50}_{-0.40}$	$7.40^{+0.35}_{-0.35}$
V1174 Ori B	0.731 ± 0.008	$0.42^{+0.08}_{-0.07}$	$9.85^{+0.45}_{-0.65}$		$0.73^{+0.00}_{-0.02}$	$8.45^{+0.55}_{-0.50}$	
EK Cep A	2.020 ± 0.010	$1.87^{+0.06}_{-0.06}$	$30.75^{+47.60}_{-8.15}$	$16.00^{+2.65}_{-2.55}$	$2.02^{+0.00}_{-0.02}$	$26.85^{+43.90}_{-6.55}$	$18.95^{+1.05}_{-2.05}$
EK Cep B	1.124 ± 0.012	$1.17^{+0.04}_{-0.03}$	$15.80^{+2.65}_{-2.60}$		$1.13^{+0.01}_{-0.01}$	$18.90^{+1.05}_{-2.00}$	
TY CrA A	3.160 ± 0.020	$2.61^{+0.29}_{-0.18}$	–	$4.25^{+2.75}_{-0.40}$	$3.16^{+0.01}_{-0.05}$	–	$3.75^{+2.65}_{-0.20}$
TY CrA B	1.640 ± 0.010	$1.52^{+0.24}_{-0.35}$	$3.10^{+2.55}_{-0.40}$		$1.64^{+0.01}_{-0.02}$	$18.90^{+1.05}_{-2.00}$	
ASAS 052821 A	1.387 ± 0.017	$1.54^{+0.08}_{-0.09}$	$3.50^{+0.50}_{-0.25}$	$3.50^{+0.15}_{-0.20}$	$1.39^{+0.01}_{-0.02}$	$3.25^{+0.15}_{-0.20}$	$3.45^{+0.10}_{-0.15}$
ASAS 052821 B	1.331 ± 0.011	$1.13^{+0.10}_{-0.10}$	$3.50^{+0.15}_{-0.20}$		$1.33^{+0.01}_{-0.02}$	$3.60^{+0.10}_{-0.20}$	
HD 113449 A	0.960 ± 0.087	$0.84^{+0.04}_{-0.05}$	$47.60^{+41.45}_{-2.40}$	–	$0.86^{+0.04}_{-0.04}$	$48.95^{+40.90}_{-1.80}$	–
HD 113449 B	0.557 ± 0.050	$0.44^{+0.03}_{-0.06}$	–		$0.48^{+0.02}_{-0.04}$	–	
NTT 045251 A	1.450 ± 0.190	$1.00^{+0.12}_{-0.14}$	$3.60^{+4.45}_{-0.65}$	$2.55^{+0.65}_{-0.35}$	$1.14^{+0.12}_{-0.11}$	$4.15^{+3.25}_{-0.90}$	$3.55^{+0.85}_{-0.50}$
NTT 045251 B	0.810 ± 0.090	$0.41^{+0.10}_{-0.10}$	$2.40^{+0.65}_{-0.35}$		$0.65^{+0.07}_{-0.08}$	$3.40^{+1.00}_{-0.50}$	
HD 98800 Ba	0.699 ± 0.064	$0.51^{+0.25}_{-0.02}$	$0.85^{+0.00}_{-0.20}$	$0.85^{+0.05}_{-0.15}$	$0.68^{+0.06}_{-0.07}$	$0.85^{+0.05}_{-0.10}$	$0.90^{+0.00}_{-0.10}$
HD 98800 Bb	0.582 ± 0.051	$0.41^{+0.17}_{-0.00}$	$0.95^{+0.00}_{-0.35}$		$0.56^{+0.05}_{-0.06}$	$1.00^{+0.00}_{-0.15}$	

Figure 1.7: HR diagrams with best fitting tracks and isochrones for the EB and AS binaries of our sample. Masses and ages are obtained using a flat mass prior and a Gaussian metallicity prior.

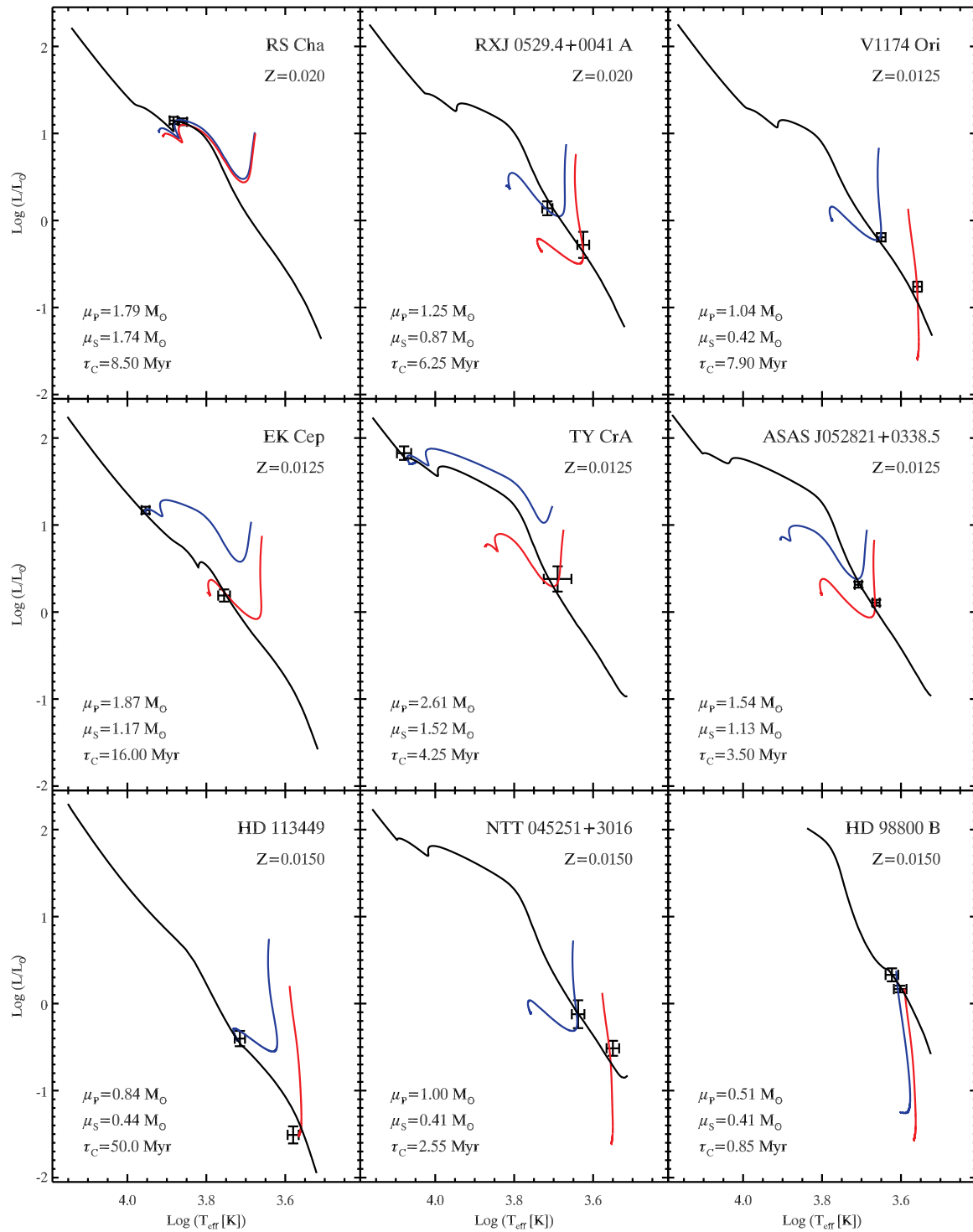
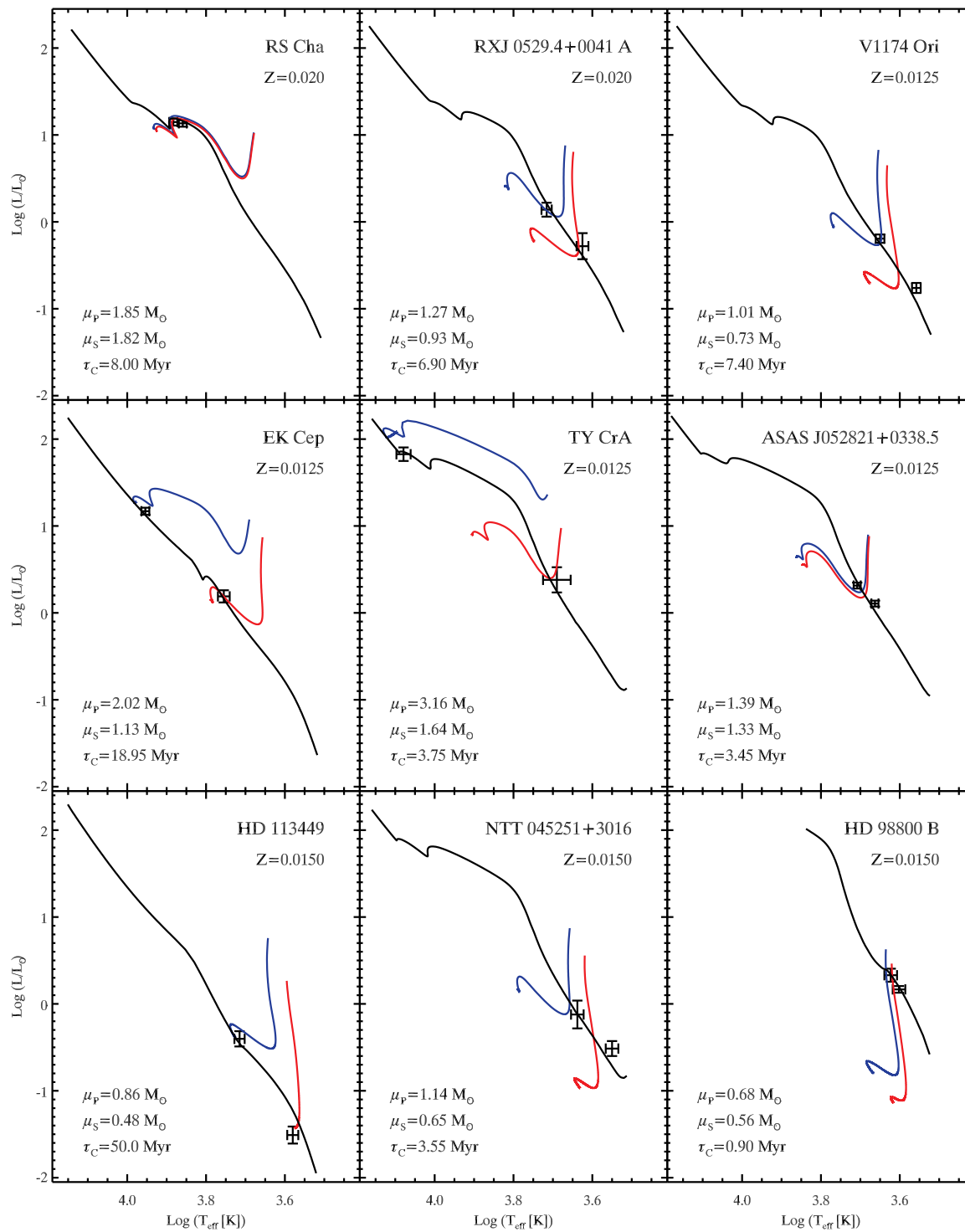


Figure 1.8: HR diagrams with best fitting tracks and isochrones for the EB and AS binaries of our sample. Masses and ages are obtained using a Gaussian mass prior and a Gaussian metallicity prior.



1.8.1 RS Cha

This double-lined EB is located in the η Cha cluster (Mamajek et al. 2000). The stellar masses and radii are from Alecian et al. (2005) who refined the values from the pioneering studies on binary stars by Andersen (1975, 1991). Alecian et al. (2005) also provide a spectroscopic measurement of [Fe/H]. Temperatures are taken from Ribas et al. (2000). Surface gravities are simply calculated as $|g| = GM/R^2$.

Previously thought to be a post-MS system (Jones 1969; Andersen 1975, 1991), the X-rays emission reported by Mamajek et al. (1999) clearly points to the PMS nature of this system. The two RS Cha components have very similar masses of $\sim 1.9M_{\odot}$ and are both close to approaching the Zero-Age MS. Recent literature estimates for the system age range from 6_{-1}^{+2} Myr (Luhman & Steeghs 2004) to 9.13 ± 0.12 Myr (Alecian et al. 2007b).

The outcomes of the comparison between our standard set of models and the RS Cha components' gravities and temperatures are shown in Fig. 1.9.

As already noted in Sect.1.6 the standard set of models slightly underestimates the mass values with $\mu_P = 1.79_{-0.07}^{+0.07}M_{\odot}$ and $\mu_S = 1.74_{-0.07}^{+0.06}M_{\odot}$ for the primary and secondary mass respectively. The dynamical masses fall outside these 68% confidence intervals, nevertheless the discrepancy is quite small –less than 5%– which is a very remarkable agreement. The relative precision of the mass estimates is strongly increased by the use of the Gaussian prior and also the mode of the mass marginal distributions for both components are more similar to the observed values with $\mu_P = 1.83_{-0.02}^{+0.02}M_{\odot}$ and $\mu_S = 1.82_{-0.03}^{+0.01}M_{\odot}$.

Even with the slight mass discrepancy, the results on the system's age are very robust. The age estimates of the two components remarkably agree among each other. From the single star's marginal age distribution we obtained the combined system age as $G(\tau)_{\text{RS Cha A}} \times G(\tau)_{\text{RS Cha B}}$. The estimated value for the system age in the case of a flat mass prior is $\tau_C = 8.50_{-0.45}^{+0.50}$ Myr which is narrowed down to $\tau_C = 8.00_{-0.25}^{+0.15}$ Myr when the Gaussian mass prior is imposed. It is worth noticing that the relative precision of the combined age is improved with respect to the single stellar ages estimates.

1.8.2 RXJ 0529.4+0041 A

The discovery of this double-lined EB located in the Orion star-forming region was reported by Covino et al. (2000). The same group refined the system parameters using new photometric observations in Covino et al. (2004). We adopt the data from the latter paper and the Orion [Fe/H] from D'Orazi et al. (2009).

Comparing the observed gravity and temperatures with our standard set of models yields stellar masses in agreement with the dynamical measurements with $\mu_P = 1.25^{+0.09}_{-0.09} M_\odot$ and $\mu_S = 0.87^{+0.10}_{-0.12} M_\odot$ when a flat mass prior is used. If a Gaussian prior is applied, then the precision improves by a factor of 10 for the estimated masses with $\mu_P = 1.27^{+0.01}_{-0.02} M_\odot$ and $\mu_S = 0.93^{+0.01}_{-0.02} M_\odot$. On the other hand the derived single stellar ages are in slight disagreement. Using a Gaussian mass prior, we obtain respectively $\tau_P = 8.70^{+1.20}_{-1.25}$ Myr and $\tau_S = 5.20^{+1.30}_{-0.70}$ Myr. Nevertheless, the two ages are both consistent with the composite age of the system, i.e. $\tau_C = 6.90^{+1.15}_{-0.85}$ Myr. The results for the standard set of models are summarized in Fig. 1.10.

By looking at the Bayes factors of Table 1.10, it appears that most of the age discrepancy might be ascribed to the poorer fit of the secondary star. For the primary star the standard set of models provides the second highest Bayes Factor value, 18.34, the highest being just 18.35 for the set with $\Delta Y/\Delta Z = 2, \alpha = 1.68$ but $Y_P = 0.23$. For the secondary the standard set provides a Bayes Factor that is ~ 1.5 times smaller than the one giving the largest evidence, i.e. $\Delta Y/\Delta Z = 2, \alpha = 1.20$ but $Y_P = 0.2485$. This is not enough to state that the latter set gives a significantly better agreement with the data, but using the latter set of meta-parameters yields an age of $6.30^{+1.65}_{-0.85}$ Myr, which is in agreement with the primary star's age within the uncertainty interval.

The fact that the secondary star is better fitted by cooler models (i.e. models with lower α) was already reported by D'Antona et al. (2000) and confirmed in Covino et al. (2004).

1.8.3 V1174 ORI

This double-lined EB was discovered by Stassun et al. (2004). We adopt stellar parameters from this paper and the average [Fe/H] abundances for Orion (D'Orazi et al. 2009).

As in the case of RXJ 0529.4+0041 A, the primary star of V1174 Ori is moving away from the Hayashi track, while the secondary is still fully convective. Also in this case the models show some difficulty in reproducing the secondary observables. The standard set of models –with a flat mass prior– predicts a secondary mass of $\sim 0.42 M_\odot$, much smaller than the dynamical mass ($\sim 0.7 M_\odot$). The primary mass is instead well recovered with $\mu_P = 1.04^{+0.07}_{-0.08} M_\odot$. The situation for the secondary does not improve much even when using the coldest set of models available.

It has been noted (see e.g. Hillenbrand & White 2004) that one of the problems in estimating the effective temperatures for PMS stars from the observed spectral type is the adoption of temperature scales that are calibrated on MS stars. For example Stassun et al. (2004) use the temperature scale for dwarf stars by Schmidt-Kaler in Aller et al. (1982). The same authors show how stellar models are not able to reproduce luminosities and temperatures for the secondary star and attribute the discrepancy to the non-adequacy of the dwarf spectral type to T_{eff} conversion when

applied to PMS stars.

At a given spectral type PMS stars are in general hotter than the corresponding MS stars. Their surface gravities indicate that a temperature scale intermediate between dwarfs and giants should be adopted. Hillenbrand & White (2004) suggest that temperature corrections as high as 100 K could be necessary to compensate for the temperature underestimates. We explored this possibility in the case of V1174 Ori, by artificially increasing the temperature of the primary by 100 K and keeping the effective temperature ratio between primary and secondary constant. The reason why we can not simply increase the effective temperature of the secondary, which is the main responsible of the disagreement with the models, is that in Stassun et al. (2004) this quantity is not directly and independently measured, but it follows from the determination of the primary effective temperature from the Spectral Type and the temperature ratio from the light curve. Hence, if any offset is present, it should be reflected in both components.

The results of the comparison of the modified observables with the standard set of models are shown in Fig. 1.12. The situation is only slightly improved compared to Fig. 1.11. The gain in the secondary mass estimate is that now the best mass is $\sim 0.49M_{\odot}$, not yet enough to be in agreement with the dynamical mass. However the primary mass is still recovered within the uncertainty interval. It is clear that a change in T_{eff} has a larger impact on the inferred stellar mass when a star is still in the vertical Hayashi track than when it is located on the almost horizontal Heyney track.

Even with the small improvement achievable by increasing the estimated T_{eff} , V1174 Ori remains a challenge for stellar evolution theory. However parallel observational efforts are required to assess the issues related to the effective temperatures determinations.

1.8.4 EK CEP

This system is known to be an EB for more than 50 years (Strohmeier 1959). Quite some time after its discovery it was recognized to host a $\sim 1.1M_{\odot}$ PMS star, together with a $\sim 2.0M_{\odot}$ primary already on its main sequence (Popper 1987). We adopted stellar parameters from this paper and the spectroscopic determination of [Fe/H] by Martin & Rebolo (1993).

With our standard set of models the stellar masses for EK Cep are not recovered within the 68% confidence interval (see Fig. 1.13). If we use a flat mass prior we obtain $\mu_P = 1.87^{+0.06}_{-0.06}M_{\odot}$ and $\mu_P = 1.17^{+0.04}_{-0.03}M_{\odot}$, while the measured dynamical values are $2.020 \pm 0.010M_{\odot}$ and $1.124 \pm 0.012M_{\odot}$ for primary and secondary, respectively. Hence the primary mass is slightly underestimated and the secondary mass slightly overestimated. It has to be noted that the absolute difference between model-predicted and dynamical masses are of the order of 7% and 4% hence

quite small. Nevertheless, the discrepancy are significant according to our definition of the confidence interval.

Given the Bayes Factors of Table 1.10, we have compared the data with models from the class with $\alpha = 1.20$, $Y_p = 0.23$, and $\Delta Y/\Delta Z = 2$, i.e. the one that gives the largest composite evidence for the system. The agreement is still not satisfactory. As shown in Fig. 1.14, a further improvement of the fit is achieved by assuming a higher metallicity (i.e. $Z = 0.0193$ rather than $Z = 0.0157$) as if the old $(Z/X)_\odot = 0.0231$ by Grevesse & Sauval (1998) was used instead of the recent one by Asplund et al. (2009). The inferred masses are in this case $\mu_P = 1.97^{+0.07}_{-0.06} M_\odot$ and $\mu_P = 1.12^{+0.14}_{-0.02} M_\odot$. This results are in very good agreement with those of Claret (2006), who using similar values, namely $Z = 0.0175$ and $\alpha = 1.3$, is able to reproduce the system observables.

This test shows how the success of a set of models in reproducing the observations might be severely affected by the current uncertainties on the meta-parameters. Paradoxically, in the case of EK Cep system models calculated with out-of-date meta-parameters seem to give a better agreement with the data than the state-of-the-art ones.

One interesting thing that this system shows about our method is the power of the combined system age marginal distribution, $G(\tau)_{\text{EK Cep A}} \times G(\tau)_{\text{EK Cep B}}$. As the primary star is already on the Main Sequence, its evolution is very slow, resulting in a very flat $G(\tau)$ and, consequently a very poor precision in the best age determination. Nevertheless the age of the system is very well determined -given the choice of the model class. As a consequence also the primary star has a very precise age determination, which is very valuable for MS stars. In the case of the standard set of model and Gaussian mass prior the system age is $\tau = 18.95^{+1.05}_{-2.05}$ Myr, while for the non-standard set used in this section, again with a Gaussian mass prior, we obtain $\tau = 26.55^{+0.85}_{-1.80}$ Myr.

1.8.5 TY CRA

This double lined EB is part of a hierarchical system with three or possibly four stellar components (see Chauvin et al. 2003). The fundamental parameters we adopted are taken from Casey et al. (1998). For this particular system we could not find any spectroscopic determination of $[\text{Fe}/\text{H}]$. Therefore, instead of applying a Gaussian prior on the metallicity, the marginalization over Z was made using a flat prior with $Z \in [0.007, 0.03]$, i.e. the range of metallicities available in our models grid.

As in the case of EK Cep, the primary star is already on the Main Sequence, while the slower evolving secondary is still on its Hayashi track. Similarly to the EK Cep case, our standard set of models is able to reproduce the secondary mass quite well, while the primary mass is once again

underestimated. The values we obtain when a flat mass prior is used are $\mu_P = 2.61^{+0.29}_{-0.18} M_\odot$ and $\mu_S = 1.52^{+0.24}_{-0.35} M_\odot$ while the dynamical masses are estimated to be $3.16 \pm 0.02 M_\odot$ and $1.64 \pm 0.01 M_\odot$ for the primary and secondary, respectively. The low relative precision of these model predictions –compared e.g to the case of EK Cep– are mainly due to the larger uncertainties on the effective temperatures and radii for the TY CrA system (see Table 1.3).

Also in this case, we tried to see whether the agreement between data and models might be improved by using the coldest set of models with $\alpha = 1.20$, $Y_P = 0.23$ and $\Delta Y/\Delta Z = 2$. As it is possible to see by comparing Figs. 1.15 and 1.16, there is a slight improvement in the primary mass determination, without losing the good agreement for the secondary mass. The results obtained with a flat mass prior are $\mu_P = 2.69^{+0.30}_{-0.18} M_\odot$ and $\mu_S = 1.49^{+0.24}_{-0.21} M_\odot$. The primary mass is still underestimated by about 15%, not a too bad result –in absolute terms– but further investigation is needed to explain this partial disagreement.

TY CrA A is on the MS, therefore its age is not well constrained. Nevertheless the mode of the age distribution for the primary is very close to the mode of the secondary, which has a better constrained age determination. From the composite age distribution $G(\tau)_{\text{TY CrA A}} \times G(\tau)_{\text{TY CrA B}}$ in the case of the standard set and applying a Gaussian mass prior we obtain $\tau = 3.75^{+2.65}_{-0.20}$ Myr. For the coldest set of models and still applying a Gaussian mass prior we obtain a slightly older age of $\tau = 5.20^{+3.05}_{-0.70}$ Myr. These age values are slightly older than the age found by Casey et al. (1998) who roughly estimate a system age of ~ 3 Myr. Also these authors show that the models have problems in consistently predicting the stellar observable for both components. While being able to reproduce the observed secondary properties, they also find that models overestimate the effective temperature of the primary star. This is equivalent to our finding of an underestimated stellar mass for the given T_{eff} and $\log g$.

1.8.6 ASAS J052821+0338.5

This is the most recently discovered double-lined EB in our data set. The stellar parameters are from Stempels et al. (2008). The two stars have very similar masses, and the slightly more massive primary ($1.387 \pm 0.017 M_\odot$) is just moving away from its Hayashi track while the secondary ($1.331 \pm 0.011 M_\odot$) is located just before the end of the fully convective phase. The [Fe/H] value we used is -0.15 ± 0.2 dex, i.e. the average of the quoted values for the primary (-0.2 ± 0.2 dex) and the secondary (-0.1 ± 0.2 dex) in Stempels et al. (2008).

The predictions of our standard set of models slightly differ from the measured masses. The values we obtain when a flat mass prior is used are $\mu_P = 1.54^{+0.08}_{-0.11} M_\odot$ and $\mu_S = 1.13^{+0.10}_{-0.10} M_\odot$. Therefore the primary mass is overestimated by $\sim 11\%$ and the secondary is underestimated by $\sim 15\%$. Stempels et al. (2008) provide a double solution for the system parameters depending

whether stellar spots are taken into account in the light-curve analysis (as in the case reported in Table 1.3) or not. We applied our method using also the measurements for the latter case and the results are shown in Fig. 1.18. Both of the predicted masses are in better agreement with the data in this case with $\mu_P = 1.53_{-0.10}^{+0.08} M_\odot$ and $\mu_S = 1.24_{-0.09}^{+0.11} M_\odot$. Hence for the primary mass the situation is slightly better with an overestimate of 10%, while the situation is much improved for the secondary which is now predicted to be 7% less massive than the observed value.

It is clear that the detailed modeling of the light curve plays an important role in determining stellar properties and, as a consequence, in constraining the models' predictions. Once again the models give an overall satisfactory agreement, being 10 or even 15% still a quite good error in stellar masses predictions. Nevertheless more work is needed to explain these differences.

The results for the age of the system are more robust with the two components having ages in good agreement. In the case where the light curve solution including star spots is used, we obtain a system age –using a Gaussian mass prior– of $3.45_{-0.15}^{+0.10}$ Myr. When using the light-curve solution without star spots, we instead obtain $3.65_{-0.20}^{+0.10}$ Myr. In both cases the age is much younger than what is found by Stempels et al. (2008) who, using solar metallicity models by Baraffe et al. (1998), found an age of ~ 10 Myr for the system. We used the $[\text{Fe}/\text{H}] \simeq -0.15$ dex quoted in the same paper to derive our Gaussian Z prior. This value is slightly sub-solar, hence part of the difference between our age estimate and that by Stempels et al. (2008) could be ascribed to that. Still it is quite hard, even using our solar metallicity models, to reproduce a $\sim 1.4 M_\odot$ star close to the base of its Hayashi track at such an old age like 10 Myr.

1.8.7 HD 113449

This system is an AS binary whose orbital parameters have been recently estimated by Cusano et al. (2010). Here we use slightly different parameters (yet unpublished) kindly provided by the same group after more accurate analysis of the data and the $[\text{Fe}/\text{H}]$ by Paulson & Yelda (2006).

As already noted by Cusano et al. (2010), there is a slight disagreement between dynamical and inferred masses by several sets of stellar models. Also the masses predicted by our standard set of stellar tracks are slightly underestimated. The primary mass is found to be $\mu_P = 0.84_{-0.05}^{+0.04} M_\odot$ while the secondary is $\mu_S = 0.44_{-0.06}^{+0.03} M_\odot$ (see also Fig. 1.19). From Table 1.5 we can see the primary dynamical mass of $0.960 \pm 0.087 M_\odot$ is still consistently recovered while for the secondary the dynamical mass of $0.557 \pm 0.050 M_\odot$ is outside the 68% confidence interval.

To see whether the discrepancy could be reduced, we used the coldest set of models and, in addition, we derived the Z value using the spectroscopic $[\text{Fe}/\text{H}]$ and the $(Z/X)_\odot = 0.0231$ by Grevesse & Sauval (1998). The results, displayed in Fig. 1.20, show a better agreement with the

observations. The improvement is not substantial, though, and the predicted stellar masses are in this case $\mu_P = 0.89^{+0.04}_{-0.05} M_\odot$ and $\mu_S = 0.45^{+0.03}_{-0.06} M_\odot$.

The stellar ages in this particular case are not very well determined. The two stars are indeed very close to their MS position, which makes age determination very hard. Nevertheless the primary shows a small peak in its $G(\tau)$ distribution at an age of $\tau \sim 50$ Myr (for both the standard and non-standard set of models). The secondary instead does not show any peak in the stellar age, with a very flat $G(\tau)$ slightly increasing towards the edge of our models age-interval (100 Myr). The system age is poorly defined as well.

1.8.8 NTT 045251+3016

The discovery of this AS binary was first reported by Steffen et al. (2001) from which we adopted the stellar parameters. In this case no spectroscopic [Fe/H] is available. This system is quite young and both the primary and the secondary are found in their fully convective phase along the Hayashi track. As pointed by Steffen et al. (2001), all the stellar models adopted by them predict too low masses for both components. The set of models that gives the best agreement with observations is the one by Baraffe et al. (1998) when a mixing length parameter $\alpha = 1.0$ is adopted. This is not surprising given that models with a lower α , being intrinsically colder, predict larger masses for given observed luminosities and temperatures.

With our standard set of models and using a flat mass prior, the two masses are found to be $\mu_P = 1.00^{+0.12}_{-0.14} M_\odot$ and $\mu_S = 0.41^{+0.10}_{-0.10} M_\odot$, severely lower than the dynamical masses by $\sim 30\%$ and $\sim 50\%$ respectively (see Fig. 1.21). From Tables 1.7 and 1.8 it is possible to see that for both of the components of NTT 045251+3016 the set of models that provides the largest Bayes Factor is, once again, the coldest set available ($Y_P = 0.23$, $\Delta Y/\Delta Z = 2$, $\alpha = 1.2$). When using this particular set and a flat mass prior, we obtain slightly larger masses of $\mu_P = 1.13^{+0.16}_{-0.13} M_\odot$ and $\mu_S = 0.50^{+0.13}_{-0.12} M_\odot$ (see Fig. 1.22). The improvement is not enough to obtain an agreement between predicted and observed mass for the secondary, while the primary mass, though still underestimated, is in agreement within the errors.

We report that using the BASE software (courtesy of Tim Schulze-Hartung, in prep) for analysing the system's astrometric measurements and radial velocities, slightly lower masses are predicted. The primary mass is found to be $\mu_P = 1.383 \pm 0.220 M_\odot$ (-4.60%) while the secondary is $\mu_S = 0.766 \pm 0.089$ (-5.41%).

Even with this latter improvements, there is still a larger disagreement in the predicted vs. dynamical mass for NTT 045251+3016 than what we found for the EBs cases or even the other two AS binaries. This suggests that part of the problem might reside in observations as well,

and we already noted in Sect. 1.5 the peculiar location of this star in the HR diagram given its measured mass. Apart from a theoretical effort, which is certainly needed, this system demands attention also from the observational side to exclude, e.g., higher order multiplicity that to-date interferometric observations are not capable to resolve.

Concerning the system composite age, the values we obtain when using a Gaussian mass prior are $\tau = 3.55^{+0.85}_{-0.50}$ Myr and $4.65^{+1.1}_{-0.65}$ Myr for the case of standard and coldest set of models, respectively.

1.8.9 HD 98800 B

This AS binary is part of a quadruple system. Boden et al. (2005) reported preliminary visual and physical orbit for the binary subsystem. They derived the components' masses of $0.699 \pm 0.064 M_{\odot}$ and $0.582 \pm 0.051 M_{\odot}$ for the primary and the secondary, respectively. We adopted the [Fe/H] value from Laskar et al. (2009). Both the components of the system are very young and located at the beginning of their Hayashi track.

For this system the standard set of models provides a good fit to both components (see Fig. 1.23). The predicted mass values in the case of a flat mass prior are $\mu_P = 0.51^{+0.25}_{-0.02} M_{\odot}$ and $\mu_S = 0.41^{+0.17}_{-0.00} M_{\odot}$. The location of the two stars in the HR diagram makes their marginal distribution extremely asymmetric. As a consequence, the best values are located quite close to (or exactly at) the boundary of the confidence intervals. This is the reason why the quoted lower error for the secondary mass is zero. The best values for both the primary and secondary are slightly smaller than the dynamical mass values but in this case there is consistency within the 68% confidence intervals.

The inferred ages for the two components are very similar and when a Gaussian mass prior is adopted we obtain $\tau_P = 0.85^{+0.05}_{-0.10}$ Myr and $\tau_S = 1.00^{+0.00}_{-0.15}$ Myr. Also in this case the marginal distributions are quite asymmetric. The composite system age is found to be $\tau_C = 0.90^{+0.00}_{-0.10}$ Myr, very young indeed.

1.9 THE STARS IN TAURUS-AURIGA

In this section we will present the results for the 9 stars found in the Taurus-Auriga star-forming region and whose masses are derived using disk kinematics (see Sect. 1.5). For all of these stars, the Gaussian metallicity prior is applied using the average value of [Fe/H] = -0.01 ± 0.05 dex for the region (D'Orazi et al. 2011).

This sample exactly coincides with the DK+DKS sample of Sect. 1.5. As it is possible to see in the rightmost panels of Fig. 1.6, most of the DK+DKS stars have strongly underestimated values of the mass. We discussed some possible reasons for this discrepancy in Sect. 1.6

We used the standard set of model to derive the ages of the Taurus-Auriga stars. The predicted values when a Gaussian mass prior is used are reported in Table 1.6. In addition to single stellar ages we also computed the composite age for the DKS system UZ Tau E. In general these age determinations have a worst precision when compared to the EB and AS sample. Moreover for the star MWC 480 the peak of the distribution is outside the 68% confidence interval. This is because the $G(\tau)$ is very flat and the corresponding peak is just barely visible. This peak is located in the area corresponding to the leftmost 16% probability that is excluded according to our definition. This is not strange given our definition of the confidence interval, it's just an indication that the age of this system is very poorly defined.

As we mentioned in Sect. 1.5 the stars UZ Tau Ea, BP Tau and MCW 480 have a peculiar location in the HR diagram. We excluded the latter two stars, while we kept UZ Tau Ea in the sample to obtain an average age of 2.1 ± 1.3 Myr where the quoted uncertainty is the standard deviation of the ages of the remaining stars. For both the stars in the UZ Tau E system we considered the composite age as the best age estimator. This average age is in very good agreement with the estimated age for the Taurus-Auriga star forming region of 1-2 Myr (see e.g Kraus & Hillenbrand 2009 and references therein).

Table 1.6: Derived ages for Taurus-Auriga DK stars.

Name	Age[Myr]	Relative Precision
UZ Tau Ea	$2.65^{+1.50}_{-0.45}$	0.373
UZ Tau Eb	$1.45^{+0.45}_{-0.70}$	0.592
UZ Tau E ^a	$1.85^{+0.45}_{-0.25}$	0.199
DL Tau	$1.20^{+0.30}_{-0.15}$	0.195
DM Tau	$3.05^{+1.10}_{-0.50}$	0.276
CY Tau	$1.85^{+0.30}_{-0.65}$	0.338
BP Tau	$17.25^{+8.85}_{-3.35}$	0.370
GM Aur	$0.50^{+0.10}_{-0.00}$	0.095
MWC 480	10.30 ^b	0.957
LkCa 15	$4.45^{+2.50}_{-0.75}$	0.371

^a Value for the composite system age

^b Uncertainty interval poorly defined

1.10 SUMMARY AND CONCLUSIONS

The importance of a stringent test of PMS models against stars with accurately known parameters (i.e. mass, luminosity, radius, effective temperature, [Fe/H]) can hardly be overestimated, as these models represent the main tool to derive masses and ages of stars observed in star forming regions and young stellar clusters. Consequently the inferred star formation histories and mass functions of young stellar groups strongly depend on the answers provided by stellar evolutionary codes.

In order to constrain PMS models we relied on a data set containing 25 PMS stars of measured mass (plus 2 MS companions in binary systems). This is the full up-to-date sample of known PMS stars with dynamical mass measurements in the range 0.2-3.0 M_{\odot} . Among them 10 PMS objects belong to double-lined eclipsing binary systems and 6 to astrometric and spectroscopic binaries; the remaining 9 objects are stars whose masses are derived using the measured orbital

velocity of their circumstellar disks.

The main novelties of our study are both the approach followed for comparing theory with observations and the set of PMS models used in the comparison. Regarding the former, we applied for the first time to the whole sample of PMS stars a very general Bayesian method. This approach allows a full exploitation of the available information about the observed objects which is included in the form of prior probability distributions. In addition it provides robust uncertainties for the inferred quantities.

The models are extracted from the very recent Pisa PMS database. They include the state-of-art input physics and are available for a large and very fine grid of metallicities, masses and ages and for different primordial helium abundances, Y_p , helium-to-metals enrichment ratios, $\Delta Y/\Delta Z$, and mixing-length parameter, α , values.

We checked the robustness and accuracy of the method in recovering stellar ages and masses against simulated binary data sets. One interesting result is that even synthetic binary stars – coeval by construction – mimic non coevality in about the 13% of cases as a consequence of the random uncertainty in the effective temperature, radius, and luminosity. This suggests that the inability to fit both components of a binary system with a single isochrone does not necessarily imply that the two stars are not coeval or that the models present some deficiency. Note that even in the non-coeval cases the inferred system age obtained using the composite age distribution is in very good agreement with the simulated age. We showed also that the ability of recovering the simulated masses and ages is a complex function of the actual position of the star in the HR diagram.

When the real data are used the Pisa PMS models show an overall agreement with the observations. With the exception of V1174 Ori B, the masses of EB stars are well recovered within 10%. The agreement progressively worsens for AS binaries and DK stars, but also the observational uncertainties become more severe for the latter objects.

With our Bayesian approach it is possible to evaluate the probability for different sets of models, i.e. the models' evidence. We analysed the entire data set using several classes of models computed with different Y_p , $\Delta Y/\Delta Z$, and α values. We calculated the evidence for each star using 9 different meta-parameters configurations. Furthermore, four combinations of the prior distributions for mass and metallicity have been used for each meta-parameter choice, for a total of 36 classes. We found that adopting a Gaussian rather than a flat mass prior significantly improves the composite evidence for the full data set; the same effect, but to a lesser degree, is obtained imposing a Gaussian metallicity prior, mainly for EBs. Although our standard set of models shows a reasonable general agreement with the data, predicting mass values almost always within 20% of the dynamical ones –and in several case even within 5%–, the general trend suggests that standard models tend to underestimate the stellar mass, confirming previous

results (see Mathieu et al. 2007 and references therein). As a consequence, the largest composite evidence is obtained with our coldest set of models, i.e. with the mixing-length parameter $\alpha=1.2$ and the lowest helium abundance at fixed metallicity.

Given that the discrepancy between theory and observations increases going from the most precise data set of EBs to the others we point out that a twofold effort is needed to achieve a better agreement. From the theoretical point of view a better understanding on the treatment of superadiabatic convection and a better characterization of the models' meta-parameters is desirable. From the observational side the significance of such a comparison could be improved in the future by a larger sample of well studied and characterized PMS stars and by a better control on the systematic errors affecting AS and DK stars' measurements.

1.A TABLES OF BAYES FACTORS

Table 1.7: Bayes factor values for the case of flat prior on the mass and flat prior on the metallicity

	$\alpha = 1.20$	$\alpha = 1.68$	$\alpha = 1.90$	$\alpha = 1.20$	$\alpha = 1.68$	$\alpha = 1.90$
	RS Cha A			RS Cha B		
$\Delta Y/\Delta Z = 2, Y_p = 0.23$	1.252	1.252	1.253	1.054	1.077	1.111
$\Delta Y/\Delta Z = 2, Y_p = 0.2485$	1.004	1.000	1.009	0.975	1.000	1.033
$\Delta Y/\Delta Z = 5, Y_p = 0.2485$	0.556	0.561	0.559	0.787	0.802	0.828
	RXJ Aa			RXJ Ab		
$\Delta Y/\Delta Z = 2, Y_p = 0.23$	1.002	1.042	1.035	1.377	1.101	1.003
$\Delta Y/\Delta Z = 2, Y_p = 0.2485$	0.955	1.000	0.996	1.292	1.000	0.900
$\Delta Y/\Delta Z = 5, Y_p = 0.2485$	0.833	0.889	0.889	1.038	0.716	0.620
	V1174 Ori A			V1174 Ori B		
$\Delta Y/\Delta Z = 2, Y_p = 0.23$	1.108	1.051	1.009	1.589	1.183	1.086
$\Delta Y/\Delta Z = 2, Y_p = 0.2485$	1.073	1.000	0.948	1.365	1.000	0.914
$\Delta Y/\Delta Z = 5, Y_p = 0.2485$	0.960	0.824	0.741	0.821	0.579	0.525
	EK Cep A			EK Cep B		
$\Delta Y/\Delta Z = 2, Y_p = 0.23$	0.950	0.955	0.956	5.684	1.181	0.946
$\Delta Y/\Delta Z = 2, Y_p = 0.2485$	0.995	1.000	1.005	4.447	1.000	0.866
$\Delta Y/\Delta Z = 5, Y_p = 0.2485$	1.451	1.457	1.460	1.386	0.712	0.712
	TY CrA A			TY CrA B		
$\Delta Y/\Delta Z = 2, Y_p = 0.23$	0.962	0.963	0.964	1.166	1.066	0.977
$\Delta Y/\Delta Z = 2, Y_p = 0.2485$	0.999	1.000	1.001	1.111	1.000	0.909
$\Delta Y/\Delta Z = 5, Y_p = 0.2485$	1.145	1.147	1.147	0.957	0.815	0.720
	ASAS A			ASAS B		
$\Delta Y/\Delta Z = 2, Y_p = 0.23$	0.922	1.036	1.052	1.251	1.083	0.943
$\Delta Y/\Delta Z = 2, Y_p = 0.2485$	0.884	1.000	1.017	1.208	1.000	0.848
$\Delta Y/\Delta Z = 5, Y_p = 0.2485$	0.784	0.906	0.913	1.071	0.745	0.580
	HD 113449 A			HD 113449 B		
$\Delta Y/\Delta Z = 2, Y_p = 0.23$	0.569	0.971	1.019	0.665	0.832	0.883
$\Delta Y/\Delta Z = 2, Y_p = 0.2485$	0.667	1.000	0.998	0.806	1.000	1.060
$\Delta Y/\Delta Z = 5, Y_p = 0.2485$	1.003	0.837	0.670	1.272	1.589	1.686
	NTT A			NTT B		
$\Delta Y/\Delta Z = 2, Y_p = 0.23$	1.422	1.098	0.976	1.776	1.173	1.043
$\Delta Y/\Delta Z = 2, Y_p = 0.2485$	1.340	1.000	0.877	1.529	1.000	0.887
$\Delta Y/\Delta Z = 5, Y_p = 0.2485$	1.101	0.723	0.607	0.946	0.612	0.541
	HD 98800 Ba			HD 98800 Bb		
$\Delta Y/\Delta Z = 2, Y_p = 0.23$	3.162	1.120	0.841	2.719	1.148	0.903
$\Delta Y/\Delta Z = 2, Y_p = 0.2485$	2.816	1.000	0.756	2.322	1.000	0.811
$\Delta Y/\Delta Z = 5, Y_p = 0.2485$	1.937	0.754	0.600	1.563	0.911	0.632
	UZ Tau Ea			UZ Tau Eb		
$\Delta Y/\Delta Z = 2, Y_p = 0.23$	1.731	1.126	0.968	2.795	1.363	0.862
$\Delta Y/\Delta Z = 2, Y_p = 0.2485$	1.540	1.000	0.846	2.228	1.000	0.614
$\Delta Y/\Delta Z = 5, Y_p = 0.2485$	1.202	0.795	0.623	0.897	0.229	0.123
	DL Tau			DM Tau		
$\Delta Y/\Delta Z = 2, Y_p = 0.23$	2.465	1.139	0.924	1.784	1.182	1.051
$\Delta Y/\Delta Z = 2, Y_p = 0.2485$	2.147	1.000	0.814	1.529	1.000	0.886
$\Delta Y/\Delta Z = 5, Y_p = 0.2485$	1.400	0.735	0.616	0.929	0.589	0.518
	CY Tau			BP Tau		
$\Delta Y/\Delta Z = 2, Y_p = 0.23$	1.551	1.131	1.025	1.103	1.058	1.045
$\Delta Y/\Delta Z = 2, Y_p = 0.2485$	1.371	1.000	0.902	1.042	1.000	0.987
$\Delta Y/\Delta Z = 5, Y_p = 0.2485$	0.996	0.735	0.646	0.890	0.848	0.832
	GM Aur			MWC 480		
$\Delta Y/\Delta Z = 2, Y_p = 0.23$	7.963	1.329	0.287	1.118	1.128	1.131
$\Delta Y/\Delta Z = 2, Y_p = 0.2485$	6.900	1.000	0.173	0.991	1.000	1.002
$\Delta Y/\Delta Z = 5, Y_p = 0.2485$	5.211	0.244	0.023	0.564	0.570	0.571
	LkCa 15					
$\Delta Y/\Delta Z = 2, Y_p = 0.23$	1.259	1.080	0.992			
$\Delta Y/\Delta Z = 2, Y_p = 0.2485$	1.202	1.000	0.904			
$\Delta Y/\Delta Z = 5, Y_p = 0.2485$	1.029	0.754	0.646			

Table 1.8: Bayes factor values for the case with Gaussian prior on the mass and flat prior on the metallicity

	$\alpha = 1.20$	$\alpha = 1.68$	$\alpha = 1.90$	$\alpha = 1.20$	$\alpha = 1.68$	$\alpha = 1.90$
	RS Cha A			RS Cha B		
$\Delta Y/\Delta Z = 2, Y_p = 0.23$	6.968	7.171	7.039	17.54	17.92	18.36
$\Delta Y/\Delta Z = 2, Y_p = 0.2485$	7.123	7.150	7.212	12.47	12.64	12.88
$\Delta Y/\Delta Z = 5, Y_p = 0.2485$	0.147	0.142	0.143	0.003	0.003	0.003
	RXJ A			RXJ B		
$\Delta Y/\Delta Z = 2, Y_p = 0.23$	11.72	16.17	13.57	11.71	13.11	12.30
$\Delta Y/\Delta Z = 2, Y_p = 0.2485$	8.582	16.72	14.98	12.81	11.93	10.14
$\Delta Y/\Delta Z = 5, Y_p = 0.2485$	2.719	14.44	15.56	12.08	3.470	1.650
	V1174 Ori A			V1174 Ori B		
$\Delta Y/\Delta Z = 2, Y_p = 0.23$	2.844	7.566	9.745	6.218	1.236	0.658
$\Delta Y/\Delta Z = 2, Y_p = 0.2485$	4.949	10.52	12.47	3.032	0.358	0.158
$\Delta Y/\Delta Z = 5, Y_p = 0.2485$	16.15	12.65	6.966	0.024	$< 10^{-3}$	$< 10^{-3}$
	EK Cep A			EK Cep B		
$\Delta Y/\Delta Z = 2, Y_p = 0.23$	9.530	9.597	9.580	18.02	17.25	9.205
$\Delta Y/\Delta Z = 2, Y_p = 0.2485$	2.259	2.254	2.256	17.48	23.61	14.84
$\Delta Y/\Delta Z = 5, Y_p = 0.2485$	0.001	0.001	0.001	28.67	14.20	21.99
	TY CrA A			TY CrA B		
$\Delta Y/\Delta Z = 2, Y_p = 0.23$	0.409	0.409	0.409	13.52	6.466	4.870
$\Delta Y/\Delta Z = 2, Y_p = 0.2485$	0.145	0.145	0.145	13.13	6.728	4.847
$\Delta Y/\Delta Z = 5, Y_p = 0.2485$	0.005	0.005	0.005	5.550	6.863	4.718
	ASAS A			ASAS B		
$\Delta Y/\Delta Z = 2, Y_p = 0.23$	3.446	0.909	2.070	8.715	12.54	7.418
$\Delta Y/\Delta Z = 2, Y_p = 0.2485$	9.576	2.131	3.682	11.10	9.666	3.843
$\Delta Y/\Delta Z = 5, Y_p = 0.2485$	29.33	7.729	12.42	21.51	0.383	0.023
	HD 113449 A			HD 113449 B		
$\Delta Y/\Delta Z = 2, Y_p = 0.23$	5.754	10.44	10.94	2.548	3.270	3.497
$\Delta Y/\Delta Z = 2, Y_p = 0.2485$	5.856	9.333	9.159	2.548	3.252	3.476
$\Delta Y/\Delta Z = 5, Y_p = 0.2485$	4.563	2.854	2.015	2.559	3.129	3.291
	NTT A			NTT B		
$\Delta Y/\Delta Z = 2, Y_p = 0.23$	3.589	1.323	0.830	2.417	0.372	0.192
$\Delta Y/\Delta Z = 2, Y_p = 0.2485$	2.837	0.880	0.516	1.391	0.166	0.078
$\Delta Y/\Delta Z = 5, Y_p = 0.2485$	1.104	0.173	0.079	0.116	0.005	0.002
	HD 98800 Ba			HD 98800 Bb		
$\Delta Y/\Delta Z = 2, Y_p = 0.23$	2.327	6.120	5.958	4.910	7.595	7.702
$\Delta Y/\Delta Z = 2, Y_p = 0.2485$	2.909	6.173	5.419	4.354	7.662	6.594
$\Delta Y/\Delta Z = 5, Y_p = 0.2485$	4.946	5.024	3.010	7.062	6.963	3.018
	UZ Tau Ea			UZ Tau Eb		
$\Delta Y/\Delta Z = 2, Y_p = 0.23$	0.077	$< 10^{-3}$	$< 10^{-3}$	46.45	16.35	9.575
$\Delta Y/\Delta Z = 2, Y_p = 0.2485$	0.030	$< 10^{-3}$	$< 10^{-3}$	33.43	9.941	5.498
$\Delta Y/\Delta Z = 5, Y_p = 0.2485$	$< 10^{-3}$	$< 10^{-3}$	$< 10^{-3}$	7.188	0.826	0.355
	DL Tau			DM Tau		
$\Delta Y/\Delta Z = 2, Y_p = 0.23$	15.75	6.815	4.181	19.31	12.15	9.790
$\Delta Y/\Delta Z = 2, Y_p = 0.2485$	14.59	4.953	2.782	16.83	8.719	6.555
$\Delta Y/\Delta Z = 5, Y_p = 0.2485$	9.141	1.225	0.515	6.555	1.297	0.675
	CY Tau			BP Tau		
$\Delta Y/\Delta Z = 2, Y_p = 0.23$	5.420	3.667	3.256	0.180	0.155	0.147
$\Delta Y/\Delta Z = 2, Y_p = 0.2485$	4.675	3.145	2.776	0.138	0.115	0.107
$\Delta Y/\Delta Z = 5, Y_p = 0.2485$	3.058	2.071	1.788	0.054	0.038	0.034
	GM Aur			MWC 480		
$\Delta Y/\Delta Z = 2, Y_p = 0.23$	59.83	9.330	1.688	0.161	0.162	0.163
$\Delta Y/\Delta Z = 2, Y_p = 0.2485$	53.20	6.241	0.865	0.306	0.309	0.309
$\Delta Y/\Delta Z = 5, Y_p = 0.2485$	40.15	0.817	0.037	2.305	2.325	2.332
	LkCa 15					
$\Delta Y/\Delta Z = 2, Y_p = 0.23$	3.908	7.764	8.856			
$\Delta Y/\Delta Z = 2, Y_p = 0.2485$	5.393	9.119	9.496			
$\Delta Y/\Delta Z = 5, Y_p = 0.2485$	10.91	8.083	5.268			

Table 1.9: Bayes factor values for the case of flat prior on the mass and Gaussian prior on the metallicity

	$\alpha = 1.20$	$\alpha = 1.68$	$\alpha = 1.90$		$\alpha = 1.20$	$\alpha = 1.68$	$\alpha = 1.90$
	RS Cha A				RS Cha B		
$\Delta Y/\Delta Z = 2, Y_p = 0.23$	0.887	0.897	0.896		1.058	1.089	1.114
$\Delta Y/\Delta Z = 2, Y_p = 0.2485$	0.752	0.752	0.764		0.978	1.002	1.044
$\Delta Y/\Delta Z = 5, Y_p = 0.2485$	0.530	0.532	0.531		0.790	0.806	0.833
	RXJ A				RXJ B		
$\Delta Y/\Delta Z = 2, Y_p = 0.23$	0.992	1.016	1.007		1.353	1.071	0.975
$\Delta Y/\Delta Z = 2, Y_p = 0.2485$	0.951	0.976	0.972		1.264	0.967	0.871
$\Delta Y/\Delta Z = 5, Y_p = 0.2485$	0.873	0.905	0.904		1.077	0.766	0.675
	V1174 Ori A				V1174 Ori B		
$\Delta Y/\Delta Z = 2, Y_p = 0.23$	1.103	1.034	0.991		1.313	0.999	0.924
$\Delta Y/\Delta Z = 2, Y_p = 0.2485$	1.066	0.984	0.929		1.110	0.836	0.772
$\Delta Y/\Delta Z = 5, Y_p = 0.2485$	0.992	0.861	0.786		0.785	0.581	0.534
	EK Cep A				EK Cep B		
$\Delta Y/\Delta Z = 2, Y_p = 0.23$	3.545	3.568	3.570		2.769	0.865	0.840
$\Delta Y/\Delta Z = 2, Y_p = 0.2485$	2.343	2.367	2.378		1.769	0.795	0.792
$\Delta Y/\Delta Z = 5, Y_p = 0.2485$	0.091	0.093	0.093		0.783	0.699	0.710
	TY CrA A				TY CrA B		
$\Delta Y/\Delta Z = 2, Y_p = 0.23$	-	-	-		-	-	-
$\Delta Y/\Delta Z = 2, Y_p = 0.2485$	-	-	-		-	-	-
$\Delta Y/\Delta Z = 5, Y_p = 0.2485$	-	-	-		-	-	-
	ASAS A				ASAS B		
$\Delta Y/\Delta Z = 2, Y_p = 0.23$	0.632	0.701	0.706		0.840	0.680	0.581
$\Delta Y/\Delta Z = 2, Y_p = 0.2485$	0.597	0.666	0.667		0.788	0.604	0.502
$\Delta Y/\Delta Z = 5, Y_p = 0.2485$	0.544	0.610	0.604		0.706	0.481	0.380
	HD 113449 A				HD 113449 B		
$\Delta Y/\Delta Z = 2, Y_p = 0.23$	0.874	1.052	0.975		1.028	1.296	1.375
$\Delta Y/\Delta Z = 2, Y_p = 0.2485$	0.986	0.948	0.827		1.325	1.636	1.731
$\Delta Y/\Delta Z = 5, Y_p = 0.2485$	1.043	0.631	0.490		1.987	2.383	2.498
	NTT A				NTT B		
$\Delta Y/\Delta Z = 2, Y_p = 0.23$	-	-	-		-	-	-
$\Delta Y/\Delta Z = 2, Y_p = 0.2485$	-	-	-		-	-	-
$\Delta Y/\Delta Z = 5, Y_p = 0.2485$	-	-	-		-	-	-
	HD 98800 Ba				HD 98800 Bb		
$\Delta Y/\Delta Z = 2, Y_p = 0.23$	1.499	0.676	0.560		1.479	0.790	0.662
$\Delta Y/\Delta Z = 2, Y_p = 0.2485$	1.287	0.614	0.501		1.075	0.708	0.538
$\Delta Y/\Delta Z = 5, Y_p = 0.2485$	1.046	0.542	0.420		0.843	0.595	0.425
	UZ Tau Ea				UZ Tau Eb		
$\Delta Y/\Delta Z = 2, Y_p = 0.23$	1.629	1.150	1.007		1.092	0.404	0.294
$\Delta Y/\Delta Z = 2, Y_p = 0.2485$	1.446	1.006	0.845		0.687	0.252	0.161
$\Delta Y/\Delta Z = 5, Y_p = 0.2485$	1.383	0.857	0.692		0.311	0.072	0.044
	DL Tau				DM Tau		
$\Delta Y/\Delta Z = 2, Y_p = 0.23$	2.058	1.052	0.892		1.474	1.015	0.914
$\Delta Y/\Delta Z = 2, Y_p = 0.2485$	1.777	0.941	0.791		1.248	0.853	0.767
$\Delta Y/\Delta Z = 5, Y_p = 0.2485$	1.372	0.822	0.708		0.893	0.604	0.542
	CY Tau				BP Tau		
$\Delta Y/\Delta Z = 2, Y_p = 0.23$	1.448	1.142	1.061		1.105	1.078	1.068
$\Delta Y/\Delta Z = 2, Y_p = 0.2485$	1.298	1.040	0.945		1.058	1.029	1.019
$\Delta Y/\Delta Z = 5, Y_p = 0.2485$	1.131	0.829	0.731		0.965	0.928	0.914
	GM Aur				MWC 480		
$\Delta Y/\Delta Z = 2, Y_p = 0.23$	7.278	0.368	0.061		0.462	0.466	0.468
$\Delta Y/\Delta Z = 2, Y_p = 0.2485$	5.192	0.218	0.027		0.313	0.316	0.317
$\Delta Y/\Delta Z = 5, Y_p = 0.2485$	4.421	0.080	0.008		0.125	0.126	0.127
	LkCa 15						
$\Delta Y/\Delta Z = 2, Y_p = 0.23$	1.243	1.048	0.959				
$\Delta Y/\Delta Z = 2, Y_p = 0.2485$	1.186	0.965	0.869				
$\Delta Y/\Delta Z = 5, Y_p = 0.2485$	1.059	0.791	0.690				

Table 1.10: Bayes factor values for the case with Gaussian prior on both the mass and the metallicity

	$\alpha = 1.20$	$\alpha = 1.68$	$\alpha = 1.90$	$\alpha = 1.20$	$\alpha = 1.68$	$\alpha = 1.90$
	RS Cha A			RS Cha B		
$\Delta Y/\Delta Z = 2, Y_p = 0.23$	17.40	17.78	17.51	26.67	27.27	27.57
$\Delta Y/\Delta Z = 2, Y_p = 0.2485$	10.23	10.24	10.23	10.36	10.60	10.85
$\Delta Y/\Delta Z = 5, Y_p = 0.2485$	0.003	0.003	0.003	0.003	0.003	0.003
	RXJ A			RXJ B		
$\Delta Y/\Delta Z = 2, Y_p = 0.23$	10.87	18.35	17.02	15.62	14.00	11.73
$\Delta Y/\Delta Z = 2, Y_p = 0.2485$	7.781	18.34	18.31	15.98	10.44	7.579
$\Delta Y/\Delta Z = 5, Y_p = 0.2485$	3.366	14.13	15.14	12.00	3.298	1.666
	V1174 Ori A			V1174 Ori B		
$\Delta Y/\Delta Z = 2, Y_p = 0.23$	2.484	12.76	16.35	0.794	0.091	0.043
$\Delta Y/\Delta Z = 2, Y_p = 0.2485$	6.836	18.37	18.09	0.217	0.016	0.006
$\Delta Y/\Delta Z = 5, Y_p = 0.2485$	22.02	13.08	7.076	0.007	$< 10^{-3}$	$< 10^{-3}$
	EK Cep A			EK Cep B		
$\Delta Y/\Delta Z = 2, Y_p = 0.23$	37.95	38.17	38.06	24.89	21.46	9.717
$\Delta Y/\Delta Z = 2, Y_p = 0.2485$	8.021	8.004	8.010	16.38	28.07	17.43
$\Delta Y/\Delta Z = 5, Y_p = 0.2485$	0.001	0.001	0.001	4.962	16.00	22.97
	TY CrA A			TY CrA B		
$\Delta Y/\Delta Z = 2, Y_p = 0.23$	-	-	-	-	-	-
$\Delta Y/\Delta Z = 2, Y_p = 0.2485$	-	-	-	-	-	-
$\Delta Y/\Delta Z = 5, Y_p = 0.2485$	-	-	-	-	-	-
	ASAS A			ASAS B		
$\Delta Y/\Delta Z = 2, Y_p = 0.23$	3.527	1.714	3.897	13.81	4.101	1.250
$\Delta Y/\Delta Z = 2, Y_p = 0.2485$	10.47	4.188	6.801	13.61	1.690	0.340
$\Delta Y/\Delta Z = 5, Y_p = 0.2485$	26.83	10.93	11.13	7.133	0.056	0.003
	HD 113449 A			HD 113449 B		
$\Delta Y/\Delta Z = 2, Y_p = 0.23$	8.426	9.087	7.972	4.084	5.100	5.393
$\Delta Y/\Delta Z = 2, Y_p = 0.2485$	7.398	6.058	4.900	4.029	4.877	5.124
$\Delta Y/\Delta Z = 5, Y_p = 0.2485$	3.911	1.671	1.155	3.304	3.765	3.882
	NTT A			NTT B		
$\Delta Y/\Delta Z = 2, Y_p = 0.23$	-	-	-	-	-	-
$\Delta Y/\Delta Z = 2, Y_p = 0.2485$	-	-	-	-	-	-
$\Delta Y/\Delta Z = 5, Y_p = 0.2485$	-	-	-	-	-	-
	HD 98800 Ba			HD 98800 Bb		
$\Delta Y/\Delta Z = 2, Y_p = 0.23$	4.598	4.732	3.154	9.824	5.134	4.441
$\Delta Y/\Delta Z = 2, Y_p = 0.2485$	5.117	3.838	2.254	5.794	4.017	2.152
$\Delta Y/\Delta Z = 5, Y_p = 0.2485$	5.514	2.523	1.264	3.389	2.762	0.925
	UZ Tau Ea			UZ Tau Eb		
$\Delta Y/\Delta Z = 2, Y_p = 0.23$	0.007	$< 10^{-3}$	$< 10^{-3}$	14.31	3.507	2.202
$\Delta Y/\Delta Z = 2, Y_p = 0.2485$	0.002	$< 10^{-3}$	$< 10^{-3}$	7.555	1.637	0.915
$\Delta Y/\Delta Z = 5, Y_p = 0.2485$	$< 10^{-3}$	$< 10^{-3}$	$< 10^{-3}$	2.198	0.252	0.123
	DL Tau			DM Tau		
$\Delta Y/\Delta Z = 2, Y_p = 0.23$	15.38	4.642	2.638	15.09	7.006	5.228
$\Delta Y/\Delta Z = 2, Y_p = 0.2485$	12.89	2.985	1.558	10.91	4.091	2.819
$\Delta Y/\Delta Z = 5, Y_p = 0.2485$	7.816	1.055	0.472	4.461	0.943	0.529
	CY Tau			BP Tau		
$\Delta Y/\Delta Z = 2, Y_p = 0.23$	4.679	3.441	3.139	0.134	0.113	0.106
$\Delta Y/\Delta Z = 2, Y_p = 0.2485$	4.056	3.024	2.706	0.099	0.080	0.074
$\Delta Y/\Delta Z = 5, Y_p = 0.2485$	3.289	2.275	1.980	0.051	0.038	0.034
	GM Aur			MWC 480		
$\Delta Y/\Delta Z = 2, Y_p = 0.23$	66.12	2.143	0.193	0.358	0.361	0.362
$\Delta Y/\Delta Z = 2, Y_p = 0.2485$	47.29	1.166	0.090	0.734	0.741	0.743
$\Delta Y/\Delta Z = 5, Y_p = 0.2485$	34.52	0.238	0.009	1.134	1.144	1.147
	LkCa 15					
$\Delta Y/\Delta Z = 2, Y_p = 0.23$	5.624	10.79	11.34			
$\Delta Y/\Delta Z = 2, Y_p = 0.2485$	8.308	11.78	10.77			
$\Delta Y/\Delta Z = 5, Y_p = 0.2485$	12.79	8.522	5.659			

1.B MASS AND AGE MARGINAL DISTRIBUTIONS

The complete figures description is given only in the first case of Fig. 1.9. The reader is referred to the caption of this figure also for the following ones.

Figure 1.9: RS Cha components mass and age distributions as obtained from the $\log g - \log T_{\text{eff}}$ diagram using the standard set of models. *All panels:* In blue the primary component, in red the secondary. Full symbols indicate the mode of the distributions, the bars mark the 68% confidence interval. The quoted numbers represent the relative precision of the mass or age estimates. In the upper panels the empty symbols and related error bars indicate the dynamical masses and their measurement errors. In the lower panels the black line represents the system age distribution. *Upper panels:* Marginalized mass distributions. *Lower panels:* Marginalized age distributions. *Left panels:* Marginalization using a flat mass prior. *Right panels:* Marginalization using a Gaussian mass prior.

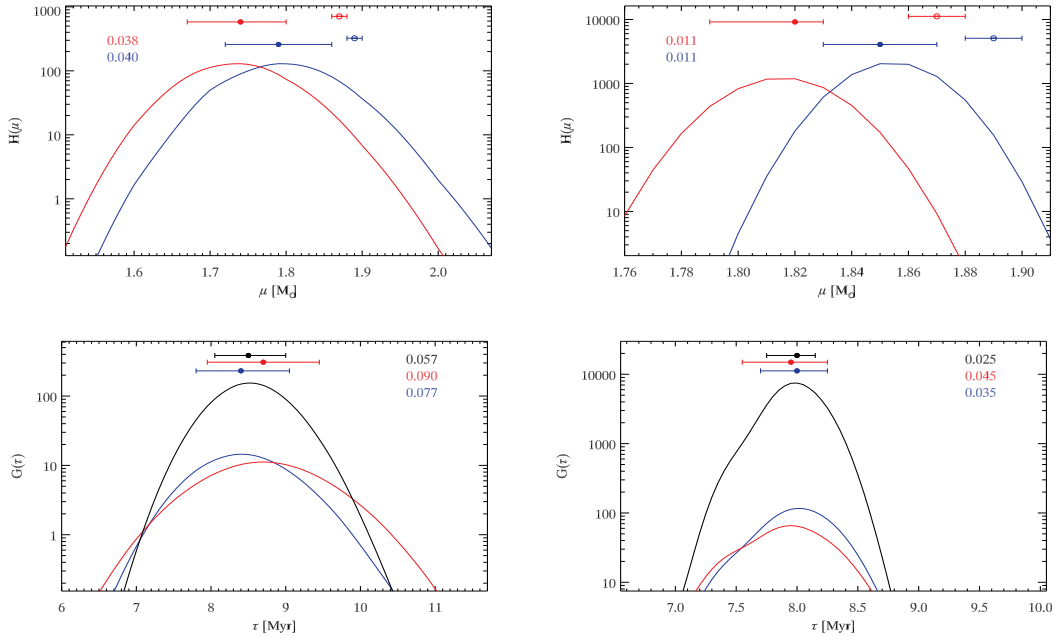


Figure 1.10: RXJ 0529.4+0041 components mass and age distributions from comparison with the standard set of models (see Fig. 1.9 for a description).

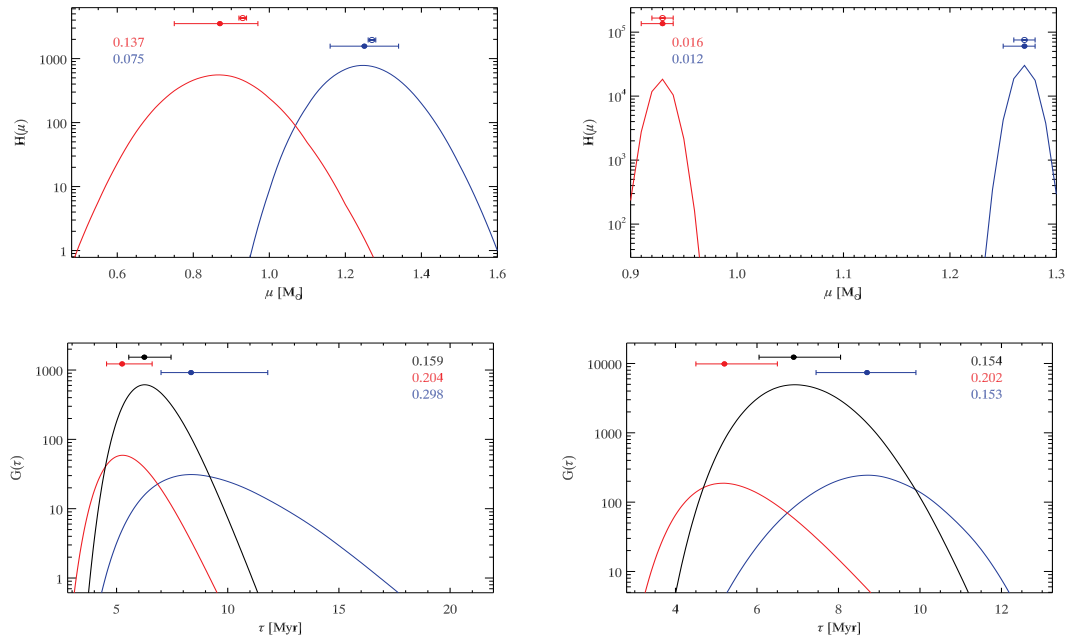


Figure 1.11: V 1174 Ori components mass and age distributions from comparison with the standard set of models (see Fig. 1.9 for a description).

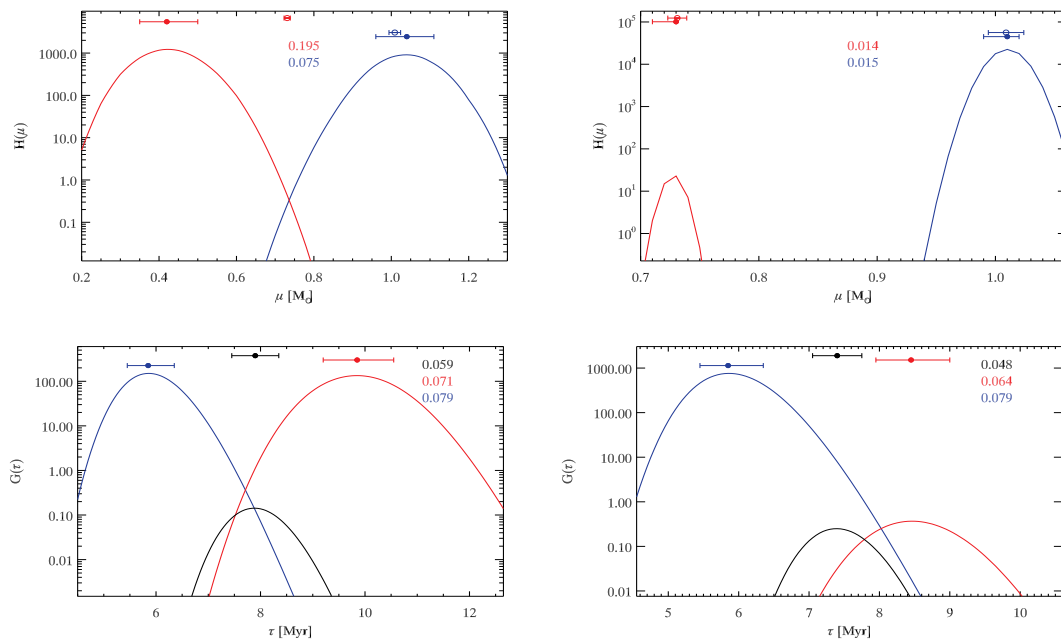


Figure 1.12: V 1174 Ori components mass and age distributions from comparison with the standard set of models (see Fig. 1.9 for a description). In this case the T_{eff} of the primary has been artificially raised by 100 K and the T_{eff} of the secondary has been raised accordingly in order to keep the T_{eff} ratio constant.

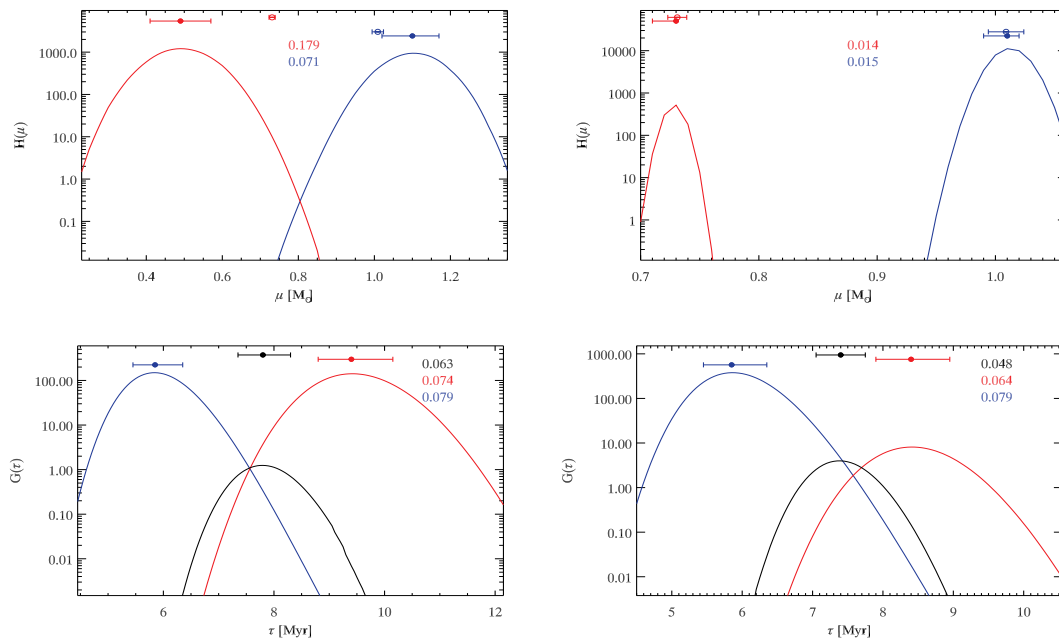


Figure 1.13: EK Cep components mass and age distributions from comparison with the standard set of models (see Fig. 1.9 for a description).

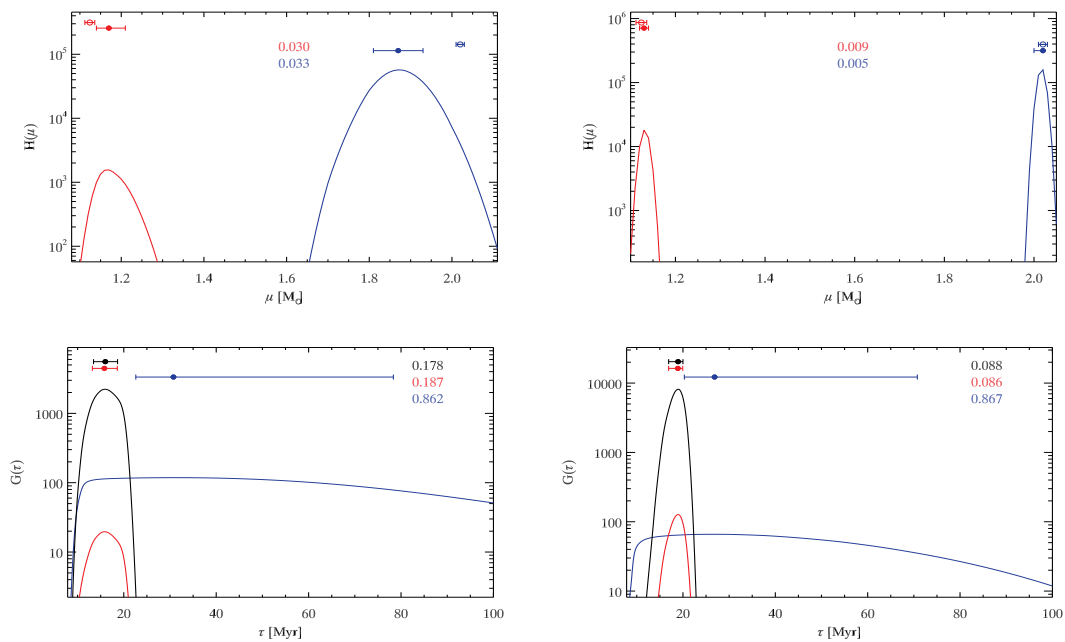


Figure 1.14: EK Cep components mass and age distributions from comparison with the set of models with $\alpha = 1.20$, $Y_p = 0.23$ and $\Delta Y/\Delta Z = 2$ (see Fig. 1.9 for a description). The stellar Z values used for this comparison have been calculated using the observed $[\text{Fe}/\text{H}]$ and $(Z/X)_\odot$ by Grevesse & Sauval 1998.

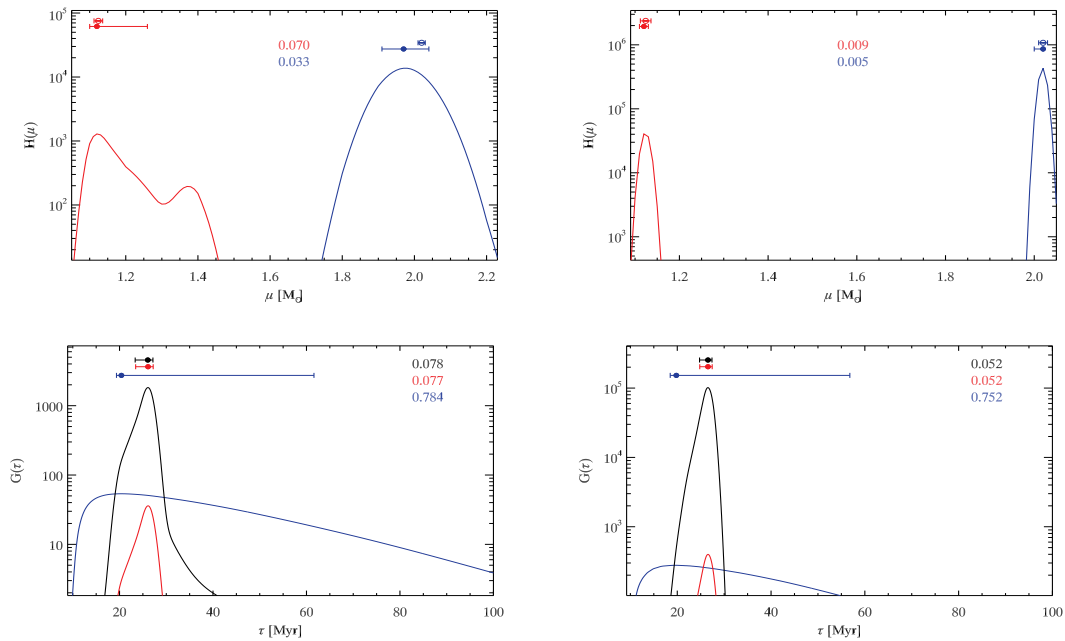


Figure 1.15: TYCrA components mass and age distributions from comparison with the standard set of models (see Fig. 1.9 for a description).

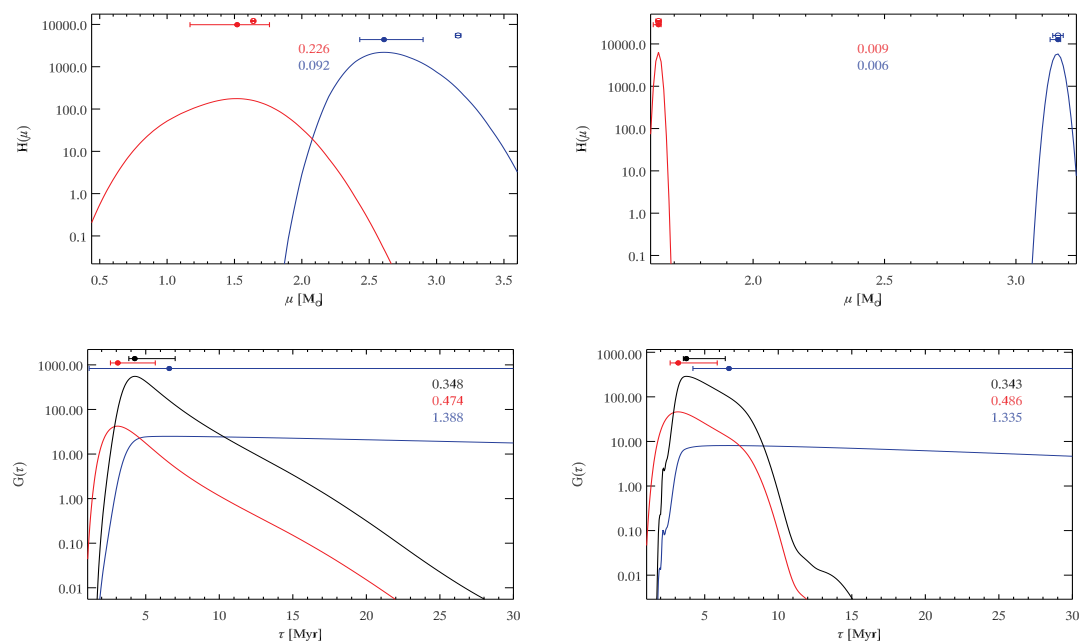


Figure 1.16: TY CrA components mass and age distributions from comparison with the set of models with $\alpha = 1.20$, $Y_P = 0.23$ and $\Delta Y/\Delta Z = 2$ (see Fig. 1.9 for a description).

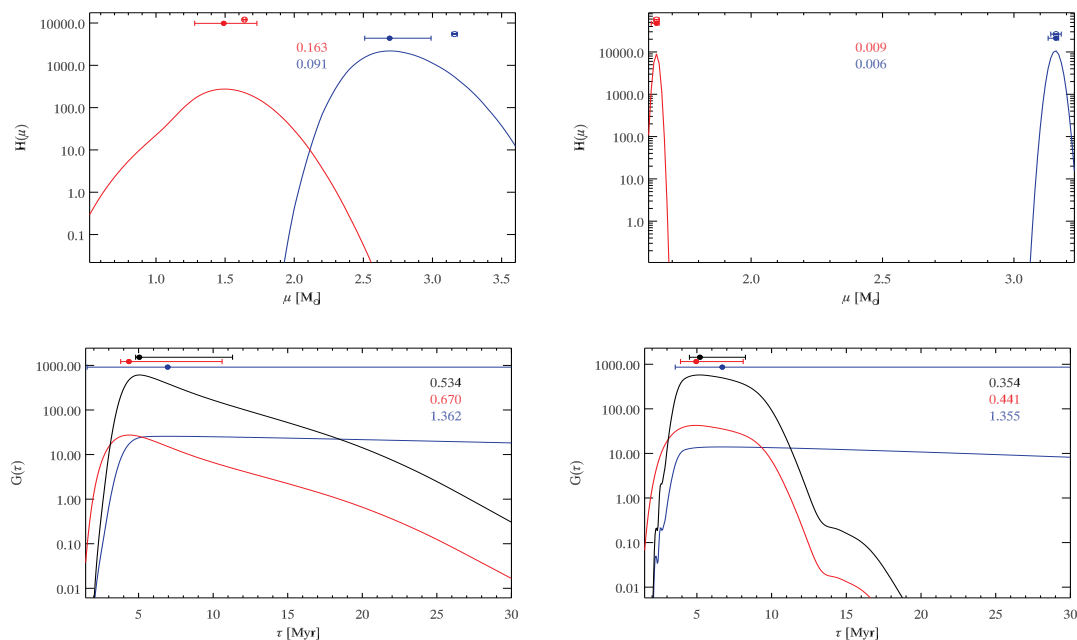


Figure 1.17: ASAS J052821+0338.5 components mass and age distributions from comparison with the standard set of models (see Fig. 1.9 for a description).

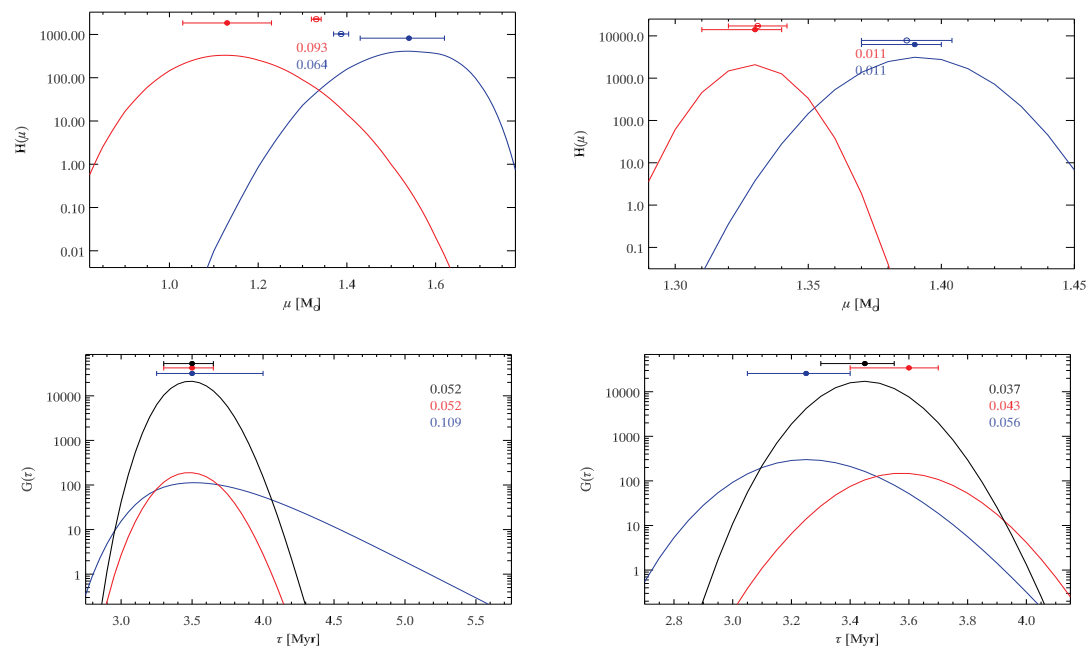


Figure 1.18: ASAS J052821+0338.5 components mass and age distributions from comparison with the standard set of models. In this case we used the data from Table 1 of Stempels et al. 2008 when no spots are included in the light-curve modeling (see Fig. 1.9 for a description).

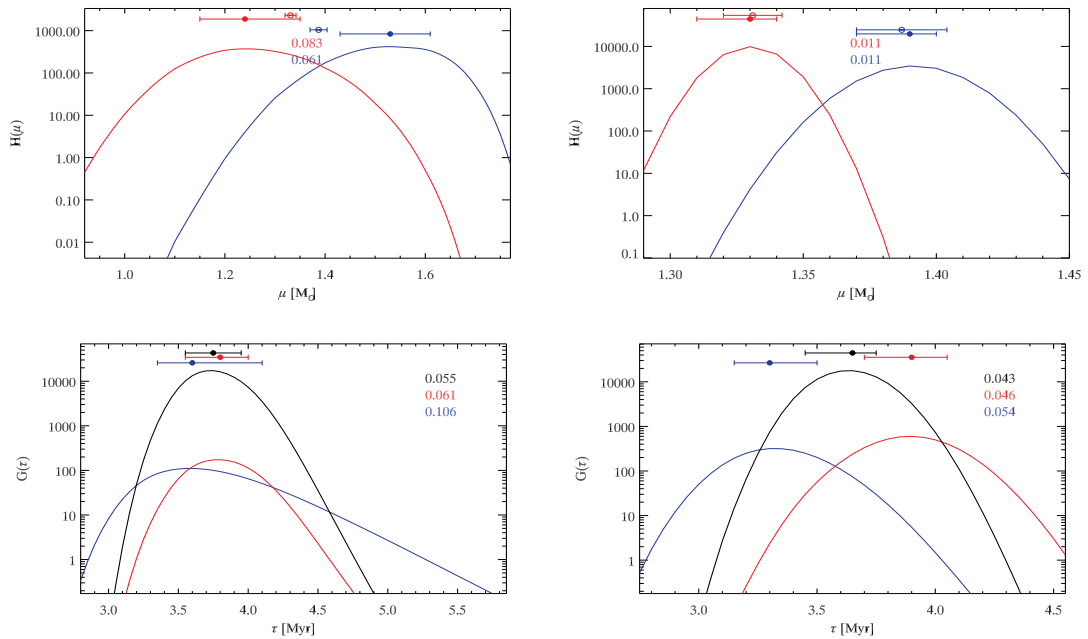


Figure 1.19: HD 113449 components mass and age distributions from comparison with the standard set of models (see Fig. 1.9 for a description).

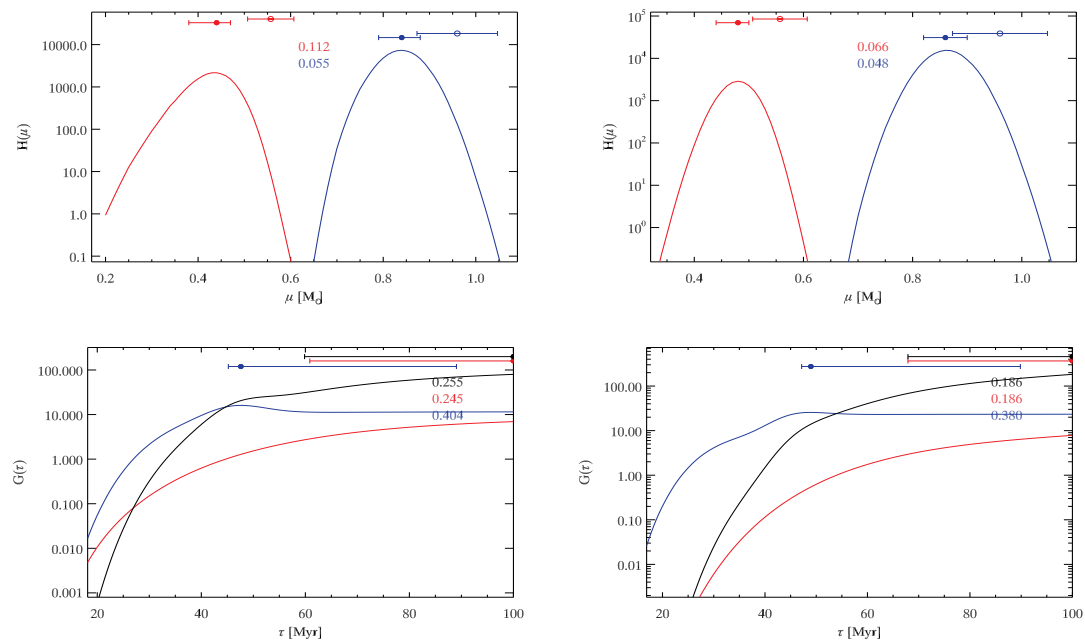


Figure 1.20: HD 113449 components mass and age distributions from comparison with the set of models with $\alpha = 1.20$, $Y_p = 0.23$ and $\Delta Y/\Delta Z = 2$ (see Fig. 1.9 for a description). The stellar Z values used for this comparison have been calculated using the observed $[\text{Fe}/\text{H}]$ and $(Z/X)_\odot$ by Grevesse & Sauval 1998.

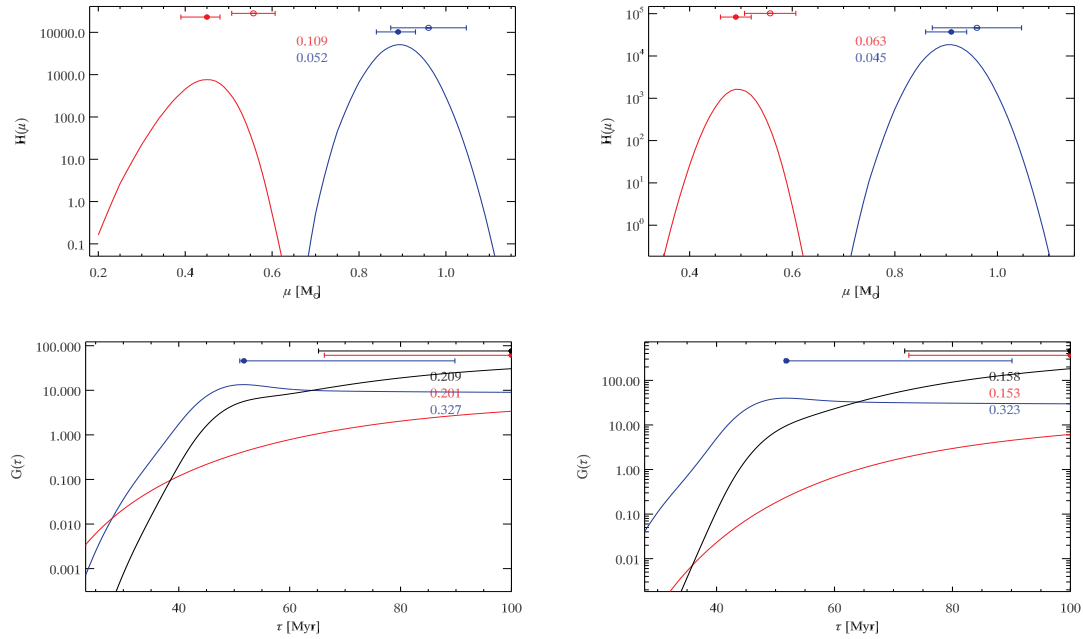


Figure 1.21: NTT 045251+3016 components mass and age distributions from comparison with the standard set of models (see Fig. 1.9 for a description).

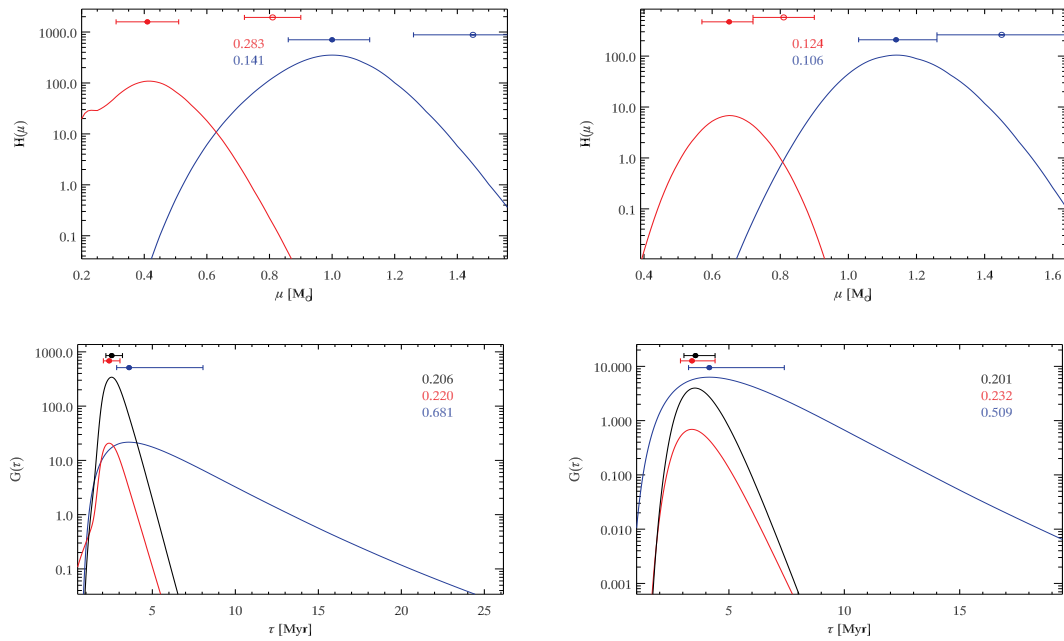


Figure 1.22: NTT 045251+3016 components mass and age distributions from comparison with the set of models with $\alpha = 1.20$, $Y_P = 0.23$ and $\Delta Y/\Delta Z = 2$ (see Fig. 1.9 for a description).

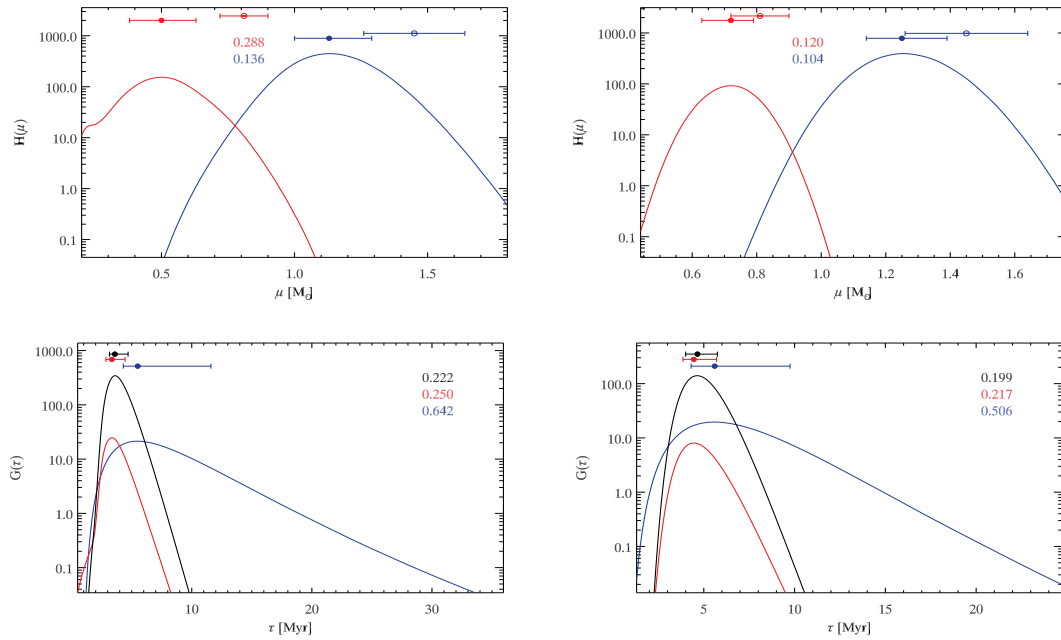
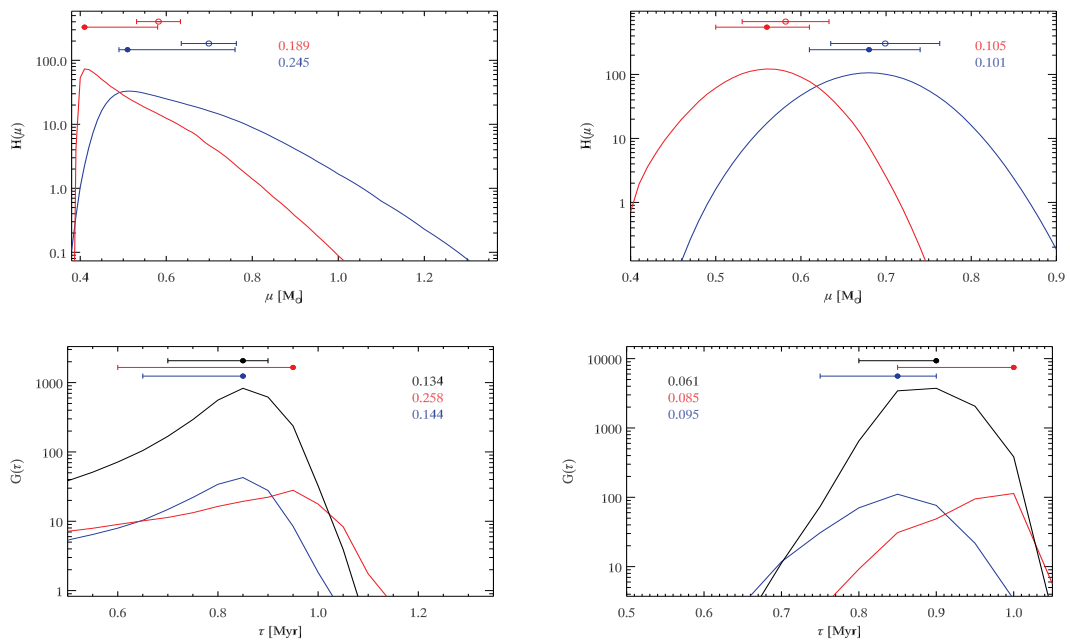


Figure 1.23: HD 98800 B components mass and age distributions from comparison with the standard set of models (see Fig. 1.9 for a description).



MASS SEGREGATION AND ELONGATION OF THE STARBURST CLUSTER WESTERLUND 1^{*,†}

2.1 INTRODUCTION

Westerlund 1 (Wd 1) is among the most massive young clusters in the Local Group. Recent studies have revived interest in this cluster, discovered already 50 years ago (Westerlund 1961). Several of these studies focus on the rich population of massive stars that are spectroscopically identified as Wd 1 members (see e.g. Clark et al. 2005; Negueruela & Clark 2005; Crowther et al. 2006; Negueruela et al. 2010a). Among this population it has been possible to find Wolf-Rayet stars, evolved OB stars, and short-lived transitional objects like Luminous Blue Variables and Yellow Hypergiants. Wd 1 is the only case in which such a rich population of these very rare objects is observable. This makes Wd 1 one of the most important templates for understanding the evolution of very massive stars after they leave the main sequence. One of the great advantages is that the progenitor’s mass of the evolved massive stars can be inferred from the observable main-sequence turn-off. While the massive stars are bright enough to be observed at optical wavelengths, observations of the intermediate- and low-mass stellar population is best performed in the near-infrared, given the high extinction towards Wd 1 of $A_V \sim 10 - 12$ mag (Piatti, Bica, & Claria 1998). A study of the Wd 1 population below $\sim 30M_\odot$ has been recently carried out by Brandner et al. (2008) –hereafter BR08. In this chapter we present comprehensive analysis of the data described in BR08.

With the present estimates of its mass –from 5×10^4 to $1.5 \times 10^5 M_\odot$ – and age –from 3 to 6 Myr– (see Clark et al. 2005; Crowther et al. 2006; Brandner et al. 2008; Mengel & Tacconi-Garman

*This chapter is adapted from the paper Gennaro et al. (2011a)

†Based on observations collected at the European Southern Observatory, La Silla, Chile and retrieved from the ESO archive (Program ID 67.C-0514)

2009; Negueruela et al. 2010a), Wd 1 represents probably the best template in the Milky Way to understand the cluster mode of star formation that can be observed in other galaxies, like the Antennae Galaxies, where Super Star Clusters with masses larger $10^5 M_{\odot}$ have been detected (see e.g. Whitmore et al. 2010).

In addition to the study of the intriguing formation scenario of such massive extragalactic clusters, Wd 1 may also serve as a template to understand the interplay between evolution of massive stars and dynamical processes that may lead to the formation of stable, bound and relaxed globular clusters. Given its mass, Wd 1 may indeed be able to retain a substantial fraction of its initial stellar population, even though, according to Munro et al. (2006), it has probably undergone ~ 65 supernova events. These, in addition to stellar winds and ionizing radiation from the most massive stars, have dispersed the residual gas reservoir of the cluster, decreasing the gravitational binding energy of the system. If massive enough to resist disruption, Wd 1 will eventually turn into a closed, virialized system. A study of the dynamical status of Wd 1 has been made by Mengel & Tacconi-Garman (2009). The authors use the measured radial velocity dispersion for a group of 10 massive stars to infer a dynamical mass of $1.5 \times 10^5 M_{\odot}$, on the upper end of the Wd 1 mass estimates available in the literature. To derive this number, the authors assume virial equilibrium and isotropy of the stellar motions hence their estimate is an upper limit. The analysis of star clusters' dynamical and structural parameters often assumes spherical symmetry. Hence, the cluster properties, like the IMF slope, the stellar density profiles, the stars' velocity distributions, are described as 1D functions depending on the distance from the centre of the cluster. However the spherical symmetry assumption may not be valid, and this is the case of Wd 1. Several studies have already shown that Wd 1 has indeed an elongated shape, based on X-Ray diffuse emission (Munro et al. 2006) and stellar counts (Brandner et al. 2008). Therefore, an unbiased study, which does not assume *a priori* any symmetry for the geometry of Wd 1, is needed to properly investigate the spatial properties of the cluster.

We focus our attention on the study of mass segregation, global and spatially varying IMF and overall cluster shape as can be derived by the study of density profiles. These macroscopic properties are, in turn, related to the formation history of the cluster, its internal dynamical evolution and its global interactions with the rest of the Galaxy. We developed new analysis techniques to take into account the observational biases related to the presence of many very bright objects that can hamper a quantitative determination of both the IMF slope and the stellar density profiles. The most important improvement compared to BR08 is that we drop any spherical symmetry assumption, regarding the cluster structure. Hence the completeness maps, the photometric errors and the density profiles are all obtained in a 2D approach. In addition, new stellar evolutionary models are used for comparison with observations. A probabilistic approach is developed to determine cluster memberships, using a nearby off-cluster image as a control frame for the field population. Stellar masses are derived using a maximum likelihood technique, taking into

account realistic photometric errors and their correlations. IMF slopes are inferred using an approach which does not require any binning but makes use of all the information contained in each star's mass-probability-density-distribution. We use 2D-elliptical-generalization of the radial density profiles by Elson, Fall, & Freeman (1987) to obtain shape properties of Wd 1 (e.g. its semimajor axis, elongation and orientation).

The structure of this chapter is as follows: we describe the data set used in Sect. 2.2. The technique to build completeness maps is introduced in Sect. 2.3. In Sect. 2.4 we use simulated stars to obtain photometric errors and their correlation. A statistical field subtraction method is introduced in Sect. 2.5. After the description of the adopted stellar models (Sect. 2.6), we use them and the clean Colour Magnitude Diagram of Wd 1 to infer its properties like extinction, age and distance (Sect. 2.7). An approach to obtain, for each star, its mass-probability-distribution (given the adopted models) is shown in Sect. 2.8 where we also derive the global IMF slope and the variation of the IMF slope across the cluster. In Sect. 2.9 we build cluster density profiles and analyze them using elliptical models. We also quantify the extent of mass segregation. The last section deals with our conclusions.

2.2 THE DATA

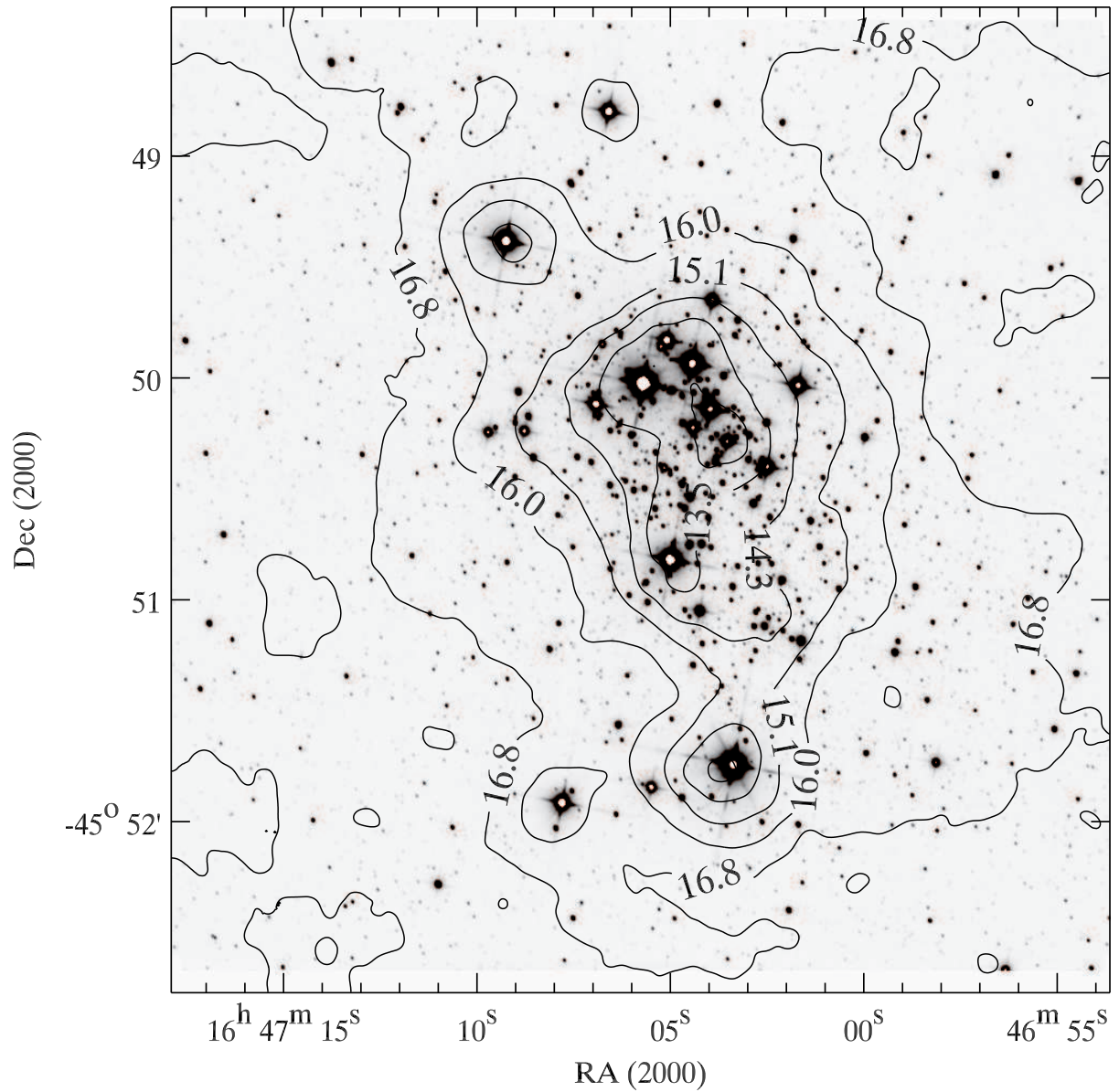
The data set used, the reduction process and the photometric analysis and calibration have been extensively described in BR08; hence we will only provide a short summary here. NTT/SofI J and K_S broad band observations of Wd 1 (centered on $RA(2000) = 16^{\text{h}}47^{\text{m}}03^{\text{s}}$, $Dec(2000) = -45^{\circ}50'37''$) and of a nearby comparison field (offset by $\approx 7'$ to the East and $\approx 13'$ to the South of Wd 1), each covering an area of 4.5×4.5 were retrieved from the ESO archive (PI: J.Alves).

Data reduction was performed using the `eclipse - jitter` routines (Devillard 2001). Point Spread Function (PSF) fitting photometry was derived using the IRAF implementation of DAOPHOT (Stetson 1987). The number of objects detected in both J and K_S bands is ≈ 7000 for the Wd 1 field and ≈ 5300 for the comparison field. Photometric zero points and colour terms were computed by comparison of instrumental magnitudes of relatively isolated, bright sources with counterparts in the 2MASS Point Source Catalogue (Skrutskie et al. 2006).

2.3 2D COMPLETENESS MAPS

To obtain a correct cluster IMF and for the analysis of Wd 1 density profile, it is necessary to derive appropriate incompleteness corrections. In BR08 the authors considered completeness

Figure 2.1: SOFI K_S band image of Wd 1. Superimposed are K_S 50% completeness contours. The labels correspond to the K_S magnitudes for which completeness is 50% along the contour.



correction as a function of magnitude and distance from the centre of Wd 1. In the present work we drop the assumption of radial symmetry and build incompleteness correction maps as a function of the position on the chip and of the magnitude.

The main source of incompleteness in our case is crowding, which severely affects seeing limited observations (see Eisenhauer et al. 1998 as an example). The effects of crowding on the detection of point sources change according to two quantities: the average stellar density and the magnitude contrast between the given point source and its neighbours. Both of these quantities may not follow a radially symmetric or regular distribution. Very bright objects are normally scattered over the field in a nonuniform way. Even when they have a regular distribution, they still can cause sudden and very well localized drops in the completeness. In addition each of them has its own brightness and causes a lack of detections in areas of different angular width over the chip. Stellar density itself does not *a priori* have to follow a symmetric distribution; indeed the actual number of stars for a given position is determined by an interplay of several factors, e.g. the intrinsic spatial distribution of stars within the cluster, varying extinction pattern (in the foreground, but also within the cluster) or changes in the fore- and background population characteristics, for example within the spiral arms. For these reasons we think that an approach that does not assume any spatial distribution in the completeness characteristics of an observed field is preferable, in contrast to integrated or averaged cluster characteristics, and is definitely recommendable when spatial properties have to be investigated. For each photometric band we built a function with 3 variables:

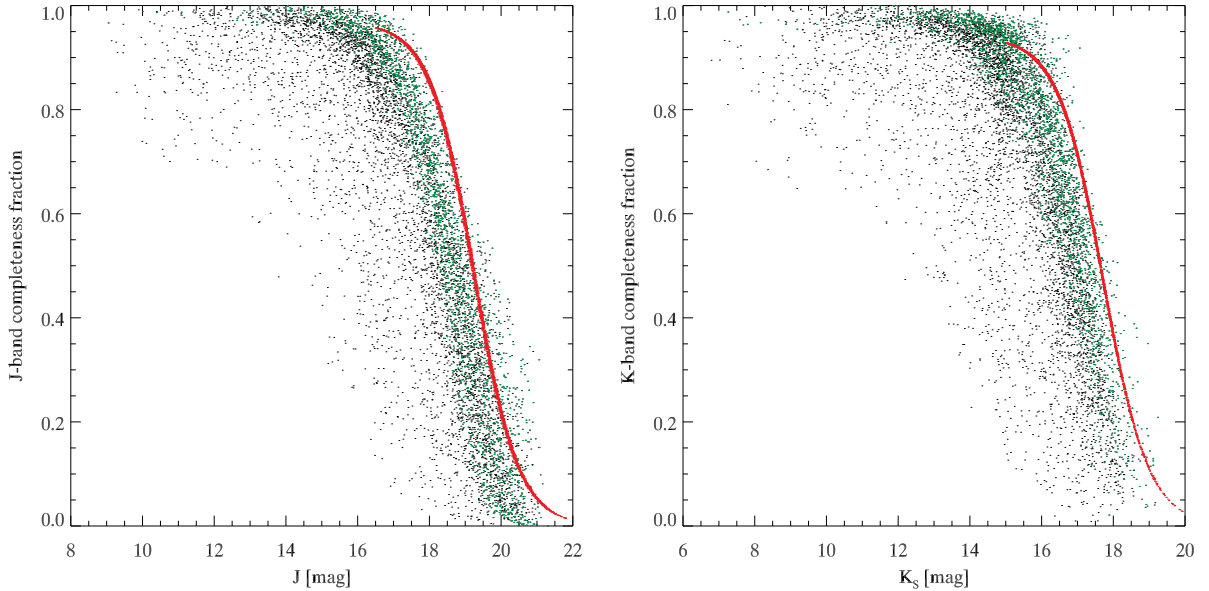
$$C_j \equiv C(M_j|x, y, \mu) \quad ;$$

where μ is the actual value of the magnitude (in the M_j band) and (x, y) the position at which completeness is evaluated. It is then possible to associate an incompleteness correction to each star for each photometric band. The total incompleteness correction for a star detected in both J and K_S bands is the product of the single corrections in each band. The reason is that each of these corrections represents the probability of detecting that given star in that specific band, and detections in each band are independent from each other. The C_j completeness maps have been obtained in several steps, which are detailed in Appendix 2.A.

A visualization of the completeness pattern for Wd 1 is shown in Fig. 2.1. We display the K_S band image of the cluster with superimposed 50% completeness magnitude-loci. The contours are labeled with the corresponding values of K_S magnitudes for which completeness drops to 50%. Such contours follow the general distribution of stars, but also show peaks around the brightest stars, as expected; from Fig. 2.1 it is clear that radial symmetry is not a perfect assumption for the completeness distribution of Wd 1.

A comparison of the completeness values between Wd 1 frame and the off-cluster frame, for both photometric bands, is shown in Fig. 2.2. Given the spatial dependence of the completeness

Figure 2.2: Comparison of the completeness values for the Wd 1 stars (black dots) and the stars in the off-cluster frame (red dots) for J and K_S bands. The green dots represent stars in Wd 1 frame, with angular distance from the cluster’s centre larger than $2'$.



for the Wd 1 frame’s stars, for them there is not an unique value of the completeness at a given magnitude; for what concerns the off-cluster frame, we assumed spatial uniformity for the completeness, so the off-cluster frame stars (red dots) have unique values of the completeness as a function of magnitude (see Sect. 2.A.4). Figure 2.2 shows that the completeness for the off-frame stars is always higher, at a given magnitude, than the average completeness for the Wd 1 frame stars. Similarly, 50% incompleteness is reached for the control field at ≈ 1 mag fainter than the average 50% incompleteness for Wd 1 field. The cause of this difference may be found in the different degree of crowding of the two fields. The green dots in the figure represent stars in Wd 1 frame located at more than $2'$ from the centre of the cluster, corresponding to ~ 2.3 pc at the cluster’s distance of 4 kpc (see Sect. 2.7.2). Even though these latter stars show –as expected– the highest completeness values for Wd 1 frame, they still have slightly lower completeness than the off-cluster frame stars. This is a reason to believe that crowding in this ”peripheral” regions of the cluster frame is still higher than in the off-cluster frame, a hint to the presence of a low-mass cluster stellar population extending quite far away from the cluster centre. In Sect. 2.9 we will show evidence that the low-mass stars of Wd 1 may indeed occupy a region with a radius of the order or even larger than 3 pc.

2.4 PHOTOMETRIC ERRORS

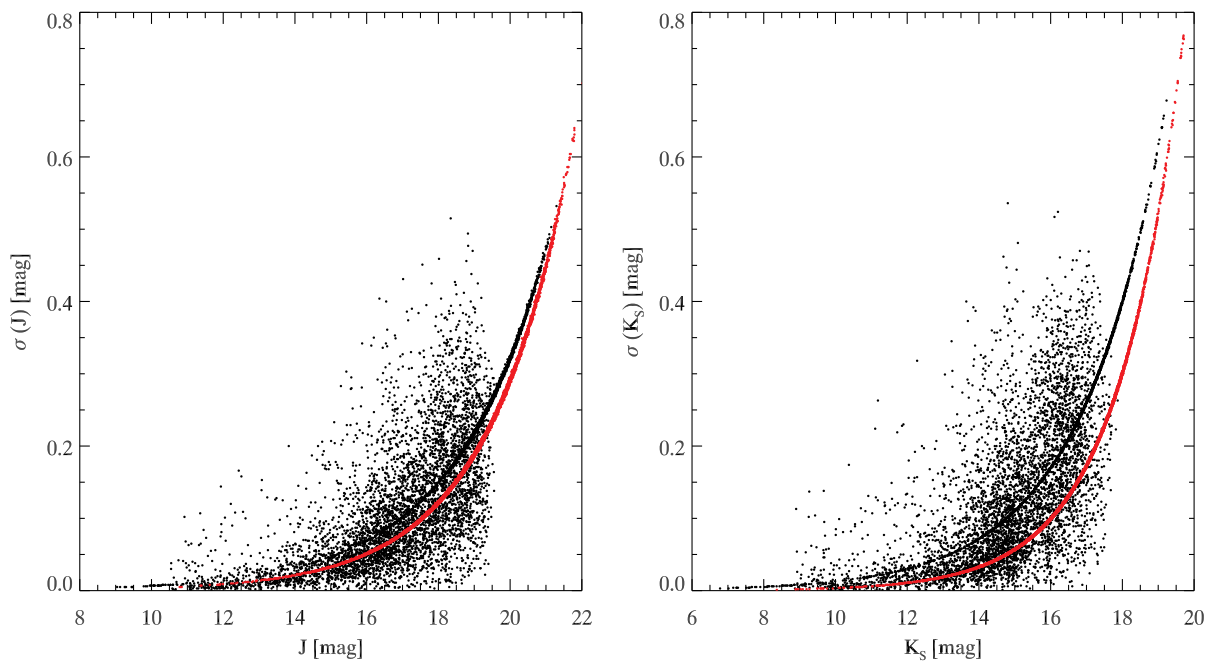
As shown in BR08, the DAOPHOT photometric errors are usually an underestimate of the true errors. DAOPHOT errors are connected to the residuals in the PSF fitting of the stellar counts. In principle this error estimate is absolutely correct for isolated stars only, so that the light is coming from the source of interest alone and only if the analytical PSF model chosen for PSF fitting is the correct representation of the true PSF shape. In this ideal case the errors would come only from the Poisson noise in stellar counts. In crowded fields, however, there are additional sources of uncertainty. The main one is the presence of bright objects. Even though the light from these sources is iteratively subtracted from the frame by the PSF fitting algorithm, the unsubtracted noise in the wings of these objects can still affect the magnitude estimate of nearby faint stars. Stellar crowding itself can cause problems when the algorithm has to disentangle very close sources even when they have similar magnitudes. We use simulated stars to estimate realistic errors as a function of magnitude and position of the stars. The new estimates of the photometric errors are derived from the difference between the inserted and recovered magnitude of the simulated stars. In addition, we examine the correlation between the estimated magnitude errors in the J and the K_S bands. The details of errors evaluation are given in Appendix 2.B. Our error estimates are shown in Fig. 2.3 as a function of magnitude.

2.5 SUBTRACTION OF THE FIELD STARS

We developed a technique for field subtraction based on a probabilistic approach. The technique takes into account the photometric errors, their correlation and the information about completeness. The natural space for our approach is an N -dimensional magnitude space. The technique is quite general and, as long as photometric errors in different bands and their correlations are evaluated, does not have to be limited to two bands. In the case of Wd 1 we only used J and K_S bands hence we will refer explicitly to them.

In the ideal case, a cluster magnitude-magnitude diagram (MMD) would look exactly the same as in the off-cluster field, plus additional stars belonging to the cluster, possibly following a separate sequence in the diagram, along an isochrone. It should be possible to compute the stellar densities at each MMD position for both the on-cluster and the off-cluster frames and compare them. Regions with an overdensity of stars would correspond to regions occupied by cluster members. The difficult part in the on-off density comparison is to compute a proper density. Usually this is accomplished by gridding the CMD and by computing a density at each grid cell. Then, according to the numbers in the cluster cells and in the off-field cells, some stars are subtracted, usually by making use of Monte Carlo techniques. This approach has been very

Figure 2.3: The newly derived photometric errors as a function of magnitude in J and K_S . Errors for the stars in the cluster's field in black, errors for the off-frame stars in red.



successful in many applications, also in our BR08. Anyway, any gridding or binning procedure always implies a loss of information. Gridding is usually performed using equal cells, and this does not take into account, for example, the fact that photometric errors increase with magnitude, making it less obvious to which cell a faint star should belong. On the bright parts of the CMD the grid size may instead be very large compared to the photometric errors. In this case the gridding would result in combining stars that, if errors would be reliable, are very distant from each other –in units of their σ_{phot} – and then should not be considered ”similar” and assigned to the same cell. We decided to change this approach and to calculate the density of stars locally, at each position in the cluster’s MMD where a star is located. Then we calculated the density in the same point of the MMD, but for the off-frame population. The ratio of the two densities is a measure of the membership probability of the star that is in that position in the cluster’s MMD.

According to its photometric errors, each star is not a single point in the MMD, but a multi-dimensional Gaussian *cloud* of probability, representing the chance of observing that object in that position. In our 2D case these Gaussians have an elliptical symmetry with semi-axis represented by σ_J and σ_{K_S} and a tilt in the MMD related to the correlation between the two magnitude errors. Since Gaussian probability is greater than 0 everywhere in the MMD, each star contributes *a bit* to the total density at each MMD position, the closest stars to that position having higher weight. Given a star with magnitudes (J_*, K_{S*}) we define the density at its position in the MMD in the following way:

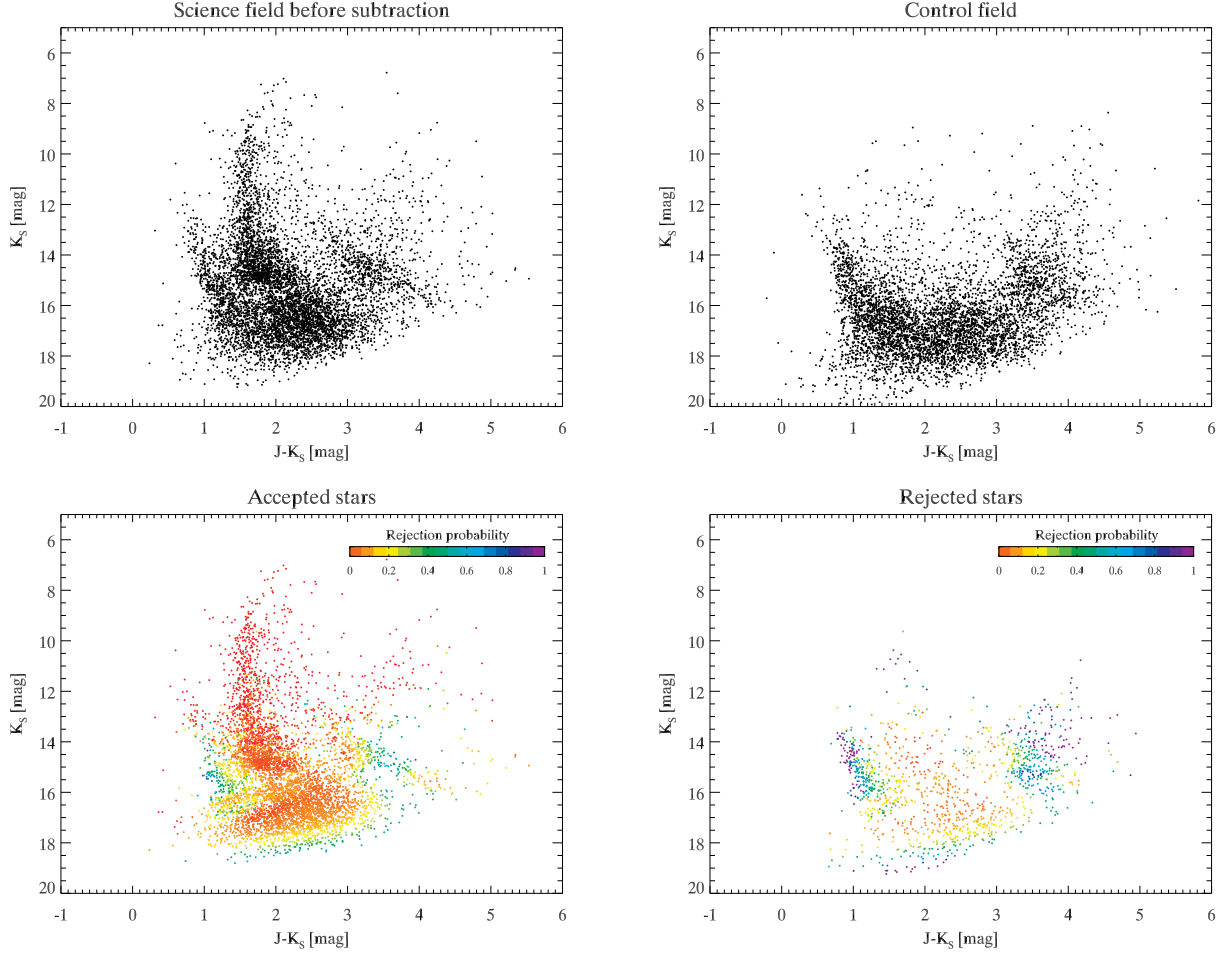
$$\rho(J_*, K_{S*}) = \sum_i \frac{1}{C_{J_*} C_{K_{S*}}} \times \frac{1}{C_{J_i} C_{K_{S_i}}} \times \frac{1}{2\pi|\Sigma_*|^{1/2}} \times \frac{1}{2\pi|\Sigma_i|^{1/2}} \times \int \exp\left[-\frac{(\mathbf{M} - \boldsymbol{\mu}_*)^T \Sigma_*^{-1} (\mathbf{M} - \boldsymbol{\mu}_*)}{2}\right] \times \exp\left[-\frac{(\mathbf{M} - \boldsymbol{\mu}_i)^T \Sigma_i^{-1} (\mathbf{M} - \boldsymbol{\mu}_i)}{2}\right] d\mathbf{M}; \quad (2.1)$$

where the asterisk refers to the star at whose position the density is evaluated, such that C_{J_*} and $C_{K_{S*}}$ are the completeness fractions for that object, while C_{J_i} and $C_{K_{S_i}}$ are the completeness fractions for the other stars. The density is calculated in both the on and the off field MMD, hence the index i may run respectively on the stars in one or the other field. The $\boldsymbol{\mu}$ vectors and the Σ matrix are, respectively, the measured magnitudes and the covariance matrix associated to them:

$$\boldsymbol{\mu}_{*/i} = \begin{pmatrix} J_{*/i} \\ K_{S*/i} \end{pmatrix} \quad \Sigma = \begin{pmatrix} \sigma_J^2 & r\sigma_J\sigma_{K_S} \\ r\sigma_J\sigma_{K_S} & \sigma_{K_S}^2 \end{pmatrix}. \quad (2.2)$$

$|\Sigma|$ is the determinant of the correlation matrix, and r is the Pearson’s correlation coefficient of equation (2.13). The \mathbf{M} vector is the vector of coordinates (J, K_S) over which the integration is

Figure 2.4: *Upper panels:* on and off field CMDs. *Lower panels:* Results of the subtraction process. The colour coding indicates the rejection probability $\mathcal{R}_{\text{rej}} = \rho^{\text{off}}/\rho^{\text{on}}$. Red represents very likely members ($\mathcal{R}_{\text{rej}} = 0$) and purple very unlikely ones ($\mathcal{R}_{\text{rej}} = 1$).



actually performed. The integration is ideally performed in the whole (infinite) magnitude space. For obvious reasons we limit the numeric integration around each star to a region within $\pm 5 \sigma_*$ for each coordinate.

Equation (2.1) deserves several comments. Its meaning is the following: the contribution of the i -th star to the density at the (J_*, K_{S*}) position is the integral of the product of that star's probability distribution, convolved with the probability distribution of the $*$ -th star. Then the total density in that position is the sum over all the i stars either in the on-field or in the off-field. The probability of each single star is normalized to 1, as it has to be, but it is important to consider the completeness factors $\frac{1}{C_{M_*}}$ and $\frac{1}{C_{M_i}}$ for $M = J, K_S$ that appear in equation (2.1). These factors account for the missing detections in both the science and the control field. It is easy to under-

stand why such correction is necessary. Imagine a star in the cluster field, with completeness factor 0.25; it means that if we detected that object, then (in an statistical sense), there are 3 other similar objects that we were unable to detect. Now imagine that at the same position in the off-cluster MMD we would detect two objects both with completeness factors equal to 1. Neglect for a moment the real "cloud" shape of the stars' probability density distributions, and consider them *ideally* as points in the MMD. By computing densities without the completeness corrections, we would obtain $\rho^{\text{off}} = 1$ and $\rho^{\text{off}} = 2$. Hence we would *oversubtract* that star from the cluster's MMD. On the other hand, the completeness factor tells us that the actual value of ρ^{on} is not 1 but 4, and then we would subtract that object only in $2/4 = 0.5$ cases or, better said, we would assign to that star a 50% membership probability (see also below).

Once we have both the on- and off-field densities at a given star's location in the MMD, we can compare them. The ratio $\mathcal{R}_{\text{rej}} = \rho^{\text{off}}/\rho^{\text{on}}$ defines a rejection probability; the higher the contrast in the two densities –the lower \mathcal{R}_{rej} is– the more likely the object is a member. On the opposite side, when we are in a region of the MMD where no cluster members are present, this number approaches 1. Hence each detected object has its associated membership probability. To decide whether or not to keep it in the catalogue of member stars, we extracted uniform random numbers $\zeta \in [0, 1]$. Then if $\zeta < \mathcal{R}_{\text{rej}}$ we discard the object, otherwise we keep it. This also means that in the following analysis the actual catalogues that we used may differ from one another, because some stars may be sometimes excluded or included according to this random selection. The uncertainties related to this selection directly propagate into, e.g., the IMF slope evaluation. To account for this we used multiple catalogue realizations and evaluate the uncertainties in the outcoming results as the scatter in the results (e.g. the IMF slope, see 2.8.2 for more details).

In Fig. 2.4 we show the CMDs¹ of Wd 1 frame and of the control frame, used as a reference for the field population, together with the results of the subtraction process. The colour coding in the lower panels indicates the rejection probability, \mathcal{R}_{rej} . As already mentioned in BR08, and as is clearly visible in the upper panels of the figure, the foreground and –especially– the background population in the two frames do not look really similar. A possible cause for the differences might be a different amount of extinction along the different lines of sight in the on and off field. This population differences cause an under-subtraction of stars in certain regions of the CMD. However, it is clear that the most likely members in the lower left panel (the red points) follow a well defined cluster sequence; nevertheless some isolated fore and background stars in the cluster's frame also show an artificially high membership probability. The reason is that there are no objects in the off field MMD at the same position.

To avoid such artificial contamination, in addition to the subtraction process, we used a σ -clipping of our CMD (see Appendix 2.C). After finding the best fitting isochrone (see Sects.

¹Even though all the procedure is performed in the MMD, for the sake of clarity we show the most commonly used CMDs, where the usual characteristics of a cluster population are better visible

2.6 and 2.7), we decided to keep only stars that lie within 3σ from it, i.e. those stars that satisfy the criterion $|J_* - J_{\text{isoc}}| < 3 \times \sigma(J_*)$ and $|K_{S*} - K_{S\text{isoc}}| < 3 \times \sigma(K_{S*})$ for at least one point $(J_{\text{isoc}}, K_{S\text{isoc}})$ on the isochrone.

2.6 THE STELLAR MODELS

In the following analysis, we use a combination of Padova main sequence (MS) isochrones (Marigo et al. 2008) and Pisa pre-main sequence (PMS) models (Degl’Innocenti et al. 2008). Padova models are accessible on the web² and are already provided in the 2MASS photometric system. For Pisa isochrones, we performed the conversion from the theoretical HR Diagram to the observational 2MASS-CMD ourselves. We used Brott & Hauschildt (2005) spectra, calculated with the PHOENIX model atmosphere code for the lowest temperature regions and Castelli & Kurucz (2003) spectra, based on ATLAS9 model atmospheres for the highest temperature in the PMS isochrones (see Table 2.1). As in BR08, we assumed a solar chemical composition for Wd 1, hence both the MS and PMS models used here have this composition. Nevertheless, given the intrinsic differences in the evolutionary codes (opacity tables, EOS, heavy elements mixture) and given also the fact that the “Solar” composition is not exactly the same in the two sets of models, they show some differences in the region of overlap. Small differences are present also between the set of PMS isochrones transformed with PHOENIX and ATLAS9 model atmospheres. We have carefully chosen the masses for the transition from one set of models to the other, in order to minimize the differences in colour between them. The colour differences are shown in Table 2.1, together with the mass and temperature ranges in which we adopt each model. The Pisa-ATLAS9 isochrones have been shifted in order to match the Padova isochrones at $4 M_{\odot}$, and the Pisa-PHOENIX have been shifted to match the Pisa-ATLAS9 ones at $2 M_{\odot}$. Table 2.1 shows that the offsets are quite small, specially when compared to the expected absolute precision in our photometry, which, taking into account the zero point errors is of the order of 0.05-0.1 mag.

2.7 FUNDAMENTAL PARAMETERS OF WESTERLUND 1

Before proceeding with the spatially dependent analysis, we derived the global, average properties of Wd 1 using the combined isochrones described above.

²At the following URL: <http://stev.oapd.inaf.it/cgi-bin/cmd>

Table 2.1: Mass, temperatures and magnitude offsets at the transition masses for our combined isochrones. The PS-AT9 offsets are: $\text{mag}(\text{Pisa-AT9}) - \text{mag}(\text{Padova})$ at $M = 4M_{\odot}$ while the PS-PHX offsets are: $\text{mag}(\text{Pisa-PHX}) - \text{mag}(\text{Pisa-AT9})$ at $M = 2M_{\odot}$.

Model	Mass [M_{\odot}]	T_{eff} [10^3K]	Offsets [mag]		
			J	H	K_S
Padova	$M \geq 4$	$T_{\text{eff}} \geq 15.4$	-	-	-
PS-AT9	$2 \leq M \leq 4$	$5.8 \leq T_{\text{eff}} \leq 15.4$	0.04	0.02	0.04
PS-PHX	$M \leq 2$	$T_{\text{eff}} \leq 5.8$	0.01	0.02	0.01

2.7.1 REDDENING AND EXTINCTION

For high mass stars on the MS, the near-infrared part of the spectrum is very well approximated by the Rayleigh-Jeans tail of a black body with temperature T_{eff} . Then, for masses above $\sim 5 M_{\odot}$, given that the SED shape is almost unchanged, the near-infrared, $J - K_S$, colours stay constant (and around 0 mag). The upper main sequence (UMS) in such a CMD looks simply like a vertical line. Therefore it is possible to estimate the reddening towards Wd 1 by fitting the $J - K_S$ colour of the UMS. To perform the fit, we used the stars for which $K_S < 13.5$ mag and $1.2 < J - K_S < 2.0$ mag and minimized the quantity:

$$\sum_j |(J - K_S)_j - (J - K_S)_{\text{isoc}}|$$

where j runs over the selected stars and the isochrone colour is taken at the same K_S of the j -th star. The $J - K_S$ colour selection reduces the contamination by stars clearly belonging to the foreground or background population. Once the $J - K_S$ reddening has been estimated, extinction A_{K_S} is computed using an extinction law. Since, by definition, $E_{JK_S} = A_J - A_{K_S}$ we have:

$$A_{K_S} = \frac{E_{JK_S}}{\frac{A_J}{A_{K_S}} - 1}$$

The knowledge of the interstellar extinction law provides the missing A_J/A_{K_S} ratio. While in BR08 the widely used Rieke & Lebofsky (1985) –hereafter RL85– extinction law was adopted, in the present work we use the much more recent Nishiyama et al. (2006) one –hereafter N06–. The authors make use of a large number of red-clump stars located in the galactic plane. These stars have intrinsically similar colours, hence the observed differences in colour are related to different amount of interstellar absorption. Red-clump stars describe a straight line in the $(H - K_S, J - H)$ diagram parallel to the reddening vector. Hence the slope of this line can be used to determine the $A_J : A_H : A_{K_S}$ selective absorption ratios. In addition to the largely improved statistics, as compared to the few sources available in RL85, the N06 selective absorption has the advantage

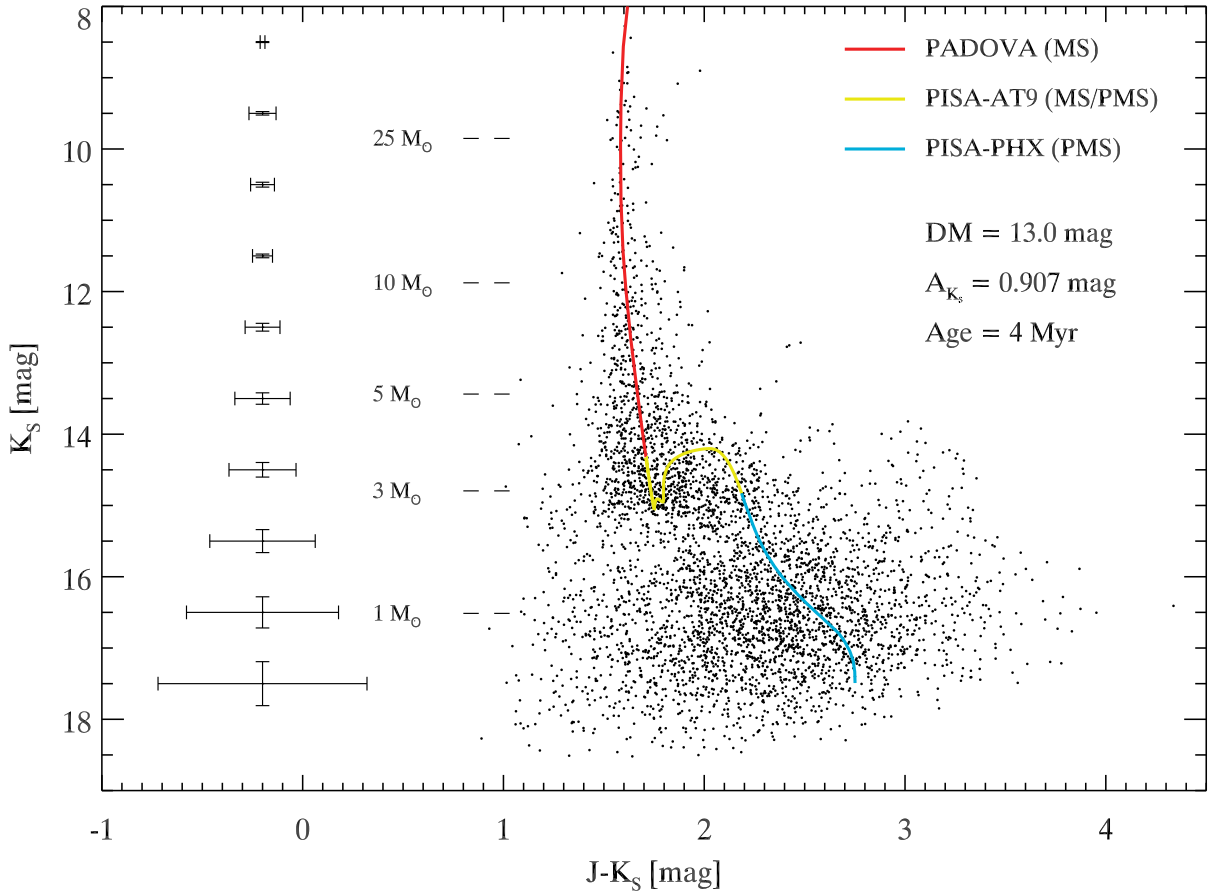
of having being measured using a K_S filter, while RL85 used K . Hence the former provides a result that is in the same photometric system as our data. The J -to- K_S selective absorption ratio in the N06 case is given by $A_J/A_{K_S} = 3.021$, slightly higher than the $A_J/A_K = 2.518$ from RL85. We checked that the obtained A_{K_S} value actually does not depend on the age of the adopted isochrone. Our best fitting isochrone of 4 Myr (see also 2.7.2) provides a value of $A_{K_S} = 0.907$ mag; if isochrones in the range 3–8 Myr are used, the scatter in the inferred A_{K_S} is less than 0.01 mag. To estimate the error on the extinction value, we followed this reasoning. The absolute scatter in $J - K_S$ colour of the UMS stars used for the reddening fitting described above is about 0.2 mag. This means that a reasonable estimate for the reddening fitting error is 0.1 mag. From this, and using the N06 reddening law coefficients, it follows that the error on the inferred total extinction can be estimated as $\Delta A_{K_S} = 0.05$ mag.

Given these errors and the results of BR08, with $A_{K_S} = 1.13 \pm 0.03$ mag, it may seem that our new findings are inconsistent with the previous ones. Nevertheless one always has to keep in mind two crucial sources of systematic uncertainty in the method used and that are not included in the error estimates above. One is of course the choice of the stellar models, which may differ from one another both in the theoretical HR diagram and also in the transformations used to convert temperatures and luminosities into colours and magnitudes. A difference of 0.05 mag in the intrinsic near-infrared colours of UMS stars is anything but unexpected. We compared the Padova models used in the present work with the Geneva models used in BR08 (Lejeune & Schaerer 2001), using in both cases solar metallicity and an age of 4 Myr and 3.9 Myr, respectively. We observed differences in $J - K_S$ intrinsic colour ranging from 0.03 to 0.1 mag, at a given magnitude, in the mass interval from 5 to 30 M_\odot , used for the reddening estimate. The other source of systematic uncertainty, is the aforementioned choice of the reddening law. In BR08 we used the RL85 law, and given that the selective absorption ratios are quite different between RL85 and N06, this explains the difference in our previous and new results for the total extinction.

To compare our findings with those by other authors, our best A_{K_S} value cannot be directly converted into an A_V using only the N06 law. This law has indeed been obtained only from J -band redwards (see also Nishiyama et al. 2009 for the extension of the N06 reddening law towards photometric bands redder than K_S). Hence we use a combination of $A_J/A_{K_S} = 3.021$ ratio from N06 and the $A_V/A_J = 3.546$ ratio from RL85 to obtain $A_V = 9.7$ mag. As already noticed in BR08 different authors report values of A_V that vary in the range from 9.4 to ~ 12.0 mag, so our final value is included well within this range.

Recently Negueruela et al. (2010a) have observed the presence of differential reddening across Wd 1. They report a range of $\Delta E_{VI} \approx 1.4$ mag. This range can be converted into a range of $\Delta E_{JK_S} = 0.51$ mag using again a combination of RL85 and N06 laws, matched at the J -band. The observed colour range for the UMS members in our data set is somewhat smaller than this and part of this spread is probably due also to photometric errors and undetected binarity.

Figure 2.5: One realization of the clean CMD after field subtraction and σ -clipping. Error bars represent the average photometric errors per magnitude bin. The best fitting combined isochrone is also shown, with three colours indicating the three different parts of which the isochrone is composed (see Sect. 2.6 and Table 2.1). Some values of the stellar mass are also shown for illustration.



Hence differential reddening across the cluster cannot be excluded, but Negueruela et al. (2010a) extinction spread has to be regarded as an upper limit.

2.7.2 DISTANCE AND AGE

As illustrated in BR08, the morphology of the PMS-MS transition region and of the whole PMS can be combined as a good age indicator for young clusters. Since extinction is determined independently (see 2.7.1), the distance modulus, DM, and the age, τ , can be determined without having extinction as a free parameter. Good age constraint is provided by those stars that have just entered the MS. These stars are located at the base of the vertical MS and have $14.9 \lesssim$

$K_S \lesssim 15.1$ mag and $1.6 \lesssim J - K_S \lesssim 1.8$ mag. No cluster members are present at magnitudes immediately fainter than that (see lower left panel in Fig. 2.4). This Zero-Age-Main-Sequence (ZAMS) region is very well identifiable in the cluster's CMD and can be used to anchor the isochrones position. It is worth mentioning that the determination of the age and DM in the present work is not done by a real fitting procedure, but through the conventional superposition of different isochrones for several values of the pair (DM, τ). The DM and age values would be degenerate if only the ZAMS position would have been used for their determination. A slightly older isochrone would have an intrinsically fainter ZAMS point, and this could be compensated by a reduction of the DM. Isochrones of different ages, however, also show different colours for the PMS branch, the younger, the redder. Hence, in our comparison, after trying to reproduce the ZAMS point, we also take into account the shape of the PMS-to-MS transition region and the PMS colour. The uncertainty on the DM determination can be reasonably quantified as $\Delta\text{DM} = 0.1$ mag from the magnitude extension of the ZAMS region. The minimum age uncertainty that we can quote is instead half of the spacing between the different isochrones in our grid, i.e. 0.5 Myr. By isochrone superposition we obtain our fiducial values of $\text{DM} = 13.0 \pm 0.1$ mag (corresponding to a distance $d = 4.0 \pm 0.2$ kpc) and $\tau = 4 \pm 0.5$ Myr.

In BR08 values of $\text{DM} = 12.75 \pm 0.10$ mag ($d = 3.55 \pm 0.17$ kpc) and $\tau_{\text{PMS}} = 3.2$ Myr for the PMS population were found, while the MS stars provided weaker constraints on the age with τ_{MS} between 3 and 5 Myr. The use of more recent PMS models partially reconciles our findings with those of other authors. For example Crowther et al. (2006), by comparing the number of WR stars and of cool hypergiants, find $\text{DM} = 13.4$ ($d = 4.8$ kpc) and $\tau = 4.5$ or 5 Myr. From observations of H I, Kothes & Dougherty (2007) find a distance $d = 3.9 \pm 0.7$ kpc. Negueruela et al. (2010a), from a comparison of their spectroscopically classified objects with models by Meynet & Maeder (2000), favour values of $d \gtrsim 5$ kpc and $\tau \gtrsim 5$ Myr. The authors point out the difficulties in spectral classification for several objects, the approximate character of the T_{eff} scale, the uncertainties in M_V values and, finally, the uncertainty in stellar evolutionary models for massive stars. The values of $d \sim 5$ kpc and $\tau \sim 5$ Myr are also supported by Ritchie et al. (2010), where the authors derive constraints on these quantities from the study a massive, interacting, eclipsing-binary. Clearly there are still difficulties in the determination of the distance and age for Wd 1 with different methods providing slightly different values. Nevertheless with the present work the differences between the values inferred using the intermediate- and low-mass end of the stellar population, on one side, and the high mass end on the other, are somehow reduced.

2.8 THE IMF OF WESTERLUND 1

The comparison of observed magnitudes with isochrones allows the determination of stellar masses. The mass probability distribution for each star was determined by taking into account the magnitude errors and their correlation. The distributions for the single stars are then combined to build the IMF of Wd 1. The detailed information on the completeness pattern across the field allows us to explore the variations of the IMF slope within Wd 1. In the following, we consider all our objects as single stars, nevertheless we are aware of the possible biases introduced by neglecting the presence of binaries (see Maíz Apellániz 2009).

2.8.1 THE MASS OF THE SINGLE STARS

Given our best-fitting isochrone (see Sect. 2.7) we used a maximum-likelihood approach to determine the mass of the member stars. Again we work in the magnitude-magnitude space. There the probability density distribution of a star is characterized by its average magnitudes, by their photometric errors and by the correlation among them. Isochrones in the MMD are curves parameterized by the mass value of the star, m . Hence the probability of a star with mass m and magnitudes $\mathbf{M}(m) = (J(m), K_S(m))$ to be observed at the $\boldsymbol{\mu}_* = (J_*, K_{S*})$ location in the MMD is:

$$p(m) = \frac{1}{2\pi|\boldsymbol{\Sigma}_*|^{1/2}} \times \exp \left\{ -\frac{1}{2} [\mathbf{M}(m) - \boldsymbol{\mu}_*]^T \boldsymbol{\Sigma}_*^{-1} [\mathbf{M}(m) - \boldsymbol{\mu}_*] \right\} \quad (2.3)$$

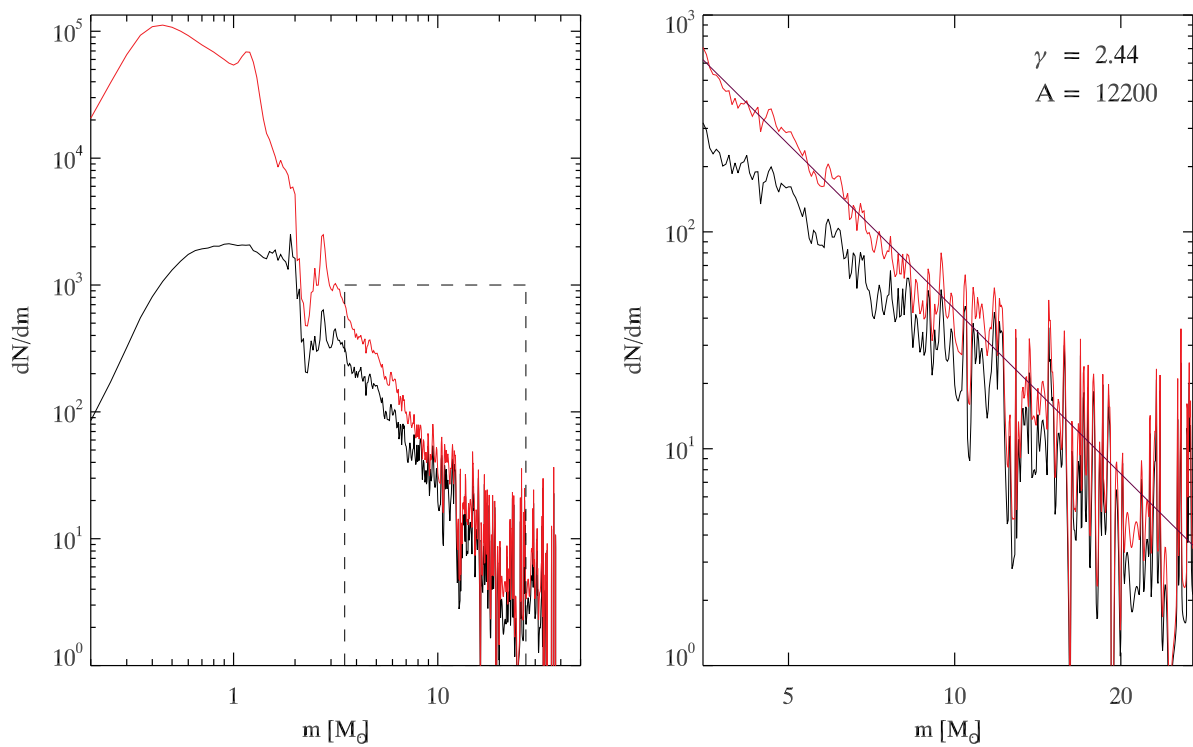
(see equations (2.1) and (2.2) for a definition of the symbols).

We imposed the condition $\int_{iso} p(m) dm = 1$, hence $p(m)$ represents a probability density distribution. With this approach, we can determine not only the most likely mass for each star, by maximizing $p(m)$, but also the reliability of the mass value obtained. If a star is indeed located very far from the best-fit isochrone (in units of its photometric σ), then its $p(m)$ will be a very *broad* function, with a poorly determined peak. On the contrary if the star lies exactly on the isochrone then, ideally, $p(m)$ will be a Dirac δ function.

2.8.2 IMF SLOPE AND TOTAL MASS DETERMINATION

A standard approach to evaluate the IMF slope of a cluster is to build a histogram of the stellar masses and then fit a power law (or a log-normal distribution) to the histogram. It is known, however, that the value of the slope is quite sensitive to the way the binning is performed and even to the space in which the fitting is done, i.e. a linear or logarithmic space for the mass

Figure 2.6: *Left:* Mass function for Wd 1; the dashed box indicates the region that is used for the fit of the IMF slope. *Right:* Zoomed version for the dashed box region; $\gamma = 2.44$ and $\mathcal{A} = 12200$ are our best estimates of the power law coefficient and IMF normalization constant, respectively. Red lines correspond to the completeness-corrected function while the uncorrected function is shown in black for comparison. The blue line in the right panel is the best-fitting power-law.



coordinate (see e.g. Maíz Apellániz 2009 for an exhaustive description of the subject). These problems were also discussed in BR08 where we showed that the cumulative mass distribution, not requiring any binning, can be used to give stronger constraints on the IMF slope. Here we introduce an alternative method that does not require any binning and makes use of the *fundamental* information on the mass probability distribution, $p(m)$, which is always ignored when only the best-mass values are used, even without binning. Given the $p_i(m)$ for each star in Wd 1 we define the observed Mass Function:

$$\frac{dN(m)}{dm} = \sum_i \frac{1}{C_{J_i}} \times \frac{1}{C_{K_{S_i}}} \times p_i(m) \quad (2.4)$$

The $\frac{dN(m)}{dm}$ function for the whole Wd 1 population is shown in Fig. 2.6. We used a restricted range of masses to determine the global slope of the IMF, γ , where $\frac{dN(m)}{dm} = \mathcal{A} \times m^{-\gamma}$ with normalization constant \mathcal{A} and $\gamma = 2.3$ for a typical Salpeter or Kroupa IMF, in the mass regime above $0.5 M_{\odot}$ (Salpeter 1955; Kroupa 2001). The lower mass limit for the slope fit is chosen to be $m_{\min} = 3.5 M_{\odot}$. At this mass we have 50% global completeness on the whole frame. Locally this value could be different. For example, in the very centre of the cluster, high incompleteness is reached at high values of the stellar mass (see the lower panels of Fig. 2.8). This may cause some additional uncertainty on the derived IMF slope. The effects of spatially-varying-incompleteness are investigated in detail in Sect. 2.8.3, where the potential bias in the cluster centre is also analyzed. The upper mass limit for the slope fit is chosen to be $m_{\max} = 27 M_{\odot}$. The reasons for this limit are: i) the magnitude limit of our data-set. Stars more massive than this are above the linearity regime of the NTT/SofI observations that we have used. ii) stars above this mass are close to the turn-off region, according to Padova isochrones. Hence the determination of their initial masses starts to be age-dependent, and the complex post-MS evolution of such massive stars is quite uncertain, from the theoretical point of view. iii) the fitting procedure: above this mass value the numbers become so small that statistical fluctuations are not negligible and could lead to a bad fit.

We show the results in bi-logarithmic plots, but the actual fit has been performed in a linear space. The global IMF slope we obtain is $\gamma = 2.44_{-0.08}^{+0.20}$, slightly steeper than an ordinary Salpeter/Kroupa IMF. We will explore in Sect. 2.8.3 local departures from this behaviour. For the normalization constant we found $\mathcal{A} = 1.22_{-0.14}^{+0.56} \times 10^4$. The best values and uncertainty of γ and \mathcal{A} are evaluated by using a bootstrap technique, as detailed in Appendix 2.D. Given the couple of values (γ_i, A_i) obtained from a single bootstrap sample, it is possible to associate to them a value of the total mass and total number of stars for Wd 1. We extrapolate the power law with index γ_i in the range $m[M_{\odot}] \in [0.5, 120]$. The upper mass limit is a reasonable estimate of the highest stellar mass that is expected to form in a massive cluster as Wd 1. From Padova isochrones, we have that stars with initial masses larger than $\sim 65 M_{\odot}$ are supposed to have already undergone supernova explosions at the estimate cluster age of 4 Myr. Hence our results are estimates of the

total initial mass and total initial number of stars for the cluster, under the assumption that the Present Day Mass Function is representative of the IMF value. For masses below $0.5 M_{\odot}$ and down to the hydrogen burning limit, i.e., $0.08 M_{\odot}$ we used the Kroupa IMF slope for this stellar regime, with a $\gamma = 1.3$. In Appendix 2.D we also show how we derived the best estimates for the total number of stars and the total mass of the cluster, given the set of $N_{tot,i}$ and $M_{tot,i}$ from the different bootstrap samples. The total number of stars is $N_{tot} = 1.04^{+6.00}_{-1.83} \times 10^5$ while the total mass of the cluster is estimated to be $M_{tot} = 4.91^{+1.79}_{-0.49} \times 10^4 M_{\odot}$.

Our present findings, based on a more complete and thorough approach, confirm the findings of BR08 and are on the lower end of the recent literature estimates for the mass of Wd 1. Using the MS turn-off mass and the identified post-MS member, by extrapolation of a Kroupa IMF down to lower masses, Clark et al. (2005) found a somewhat higher value for the total mass of $\sim 10^5 M_{\odot}$. Part of this discrepancy could be ascribed to the model-dependent uncertainties in the determination of the progenitor mass for the post-MS identified members. Additionally one has to be cautious when counting only the very massive stars to normalize the Kroupa IMF and then extrapolate it all the way down to low-mass stars. Only few young clusters in the Milky Way are known for which the IMF can be actually measured up to this masses, hence the nature of the IMF and its exact form is not known with great certainty in this regime. Moreover, also in the case that a standard IMF is valid for the very massive stars, high stochastic (Poissonian) fluctuations are expected when the numbers become small as towards the very high mass end of the Wd 1 population. A completely different approach was used by Mengel & Tacconi-Garman (2009) to determine a gravitating mass of Wd 1, $M_{dyn} = 1.5^{+0.9}_{-0.7} \times 10^5 M_{\odot}$. The authors measured the radial velocity of ~ 10 stars from their spectra. From the dispersion of these velocity measurements, the total mass of the system is derived, under the hypothesis of virial equilibrium, using the following equation:

$$M_{dyn} = \frac{\eta \sigma^2 r_{hp}}{G};$$

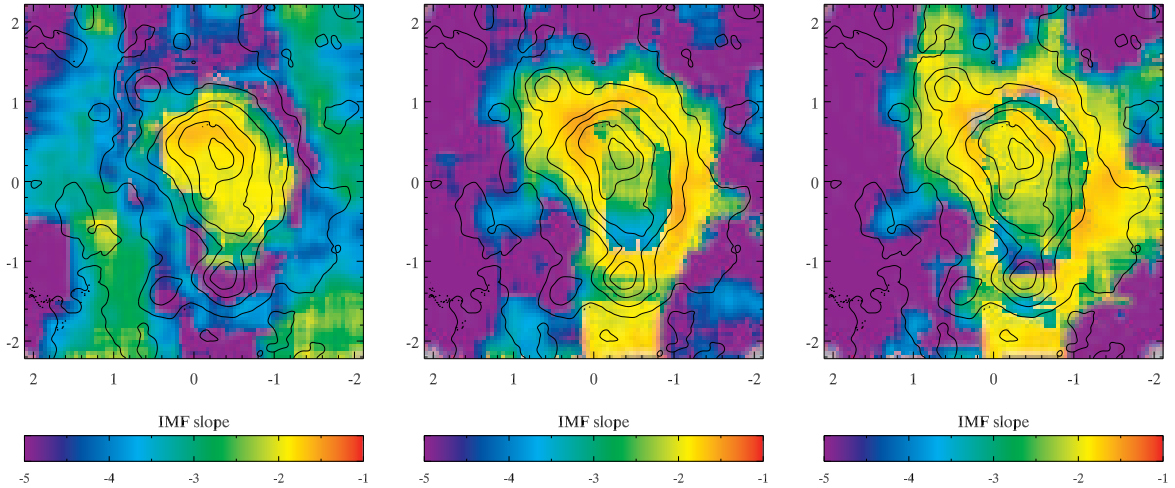
here r_{hp} is the projected half-mass radius, σ the velocity dispersion and η is a factor that the authors use under the additional assumption of isotropy. Possible pulsations in the 5 yellow hypergiants (YHGs) of the sample, which would cause a wrong estimate of their radial velocities, may cause an overestimate of the true σ . Ritchie et al. (2009) demonstrate indeed that one of the YHG observed in Wd 1, W243, shows a very complex, time-varying spectrum with signs of pulsation and mass loss that may hamper a precise determination of the radial velocity. This star is not in the Mengel & Tacconi-Garman (2009) sample, but it exemplifies that velocity dispersions derived from radial velocity measurements of evolved stars can lead to an overestimate of the true dispersion. In addition to this, we think that part of the discrepancy in the inferred dynamical mass could derive from the fact that Wd 1 is actually non spherical (see Sect. 2.9) and this anisotropy might be reflected also in the stellar motions. Therefore the η factor used by the authors should be slightly modified, possibly giving better agreement with other findings.

Indeed the velocity distribution seems to be not isotropic from our preliminary analysis of stellar proper motion using multi-epoch near-infrared AO data (Kudryavtseva et al. *in preparation*). On the other hand Fleck et al. (2006) showed that the η parameter is a time-dependent quantity, which changes rapidly, specially in very rich clusters, due to the effects of mass segregation. The authors found that the use of an $\eta \approx 10$, like in Mengel & Tacconi-Garman (2009), may lead to *underestimates* of clusters masses. We will show in the following that Wd 1 is mass-segregated. In such a case an increase in η is needed to correctly estimate its dynamical mass. This would lead to an even stronger discrepancy with our photometric mass estimate. A possible interpretation of this difference could be that Wd 1 is indeed *out of virial equilibrium*, with stellar motions still not relaxed after the gas-expulsion phase that followed the first supernovae explosions. An effect that could balance the effects of mass segregation on the η value is the inclusion of binaries in the estimates of this parameter. Binaries orbital motions increase the measured value of the velocity dispersion; consequently the true mass of a cluster is *overestimated* if the binary contribution is not properly taken into account. Kouwenhoven & de Grijs (2008) showed the dependency of the η value on binary properties and cluster density. For the densest clusters ($N \gtrsim 10^7$ stars pc $^{-3}$) the bulk motions dominate the total value of σ^2 while for the sparsest clusters, with $N \sim 0.1$ stars pc $^{-3}$, the velocity dispersion is fully dominated by orbital motions. Wd 1 density is in between these two extreme values. In this case the dynamical mass can be overestimated by 10-100%, depending on the properties of the binary population. Gieles, Sana, & Portegies Zwart (2010b), including mass-dependent mass-to-light ratio of stars and the intrinsically different binary properties of massive stars, found that the contribution to σ^2 from binaries orbital motions is already very important for young (~ 10 Myr), moderately massive ($M \sim 10^5 M_\odot$) and compact ($r_{hp} \sim 1$ pc) star clusters, comparable to Wd 1.

2.8.3 SPATIAL VARIABILITY OF THE IMF

In BR08 it was shown that, considering concentric annuli centered on Wd 1 centre, and computing the slope of the IMF for the stars in the annuli, there is a tendency for a flattening of the IMF when going closer to the centre. The IMF slope was computed using stars more massive than $3.4M_\odot$ only, to avoid any bias due to the lower degree of completeness in the crowded centre of the cluster. Still, close to the brightest stars, 50% incompleteness is reached already at higher masses of up to $6M_\odot$. This may still cause an artificially flatter IMF in the central parts of Wd 1, because, even though the IMF slope is obtained using the incompleteness corrected number of detected stars, the correction itself becomes quite uncertain when one uses it for much lower levels than 50% completeness. We have also shown that the completeness pattern in Wd 1 is not really radially symmetric and we will show in the following Sect. 2.9 that the shape of the cluster itself is elongated; hence using concentric annuli can smooth out some of the intrinsic spatial variations of the IMF. With our new approach we determine the IMF slope locally, in order to

Figure 2.7: 2D maps of the IMF slope of Wd 1. Within our definition, the colour coding corresponds to values of $-\gamma$. The three maps are built using only stars with a completeness factor, $C_J \times C_{K_S}$, down to 0.125, 0.25, 0.375 (from left to right); overplotted are the contours of $J_{\text{half}} \times K_{S\text{half}}$. The x and y axes correspond to RA and Dec offsets, in arcminutes, relative to the centre of the reduced image, $(\text{RA}, \text{Dec})_{\text{J2000}} = (16^{\text{h}}47^{\text{m}}06^{\text{s}}, -45^{\circ}50'33'')$

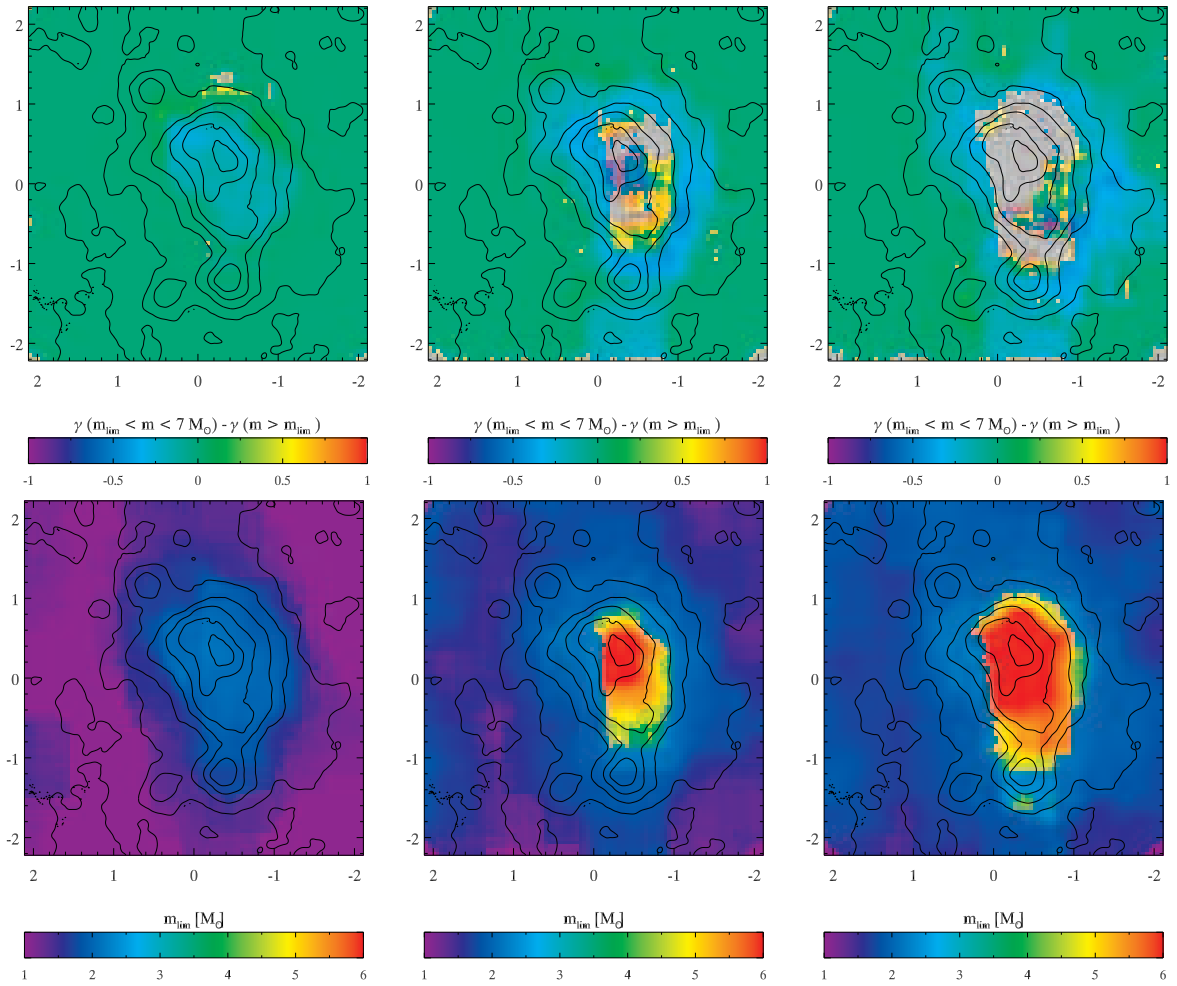


follow its real pattern within Wd 1.

To calculate the IMF slope at each position, we used a moving box, 200 pixels in size. The slope was obtained by the same technique described in Sect. 2.8.2, applied only to the stars in the box. At each position we additionally selected stars such that the total completeness factor $C_J \times C_{K_S}$ is always higher than some fixed threshold values. In this way we can compare results for varying completeness thresholds. Hence, at each position the minimum mass considered can be different. The upper mass limit is determined by the stochastic distribution of non-saturated high-mass stars within the moving box. The fit is performed only when the number of stars inside the box is larger than 30. The calculation is repeated at each pixel. Anyway we are forced to use a moving box that is much bigger than the sampling scale because we need enough stars to perform the IMF slope fit. Hence the adjacent-pixel slope-values are not independent from each other. The final maps are obtained by convolving the adjacent-pixel slope-values with a Gaussian kernel of FWHM = 100 pixels (half-box size) At the distance of Wd 1 (≈ 4 kpc) and with a plate scale of $0''.29/\text{pixel}$ 100 pixels corresponds to ~ 0.5 pc in linear scale.

Results for three values of $C_J \times C_{K_S} = 0.125, 0.25$ and 0.375 , are shown in Fig. 2.7. With our definitions, the *conventional* 50% threshold in one band is replaced by a $0.5 \times 0.5 = 0.25$ combined threshold. The green areas correspond to an ordinary Kroupa-like slope ($\gamma \approx 2.3$). The yellow-red areas in the centre indicate regions with a flatter IMF, i.e., with more high-mass stars than what is predicted by a Kroupa IMF. Blue-purple areas are areas with a paucity of massive

Figure 2.8: *Upper panels:* Differences in the γ values using stars between the completeness-threshold mass and $7M_{\odot}$ and using all stars above the threshold mass. *Lower panels:* Values of the completeness-threshold mass. Columns from left to right correspond to $C_J \times C_{K_S} = 0.125, 0.25$ and 0.5 respectively. Gray areas are areas with not enough stars to perform a reliable fit of the IMF slope. The x and y axes meaning is the same as in Fig. 2.7



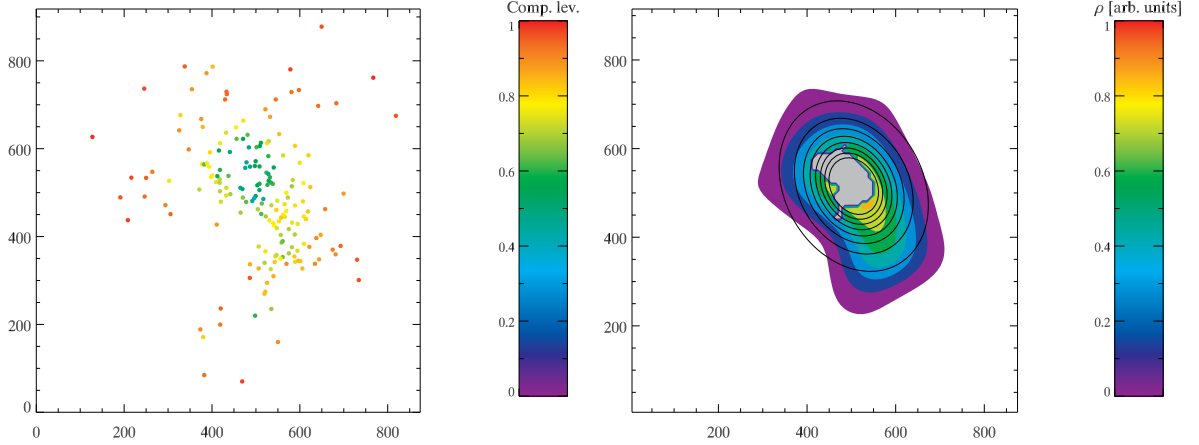
stars. Hence, when fitting a power law we obtain a very steep function due to the overabundance of low-mass stars. The contours in the three panels are the contours for the $C_{J_{\text{half}}} \times C_{K_S_{\text{half}}}$ function, i.e. the product of the J and K_S 50% completeness magnitudes. These contours trace the shape of the total completeness correction factor.

The overall pattern of the IMF slope remains unchanged among the three different maps of Fig. 2.7. Nevertheless, some differences can be noticed. Going to lower and lower completeness thresholds (i.e., from right to left in the figure), the yellow region in the centre of the image "shrinks", leaving space for regions of slightly steeper IMF around it. Hence, when completeness corrections are properly taken into account, there are strong hints that low-mass stars are overabundant outside the very centre of Wd 1. On the other hand, the yellow-red regions still visible in the centre of the maps, even for the lowest completeness threshold, indicate an overabundance of massive stars that is very likely to be intrinsic and not just a result of missing detections in the low-mass end. A similar "shrinking" behaviour is observed for the "purple" outer regions that are very pronounced in the two rightmost panel of the Fig. 2.7 and less in the leftmost. In this case the effect is due to the difference in the mass intervals used for the fit of the IMF slope. At higher completeness thresholds, only few mass-points are available, and the differences in number counts between the low-mass and high mass limits within the fitting interval are very high when few high-mass stars are present. When lowering the completeness threshold, star counts are added at lower masses, hence the observed mass function becomes more "regular" and the results of the fit of the slope are less extreme.

Given the low number of stars towards the high-mass end, statistical fluctuations in this regime may increase the uncertainty of the IMF slope. To see whether this effect is important, we compared the γ values for all stars with $m > m_{\text{lim}}$ and the γ values for stars with $m_{\text{lim}} < m < 7 M_{\odot}$ only. The results are shown in the upper panels of Fig. 2.8. The grey regions in the centre are regions where the number of stars in the fitting interval was too low to perform a good fit. Excluding these regions, it is clear that the difference between the two slopes is almost everywhere zero. This tells us that the fit is dominated by the low-mass regime of the fitting interval, where the stars are more numerous and where the overall shape of the IMF is very well determined since statistical fluctuations are less pronounced. The only differences between the two slopes are observed in the very centre, where m_{lim} becomes very close to the upper-mass limit of $7 M_{\odot}$. In these regions, indicated by a cyan colour, the inferred IMF is flatter when the high-mass end is neglected. Anyway, the incompleteness level in the very centre is high, hence these small differences ($\Delta\gamma \lesssim 0.3$) cannot be considered significant.

Summarizing, we can say that the overall IMF shape is consistent with a Salpeter or Kroupa galactic IMF in the range of masses between 3.5 and $27 M_{\odot}$. This slope is the spatial average of a slope that varies across Wd 1. A trend in the local IMF slope values can be observed in Fig. 2.7, with central regions having flatter IMF compared to the outer regions of the cluster.

Figure 2.9: Example of surface density contours and a fit using the GEF profile, in pixel coordinates on the frame. *Left:* stars with $m > 7.5 M_{\odot}$ and $C > 0.375$; completeness factors for the single stars are colour-coded. *Right:* the corresponding density contours (in colours). The density is in arbitrary units and the colour-coding goes from the minimum to the maximum density. The gray area corresponds to the area where the average completeness for the whole cluster’s population is below 0.25; this area is masked-out when performing the GEF profile fit. The results of the fit are displayed as black elliptical contours.



This is a robust indication that Wd 1 is mass segregated. We will show additional evidence of this mass segregation in Sect. 2.9, where we will also discuss its possible origins.

2.9 MORPHOLOGY OF WESTERLUND 1

Several recent studies indicate that Wd 1 is elongated (see e.g. Munro et al. 2006). In BR08, assuming an elliptical shape with a and b as semi-major and semi-minor axis respectively, an ellipticity of the cluster $\eta = 1 - \frac{b}{a} = 0.19$ was found when stars with masses in the range 10 to $32 M_{\odot}$ were considered. The value slightly decreased, to $\eta = 0.15$, using masses between 3.5 and $10 M_{\odot}$. Elongation was computed by calculating the half-mass radius as a function of the position angle (PA), considering for each PA only stars within $\pm 45^{\circ}$ around PA and, correspondingly, around PA + 180° . We also showed that the overall surface mass density profile of the cluster follows a $\Sigma(r) \propto [1 + (r/\alpha)^2]^{-\beta}$ radial law (see Elson et al. 1987 –hereafter EFF87), with core radius related to the α parameter by EFF87 equation (22), i.e., $r_c \approx \alpha(2^{2/\beta} - 1)^{1/2}$ and $\beta = 2$ for Wd 1. At large distances from the center, the 3D density profile goes like $\rho(r) \propto r^{-2\beta-1}$ –see EFF87 equations (13a) and (13b). Hence an index $\beta = 2$ for the 2D density profile implies a 3D density that goes like r^{-5} , which corresponds to a Plummer (1911) model. A $\beta = 0.5$ corresponds instead to an isothermal sphere with 3D density going like r^{-2} . The density profile of Wd 1 falls more rapidly compared to the case of R136 cluster in the Large Magellanic Cloud. This cluster

has a mass comparable to that of Wd 1 and slightly younger age of ~ 3 Myr but shows a profile that is closer to isothermal, with $\beta \approx 0.8$ (Andersen et al. 2009; Campbell et al. 2010)

Our 2D incompleteness mapping enables a study of the cluster's 2D stellar density distribution. We calculated the surface number density for several mass ranges and used four values for the completeness threshold. Given a lower-mass threshold, m_{low} , and a completeness threshold, C_{tr} , we considered all the stars above these thresholds for calculating the stellar surface number density. The number density was computed using a moving box 100 pixels in size³, which was moved pixel-by-pixel. After counting the stars at each position, we convolved the counts with a Gaussian kernel of FWHM = 50 pixels, i.e. half-box-size, to account for the fact that the density value computed at each pixel position is not independent of the values computed at nearby pixels. In this way we have been able to build smooth number density maps for Wd 1. These density profiles are always elongated, hence we decided to perform a fit by using an elliptical generalization of the EFF87 profile, a natural extension of the work done in BR08. We will refer to this profile as GEFf.

The GEFf profile can be described in the following way:

$$\Sigma_{\text{GEFF}} = \Sigma_{\text{BG}} + \Sigma_{\text{c}} (1 + L^2)^{-\Gamma} \quad ; \quad (2.5)$$

where Σ_{BG} is a stellar background density, Σ_{c} is the density in the centre and Γ represents the density decay for large distances from the centre ($L \gg 1$).

The quantity L^2 is given by:

$$L^2 = \left(\frac{x'}{a}\right)^2 + \left(\frac{y'}{b}\right)^2 \quad . \quad (2.6)$$

In analogy with the EFF87 α parameter, which is related to the core radius, a and b are related to the core semi-major and semi-minor axes of the elliptically symmetric GEFf profile. The quantities x' and y' are given by:

$$\begin{pmatrix} x' \\ y' \end{pmatrix} = \begin{pmatrix} \cos \theta & -\sin \theta \\ \sin \theta & \cos \theta \end{pmatrix} \times \begin{pmatrix} x - x_{\text{c}} \\ y - y_{\text{c}} \end{pmatrix} ; \quad (2.7)$$

where $(x_{\text{c}}, y_{\text{c}})$ are the pixel-coordinates of the centre of the ellipse and θ is the tilt angle between the semimajor axis and the x axis, measured counterclockwise.

Summarizing, a GEFf profile has 8 different parameters: $\mathbf{P} = (\Sigma_{\text{BG}}, \Sigma_{\text{c}}, \Gamma, a, b, x_{\text{c}}, y_{\text{c}}, \theta)$. In the fit we left all of them free, apart from the exponent Γ . Since the equivalent exponent for an EFF87 profile was found to be $\beta = 2$ in BR08, we constrained our Γ to stay between 1 and 3.

³This is half of the box size used for the computation of the local variations of the IMF (see Sect. 2.8.3). Since here we just need to count the stars, we do not need large numbers within the box.

Moreover, given that the completeness correction in the very centre of Wd 1 may be uncertain, we performed the fit by neglecting the region in which the stars have, on average, a completeness factor smaller than 0.25. An example of stellar density contours and the relative GEF fit is given in Fig. 2.9.

2.9.1 RESULTS OF THE GEF FIT

We calculated the stellar density for several combinations of the mass and completeness thresholds; the values used are: $m[M_{\odot}] = [2.5, 3.5, 4.5, 6.0, 7.5, 10.0, 12.5, 15.0]$ and $C = [0.125, 0.25, 0.375, 0.5]$. A summary of the outcome of the GEF fit for all these combinations can be found in Fig. 2.10. For clarity, we emphasize that, given the value of the mass threshold, we consider all the stars with $m > m_{\text{low}}$. Hence, in the plots of Fig. 2.10, going from right to left along the mass axis, it is possible to see the *cumulative* effect of including lower and lower mass stars. The different symbols represent different completeness thresholds, as indicated.

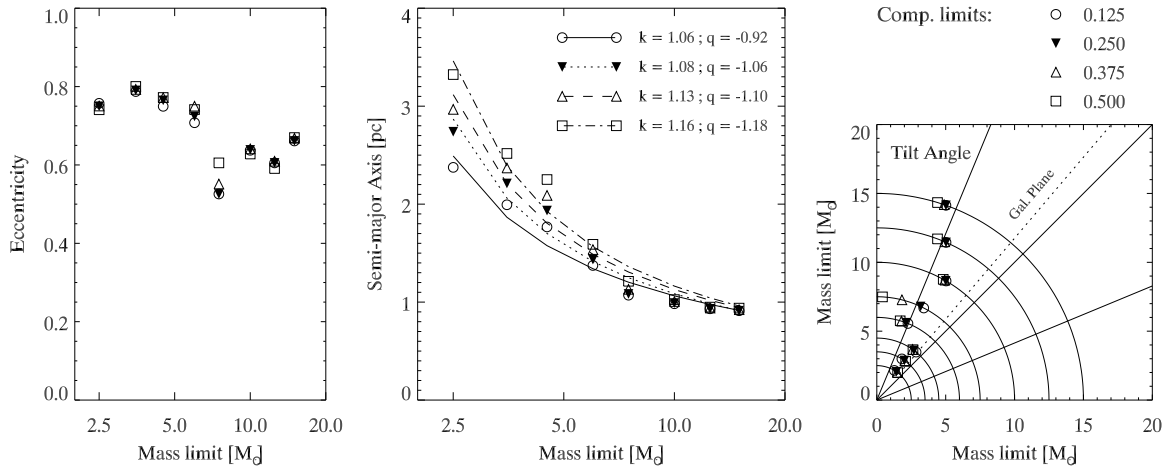
In the left panel of the figure we show the eccentricity, $\epsilon = \sqrt{1 - \left(\frac{b}{a}\right)^2}$. With this definition, the ellipticity values, $\eta = 0.15$ and 0.19 , of BR08 become $\epsilon = 0.53$ and 0.59 , respectively. The eccentricity values are almost constant with mass. Their average values are somewhat higher than what found in BR08, with $\epsilon \approx 0.75$ indicating an axis ratio $a : b = 3 : 2$. The fact that the numbers are slightly different compared to BR08 is not surprising. The adoption of a radially symmetric completeness correction in BR08 has partially smoothed out some of the asymmetry and intrinsic elongation of the cluster. Our new results clearly reveal the elongated 2D density distribution of main-sequence stars with masses between ≈ 3 and $\approx 30 M_{\odot}$, with higher elongation observed for lower mass stars. This might be related to the fact that more massive stars are also more centrally concentrated (see below), hence their average collision time is shorter than that of the less massive stars. Consequently, massive stars undergo more dynamical interactions and their momenta become more isotropic.

For completeness values between 0.125 and 0.5 we also performed a least-square fit of the semi-major axis values, using the functional relation:

$$a = k \times [\log(m)]^q . \quad (2.8)$$

The results of the fits are shown in the central panel of Fig. 2.10. In general the cumulative semimajor axis decreases almost like $1/\log(m)$. We already found an indication of mass segregation by investigating the IMF spatial variations (see Sect. 2.8). The finding here confirms that massive stars are more centrally concentrated. The figure also shows that adopting a lower completeness threshold, the actual size of the semi-major axis decreases, at fixed mass. The reason is the inclusion of more and more stars in the centre of the cluster, where, of course, the total

Figure 2.10: *Left:* Eccentricity values as a function of the minimum mass; *Middle:* Semi-major axis values as a function of the minimum mass; the quoted k and q values are obtained by fitting functions as described in equation (2.8); *Right:* Tilt angle between semi-major axis and x axis, measured counterclockwise; each of the concentric rings helps to distinguish the different values as a function of the minimum mass used. Different symbols correspond to different completeness thresholds.



completeness is lower. Consequently, going to lower completeness thresholds the stellar density has a more pronounced peak in the centre, while the density in the outer regions of the cluster does not change as much. Since a is a measure of the length-scale of the density decay with distance from the centre, we obtain lower a values when the density contrast between the centre and the outskirts is more pronounced.

From Fig. 2.10, right panel, it is also very interesting to note that Wd 1's direction of elongation lies very close to the galactic plane.

2.9.2 POSSIBLE SOURCES OF ELONGATION

In the following, we carry out a qualitative discussion of possible sources of elongation. The typical orbital period for a star at 1pc distance from a central point source with mass $M = 10^5 M_{\odot}$ is about $t_d \approx 3 \times 10^5$ Myr. This timescale is much shorter than the typical half-mass relaxation time of about $t_{rh} \approx 10^8 - 10^9$ yr, as determined for a typical globular cluster –comparable in stellar mass to Wd 1–, and defined as the time required for the central half of the cluster mass to reach equilibrium (see Sect. 1.1 in Spitzer 1987). Given the difference in the two timescales, it is clear that the observed deviation from spherical symmetry cannot be ascribed to the global evolution of the cluster as an *isolated* system; after few orbits and encounters, the phase-space distribution

of stars for an isolated system is expected to be isotropic (in \mathbf{v}) and spherically symmetric (in \mathbf{r}). The deviation from the spherical cluster shape must be explained either by unusual initial conditions still reflected in the present cluster appearance or by some interaction with the rest of the Galaxy.

A net angular momentum of the giant molecular cloud forming Wd 1 or a formation of Wd 1 out of two or more subclusters might either be responsible for its elongated shape. Differential galactic rotation exerts a shear on molecular clouds which might lead to a net angular momentum. According to a recent study by Ballesteros-Paredes et al. (2009), galactic shear and tides have rather strong effects on initially elongated clouds, eventually quenching star formation and disrupting the clouds. Hence differential rotation is an unlikely source for the elongation of Wd 1. An other intriguing possibility would be a "hierarchical" formation scenario, with merging of two or more smaller subclusters. The existence of a non-negligible fraction of possible binary clusters is supported by observations (see e.g. de la Fuente Marcos & de la Fuente Marcos 2008). A hierarchical organization of the ISM and of young stellar groups and clusters is indeed observed on many scales (Elmegreen 2009). Negueruela et al. (2010a) report the presence of a subclump of massive stars in the S-E region of Wd 1, even though they also warn that fluctuations in the star counts could be responsible for this observed clump. Clark et al. (2005) suggest that an age spread within the Wd 1 massive star population is really unlikely, hence any possible merging or capture event must have happened in the very beginning of the cluster's history. Otherwise this episode could have happened also more recently, but under the condition that the subclusters are coeval, i.e. star formation has occurred at almost the same time in different regions of the giant molecular cloud. If this scenario would be true, the modest amount of dynamical crossing times occurred from Wd 1 formation (age $\simeq 10 t_d$) may be the reason why the stellar motion have not yet reached an isotropic distribution. No dynamical simulations that include such a large number of particles as Wd 1 members have been performed so far. Nevertheless, recent studies suggest that merging is indeed possible over a wide range of initial conditions (see Portegies Zwart & Rusli 2007; de la Fuente Marcos & de la Fuente Marcos 2010 and references therein).

We evaluate whether tidal effects in the Galactic central field could be responsible for the Wd 1 shape. Under the simplifying assumption of a circular restricted 3-body problem, with primary mass at the Galactic Centre position and secondary at the cluster centre, we find that r_L , i.e. the distance of the inner Lagrangian point from Wd 1 centre is:

$$r_L^3 = \frac{1}{3} \frac{M_{\text{Wd1}}}{M_{\text{MW}}} R_G^3 ;$$

where $M_{\text{Wd1}} = 5 \times 10^4 M_\odot$ is our Wd 1 mass estimate, $M_{\text{MW}} = 6 \times 10^{11} M_\odot$ is the mass of the Milky Way and $R_G = 4 \text{ kpc}$ is the Wd 1 galactocentric distance. With these numbers, we obtain $r_L = 12 \text{ pc}$; given that $M_{\text{Wd1}} \ll M_{\text{MW}}$ this is also the distance for the external Lagrangian point from the Wd 1 centre. This estimate for the tidal radius is a lower limit, since it was assumed that all the mass of the Galaxy is confined within the orbit of Wd1. A more correct estimate, taking

into account only the enclosed galactic mass at radius R_G , would lead to an even larger value of r_L . Consequently, it is clear that Wd 1 is far from filling its Roche lobe, while we measure elongation already on a scale of ~ 1 pc from the cluster core. Hence tidal distortion from the whole Galaxy is unlikely the reason for the elongation of Wd 1.

An other important tidal effect could be caused by the galactic disk gravitational field. The disk potential is constant far away from the galactic midplane, where the matter density distribution of the disk drops to zero. On the contrary within the disk the potential has a non-zero divergence in the direction perpendicular to the plane (Z axis). This divergence causes a net acceleration of the stellar motions in the Z direction, and, as a result, an initially spherical and isotropic cluster moving across the disk midplane is *compressed* along the Z direction. This phenomenon is known as "compressive gravitational shock" and an analytical solution is presented in Chapter 5 by Spitzer (1987). Unfortunately the conditions that are required to apply this analytical treatment do not hold for Wd 1. In Spitzer (1987) the galactic plane tidal field is treated as a fast time-dependent perturbation to the motion of stars within Globular Clusters which cross the midplane at a speed of hundreds of km/s. Hence the duration of the perturbation is short compared to the stellar orbital period around the cluster centre. However, Wd 1 is moving much slower in the Z direction. From a preliminary analysis of our AO multi-epoch observation, we can set a limit on the net bulk motion of $\lesssim 10$ km/s along the galactic longitude coordinate b (Kudryavtseva et al. *in preparation*). For this reason the Spitzer (1987) analytical solution cannot be used here, but it could be worth to investigate the effects of the disk tidal field in detail with dynamical simulations.

2.9.3 THE EFFECTIVE CUMULATIVE RADIUS

As an alternative to study of mass segregation, in addition to the estimate of the GEF best fit semi-major axis, a , we used an independent quantity that we call the effective cumulative radius:

$$r_{\text{eff}}(m) = \sqrt{\frac{\sum_{m_i > m} \left(\frac{r_i}{C_{J_i} \times C_{K_{S_i}}} \right)^2}{\sum_{m_i > m} \left(\frac{1}{C_{J_i} \times C_{K_{S_i}}} \right)^2}} . \quad (2.9)$$

This quantity is obtained by taking all the stars with mass $m_i > m$ and computing their geometric-averaged distance from the centre of the cluster. The distance from the centre for the single stars is r_i ; the completeness factors, C_i are needed to take into account, in a statistical sense, the undetected sources.

Figure 2.11 shows the quantity r_{eff} as a function of mass. Looking from right to left it is evident that the inclusion of less and less massive stars in the computation of r_{eff} leads to an increase of

the average distance from the centre of the cluster, meaning that more massive stars are located on average at smaller effective radii compared to less massive stars. The first few points on the right of the plot don't follow this relation. This is due to the fact that the definition of an *average* distance for the most massive stars is problematic, given the low numbers considered. Indeed, the most massive star in our data set is a bit off-centre, hence the effective radius for this star is quite large; this star also affects the effective radius of the first ~ 10 points on the right of the diagram, because its distance from the centre enters the computation of the average distance for the other stars. As long as the number of stars included in the computation of r_{eff} increases, the results converge towards a more stable averaged distance.

The smooth increase of r_{eff} with decreasing mass confirms the findings for the semi-major axis length of Sect. 2.9.1. Hence we can state that Wd 1 is clearly mass segregated.

2.9.4 THE ORIGIN OF MASS SEGREGATION FOR WESTERLUND 1

Mass segregation is a phenomenon observed in many young clusters; some examples are the Orion Nebula Cluster (Hillenbrand & Hartmann 1998), the NGC 3603 Young Cluster (Stolte et al. 2006; Harayama et al. 2008), the Arches Cluster (Stolte et al. 2005a; Kim et al. 2006; Espinoza et al. 2009), and debate is still open whether this phenomenon is either primordial or due to dynamical evolution. If only two-body encounters are considered, the half-mass relaxation time for a cluster is given by (Binney & Tremaine 1987):

$$t_{\text{rh}} = \frac{6.5 \times 10^8 \text{ yr}}{\ln(0.4 N)} \left(\frac{M}{10^5 M_{\odot}} \right)^{\frac{1}{2}} \left(\frac{1 M_{\odot}}{\langle m \rangle} \right) \left(\frac{r_{\text{h}}}{1 \text{ pc}} \right)^{\frac{3}{2}}$$

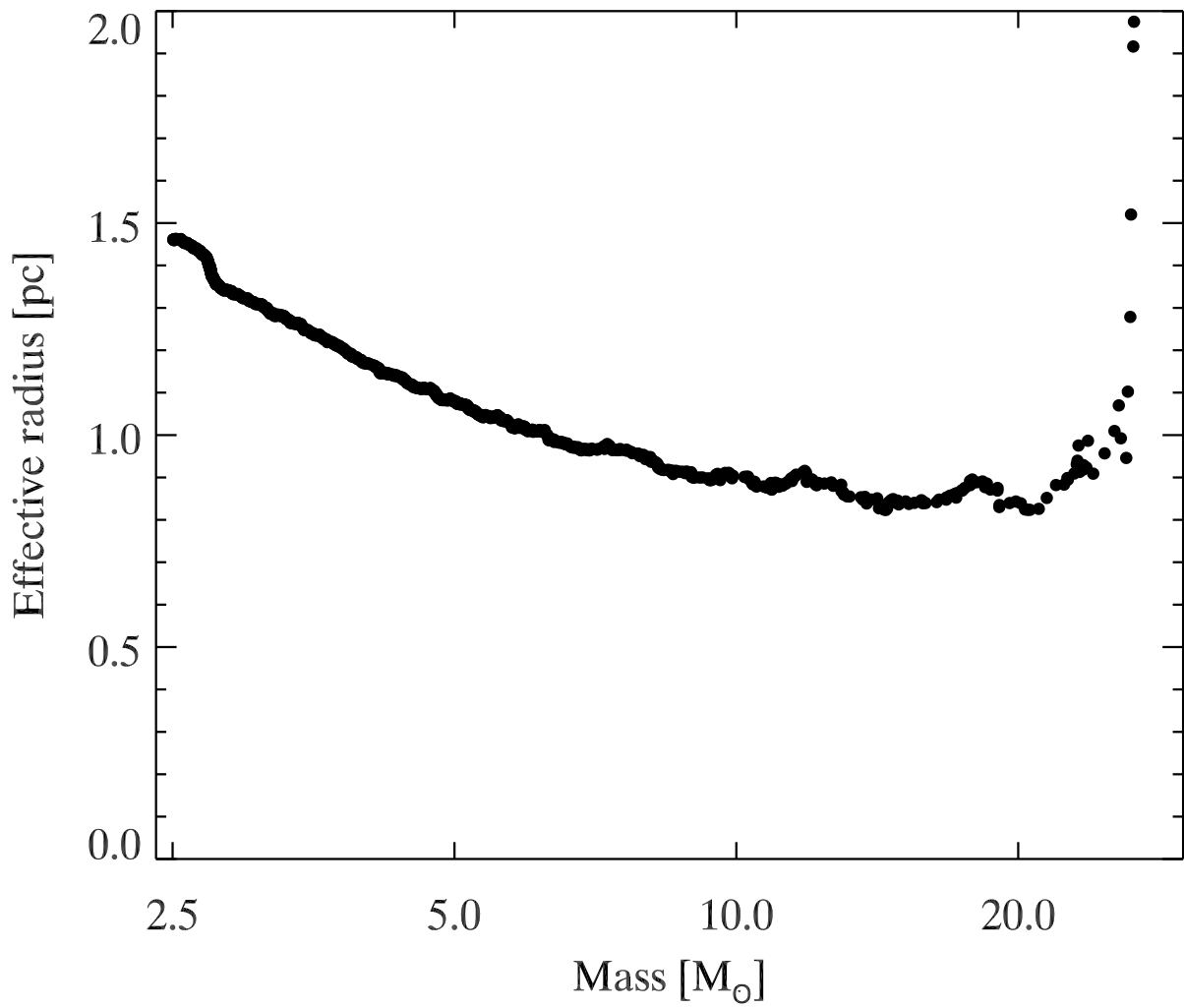
where N is the total number of stars, $\langle m \rangle$ is the mean stellar mass and r_{h} the deprojected half-mass radius, equal to $4/3$ of the projected half-mass radius. Considering $N = 10^5$, $M = 5 \times 10^4 M_{\odot}$, $r_{\text{h}} = 4/3 \times 1.1 \text{ pc}$ (see BR08) and $\langle m \rangle = 0.6 M_{\odot}$, we get an estimate of $t_{\text{rh}} \approx 130 \text{ Myr}$, much larger than the age of the cluster. This discrepancy between relaxation time and age is common to many clusters and has been used as an argument in favor of the primordial segregation scenario (Bonnell & Davies 1998). Nevertheless one has to consider that the time for a star with mass m_* to drift towards the cluster centre due to dynamical friction is:

$$t_{\text{df}} = \frac{\langle m \rangle}{m_*} \times t_{\text{rh}}$$

In the case of Wd 1 this segregation time can be as short as 2% of t_{rh} , i.e. 2.6 Myr for a star of $\sim 30 M_{\odot}$, i.e. the most massive stars in our sample. Hence primordial segregation would not be necessary to explain the observed mass segregation. Furthermore the evolution of Wd 1 has probably been more complex, and the value of t_{rh} might have changed in time. Mass loss from

stellar winds, supernovae explosions and gas removal might have caused a global expansion of Wd 1, meaning that t_{rh} was shorter in the past Gieles et al. (2010a). Gürkan et al. (2004) and Portegies Zwart et al. (2004) showed that the core collapse time for massive clusters is about 0.1-0.2 t_{rh} . It is therefore not unlikely that the core of Wd 1 has undergone a dynamical collapse, which is then also followed by expansion that could increase the relaxation time. This would push down the mass limit which we expect to be affected by mass segregation. McMillan, Vesperini, & Portegies Zwart (2007) have proposed an alternative scenario to the primordial segregation one, in order to explain mass segregation observed in young cluster. This scenario predicts that mass-segregated young, massive clusters could be the product of merging of several smaller subclusters. Substructure in molecular clouds is observed in both density and kinematics (Williams 1999; Williams et al. 2000) and this substructure is reflected as well in young clusters (Larson 1995; Testi et al. 2000; Gutermuth et al. 2005; Allen et al. 2007). In a hierarchical formation scenario, a massive cluster could be formed by the merging of several subclusters and still might show mass segregation. Given their smaller N , the subclusters can rapidly reach a mass segregated status before they merge and regardless of the initial spatial distribution of stars. The mass segregation in these smaller clusters is favored by shorter t_{rh} . In addition, Allison et al. (2009a, 2010) show that clusters may undergo an initial collapse phase which can significantly accelerate mass segregation. In this phase the cluster forms a very dense and clumpy core, where the massive stars can rapidly segregate given the short crossing time and large number of encounters. The timescale for such a process in a cluster with $N \sim 10^3$ is $\lesssim 1\text{Myr}$. The simulations by McMillan et al. (2007) additionally show that mass segregation developed by single subclusters is preserved during merging. Consequently the final massive cluster exhibits mass segregation at an age much smaller than its global relaxation time. While merging might not be required to explain mass segregation, it could also explain the elongated shape of Wd 1. Hence we think that this is a very interesting scenario for Wd 1 formation. We point out that McMillan et al. (2007) have carried out pure N-body simulations. Recently, Bate (2009) has performed hydrodynamic simulation of star-forming regions that include gas drag and gas accretion onto stars, in addition to the mutual gravity between them. The final cluster that is formed is the result of the merging of 5 subclusters. The author finds no evidence for mass segregation. However the number of stars formed in his simulations is of the order of 10^3 with the most massive star of only $\approx 5M_{\odot}$. Hence the simulated cluster cannot be directly compared to Wd 1. More recently, using the final stellar positions of Bate (2009), and applying their own segregation detection method, Moeckel & Bonnell (2009) found evidence of segregation at least for the most massive stars. This last scenario, in which only the few most massive members are found in the cluster's core, is more similar to what is observed for the Trapezium stars in the ONC, than to what we observe in Wd 1, i.e. an evidence of continuous mass segregation across the whole stellar mass spectrum.

Figure 2.11: Effective cumulative radius for Wd 1 stars. Note that the ~ 10 rightmost points are affected by the off-centre location of the one most massive star in our data.



2.10 CONCLUSIONS

We have presented a new, thorough analysis of near-infrared data for the intermediate- and low-mass stellar population of the massive young cluster Westerlund 1. Using artificial stars, we have been able to sample spatial variations of photometric completeness on a scale of few stellar FWHM. The same artificial stars have been used to infer realistic photometric error estimates, as well as the correlation between errors in different bands. Incompleteness corrections and errors were used to apply a novel statistical field subtraction technique to the data. Using a nearby control field we obtained a clean sample of cluster members. The clean catalogue of stars, together with state-of-the-art stellar models, has been used to determine the cluster's properties. We derived an extinction $A_{K_S} = 0.91 \pm 0.05$ mag, an age $\tau = 4 \pm 0.5$ Myr and a distance $d = 4.0 \pm 0.2$ kpc.

We investigated the cluster's IMF slope using a new approach to stellar mass determination. The information on magnitude errors and their correlation has been used to derive the mass-probability-distribution for each star, given the best-fit isochrone. The completeness-corrected IMF has a slope of $\gamma = 2.44^{+0.20}_{-0.08}$, slightly steeper than the Salpeter or Kroupa IMF; this slight discrepancy could be partially reconciled if we consider that, for the sake of simplicity, we are neglecting the influence of (unknown) undetected binarity, hence our quoted error is probably an underestimate of the total, statistical plus systematic error (Maíz Apellániz 2009). From the IMF slope and its normalization constant we found a total mass for the cluster of $M_{\text{Wd1}} = 4.91^{+1.79}_{-0.49} \times 10^4 M_{\odot}$.

The spatially varying completeness, combined with the probabilistic mass determination, enabled us to investigate the spatial variations of the IMF. The Wd 1 starburst cluster is mass segregated, with massive stars more centrally concentrated. Other indications of mass segregation come from the analysis of the stellar density distribution. In order to study the 2D density distribution as a function of stellar mass, we fitted 2D elliptical profiles. This analysis revealed a tight dependency of the ellipses semi-major axis length on mass: $a(m) \propto 1/\log(m)$. Given the young age of Wd 1, its global mass segregation cannot be explained by simple 2-body relaxation. Interestingly, from the density distribution analysis, we found that Wd 1 is elongated along the Galactic Plane with an axis ratio $a : b = 3 : 2$. The mass segregation and the elongation together hint at a formation scenario involving the merging of multiple subclusters formed almost coevally in the parental giant molecular cloud.

2.A COMPLETENESS MAPS

In this appendix we will illustrate, step-by-step, how the 2D completeness maps for Wd 1 were obtained.

2.A.1 ADDING AND DETECTING ARTIFICIAL STARS

The basic idea is to use the same PSF that was obtained by PSF-fitting with DAOPHOT to add stars (using the DAOPHOT `addstar` task) in the reduced images and then run the same PSF fitting photometry scheme to see whether artificial stars can be recovered or not. 50 stars per run were added, in order not to change the crowding characteristic of the frame. Stars are positioned randomly on the frame and have an uniform distribution in magnitude. To achieve sufficient spatial resolution we iterate the procedure until we have added 4500 stars per unit magnitude. The actual size of the magnitude bin used is 0.5 mag, and we consider that artificial stars are recovered if the detection yields a difference between the input and output magnitude of less than 0.5 mag. The ranges of magnitude spanned by the simulations are those typical of the Wd 1 member stars detected in the NTT/SofI observations, above the linear-regime limit and below the detection threshold i.e. $J \in [11.35, 19.35]$ mag and $K_S \in [9.8, 17.8]$ mag; these magnitude ranges correspond to masses between 0.3 and $30 M_{\odot}$, the exact values depending on the age, distance and extinction values (see Sect. 2.7). The full magnitude ranges are divided in 16 bins, 0.5 mag wide, per each of the two bands.

With an effective detector area of $A_{\text{eff}} = L_x \times L_y = 876 \times 920 \text{ pixel}^2$, resulting from the area in common between the observations in the different filters, the numbers we just quoted correspond to a typical separation between simulated stars (within the 0.5 mag bin) of:

$$\langle d \rangle = \sqrt{\frac{A_{\text{eff}}}{\pi N_{\text{bin}}}} \approx 10.8 \text{ pixel} \quad (2.10)$$

where $N_{\text{bin}} = 2225$ is the number of simulated stars in the 0.5 mag-wide bin. Given the SofI plate scale of $0''.29/\text{pixel}$ and given the typical seeing of $\approx 0''.8$ it means that we sample the whole frame on a scale which is about 3.5 times the PSF Full-Width at Half Maximum (FWHM). The effective sampling scale is a bit larger, due to the use of a certain number of nearest neighbours to calculate the local value of completeness at the position of each simulated star. The natural limit, i.e. the minimum length-scale at which completeness can be sampled by our method, is the FWHM of the PSF itself, which characterizes the ability to distinguish two different point sources. The resolution of the incompleteness map could not be improved further, even if the number of simulated stars would be increased in order to achieve a spatial sampling smaller

than the PSF-FWHM. Our choice of the total number of stars is a compromise between a short sampling scale and a reasonable number of simulations.

2.A.2 BUILDING THE 2D MAPS

Each simulated star can be either recovered or not by DAOPHOT PSF fitting, meaning that for that specific star completeness is either 0 or 1. Starting from this series of sparsely sampled 0-s and 1-s, several steps are necessary to obtain a smooth function, which is determined at each point on the frame. In the following we will indicate the position of simulated stars with a hat symbol, (\hat{x}, \hat{y}) , while the coordinate grid on which we actually calculated the function will be simply (x, y) , which corresponds to the pixels grid of the chip. We will refer in this section only to a single magnitude bin and to a single photometric band; interpolation in the magnitude dimension will be treated in Sect. 2.A.3.

The first step is to create average completeness values at each (\hat{x}_i, \hat{y}_i) for $i = 1, N_{bin}$. This is accomplished by considering a certain number ν of nearest neighbours to the i -th simulated star and defining the completeness fraction as:

$$C_0(\hat{x}_i, \hat{y}_i) = \frac{\text{recovered stars}}{\nu + 1} \quad ; \quad (2.11)$$

where the recovered stars are counted among the ν neighbours of the i -th one, which is also included, hence the +1 in the denominator. The actual value of ν is somewhat arbitrary and has to satisfy two opposite requirements; the higher it is, the less the completeness values will be affected by statistical noise. On the other hand, a too large value would imply a loss in spatial resolution for our completeness maps. As mentioned in Sect. 2.A.1 the effective sampling scale is not the $\langle d \rangle$ of equation (2.10) but more precisely:

$$d_{\text{eff}} = \langle d \rangle \times \sqrt{\nu} \quad .$$

After several experiments we decided to use $\nu = 16$, which degrades our completeness sampling scale by a factor 4, giving $d_{\text{eff}} \approx 43.2$ pixels, corresponding to about 14 times the FWHM of the image PSF.

At this stage the C_0 is known only point-wise in the set of (\hat{x}, \hat{y}) positions occupied by the simulated stars. The next step is to interpolate this function into a regular grid of points. This is accomplished via the IDL procedure GRIDDATA, using the Kriging method of interpolation with an exponentially decreasing model for the variogram. Kriging allows to interpolate a random field known in a set of positions into another set, under some assumptions about its covariance. In our case the random field is the completeness itself, with its Poissonian error due to the finite

number of simulated stars considered in equation (2.11). An exponential model for the covariance is appropriate here, because the estimated values of C_0 at some location (\hat{x}_i, \hat{y}_i) are correlated with those for other stars and the correlation is stronger for closer simulated stars than for those separated by a large distance. We have chosen an e -folding scale equal to d_{eff} .

After the interpolation we performed a smoothing of the completeness. The grid used for the interpolation is indeed finer than d_{eff} , meaning that the interpolated function may show artificial variations on a scale smaller than our minimum size, which would be unrealistic. That is why we additionally smoothed the maps with a boxcar kernel with a size of d_{eff} . The boxcar model is appropriate given the uniform spatial distribution of simulated stars.

2.A.3 INTERPOLATION IN MAGNITUDE

Once the maps are available in magnitude layers, we enforced that at each location (x, y) , completeness is a decreasing function of magnitude. We fitted pixel-by-pixel a monotonically decreasing function of Fermi-like type:

$$C_j(x, y, \mu) = \frac{\alpha(x, y)}{e^{\frac{\mu - \beta(x, y)}{\gamma(x, y)}} + 1} \quad (2.12)$$

The meaning of the three coefficients is the following:

α is the normalization and is always ≤ 1 ;

β is the magnitude for which completeness is $\alpha/2$;

γ represents the rapidity with which C_j drops down.

Once the (α, β, γ) coefficients triplets are calculated, it is straightforward to assign to each real star its completeness value using the coefficients evaluated at the star's position.

2.A.4 COMPLETENESS FOR THE CONTROL FIELD

The offset field that we used for field decontamination of the colour-magnitude diagram (CMD) is also affected by incompleteness. In this case, however, it is not necessary to investigate the 2D structure of the completeness pattern; under the assumption that the spatial distribution of the stars in the control field is uniform, we only consider spatially uniform incompleteness correction.

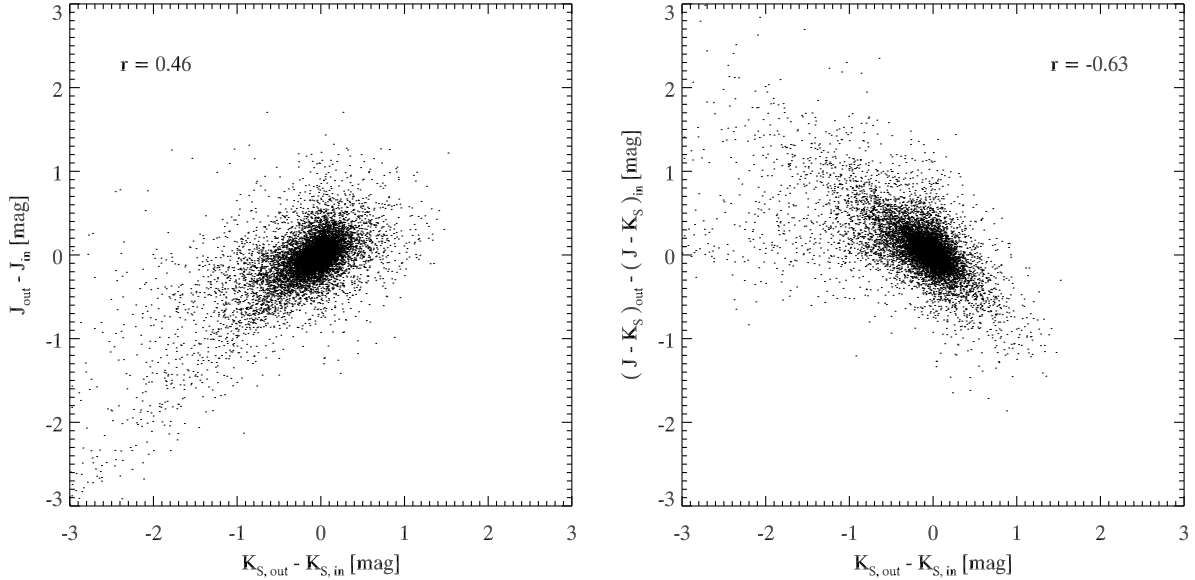
When using a control field for decontamination of a star cluster's CMD, one implicitly assumes that the stars are, on average, representative of the foreground/background population in the cluster's field. This assumption has a series of shortcomings. For example, the copious cluster population itself may partially "shield" background stars. In addition to that, in the Galactic Plane, variable extinction may cause differences in the observed population of stars. Furthermore, the population along different lines of sight could be *intrinsically* different, due to the different galactocentric distances sampled at the same heliocentric distance or changes within the spiral arms. This two latter problems are reduced by choosing nearby fields, so that the fore/background populations show similar distributions in age and extinction –hence in magnitude and colour– as along the cluster's line of sight. Hence the choice of the control field is done in order to have a population that *on average* looks like the contaminating population in the cluster frame.

For these reasons it is not necessary to try the same 2D approach to assign completeness values to the off-cluster frame stars. We only populated the whole frame in a uniform way with 250 stars per each 0.5 magnitude-wide bin; only 50 stars were added in each run, not to alter the crowding characteristics of the field. Then we computed the fraction of recovered stars over the total number of simulated ones and fit a function like that of equation (2.12), this time without any spatial dependence. Last step was to assign also to the single stars in the control field their corresponding completeness value in each photometric band.

2.B EVALUATING THE PHOTOMETRIC ERRORS AND THEIR CORRELATIONS

In BR08 simulated stars were used to estimate the photometric errors. It was shown that for stars with known input magnitudes the output magnitudes were often in disagreement at a level of more than 1σ , where the the DAOPHOT fitting errors were taken as σ values. Hence, the difference between input and output magnitude seemed to be a more conservative and robust estimate of the real photometric error. Simulated stars are used here also to estimate the correlation between magnitude errors. The photon counts associated to an isolated star in two different bands are uncorrelated. In reality, even though the photon counts are independent, the inferred magnitude values may not be. The reason why J and K_S magnitude errors are correlated is the presence of bright stars or, more generally, crowding. When a faint star is located close to a bright star, the residuals of PSF fitting procedure of the bright star (which is usually bright in both bands) may lead to magnitude errors in both bands. If the bright star's wings are not properly subtracted, then there will be an excess in the flux that is assigned to the nearby faint star. The bright star's wings may also be over-subtracted (e.g. because the core is not well fitted), leading to too small flux estimates. This can lead to a correlation of the photometric errors. Crowding from stars of comparable magnitudes will lead to a similar behaviour.

Figure 2.12: Left: correlation between J and K_S magnitude errors for the simulated stars. Right: same, but using $(J - K_S)$ colour instead of J magnitude. The r quantities are the values of Pearson's correlation coefficients for the two samples.



That J and K_S magnitude errors are correlated is obvious from Fig. 2.12. In the left panel we show $J^{out} - J^{in}$ vs. $K^{out} - K^{in}$ for the simulated stars. In the right panel we show $(J - K_S)^{out} - (J - K_S)^{in}$ vs. $K^{out} - K^{in}$. Since the two magnitude estimates are correlated, the composed quantity $J - K_S$ is also correlated to the single magnitude values. The coefficient r in the figures is the Pearson's correlation coefficient for the whole sample of simulated stars, i.e.

$$r_{X,Y} = \frac{\sum_i (X_i - \bar{X})(Y_i - \bar{Y})}{\sqrt{\sum_i (X_i - \bar{X})^2} \sqrt{\sum_i (Y_i - \bar{Y})^2}} ; \quad (2.13)$$

where X and Y are the respective abscissa and ordinate in the two plots. From its definition it is clear that Pearson's r is equivalent to the X and Y covariance divided by the product of X and Y standard deviations. A value of r very close to +1 (-1) indicates a very tight correlation (anti-correlation) between the two random variables, while two totally uncorrelated random variables would show a value of $r = 0$. The values of the Pearson's coefficients in Fig. 2.12 indicate a quite significant correlation of the magnitude errors as well as an even tighter anticorrelation between magnitude and colour errors. Given that r is not a robust, outlier-resistant quantity, the actual values were calculated removing the outliers, i.e. stars for which input and output magnitudes differ more than 1 mag in at least one band. The number of stars inside this limits is 97 % of the total number of simulated stars. Therefore, the exclusion of the outliers does not represent

a shortcoming in the evaluation of a robust estimate for the overall correlation coefficient of the sample.

2.B.1 ASSIGNING PROPER PHOTOMETRIC ERRORS AND THEIR CORRELATION TO EACH DETECTED STAR

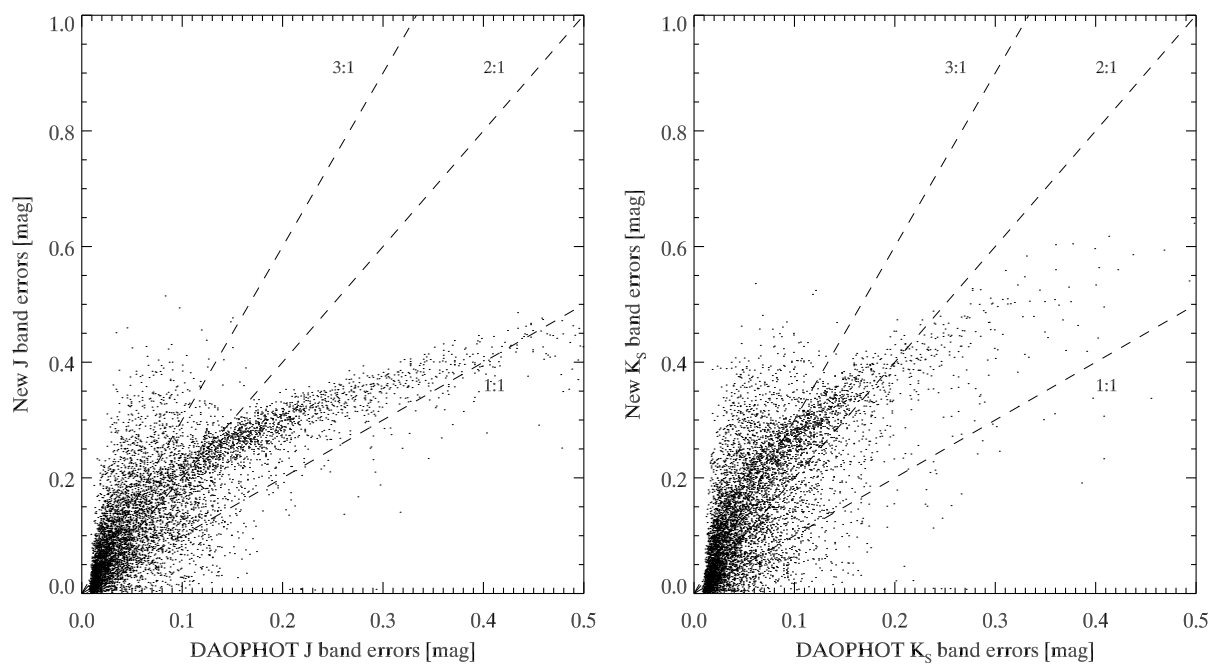
For each detected star we selected a number of at least 7 simulated stars (using the same stars of Sect. 2.A.1) that were positioned in its *neighbourhood*. By neighbours we mean simulated stars whose distance from the position of the real star was not larger than 50 pixels and whose magnitude differs no more than 1 magnitude –in each band– from the real star. The distance of 50 pixels represents the average *radius-of-influence* of the bright stars, i.e. the typical extent of their halos, as derived by the analysis of Wd 1 NTT/SofI images. For each of the neighbours in the subsample we calculated $J^{out} - J^{in}$ and $K^{out} - K^{in}$. The standard deviations of the two quantities, within the subsample, have been used as estimates for the photometric errors of the real stars. We also calculated the Pearson coefficient between the two quantities in the neighbours subsample and assigned it to the detected star. The comparison between DAOPHOT errors and our newly estimated errors for the Wd 1 field are shown in Fig. 2.13. The new error estimates are, on average, larger than what predicted by DAOPHOT, especially in the K_S band.

Some of the real stars do not have a sufficient number of neighbours to perform this kind of estimate. This is true especially for faint stars, since the majority of the simulated stars at the faintest magnitudes cannot be recovered. Hence these simulated stars cannot be used for the error estimate, because they don't have a M^{out} value. For stars without enough useful simulated neighbours, we used a different error estimate. We first divided the real stars for which the error determination worked fine in several magnitude bins. Then we calculated the mean error per each magnitude bin and fitted an exponential relation to the *mean error vs. bin-magnitude* points. This relation has been used to assign their errors to the stars that lack a sufficient number of neighbours. The new errors, as a function of the stars' magnitudes are shown in Fig. 2.3. The figure shows the exponential extrapolation used to determine the errors of the faintest stars. Together with the new errors for the cluster's field stars, we show, in red, the new errors for the control field stars, whose derivation is illustrated in Sect. 2.B.2.

2.B.2 PHOTOMETRIC ERRORS FOR THE CONTROL FIELD

A similar method was used to derive new photometric errors for the control field stars. Since we assume that these stars are uniformly distributed, there is no need to treat the spatial variation of the errors. Using the same simulated stars as in Sect. 2.A.4, we computed the $\Delta M_j(i) =$

Figure 2.13: Comparison between DAOPHOT photometry errors and our newly derived errors for J band (left) and K_S band in the case of Wd 1 field. The dashed lines are 1:1, 2:1 and 3:1 relations between new and DAOPHOT errors.



$M_j^{out}(i) - M_j^{in}(i)$ for $M_j = J, K_S$ and i running over the simulated stars; then we binned the stars in 0.5 mag wide bins (in the input magnitudes) and for each bin we computed the standard deviation of the ΔM_j over the bin. The last step was to fit the $(\sigma[\Delta M_j], M_j[\text{bin}])$ points with an exponential relation; here $M_j[\text{bin}]$ is the central magnitude of the bin. This relation was used to assign an error to the real stars as a function of magnitude. The average value of the correlation between J and K_S was calculated for the whole sample and is $r = 0.25$. This value was assigned to each real star in the control field.

Figure 2.3 shows that, on average, the photometric errors in the control field are smaller than those in the cluster's field. This behaviour is expected, and can be explained by the higher degree of crowding for Wd 1's field. For the same reason, the detection limit for the control field is ~ 0.5 mag fainter than the Wd 1 field in both photometric bands.

2.C σ - CLIPPING

Because of some dissimilarities between the on- and off-field fore/background populations, the CMD of Wd 1, even after subtraction, does not look perfectly clean. For this reason, after having chosen the best fitting isochrone, i.e. the 4 Myr one, before any further analysis, we additionally subtracted those stars that lie more than 3σ away from the reference isochrone in the magnitude-magnitude space (see the end of Sect. 2.5). After clipping, essentially all stars with colours and magnitudes consistent with the 4 Myr cluster population are included in the final source selection. Our clipping criteria may retain some arbitrariness; nevertheless they do not affect our further analysis. The main reason is the cut only affects the faint stars, with large photometric errors. Some of them could be excluded or included in the catalogues by slightly changing the σ threshold. Anyway, in the computation of the IMF (see Sect. 2.8) and of the stellar density (see Sect. 2.9), we only consider stars above a given *completeness* or *mass* threshold. Stars with uncertain membership are mostly excluded by these two additional cuts hence they do not affect the final results.

One realization of the clean cluster's CMD is shown in Fig. 2.5, together with the best fitting isochrone. The error bars shown in the diagram are the average $J - K_S$ and K_S errors per magnitude bin. The colour errors are calculated for each star as:

$$\delta(J - K_S) = \sqrt{\sigma^2(J) + \sigma^2(K_S) + 2r_{JK_S}\sigma(J)\sigma(K_S)} \quad (2.14)$$

Pearson's r is equal to the covariance divided by the product of the two standard deviations (see equation 2.13); hence the third addend on the r.h.s. of equation (2.14) is equal two twice the covariance of J and K_S .

Table 2.2: Detections in the on and off frames.

Field	Number of stars
on	7036
off	5381
on (after subtraction)	5810 ± 25
on (after subtraction and σ -clipping)	4300 ± 23

In Table 2.2 we summarize the number of stars left after field subtraction and additional clipping. The mean values and their uncertainties are derived by iterating the probabilistic subtraction technique. We repeated the extraction of ζ for each star, to generate 100 different catalogues (see Sect. 2.5). We then calculated mean and standard deviations of the number of members over the 100 samples.

2.D BOOTSTRAP ESTIMATE OF THE IMF PARAMETERS AND THEIR ERRORS

Bootstrapping is a resampling technique for error estimation (see e.g. Efron 1979; Hastie et al. 2009; Andrae 2010). Given a data set from which some parameters are estimated, bootstrapping consists in resampling the data to create *alternative* data sets. From these, it is possible to repeatedly estimate the parameters of interest, monitoring their distribution. We generated 10^5 bootstrap samples to probe the parameter space of (γ, A) , assuming for the IMF the functional form $\frac{dN(m)}{dm} = \mathcal{A} \times m^{-\gamma}$. From our data set, we created 100 different realizations of the members catalogue. Each catalogue has a slightly different number of members $N_{c,j}$ with $j = 1, 100$, after statistical field subtraction and σ -clipping (see Appendix 2.C). From the members of each j -th catalogue 1000 bootstrap samples were created. The new samples consist of the same number of stars as in the member catalog, $N_{c,j}$, but the drawing is made with replacement, i.e., the same star can occur multiple times in a bootstrap sample. This sample of stars is then used to build the IMF as in equation (2.4) where now i runs on the stars of the specific bootstrap sample. At each iteration a power-law fit is performed to obtain a couple $(\gamma_{j,k}, A_{j,k})$ with $j = 1, 100$ and $k = 1, 1000$. As already detailed in Sect.2.8.2, the fitting interval is restricted to $m \in [3.5, 27] M_{\odot}$. Given the $(\gamma_{j,k}, A_{j,k})$ values, we obtained the corresponding total mass, $M_{j,k}$, and total number of stars, $N_{j,k}$, by integrating the power law in the interval $m \in [0.08, 120M_{\odot}]$.

A 2D density plot of the output values (γ, A) is shown in Fig. 2.14. It is clear that the γ and A parameter are tightly correlated. This is easy to understand. For each bootstrap sample we have

Table 2.3: Best values and their confidence intervals for the IMF parameters, the total mass and the total number of stars of Wd 1..

Quantity	Best value	Lower limit	Upper limit
γ	2.44	2.36	2.64
$A/10^4$	1.22	1.08	1.78
$M_{\text{tot}}[10^4 M_{\odot}]$	4.91	4.42	6.70
$N_{\text{tot}}/10^4$	10.4	8.6	16.4

a number N_{fit} of stars that are actually inside the fitting interval. Given the different catalogue realizations, this number can be slightly different, but is mostly in the interval [1250, 1500]. The IMF fit has to satisfy the condition:

$$N_{\text{fit}} = A \times \int_{3.5}^{27} m^{-\gamma} dm$$

From which we get:

$$A = \frac{N_{\text{fit}}(1 - \gamma)}{27^{1-\gamma} - 3.5^{1-\gamma}}$$

This relation between A and γ is overplotted in Fig. 2.14 for $N_{\text{fit}} = 1000, 1250, 1500, 1750$ (dotted lines). Given that the 2D distribution of (γ, A) pairs is clearly non Gaussian, the definition of the best values and the confidence intervals for the two parameters is not straightforward. The maximum of the 2D distribution is located at $(\gamma_{\text{max}}, A_{\text{max}}) = (2.46, 1.31 \times 10^4)$. With this pair of values we obtain a total mass, $M_{\text{max}} = 5.13 \times 10^4 M_{\odot}$ and a total number $N_{\text{max}} = 1.10 \times 10^5$ stars.

On the other hand, using the 2D joint distribution is not the most suitable choice for defining the best values and confidence interval for the parameters (γ, A) and for M_{tot} and N_{tot} . For this purpose, in the case of γ and A , we used the marginal distributions. These are obtained by integration of the joint distribution with respect to the other variable. For M_{tot} and N_{tot} we similarly used the distributions of $M_{j,k}$, and $N_{j,k}$ obtained after each bootstrap iteration. The best values are obtained by maximizing the distributions. The confidence intervals are obtained by integrating the distributions from left and right until 16% of the total area under the distribution is reached on each side. This means that the limits of the asymmetric confidence interval comprise 68% of the total area under the distribution function. The marginal distributions for γ and A , as well as the distributions of $M_{j,k}$, and $N_{j,k}$ are shown in Fig. 2.15. The best values and the confidence intervals are given in Table 2.3.

Figure 2.14: Density of the occurrences of (γ, A) from our bootstrap procedure. The black dot indicates the location of the maximum of the 2D density: $(\gamma_M, A_M) = (2.46, 1.31 \times 10^4)$. Dotted lines are lines of constant number of stars in the fitting interval; from bottom to top $N_{\text{fit}} = 1000, 1250, 1500, 1750$.

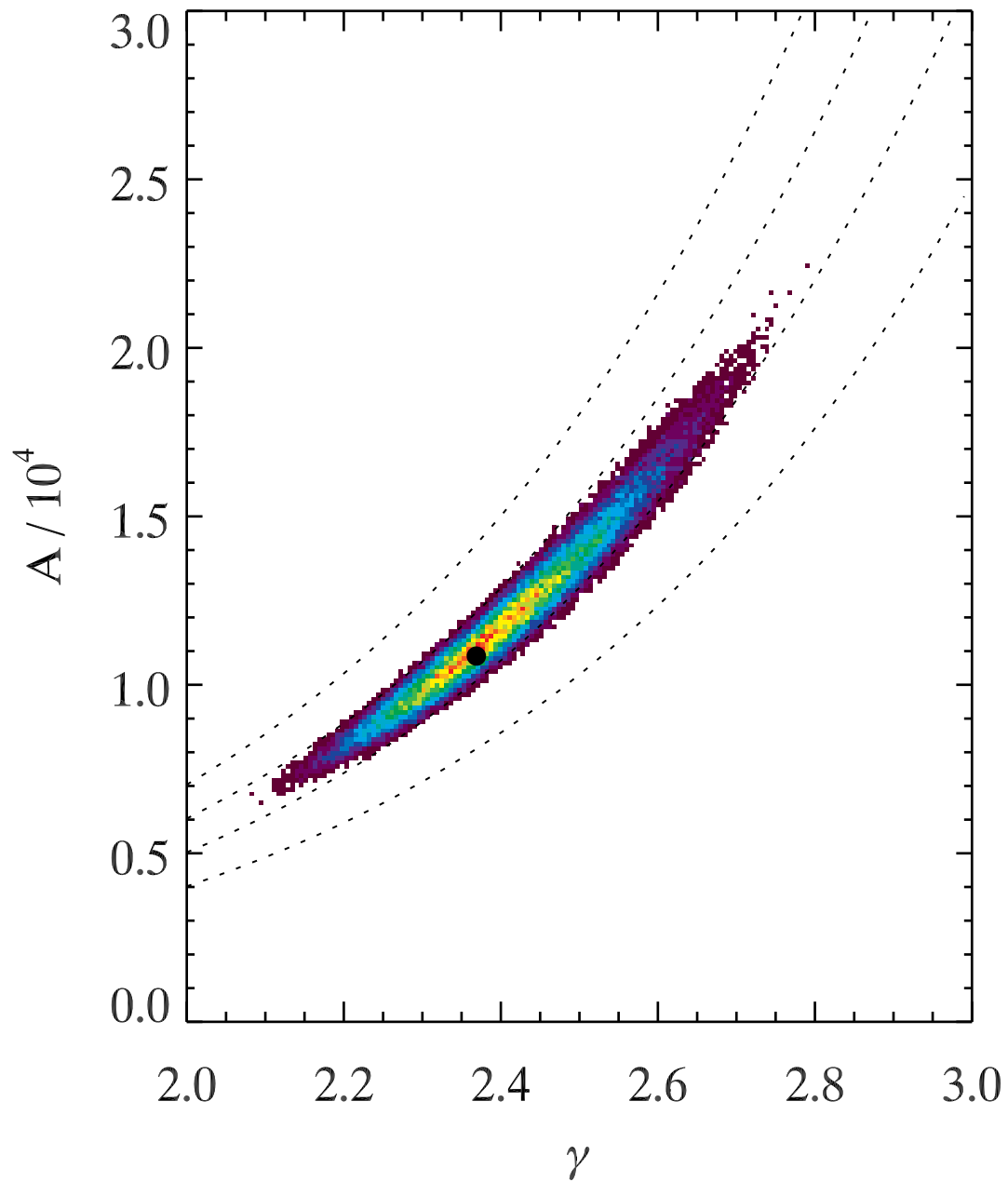
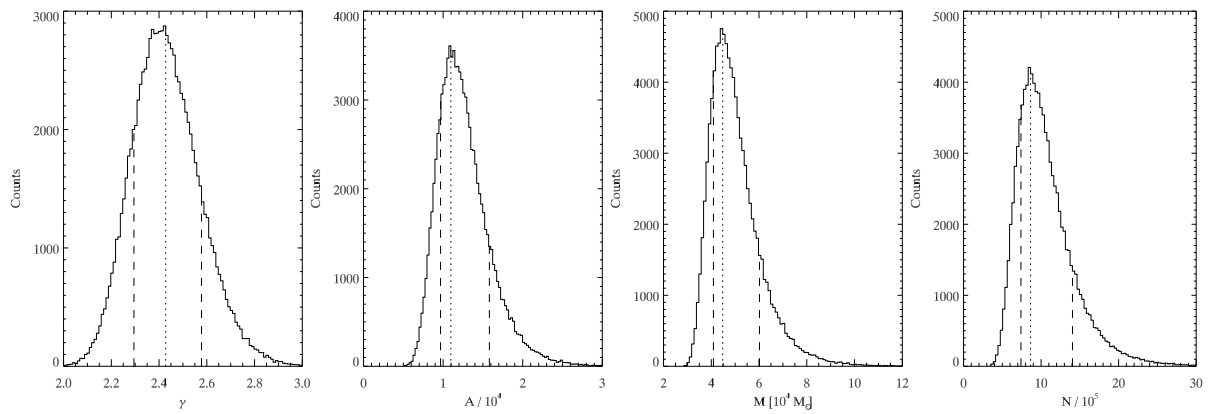


Figure 2.15: From left to right: Marginal distributions for γ and A and distributions of $M_{j,k}$, and $N_{j,k}$. The best values are marked by dotted lines; the confidence intervals are marked by dashed lines.



MULTIPLE EPISODES OF STAR FORMATION IN THE CN15/16/17 MOLECULAR COMPLEX*

3.1 INTRODUCTION

The CN15/16/17 complex of molecular bubbles is a star-forming region hosting young stars in different evolutionary phases. The region is projected towards the Galactic Center ($l = 0^{\circ}58$, $b = -0^{\circ}85$) and has first been detected by Churchwell et al. (2007). The authors visually searched the inner 20° of the Galaxy for molecular bubbles, using mid-infrared data from the GLIMPSE-II survey (Benjamin et al. 2003). The Spitzer/IRAC images of the region show a very pronounced diffuse emission in the $8\mu\text{m}$ channel, coming from PAH emission. Two stellar clusters are associated with the region and are visible in the near infrared. The clusters were first identified by Dutra & Bica (2000) using 2MASS images (Skrutskie et al. 2006). One of them already emerged from its parental cloud and its stellar population is detectable in the near infrared. The second is still deeply embedded and the high extinction only allows the detection of the brightest sources. Dutra et al. (2003b) further studied the clusters using H and K_S band imaging obtained with the SofI instrument at the NTT ESO telescope in La Silla, Chile. Using the author's convention we will refer to the clusters as DB11 -the older- and DB10 -the younger, more embedded. A third, very deeply embedded star-forming region is also present. This youngest region consists of a group of YSOs visible in the Spitzer images and is associated with a radio detected Ultra Compact H II region as well as several methanol masers (Walsh et al. 1998).

We reobserved the region using NTT/SofI as part of a larger program (P.I. Gennaro, M.) in which we targeted several molecular bubbles hosting young massive cluster candidates and located in

*Based on observations collected at the European Southern Observatory, La Silla, Chile (Program ID 085.D-0780)

projection close to the Galactic Center. The observing strategy consisted of a combination of deep JHK_S photometry and long slit K-band spectroscopy of the brightest candidate members. Combining photometry and spectroscopy we have been able to confirm the presence of massive OB stars and constrain the region's distance using spectral-type classification.

In Fig. 3.1, left panel, we show a JHK_S bands composite image of the region from our SofI observations. Objects DB10 and DB11 are clearly visible. DB11 is the central, larger cluster, while DB10 is the smaller cluster to the right side of DB11. The red diffuse emission around the clusters comes from Br γ nebular emission inside the H II regions. In the right panel of the figure it is possible to see the bright PAHs emission in the Spitzer/IRAC $8\mu m$ channel. The contours indicate the radio continuum flux at 1.4 GHz as mapped by the NRAO VLA Sky Survey (hereafter NVSS, see Condon et al. 1998). From the radio contours one can identify two H II regions, one associated with DB11, while the other is the aforementioned Ultra Compact H II region associated with the deeply embedded third site of star formation in the complex. In the latter, a group of YSOs can be seen in the IRAC channels, but most of them are too embedded to be seen in the JHK_S image and only two are visible as very red sources. Weaker, but still visible radio emission is also observed at DB10's position, resulting in an elongation of the contours.

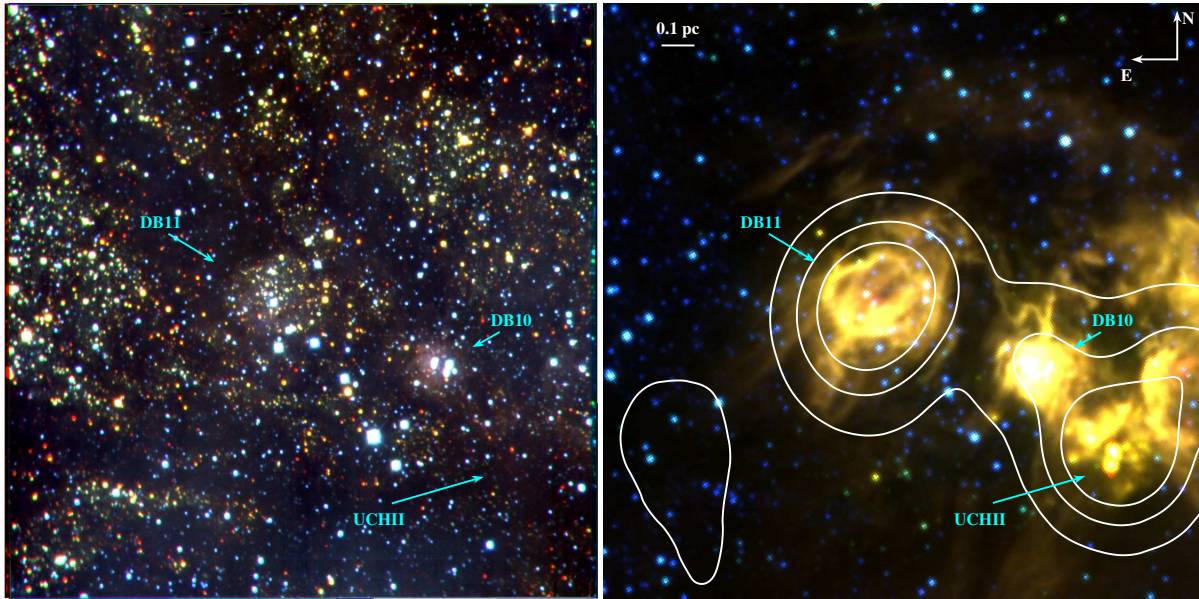
From this collection of observational evidence it is clear that the CN15/16/17 complex is a site hosting multiple episodes of star formation with the presence of young massive stars. A plausible scenario to explain the features observed at multiple wavelengths is described in Watson et al. (2008). The authors use a set of GLIMPSE-I bubbles, similar to those considered here, to infer the role played by massive stars in such molecular complexes. They conclude that massive stars a) provide the ionizing flux for the H II region, b) blow out the bubble with their powerful winds and c) excite the PAH just outside the H ionization front with the soft UV component, hence powering the $8\mu m$ emission.

3.2 JHK_S PHOTOMETRY

Observations were performed on the 27th of June 2010. A summary of the integration times can be found in Table 3.1. DIT is the single frame Detector Integration time in seconds. The DIT times were chosen to be short enough to avoid saturation of stars brighter than 9 mag in each of the JHK_S bands. At each position, N_{DIT}=10 frames are averaged to produce a single raw frame. N_{INT} = 5 dithering offset positions are used. The total exposure time is DIT*N_{DIT}*N_{INT}.

Given the SofI field of view (FoV) of $4.5' \times 4.5'$ and their projected distance on the sky of $1.6'$, both clusters DB10 and DB11 could be imaged at the same time in each dither frame. We spent an equal amount of time on the target and on a nearby field located $\sim 6'$ to the East, $\sim 4'$ to the

Figure 3.1: Left: SOFI JHK_S band composite image of the CN15/16/17 molecular bubbles complex. Right: same region of the sky in Spitzer/IRAC 3.6, 5.8 and 8.0 μm composite image. The white contours are NVSS radio-continuum maps. Both images are centered on RA(J2000) = $17^{\text{h}}50^{\text{m}}23^{\text{s}}$, Dec(J2000) = $-28^{\circ}53'15''$; image size is $\sim 5' \times 5'$; North is up, East is left. The physical length-scale is estimated at 1200 pc distance.



North from the center of our science field. This control field has been observed for two reasons. The first was to build an image of the sky free of the nebulous emission, which characterizes the CN15/16/17 region, especially in the K-band. The second reason was to use the control field's population for statistical field-stars decontamination. Image reduction was performed using a combination of `eclipse` routines (Devillard 2001) and custom-made IDL routines.

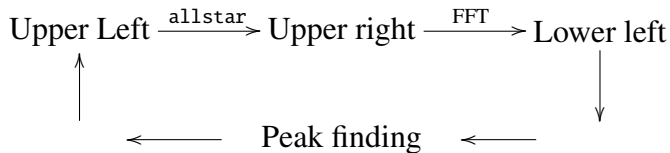
Photometry was performed on the reduced frames using the IRAF implementation of the DAOPHOT package (Stetson 1987). Due to the bright and highly variable background, specially in the K_S band, the detection of faint sources in some parts of the image is problematic. We circumvented the problem by performing spatial filtering of the image using the Fast-Fourier-Transform (FFT) as implemented in IDL. After running DAOPHOT on the frames once, we used the task `substar` to remove the detected sources. At this stage the image consists of three components: the light from the missed sources, $\mathcal{S}(x, y)$, the nebular diffuse emission, $\mathcal{N}(x, y)$ and the residual noise from the bright infrared sky background, $\mathcal{B}(x, y)$.

We used the following procedure to reduce the $\mathcal{N}(x, y)$ term. In the previous DAOPHOT steps we have built an image for the stellar point spread function (PSF) using bright, isolated sources in the field. The FFT of the PSF has been used as a high-pass filter to remove the power associated with small wave numbers, i.e. long-scale variation of the diffuse nebosity. Spatial filtering

consists of multiplying the FFT of the image by the FFT of the PSF. The inverse FFT of the multiplied images is then calculated. In this final image the power associated with the $\mathcal{N}(x, y)$ component is much reduced. The high-pass filter removes most of the power associated with wave numbers $k \lesssim 1/\Lambda$, where Λ is the typical length scale of the PSF (for example the full width at half-maximum (FWHM) in the case of a Gaussian PSF).

The spatial filtering does not cut out the $\mathcal{B}(x, y)$ noise as well as the Poisson noise associated with the $\mathcal{N}(x, y)$ signal. Both of these components are indeed highly variable, i.e. their characteristic length-scale is $l \lesssim \Lambda$. The presence of these two components sets the ultimate detection limit for the faint sources. After applying the image processing steps, a second run of the `daofind` peak-finding routine on the subtracted and filtered image allows detection of many additional sources, without the need of artificially lowering the detection threshold. We want to emphasize that only the peak-finding step is run on the artificially processed images. The PSF-fitting task `allstar` is subsequently performed on the original, unsubtracted and unfiltered image, using an input list obtained by merging the previous detections and the newly found peaks. We iterate the scheme one more time to obtain the final list of instrumental stellar magnitudes in each band.

Figure 3.2 shows the images before and after the spatial filtering is applied. The upper-left panel shows the original image in the K_S band. The upper-right panel is the result after one `allstar` passage. The detected sources are fitted and subtracted from the original image. The residual light is coming from the undetected sources, the nebula and the sky background. In the lower-left panel the subtracted image is FFT-filtered, with the lower-right panel showing the subtracted nebulosity. Schematically we have that:



It is worth noticing that the image displaying levels are set to be the same in all four panels. In such a way it becomes evident how bright the subtracted nebulosity is and how large its luminosity contrast between different areas is.

As already mentioned, our spatial filtering method is not removing any variation in $\mathcal{N}(x, y)$, which happens on spatial scales of the order of Λ . It is possible that part of the detections in a single band might be non-stellar sources, i.e. small-scale, large-gradient variations in the diffuse nebulosity. However most of the false detections are removed from the final catalog once the three separate lists of detections for J , H and K_S are matched. For the positional matching we use the K_S band detections list as a master catalogue and assume that any real object detected in the H band must have a K_S band counterpart and any J band detection must have counterpart in both H and K_S bands. A total of 3332 stars are detected across the SofI FoV in J , H and K_S

bands. In addition 1823 stars are detected in H and K_S only.

Instrumental magnitudes have been transformed into the 2MASS photometric system by matching our detections with bright and isolated 2MASS sources. A linear fit was performed between the matched stars, allowing for a color term in the calibration. The resulting photometry for the entire region is displayed in Fig. 3.3.

Table 3.1: Observing strategy for JHK_S imaging. Seeing is the average full width at half maximum of the stellar images during the observations.

Band	DIT [s]	NDIT	NINT	Exposure Time [s]	Seeing [arcsec]
J	10	10	5	500	1.2
H	6	10	5	300	1.1
K_S	2.5	10	5	125	1.0

3.3 IRAC MID-INFRARED PHOTOMETRY

In addition to the near infrared photometry from SofI, we used the mid infrared photometry for the region in the 4 IRAC bands centered at $3.6\ \mu\text{m}$, $4.5\ \mu\text{m}$, $5.8\ \mu\text{m}$ and $8.0\ \mu\text{m}$. The region has been observed within the GLIMPSE II survey (Benjamin et al. 2003). The latter is a survey of the inner part of the Galactic plane (Galactic Coordinates: $|l| < 10^\circ$, $|b| < 1^\circ$), observed in all 4 channels of Spitzer/IRAC. The products of the survey such as image mosaics and detected point sources catalogs are available online¹. We used the GLIMPSE II Epoch 2 November '09 Point Sources Catalog.

In an area of $6' \times 6'$ centered on DB11 there are 342 sources with IRAC photometry in all 4 bands. Among these objects, class I and class II YSOs can be classified using their mid-infrared excess due to the circumstellar envelopes and disks, respectively. Allen et al. (2004) showed that these two classes of objects occupy different areas in the $[3.6]-[4.5]$ vs. $[5.8]-[8.0]$ color-color diagram with respect to "purely photospheric" objects. The latter are clustered around the (0,0) position in this diagram. Even though there might be a small overlap between the class I and class II objects, Megeath et al. (2004) proposed a working criterion to identify the two classes

¹At the following URLs:

irsa.ipac.caltech.edu/data/SPITZER/GLIMPSE/ (images)

irsa.ipac.caltech.edu/cgi-bin/Gator/nph-scan?submit=Select&projshort=SPITZER (catalogs)

Figure 3.2: Result of the FFT image filtering. *Upper left:* original K_S band image. *Upper right:* image after one allstar passage. The light from the detected sources is subtracted. *Lower left:* The subtracted image is cleaned using the FFT filtering. *Lower right:* the filtered-out nebulosity.

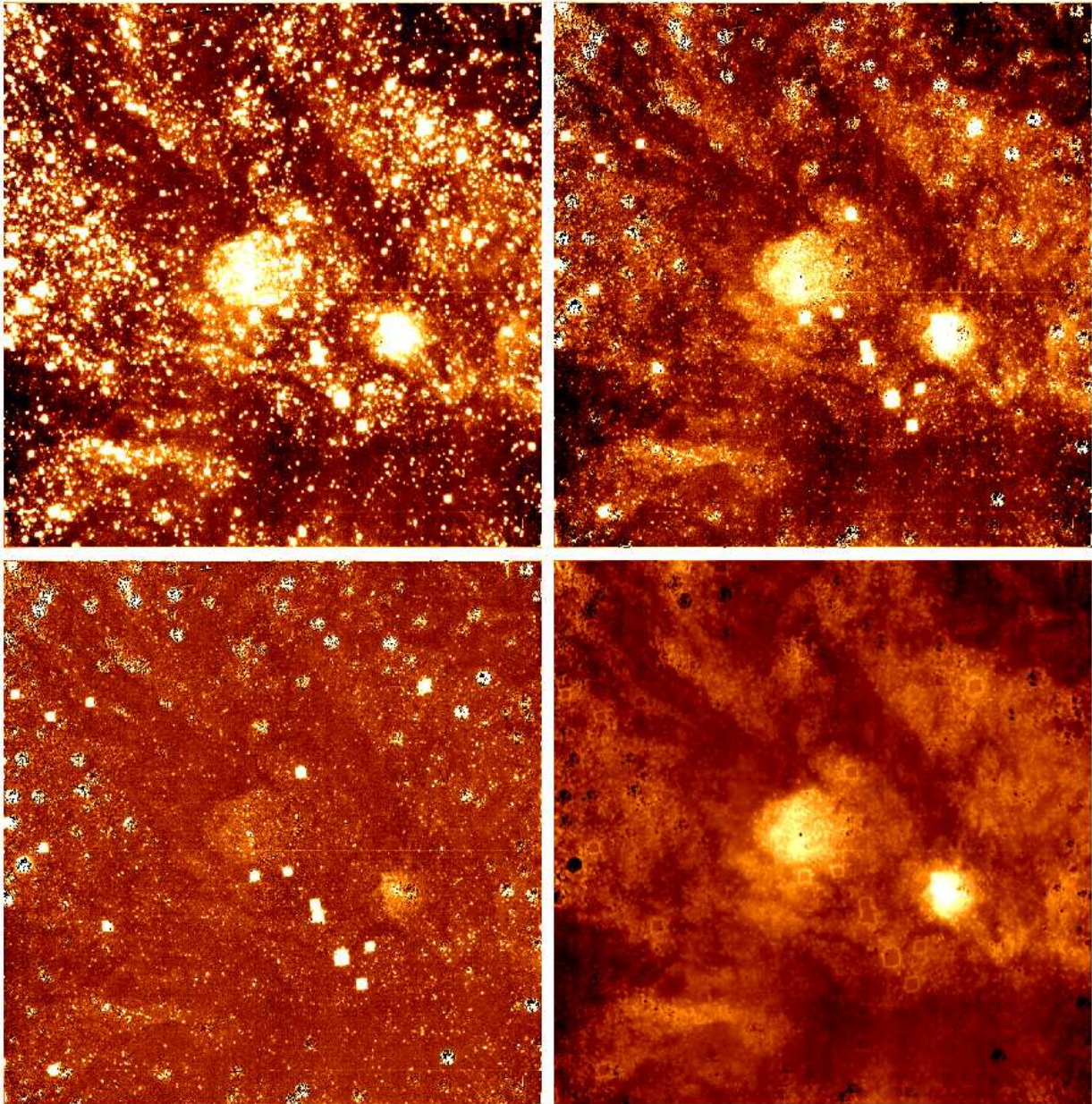
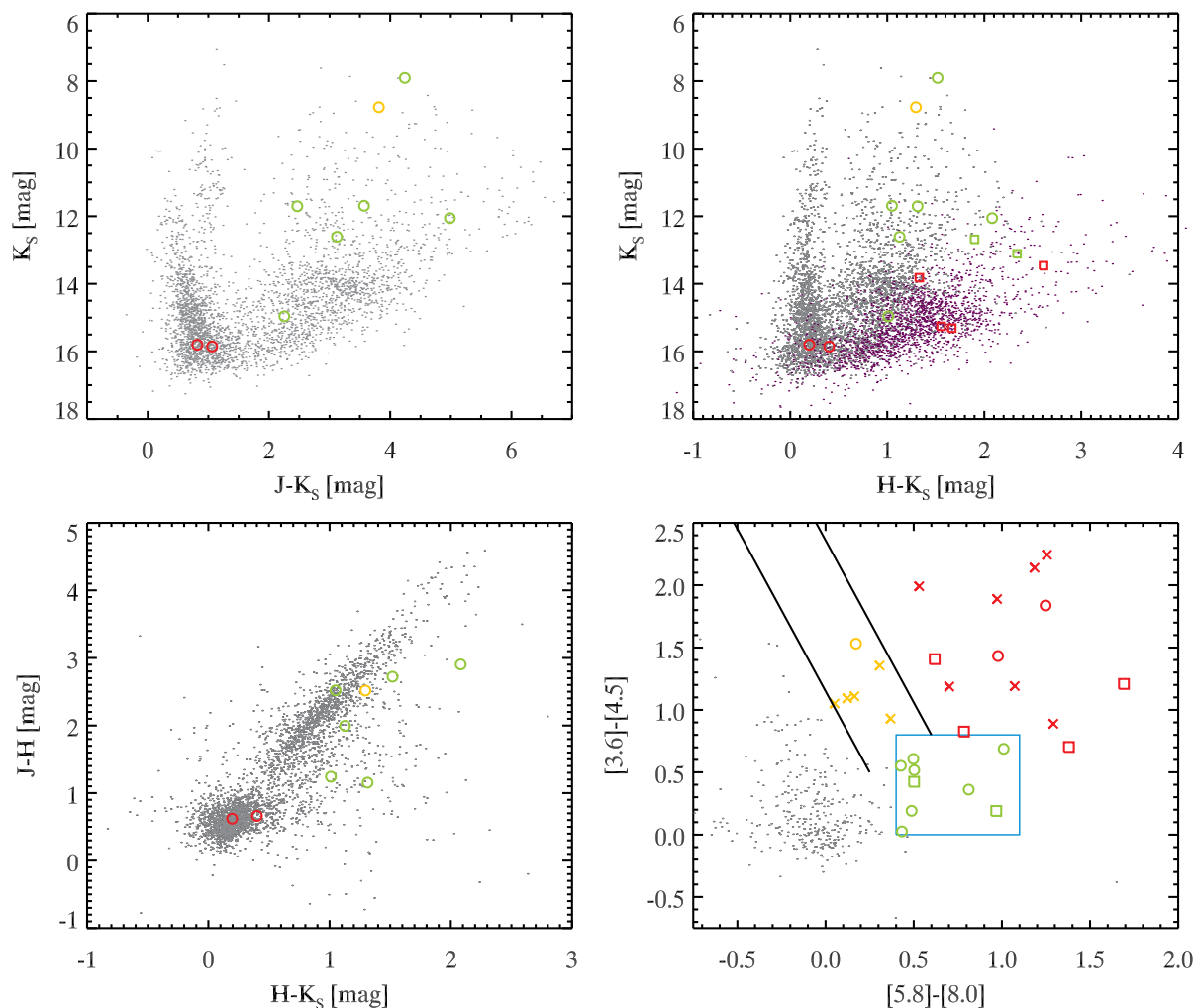


Figure 3.3: Photometry of the CN15/16/17 region. *Upper left:* K_S vs. $J - K_S$ diagram. The red, yellow and green circles correspond to class I, reddened class II and class II YSOs identified in the IRAC color-color diagram. *Upper right:* K_S vs. $H - K_S$ diagram. Gray dots are stars identified also in J band. Purple dots are stars identified only in H and K_S . Green, yellow and red circles as in the upper-left panel. Green and red squares are class I and II objects not identified in J band. *Lower left:* $J - H$ vs. $H - K_S$ diagram. Symbols as in the upper-left panel. *Lower right:* IRAC [3.6]-[4.5] vs [5.8]-[8.0] color-color diagram. The cyan box indicates the locus of class II objects according to (Allen et al. 2004). The two black lines are parallel to the reddening vector derived by the Mathis (1990) extinction law and correspond to the region of reddened class II objects according to Megeath et al. (2004). YSOs are in red (class I), green (class II) and yellow (reddened class II). Among the YSOs, circles are sources with JHK_S photometry, squares are objects with only HK_S detections and crosses are objects not detected in either J , H or K_S .



of objects and separate them from the more evolved, envelope and disk-free stellar sources. From the models of the emission of class I and II objects by Allen et al. (2004), they identify a rectangular area with $0.0 \text{ mag} \leq [3.6] - [4.5] \leq 0.8 \text{ mag}$ and $0.4 \text{ mag} \leq [5.8] - [8.0] \leq 1.1 \text{ mag}$ as the locus of class II YSOs. This box is displayed in the lower-right panel of Fig. 3.3. The area of the diagram above and to the right of the box is occupied by class I objects. Part of class II objects might reside in a reddening stripe on the upper left of the unreddened class II box. The two parallel lines in the same figure show the direction of the reddening vector for the extinction law of Mathis (1990).

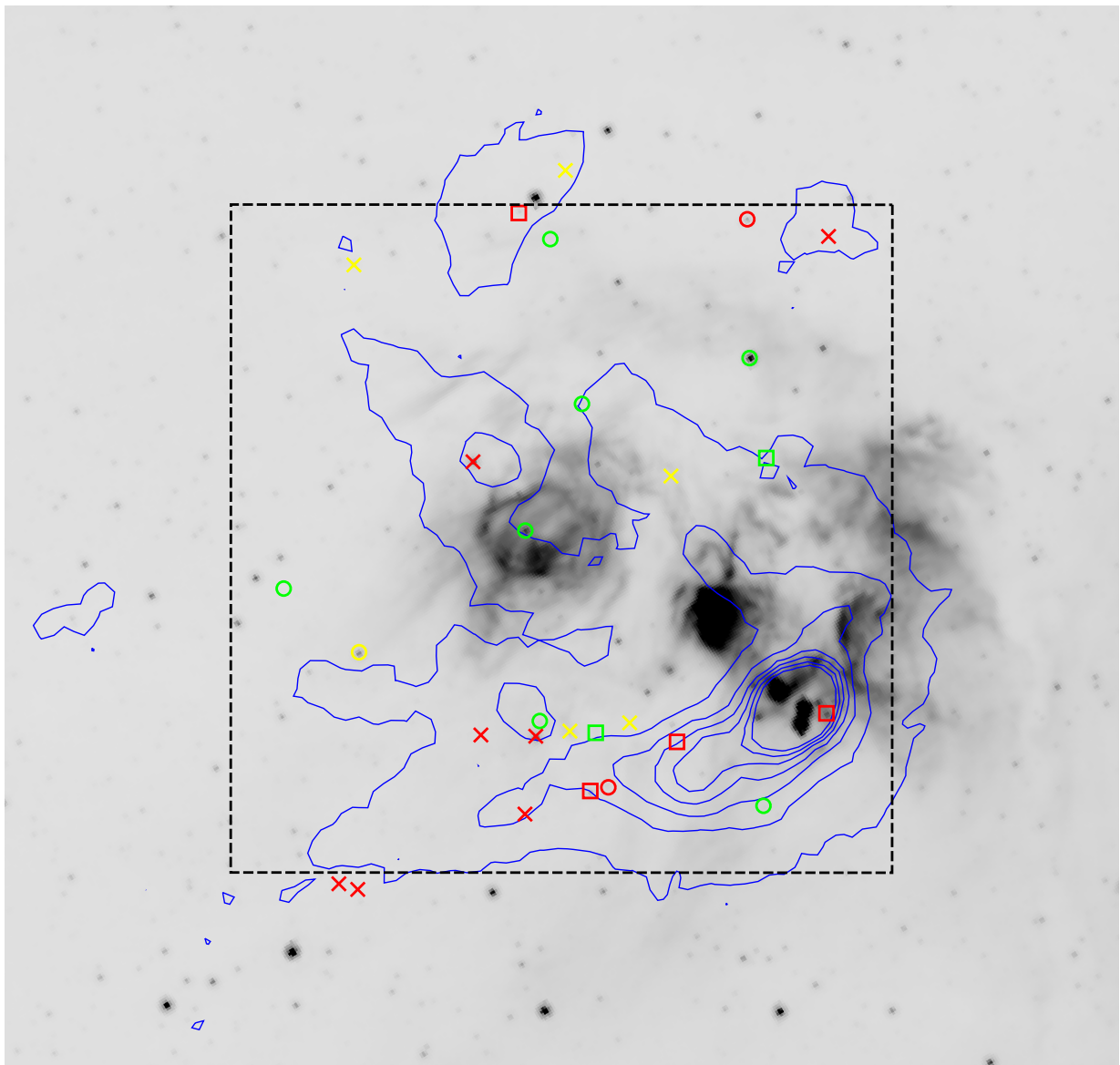
We identify 9 class II objects, 6 reddened class II objects and 13 class I objects. Of the 9 class II sources 6 have also JHK_S photometry, and 2 have HK_S photometry but are not detected in J . Among the class I objects we have 2 JHK_S sources and 4 HK_S ones; two more class I objects are only detected in K_S band. The reddened class II objects are heavily extincted. A reddening of 0.4 mag in $[3.6]-[4.5]$ corresponds to about 30 mag in A_V . Using the extinction law by Rieke & Lebofsky (1985) this corresponds to $A_J = 8.46 \text{ mag}$, $A_H = 5.25 \text{ mag}$ and $A_{K_S} = 3.36 \text{ mag}$. Therefore only one of the reddened class II YSOs is detected in JHK_S , while 3 of them are detected only in K_S . In addition to the IRAC color-color diagram we display the class I and class II objects with near infrared detections in the other panels of Fig. 3.3. Given that the region is projected close to the Galactic Center ($l = 0^\circ.58$, $b = -0^\circ.85$) some contamination from AGB stars might be present in our YSO sample. According to Marengo et al. (2008) the loci of oxygen rich AGB stars and supergiants slightly overlap with class II YSOs. Only spectroscopy of these sources might help discriminating between different stellar types. The class I sample should instead be free of this contamination.

The positions of the identified YSOs are displayed on the IRAC- $8 \mu\text{m}$ image of Fig. 3.4. From their spatial distribution it is clear that the entire region is experiencing star formation events, not only the two clusters DB11 and DB10. A small clustering of YSOs is visible towards the southern part of the region. This area appears very dark in the near infrared image, due to extinction coming from the molecular cloud hosting this group of YSOs. On the contrary the DB11 and DB10 clusters show a paucity of YSOs. This might be partially due to the high brightness of the nebula in the mid infrared, which hampers the detection of point sources.

3.4 SUB-MM CONTINUUM EMISSION

Extinction is well traced by the cold dust emission at $870 \mu\text{m}$ from the ATLASGAL survey of the Galactic Plane (Schuller et al. 2009). Overplotted in Fig. 3.4 are the dust emission contours for the region (courtesy of H. Beuther). The cold dust traces very well the positions of the identified YSOs in the southern part of the CN15/16/17 complex. Also the more isolated YSOs in the

Figure 3.4: IRAC 8 μm image with the marked positions of the identified YSOs. Crosses correspond to objects which are not identified in the JHK_S bands. Squares are objects identified in H and K_S , circles are objects identified in J , H and K_S . Class I objects are in red, class II in green, while in yellow we display the sources identified as reddened class II. The dashed black box corresponds to the observed SofI field, centered on $\text{RA}(J2000) = 17^{\text{h}}50^{\text{m}}23^{\text{s}}$, $\text{Dec}(J2000) = -28^{\circ}53'15''$. The blue contours trace the emission of cold dust at 870 μm from the ATLASGAL survey of the Galactic Plane.



northern area are surrounded by emission at $870\ \mu\text{m}$. The peak of $870\ \mu\text{m}$ emission is exactly on top of the bright Ultra Compact H II region in the south-west area. This densest region (as it appears from dust emission which traces the dust column density) is therefore associated to a region of high mass star formation (the ionization of H II requires the presence of hot, high-mass objects). The remaining YSOs population in the southern area lies along an arc of $870\ \mu\text{m}$ emission and is not associated to H II emission, as visible in Fig. 3.1, where no radio emission can be observed in this area. Hence these are likely less massive YSOs, which are not able to ionize the surrounding regions.

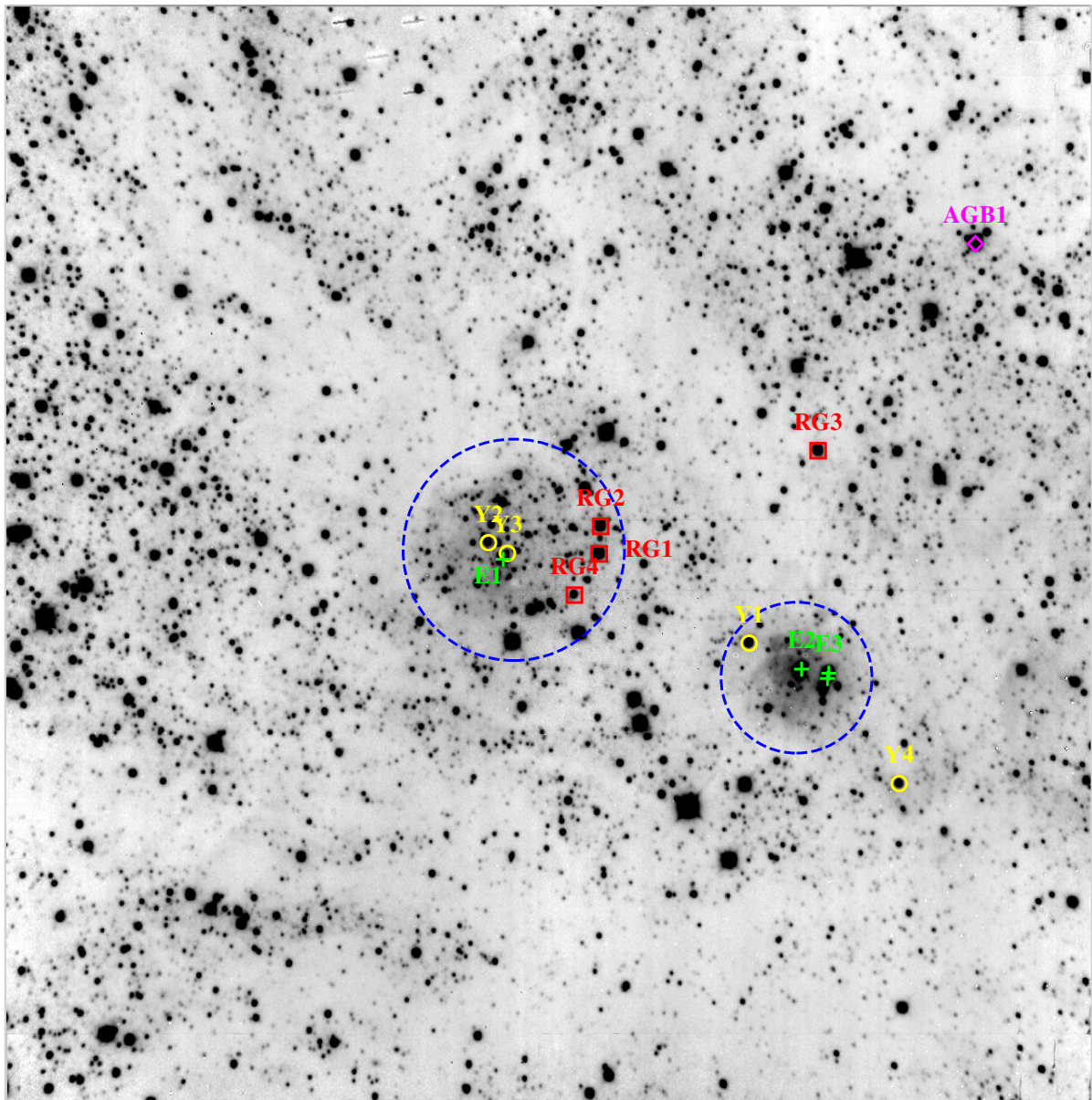
3.5 K-BAND SPECTROSCOPY

Spectroscopic observations were also performed on the 27th of June 2010. The typical seeing during the observations varied between $1''.2$ and $1''.6$. The spectroscopic targets were previously selected from the 2MASS point source catalog, by choosing the brightest stars. Our aim was to observe massive stars in the CN15/16/17 region and, by classifying their spectral type, infer the region's distance as well as the extinction towards those objects. To minimize foreground dwarf stars contamination, only candidates with $H - K_S > 0.3$ mag were kept in the list. In this way it was not possible to exclude contamination from field giants though. The latter can have similar photometric properties as more distant or more reddened main sequence massive stars. Five different slit positions were used. The positions were chosen in order to observe the 10 brightest stars in the region, but given the high degree of crowding, 11 more stars fell into the slits. For some of the additional 11 sources the spectra have too low signal-to-noise to extract any reliable information, though.

We used the spectroscopic mode of NTT/SofI in the following configuration: the third order of the HR Grism was adopted, with a dispersion of $4.63\ \text{\AA}/\text{pixel}$ in the $2.00\text{-}2.30\ \mu\text{m}$ wavelength range. We always used an $0''.6$ slit, resulting in a spectral resolution of 2200. In the chosen spectral range several lines that allow for spectral classification of early-type stars are present, such as Br γ (H I, $2.166\ \mu\text{m}$), and He I lines (2.059 , $2.113\ \mu\text{m}$). Other lines are present allowing for the classification of the late-type giants contaminants, such as Na I (2.206 , $2.209\ \mu\text{m}$) and Ca I (2.261 , 2.263 , $2.265\ \mu\text{m}$), as well as the CO absorption band at $2.3\ \mu\text{m}$.

For each slit multiple nodding cycles (NC) were observed. The slit was first put in position A and then shifted along its direction to position B. Taking the difference of the A and B positions efficiently removes the sky background. The number of NC was optimized, depending on the brightness of the sources, to obtain a signal-to-noise ratio (SNR) in the final spectra sufficient to perform spectral classification.

Figure 3.5: K_S band image of CN15/16/17. Superimposed are the positions of the stars with spectral classification. Green crosses are early-type stars, yellow circles are candidate YSOs, the magenta diamond is an AGB star, red squares are red giants. IDs correspond to the first column of Table 3.2. The two blue dashed circular regions are the areas corresponding to clusters DB10 (lower right, $21''$ -0.12 pc at 1200 pc- in radius) and DB11 (center, $32''$ -0.18 pc at 1200 pc- in radius).



Reduction was performed using the ESO `gasgano` pipeline. The pipeline applies flat-fielding and dark subtraction for each raw image. It also uses Xenon and Neon arc lamps images to correct for slit curvature. For each nodding cycle the (A-B) + (B-A) sky-subtracted images are obtained. The final step is the shift and sum of the 2*NC sky-subtracted images. Wavelength calibration was also done using the Xenon and Neon arcs.

To extract the spectra we used the IDL - `optspecextr` optimal extraction package². This software traces the spectra and extracts the signal using the algorithm of Horne (1986) to optimize the signal-to-noise ratio of the final spectrum.

Throughout the observing run we obtained spectra of late-B and early-A type reference stars in order to correct for telluric absorption in the atmosphere. These stars have the advantage of an almost featureless spectrum in the *K*-band. The positions of the standard stars were chosen to minimize the airmass difference with the CN15/16/17 targets. Telluric standard were observed about every 30 minutes in order to have similar atmospheric conditions between the standards and the targets. The only prominent feature in these early type telluric standard is their Bry photospheric absorption. Therefore the extracted standard star spectra were first corrected by removing the Bry line. This was accomplished using the IRAF/`splot` task, fitting a Voigt profile to the Bry line and subtracting the result of the fit from the spectrum. We then used the IRAF/`telluric` task to optimize the telluric correction. The spectrum of each target star was divided by the telluric standard star spectrum (with Bry subtracted). The `telluric` task allows iterative optimization of the atmospheric correction to compensate for slight variations in airmass and atmospheric conditions between the science target and the standard star observation. This is accomplished by scaling the amount of atmospheric absorption and shifting the spectrum in wavelength until a satisfactory correction is achieved.

The SNR per spectral resolution element required to achieve a good spectral classification was of the order of 100. Due to bad seeing conditions throughout the observing run, the achieved SNR is lower, ranging between 50 and 80 (depending on the stars). This leads to a more uncertain spectral classification than expected, with a typical uncertainty of ~ 2 spectral subclasses for the early type stars in our sample.

3.6 SPECTRAL CLASSIFICATION

The extracted and corrected spectra for which classification was possible are shown in Fig. 3.7. A total of four early B-type stars was identified and four YSOs candidates as well. The rest of

²The software is publicly available at:
<http://physics.ucf.edu/~jh/ast/software/optspecextr-0.3.1/doc/>

the classified stars are background giants. Among the latter four are classified as red giants and one as an asymptotic giant branch (AGB) star. The results of the classification procedure are summarized in Table 3.2, with the spectra displayed in Fig. 3.7. The positions of the classified star are marked in Fig. 3.5, superimposed on the SofI K_S band image of the region.

Classification of the early type stars was done by comparing our observed spectra with the medium resolution near infrared spectral atlas of O and Early-B Stars by Hanson et al. (2005), complemented using spectra by Bik et al. (2005). To compare these high quality spectra with our lower SNR, lower resolution ones in a sensible way we used the following procedure. We first convolved the atlas spectra with a Gaussian kernel with a σ equal to $4.6 \text{ \AA}/\text{pixel}$, i.e. the SofI wavelength dispersion in K band. In this way we put the atlas spectra on the same spectral resolution as the observed ones preserving the flux per unit wavelength. The following step consists in measuring the SNR in a featureless part of the observed spectrum and add noise to the atlas spectra until they reach a comparable SNR. A set of atlas spectra is shown in Fig. 3.6. Both the original and the degraded versions are shown, as well as the spectrum from our E1 source, classified as B0V-B2V star.

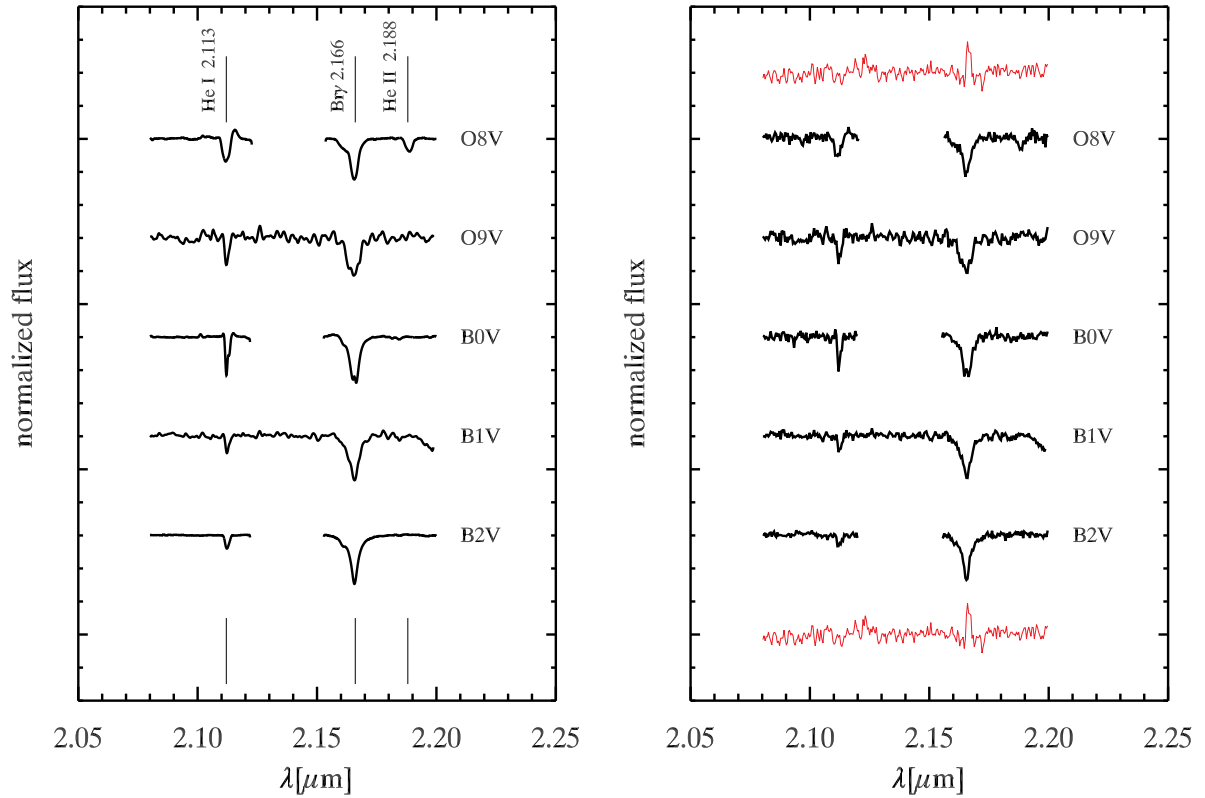
The spectral classification is then performed by visual comparison of the observed spectra with these degraded atlas spectra. The strength of the $\text{Br}\gamma$ absorption line and of several Helium lines in this spectral range ($\text{He I } 2.059 \mu\text{m}$, $2.113 \mu\text{m}$) is used to get the best match. The $\text{Br}\gamma$ lines of the early type stars inside DB10 and DB11 are contaminated by the nebular emission in $\text{Br}\gamma$ from the recombination of electrons and free protons. This emission, though, is quite narrow and does not affect the wings of the photospheric absorption $\text{Br}\gamma$ lines. Hence the absorption wings can still be used for spectral classification.

Given the estimated spectral type for the early-type stars, it is possible to obtain an estimate of their reddening and distance. This is accomplished by placing the star in the near infrared color magnitude diagram and by shifting its position along the reddening vector until it reaches the main sequence locus. The shift in color, assuming a reddening law, provides an estimate of the extinction. The additional vertical shift required to match the predicted magnitude for the given spectral type allows to estimate the distance to the object.

The results from the early type stars are all consistent with DB10 and DB11 being at a distance of $\sim 1 \text{ kpc}$. The total visual extinction for the only B star identified in DB11 (E1) is $A_V = 4.2 \text{ mag}$, while the 3 B stars identified in DB10 (E2, E3, E4) provide a slightly larger average value of the extinction of $A_V \sim 5.5 \text{ mag}$, consistent with DB10 being younger and more embedded.

The identified YSOs are characterized by featureless, red spectra (see Fig. 3.7). Some of them (Y2, Y3, Y4) show $\text{Br}\gamma$ emission and Y2 also shows He I emission at 2.059 and $2.113 \mu\text{m}$. This emission might come from the nebula, but might also come from the circumstellar material, similarly to Be stars (Clark & Steele 2000).

Figure 3.6: Atlas spectra for some representative spectral types. On the left the original spectra by Hanson et al. (2005) –O8V, B0V and B2V– and Bik et al. (2005) –O9V and B1V; on the right the degraded spectra used for comparison. The red lines show the spectrum for our source E1, classified as B0V-B2V.



For the classification of giants we used the atlas by Rayner et al. (2009). Given the similar resolution between our observations ($R = 2200$) and the spectra of this atlas ($R = 2000$) we did not degrade the spectra. We only classified them by direct comparison of the observable features, such as the CO absorption band at 2.3 μm and Na I (2.206, 2.209 μm) and Ca I (2.261, 2.263, 2.265 μm) absorption lines.

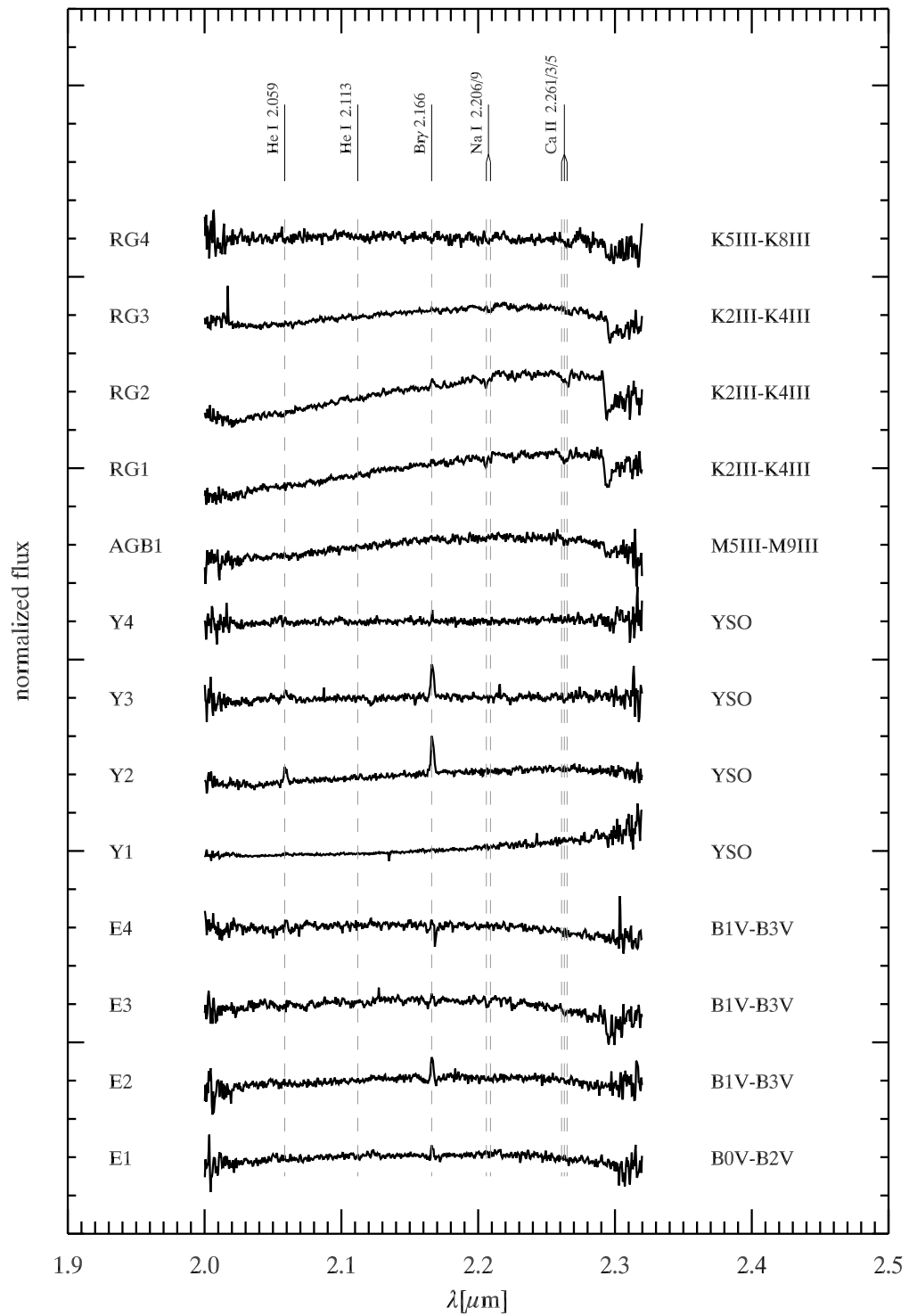
Figure 3.7: Spectra of the classified objects. The IDs correspond to the first column of Table 3.2.

Table 3.2: Spectral Types of the classified stars. For early type stars the inferred extinction and distances are indicated as well.

ID	R.A.(2000) h m s	Dec.(2000) o ' "	Spectral Type	K_S [mag]	$J - K_S$ [mag]	$H - K_S$ [mag]	A_V [mag]	A_{K_S} [mag]	Distance [kpc]
Early Type									
E1	17:50:24.03	-28:53:07.8	B0V – B2V	10.36	0.73	0.21	4.2 ± 0.1	0.47 ± 0.01	$1.06 - 2.77$
E2	17:50:17.53	-28:53:39.2	B1V – B3V	10.44	0.87	0.32	5.7 ± 0.1	0.64 ± 0.01	$0.83 - 1.40$
E3	17:50:16.94	-28:53:40.4	B1V – B3V	9.75	0.93	0.26	4.7 ± 0.1	0.53 ± 0.01	$0.63 - 1.07$
E4	17:50:16.97	-28:53:41.9	B5V – B9V	11.08	0.89	0.36	6.0 ± 0.1	0.67 ± 0.01	$0.67 - 0.94$
Young Stellar Objects									
Y1	17:50:18.68	-28:53:31.8	red spectrum	10.82	4.63	1.51	–	–	–
Y2	17:50:24.35	-28:53:03.1	B γ , He I 2.059, 2.113 μ m (all in emission)	11.70	2.46	1.31	–	–	–
Y3	17:50:23.94	-28:53:06.1	featureless, B γ emission	13.49	1.67	0.96	–	–	–
Y4	17:50:15.41	-28:54:11.9	featureless, B γ emission	11.48	0.97	0.36	–	–	–
Asymptotic giant branch									
AGB1	17:50:13.75	-28:51:38.0	M5 – M9 III	8.86	5.35	1.80	–	–	–
Red Giant Branch									
RG1	17:50:21.94	-28:53:06.3	K2 – K4 III	9.73	4.56	1.49	–	–	–
RG2	17:50:21.90	-28:52:58.5	K2 – K4 III	9.99	4.82	1.78	–	–	–
RG3	17:50:17.17	-28:52:37.0	K2 – K4 III	9.98	4.73	1.55	–	–	–
RG4	17:50:22.48	-28:53:18.0	K5 – K8 III	11.55	3.53	1.18	–	–	–

3.7 NEBULAR EMISSION

An additional constraint on the earliest possible spectral type for a star inside DB10 and DB11 can be obtained from the intensity of the diffuse nebular emission. Hanson et al. (2002) showed how the $\text{Br}\gamma$ and $\text{He I } 2.113 \mu\text{m}$ lines can be used to give constraints on the spectral type of the most massive ionizing source inside an H II region. The ratio of the fluxes of these two lines is indeed an indicator of the temperature of the ionizing source.

We measured the line fluxes in the nebulae of DB11 and DB10 using the portions of the 2D long-slit spectra, which correspond to the nebular regions. In order to obtain the maximum SNR and the best possible constraints on these two fluxes, we combined all the 5 slit positions for which we obtained spectra.

Since exposure times and observing conditions were different among the 5 slit positions, we first calibrated the 2D frames in flux. We used the spectra of the telluric standard that was observed immediately after or before the given slit. We integrated the measured counts convolved with the 2MASS K_s filter response curve, and used the available magnitude for the star to obtain an absolute calibration of the flux for the standard star. By dividing the 2D frames for this calibrated standard spectrum and adjusting for the different exposure times we obtained 2D flux calibrated frames.

After this step, the 5 slits could be used together to obtain the nebular flux. We identified in each 2D frame the spatial regions of diffuse $\text{Br}\gamma$ emission associated to either of DB10 and DB11. We extracted subarrays from the 2D image at those spatial positions and then summed all the flux together along the spatial direction. The summed fluxes for the 5 slits were in turn coadded to obtain the total nebular flux from the different slit positions.

The results are shown in Fig. 3.8 for both DB10 and DB11 nebular emission. In both cases no $\text{He I } 2.113$ emission is detected. Since no flux can be measured for this line, we put upper limits on what the flux could be, given the SNR of the spectra. According to Hanson et al. (2002) a $\text{He I } (2.113)/\text{Br}\gamma$ flux ratio between 1% and 3% would imply that some late-O type stars are in the cluster. Lower values of this ratio would imply that no O star is present.

In Fig. 3.8 we show what the peak value of $\text{He I } (2.113)$ would be in the case of a 1 and 3% flux ratio. This is done by simply scaling the clearly visible peak of the $\text{Br}\gamma$ line and assuming the same shape and FWHM for the two lines. Superimposed we also show the 1 and 3σ levels of the spectra above the continuum; σ is the standard deviation of the flux in some wavelength interval with respect to the average signal in that interval. The σ is measured in an adjacent featureless region of the spectrum. In both DB10 and DB11 a 3% flux ratio can be excluded at 1σ level. Given the large value of the noise, this value can not be excluded at a larger significance level. A

1% He I (2.113) flux could instead be still present and hidden in the noise at 1σ level.

Even though these findings do not put stronger constraints on the spectral type of the ionizing sources inside DB10 and DB11, they are consistent with the earliest type being early-B or at most late-O stars. Early-O stars are excluded.

3.8 INTEGRATED RADIO CONTINUUM FLUX

The radio flux from the two H II regions in the CN15/16/17 complex can be used to put additional constraints on the spectral type of the most luminous ionizing source. The amount of ionizing flux is a very steep function of the spectral type (Martins et al. 2005). Consequently, the total ionizing flux within an H II region is dominated by the hottest, earliest type star.

The free electrons inside the H II region interact with the ions producing Bremsstrahlung radiation. This free-free radiation flux, measured at a given wavelength, can be converted into an ionizing flux. Assuming that each energetic photon ionizes an atom (no leakage), assuming that the nebula is optically thin for free-free continuum emission and assuming that ionization and recombination are in equilibrium, the amount of energetic photons and radio continuum emission can be related to each other.

The values of the integrated radio flux at 1.4 GHz are taken from the NVSS catalog (Condon et al. 1998). The ultra compact H II region is the brightest radio emitter with a flux of 657 mJy, while the flux of the H II region associated with DB11 is 572 mJy. The observed radio flux has first to be converted into an emitted flux by multiplying it with $4\pi d^2$. We estimate an average distance to the region using the spectro-photometric distances from our spectral classification. We considered the central value of the distance interval for each of the 4 classified early-B stars and obtained $d = 1.2 \pm 0.5$ kpc. The quoted uncertainty is the standard deviation of the 4 central values.

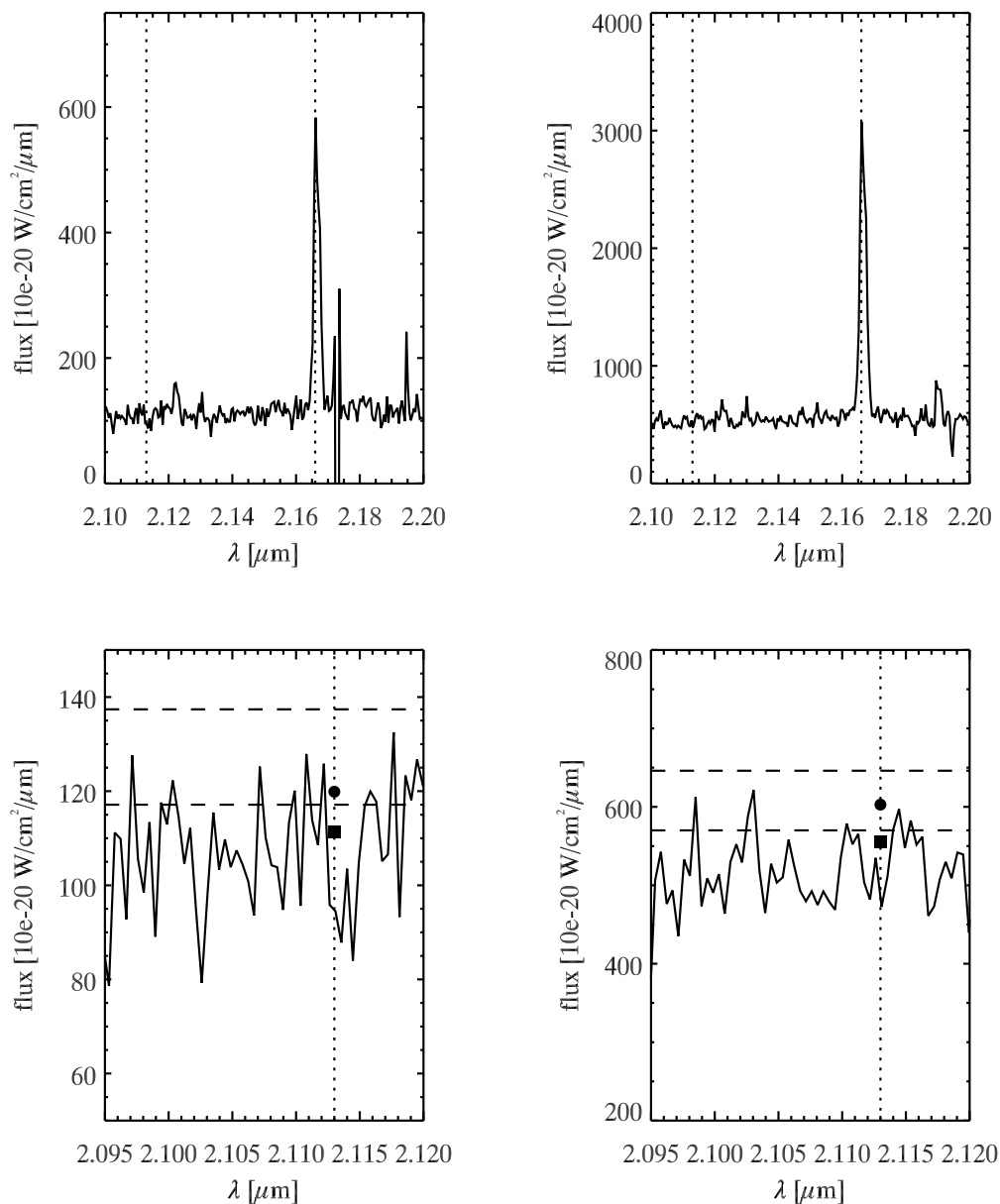
We used the relations by Kurtz et al. (1994) to obtain an estimate of the ionizing fluxes. Given the uncertainty on the distance we obtain:

$$\log Q_0^{\text{DB11}}[\text{photons s}^{-1}] = 46.8_{-0.5}^{+0.3} \quad \text{and} \quad \log Q_0^{\text{UCHII}}[\text{photons s}^{-1}] = 46.9_{-0.5}^{+0.3}$$

where the flux Q_0 is the number of photons with $\lambda < 912 \text{ \AA}$ emitted per second.

From these values, using the calibration by Martins et al. (2005) we derived an upper limit for the spectral types of the ionizing sources inside the DB11 and the Ultra Compact H II region. Depending on the T_{eff} scale adopted, the flux expected from the latest spectral type available in Martins et al. (2005) -an O9.5V- varies between $\log Q_0 \sim 47.56$ and $\log Q_0 \sim 47.88$. The fluxes

Figure 3.8: Spectra of the diffuse nebulae in the DB10 (left) and DB11 (right) regions. The position of Br γ and He I 2.113 line are marked by vertical dotted lines. The lower panels are a zoomed-in version centered at the position of the He I 2.113 line. The horizontal dashed lines represent 1 and 3 σ levels above the continuum. The squares and the circles represent the expected peak values of the He I 2.113 line in the case of a 1% and 3% He I/Br γ flux ratio, respectively.



we obtain are below these values and hence are consistent with the earliest type of our classified stars being early-B.

3.9 DB10 AND DB11 CLUSTERS

In this section we will focus on the two clusters in the region, DB10 -more embedded and compact- and DB11 -less embedded, more extended. We consider two circular regions as the clusters areas. DB10 is centered at $(\text{RA}, \text{Dec})_{\text{J2000}} = (17^{\text{h}}50^{\text{m}}17^{\text{s}}.64, -28^{\circ}53'41''.6)$, $(l, b)_{\text{gal}} = (0.564, -0.854)$, with a visual radius of $21''$. Object DB11 is centered at $(\text{RA}, \text{Dec})_{\text{J2000}} = (17^{\text{h}}50^{\text{m}}23^{\text{s}}.79, -28^{\circ}53'05''.1)$, $(l, b)_{\text{gal}} = (0.584, -0.868)$, with a visual radius of $32''$. These areas correspond to the diffuse nebulosity areas visible in the K_S band image. At a distance of 1200 pc the radii of the clusters are ~ 0.12 pc and ~ 0.18 pc for DB10 and DB11 respectively. The two circular regions are marked in Fig. 3.5.

The near infrared color-magnitude and color-color diagrams for the two clusters are shown in Fig. 3.9. Overplotted is a 1 Myr isochrone by Marigo et al. (2008). We have chosen this value of the age based on the presence of the molecular material in the surrounding bubble. This material is going to be removed by the massive stars with their winds and radiation pressure. A slightly older age, up to few Myr might still be possible but we consider 1 Myr as a typical value. A more precise age determination can be obtained with deeper and higher angular resolution images revealing the pre main sequence population.

We adopted the average value of the spectro-photometric distance obtained from the classified B stars, $d = 1.2$ kpc. Extinction from the same spectra was used. In the DB10 case we used the average extinction of stars E2, E3, E4, $A_V = 5.5$ mag ($A_J = 1.54$ mag, $A_H = 0.96$ mag and $A_{K_S} = 0.61$ mag). For DB11 we adopted the value from E1, $A_V = 4.2$ mag ($A_J = 1.18$ mag, $A_H = 0.74$ mag and $A_{K_S} = 0.47$ mag). Extinction in the near-infrared bands was derived using Rieke & Lebofsky (1985) extinction law. Spectral types from Martins & Plez (2006) for O stars and Kenyon & Hartmann (1995) for later type stars are shown.

The big squares indicate the magnitudes of the classified objects, with early-type stars in black, YSOs in green and red giants in red. The bright nebulosity in the DB10 area hampers the detection of faint K_S -band sources. Hence the diagrams appear quite empty in redder areas. In the DB11 region the nebulosity is less bright; as a consequence fainter (and redder) sources can be seen in the diagram.

The classified B stars nicely follow the 1 Myr isochrone. Moreover their magnitudes are in agreement with the magnitudes expected for their spectral type at 1200 pc, with the adopted extinction values.

The spectroscopically identified YSOs appear redder than the main sequence locus in both K_S vs $J - K_S$ and K_S vs $H - K_S$ diagrams. From the color-color diagram, in the case of DB11, it is clear that the redder YSO colors are not due to extinction but are related to near infrared excess from the circumstellar material. In this diagram the two DB11 YSOs (Y2, Y3) are indeed located below the reddening sequence. The YSO Y2 is identified in the GLIMPSE II catalog as well. With its colors of $[5.8]-[8.0] = 1.01$ mag and $[3.6]-[4.5] = 0.69$ mag it is indeed one of the objects identified as class II YSO in the IRAC color-color diagram of Fig. 3.3 In the DB11 diagrams Y2 is the reddest ($J - K_S = 2.47$ mag) of the two marked YSOs. The YSO in DB10 (Y1) does not show the same near infrared excess. This object might indeed be more embedded as it appears from the high extinction in the color-color diagram. Unfortunately we could not find a match for this source in the GLIMPSE II catalog, but the very red and featureless spectrum indicates a class I type.

The three red giants classified in the DB11 area (RG1, RG2, RG4) all appear to be very reddened background sources, most likely in the Galactic Bulge.

The cluster DB11 was already studied in Dutra et al. (2003b) without the help of spectroscopy and with very different results. After performing statistical field subtraction, the authors identified a much redder main sequence for the region, with $H - K_S \sim 1.12$ mag. Fitting this sequence they derived an A_V of 15 mag ($A_{K_S} = 1.68$ mag). Our classified B star in DB11 (E1) shows a much bluer $H - K_S$ color of 0.21 mag and a much lower extinction $A_V = 4.6$ mag ($A_{K_S} = 0.47$). Three of our classified objects lie in the region $H - K_S \sim 1.12$. One of them is a red giant and the other two are the Y2 and Y3 YSOs. The presence of the first is an indication that this part of the DB11 color magnitude diagram is contaminated by red giants. Moreover the color-color diagram shows how the two YSOs clearly have a K_S band excess, being displaced from the main sequence by ~ 0.6 mag. If the main sequence of DB11 in the K_S vs $H - K_S$ diagram was indeed at $H - K_S \sim 1.12$ mag we would expect the two YSOs to be ~ 0.6 mag redder than what they are.

Assuming that the 10th brightest star of the cluster was a B0V star, Dutra et al. (2003b) derived a distance to the cluster of 7.6 kpc. This scenario was corroborated by the value of the kinematic distance for the associated H II region. Kuchar & Clark (1997) estimated a velocity along the line of sight of 15 km/s. This value of the velocity can be translated into a distance once a model of the Galactic Rotation curve is adopted. Given the line of sight for this region -very close to the Galactic Center- a very small radial velocity is expected for all orbits but those very close to the Galactic center. The derived kinematic distances are indeed 7.5 kpc (near) and 9.5 kpc (far) using the Galactic rotation model by Brand & Blitz (1993) with a distance of the Sun from the Galactic Center $R_0 = 8.5$ kpc and an orbital velocity at R_0 , $\theta = 220$ km s⁻¹. Such a value is very uncertain though. For objects that are moving almost perpendicular to the line of sight, the peculiar orbital motions and the internal motion of the HII region can dominated the value of the line of sight velocity.

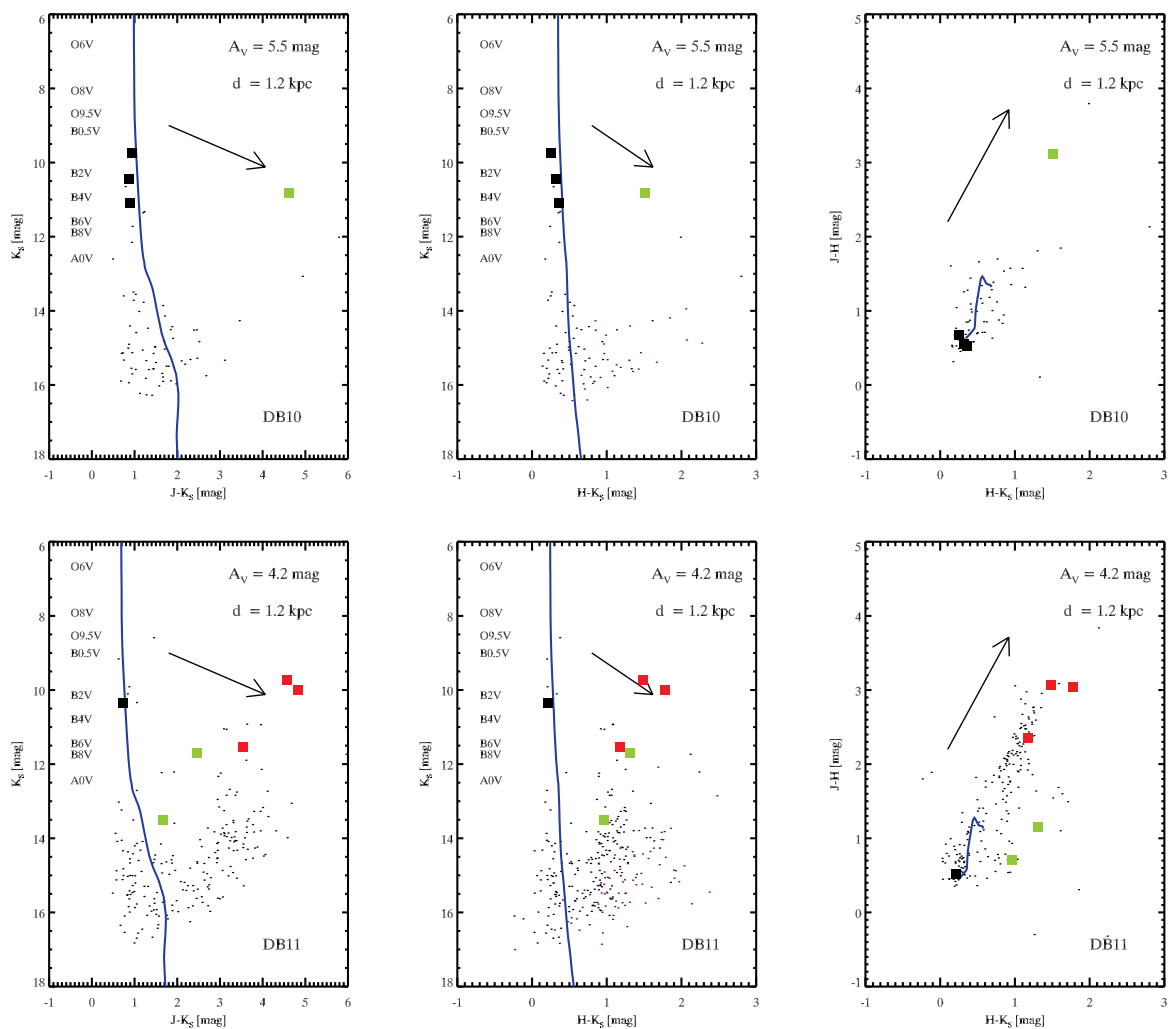
Our spectroscopic observations rule out this proposed distance for the cluster. We argue that the observed sequence of Dutra et al. (2003b) is an artifact of the subtraction technique. In order to decontaminate the color magnitude diagram from background stars, a region of the sky close enough and with similar extinction has to be used. Unfortunately, when looking towards the Galactic center, the extinction pattern might be very patchy and strong differences can be observed between adjacent areas (see e.g. Habibi et al. 2011). This is also the case for the CN15/16/17 region where, as visible in Fig. 3.4, local concentration of cold dust correspond to large values of extinction. The area centered on DB11 has been cleared of the molecular material by the early-type stars with their winds. This material accumulates in the rims of the bubble, but not directly at the cluster position; as a consequence extinction is smaller in the cluster's area. Therefore it might be possible that a larger fraction of background stars is visible along the DB11 line of sight, when compared to the neighboring regions used by Dutra et al. (2003b) for statistical field subtraction.

If the 10-th most massive star of the cluster would have been of B0V type -as proposed by Dutra et al. (2003b) and in agreement with the kinematic distance to the cluster of 7.5 kpc- the presence of several O stars would be expected. We ruled this out by showing that both the nebular emission and the radio flux are consistent with the brightest stars being B-type. In our target selection for spectroscopy we have chosen the brightest stars in the region and identified them as early B stars. We might have missed some earlier-type stars, for example because they might be more extinguished and appear fainter. In this case though the diffuse emission and the radio data would not have been consistent with DB11 hosting at most early-B or very late-O stars and being at a distance of 1.2 kpc. A distance of 7.5 kpc would imply the presence of early O stars, whose presence we should have been able to detect by a much larger HeI nebular emission at $2.113 \mu\text{m}$.

Assuming that we identified the most massive star in DB10 (B1V, $\sim 12M_{\odot}$) and DB11 (B0V, $\sim 15M_{\odot}$) and using the relation between the mass of the most massive star in a cluster and its total mass by Larson (2003), we can give an estimate of the clusters masses. We obtain $M_{\text{DB10}} \approx 170M_{\odot}$ and $M_{\text{DB11}} \approx 275M_{\odot}$, both comparable to the mass of the σ Ori cluster in the Orion OB1b association, $M_{\sigma\text{Ori}} \approx 225 \pm 30M_{\odot}$ (Sherry et al. 2004).

Considering this collection of evidence from multiple wavelength regimes, a qualitative picture of the star formation history of the region can be traced. The central object -DB11- is the oldest star formation site, followed by the younger DB10 and the youngest Ultra Compact H II region. Star formation is proceeding sequentially from DB11 towards the south-west direction. This is corroborated by the presence of the cold dust arc in the south west, which is associated, in turn, with the most populous group of YSOs of the region. In addition two small sub-groups of YSOs are visible in the north and north-west, again associated with cold dust emission. These two smaller concentrations are at a similar projected distance from DB11 as the south-west arc. All the evidence is highly suggestive that star formation may have been initiated in DB11 and is

Figure 3.9: Color-magnitude and color-color diagrams for DB10 (top) and DB11 (bottom). In blue a 1 Myr isochrone from Marigo et al. (2008). Spectral types from Martins & Plez (2006) -for O stars- and Kenyon & Hartmann (1995) -for later type stars are shown. Big squares are the classified stars, early type in black, YSOs in green, red giants in red. The arrows indicate the direction of the reddening vector; their length corresponds to $A_V = 10$ mag.



proceeding outwards in all directions.

3.10 CONCLUSIONS

We performed a multiple wavelength study of the young star forming region CN15/16/17, projected towards the Galactic Center. We derived a consistent picture of the region combining near infrared spectroscopy, near and mid infrared photometry, sub-mm continuum emission and radio integrated fluxes.

The region hosts two near-infrared clusters (DB10 and DB11, visible in the SofI images) and one loose association of YSOs identified in the GLIMPSE-II point-sources catalog. The DB11 cluster is associated with an H II region visible in the NVSS radio continuum maps. An other H II region is also visible, associated to a small group of very embedded mid infrared bright sources.

From ATLASGAL sub-mm contours we identify an arc-like structure in the south-west part of the region. This arc of cold, dense material is associated with the southern group of YSOs.

We propose a scenario in which star formation has been initiated in the central cluster DB11 and is proceeding towards the outer parts of the complex. A sequence in age between DB11, DB10, the ultra compact H II region and the YSOs-cold arc can be depicted. Further investigation is required to understand whether the younger events have been triggered by the older or not.

Thanks to spectroscopic characterization of the brightest members of the DB10 and DB11 clusters, we obtained a spectro-photometric distance to the region as well as the extinction value towards the clusters. We found that the region is at $d = 1.2 \pm 0.5$ kpc, i.e. much closer than previously thought when only H and K_S photometry was used for the analysis of the DB11 cluster. We estimate the stellar cluster masses to be $M_{\text{DB10}} \approx 170M_{\odot}$ and $M_{\text{DB11}} \approx 275M_{\odot}$.

This work confirms the importance of a multi-wavelength approach and the power of a combination of imaging and spectroscopy in order to obtain a complete analysis of young star forming regions.

SUMMARY AND FUTURE WORK

Throughout this work we followed a path aiming to reach a better understanding of massive stellar clusters. The role of stellar evolutionary models in deriving the properties of clusters' members and a proper treatment of observational and theoretical uncertainties have been the major focuses of the Thesis.

In Chap. 1 I have used very precise data to test the ability of the current generation of pre-main sequence models in reproducing the observed properties of young stars. The adopted Pisa models show a good overall agreement with the observations, especially when data from eclipsing binaries are used. The agreement gets progressively worse for astrometric binaries and stars whose masses are derived from their circumstellar disk kinematics. I have discussed how the observational uncertainties become more severe for the latter objects, making the comparison less conclusive. Moreover, I have shown the caveats in the use of stellar models for deriving precise quantities such as stellar masses and ages. The systematic effects due to the poor knowledge of stellar metallicity and helium content, the uncertainties on the solar chemical composition and on the treatment of superadiabatic convection have been critically discussed.

I am currently working on applying the Bayesian method of Chap. 1 on a totally different case. I am using a similar approach and Pisa models to constrain the masses of a unique eclipsing binary system observed in the Large Magellanic Cloud. This system hosts a Cepheid and a slightly more evolved star that has recently evolved away from the Cepheid instability strip (Pietrzyński et al. 2010). This binary, with precisely determined dynamical masses, offers a great opportunity to study the discrepancy problem between the Cepheids' pulsational and evolutionary mass. Moreover it will help constraining the role of core overshooting in intermediate-mass stars.

In Chap. 2 I have presented a thorough analysis of near infrared photometric data of the massive

cluster Westerlund 1, the most massive young cluster in the Milky Way. The results on the cluster's morphology and on its mass segregation status pose interesting question to be explored by stellar cluster theorist. The strong elongation of Westerlund 1 is a very interesting finding and a puzzle for stellar dynamics studies.

We are continuing our efforts to understand Westerlund 1 peculiarities from both the observational and the theoretical point of view. The cluster has been recently observed using the Hubble WFC3 and analysis is currently ongoing (Andersen 2008). I contribute to this study. I am also trying to obtain a more quantitative estimate of the mass segregation status of Westerlund 1. I am currently building a more complete catalog, combining our near-infrared data with optical photometry of the bright stars, which are saturated in the near infrared images. Mass segregation will be quantified using the minimum spanning tree algorithm (Allison et al. 2009b; Olczak et al. 2011).

In Chap. 3 I have presented a study of a young star forming region: the complex of molecular bubbles CN15/16/17. This study, in which I derived the first spectro-photometric distance estimate to the region, shows the importance of combining spectroscopy and photometry to fully understand the properties of star forming environments.

I obtained new data for this region within a larger program aimed at studying several cluster candidates in the Milky Way. After this prototypical example, I intend to continue with the analysis of the data for 10 additional regions I observed with the SofI/NTT instrument.

BIBLIOGRAPHY

- Alecian, E., Catala, C., van't Veer-Menneret, C., Goupil, M.-J., & Balona, L. 2005, *A&A*, 442, 993
- Alecian, E., Goupil, M., Lebreton, Y., Dupret, M., & Catala, C. 2007a, *A&A*, 465, 241
- Alecian, E., Lebreton, Y., Goupil, M.-J., Dupret, M.-A., & Catala, C. 2007b, *A&A*, 473, 181
- Allen, L., et al. 2007, B. Reipurth, D. Jewitt, K. Keil, eds., *Protostars and Planets V* University of Arizona Press, Tucson, 361
- Allen, L. E., et al. 2004, *ApJS*, 154, 363
- Aller, L. H., et al., eds. 1982, *Landolt-Börnstein: Numerical Data and Functional Relationships in Science and Technology - New Series* "Gruppe/Group 6 Astronomy and Astrophysics" Volume 2 Schaifers/Voigt: *Astronomy and Astrophysics / Astronomie und Astrophysik* "Stars and Star Clusters / Sterne und Sternhaufen
- Allison, R. J., Goodwin, S. P., Parker, R. J., de Grijs, R., Portegies Zwart, S. F., & Kouwenhoven, M. B. N. 2009a, *ApJ*, 700, L99
- Allison, R. J., Goodwin, S. P., Parker, R. J., Portegies Zwart, S. F., & de Grijs, R. 2010, *MNRAS*, 407, 1098
- Allison, R. J., Goodwin, S. P., Parker, R. J., Portegies Zwart, S. F., de Grijs, R., & Kouwenhoven, M. B. N. 2009b, *MNRAS*, 395, 1449
- Alvarez, C., Feldt, M., Henning, T., Puga, E., Brandner, W., & Stecklum, B. 2004, *ApJS*, 155, 123
- Andersen, J. 1975, *A&A*, 44, 445
- . 1991, *A&A Rev.*, 3, 91
- Andersen, M. 2008, in *HST Proposal*, 11708
- Andersen, M., Zinnecker, H., Moneti, A., McCaughrean, M. J., Brandl, B., Brandner, W., Mey-

- Ian, G., & Hunter, D. 2009, *ApJ*, 707, 1347
- Andrae, R. 2010, *ArXiv:1009.2755v3*
- Angulo, C., et al. 1999, *Nuclear Physics A*, 656, 3
- Arnaboldi, M., Neeser, M. J., Parker, L. C., Rosati, P., Lombardi, M., Dietrich, J. P., & Hummel, W. 2007, *The Messenger*, 127, 28
- Asplund, M., Grevesse, N., & Sauval, A. J. 2005, in *Astronomical Society of the Pacific Conference Series*, Vol. 336, *Cosmic Abundances as Records of Stellar Evolution and Nucleosynthesis*, ed. T. G. Barnes, III & F. N. Bash, 25
- Asplund, M., Grevesse, N., Sauval, A. J., & Scott, P. 2009, *ARA&A*, 47, 481
- Bailer-Jones, C. A. L. 2011, *MNRAS*, 993
- Ballesteros-Paredes, J., Gómez, G. C., Pichardo, B., & Vázquez-Semadeni, E. 2009, *MNRAS*, 393, 1563
- Baraffe, I., Chabrier, G., Allard, F., & Hauschildt, P. H. 1998, *A&A*, 337, 403
- . 2002, *A&A*, 382, 563
- Baraffe, I., Chabrier, G., & Gallardo, J. 2009, *ApJ*, 702, L27
- Bastian, N., Covey, K. R., & Meyer, M. R. 2010, *ARA&A*, 48, 339
- Basu, S., & Antia, H. M. 2008, *Phys. Rep.*, 457, 217
- Bate, M. R. 2009, *MNRAS*, 392, 590
- Benjamin, R. A., et al. 2003, *PASP*, 115, 953
- Bica, E., Dutra, C. M., Soares, J., & Barbuy, B. 2003, *A&A*, 404, 223
- Bik, A., Kaper, L., Hanson, M. M., & Smits, M. 2005, *A&A*, 440, 121
- Binney, J., & Tremaine, S. 1987, *Galactic dynamics*, Princeton University Press, Princeton
- Boden, A. F., et al. 2005, *ApJ*, 635, 442
- . 2007, *ApJ*, 670, 1214
- Böhm-Vitense, E. 1958, *Zeitschrift für Astrophysik*, 46, 108
- Bonnell, I. A., & Davies, M. B. 1998, *MNRAS*, 295, 691
- Bonnell, I. A., Smith, R. J., Clark, P. C., & Bate, M. R. 2011, *MNRAS*, 410, 2339
- Borissova, J., et al. 2011, *A&A*, 532, A131
- Brand, J., & Blitz, L. 1993, *A&A*, 275, 67
- Brandner, W., Clark, J. S., Stolte, A., Waters, R., Negueruela, I., & Goodwin, S. P. 2008, *A&A*, 478, 137
- Brott, I., & Hauschildt, P. H. 2005, in *ESA Special Publication*, Vol. 576, *The Three-Dimensional Universe with Gaia*, ed. C. Turon, K. S. O’Flaherty, & M. A. C. Perryman, 565
- Campbell, M. A., Evans, C. J., Mackey, A. D., Gieles, M., Alves, J., Ascenso, J., Bastian, N., & Longmore, A. J. 2010, *MNRAS*, 405, 421

- Carigi, L., & Peimbert, M. 2008, *RMXAA*, 44, 341
- Casagrande, L., Flynn, C., Portinari, L., Girardi, L., & Jimenez, R. 2007, *MNRAS*, 382, 1516
- Casey, B. W., Mathieu, R. D., Vaz, L. P. R., Andersen, J., & Suntzeff, N. B. 1998, *AJ*, 115, 1617
- Castelli, F., & Kurucz, R. L. 2003, in *IAU Symposium*, Vol. 210, *Modelling of Stellar Atmospheres*, ed. N. Piskunov, W. W. Weiss, & D. F. Gray, 20
- Chauvin, G., et al. 2003, *A&A*, 406, L51
- Churchwell, E., et al. 2006, *ApJ*, 649, 759
- . 2007, *ApJ*, 670, 428
- . 2009, *PASP*, 121, 213
- Cignoni, M., Tosi, M., Sabbi, E., Nota, A., Degl’Innocenti, S., Prada Moroni, P. G., & Gallagher, J. S. 2010, *ApJ*, 712, L63
- Cignoni, M., et al. 2009, *AJ*, 137, 3668
- Claret, A. 2006, *A&A*, 445, 1061
- Clark, J. S., Negueruela, I., Crowther, P. A., & Goodwin, S. P. 2005, *A&A*, 434, 949
- Clark, J. S., & Steele, I. A. 2000, *A&AS*, 141, 65
- Clark, J. S., et al. 2009, *A&A*, 498, 109
- Condon, J. J., Cotton, W. D., Greisen, E. W., Yin, Q. F., Perley, R. A., Taylor, G. B., & Broderick, J. J. 1998, *AJ*, 115, 1693
- Covino, E., Frasca, A., Alcalá, J. M., Paladino, R., & Sterzik, M. F. 2004, *A&A*, 427, 637
- Covino, E., et al. 2000, *A&A*, 361, L49
- Cox, J. P., & Giuli, R. T. 1968, *Principles of stellar structure*, Gordon and Breach, New York
- Crowther, P. A., Hadfield, L. J., Clark, J. S., Negueruela, I., & Vacca, W. D. 2006, *MNRAS*, 372, 1407
- Cusano, F., Guenther, E. W., Esposito, M., & Gandolfi, D. 2010, in *Revista Mexicana de Astronomía y Astrofísica*, vol. 27, Vol. 38, *Revista Mexicana de Astronomía y Astrofísica Conference Series*, 34–34
- Cybert, R. H., Fields, B. D., & Olive, K. A. 2004, *Phys. Rev. D*, 69, 123519
- D’Antona, F., & Montalbán, J. 2003, *A&A*, 412, 213
- D’Antona, F., Ventura, P., & Mazzitelli, I. 2000, *ApJ*, 543, L77
- Davies, B., Figer, D. F., Kudritzki, R.-P., MacKenty, J., Najarro, F., & Herrero, A. 2007, *ApJ*, 671, 781
- de la Fuente Marcos, R., & de la Fuente Marcos, C. 2008, *ApJ*, 672, 342
- . 2010, *ApJ*, 719, 104
- Degl’Innocenti, S., Prada Moroni, P. G., Marconi, M., & Ruoppo, A. 2008, *Ap&SS*, 316, 25
- Devillard, N. 2001, in *Astronomical Society of the Pacific Conference Series*, Vol. 238, As-

- tronomical Data Analysis Software and Systems X., ed. F. R. Harnden Jr., F. A. Primini, & H. E. Payne, 525
- D’Orazi, V., Biazzo, K., & Randich, S. 2011, *A&A*, 526, A103
- D’Orazi, V., Randich, S., Flaccomio, E., Palla, F., Sacco, G. G., & Pallavicini, R. 2009, *A&A*, 501, 973
- Dunkley, J., et al. 2009, *ApJS*, 180, 306
- Dutra, C. M., & Bica, E. 2000, *A&A*, 359, L9
- Dutra, C. M., Bica, E., Soares, J., & Barbuy, B. 2003a, *A&A*, 400, 533
- Dutra, C. M., Ortolani, S., Bica, E., Barbuy, B., Zoccali, M., & Momany, Y. 2003b, *A&A*, 408, 127
- Dutrey, A., Guilloteau, S., & Simon, M. 2003, *A&A*, 402, 1003
- Efron, B. 1979, *Ann. Statist.*, 7, 1
- Eisenhauer, F., Quirrenbach, A., Zinnecker, H., & Genzel, R. 1998, *ApJ*, 498, 278
- Elmegreen, B. G. 2009, in *Globular Clusters - Guides to Galaxies*, ed. Richtler, T. & Larsen, S., 87
- Elson, R. A. W., Fall, S. M., & Freeman, K. C. 1987, *ApJ*, 323, 54
- Epchtein, N., et al. 1999, *A&A*, 349, 236
- Espinoza, P., Selman, F. J., & Melnick, J. 2009, *A&A*, 501, 563
- Feldt, M., Stecklum, B., Henning, T., Launhardt, R., & Hayward, T. L. 1999, *A&A*, 346, 243
- Ferguson, J. W., Alexander, D. R., Allard, F., Barman, T., Bodnarik, J. G., Hauschildt, P. H., Heffner-Wong, A., & Tamanai, A. 2005, *ApJ*, 623, 585
- Figer, D. F., Kim, S. S., Morris, M., Serabyn, E., Rich, R. M., & McLean, I. S. 1999, *ApJ*, 525, 750
- Figer, D. F., MacKenty, J. W., Robberto, M., Smith, K., Najarro, F., Kudritzki, R. P., & Herrero, A. 2006, *ApJ*, 643, 1166
- Fleck, J., Boily, C. M., Lançon, A., & Deiters, S. 2006, *MNRAS*, 369, 1392
- Flynn, C. 2004, *PASA*, 21, 126
- Gennaro, M., Brandner, W., Stolte, A., & Henning, T. 2011a, *MNRAS*, 412, 2469
- Gennaro, M., Prada Moroni, P. G., & Degl’Innocenti, S. 2010, *A&A*, 518, A13
- Gennaro, M., Prada Moroni, P. G., & Tognelli, E. 2011b, accepted for publication in *MNRAS*; arXiv:1110.0852
- Gerhard, O. 2001, *ApJ*, 546, L39
- Gieles, M., Baumgardt, H., Heggie, D. C., & Lamers, H. J. G. L. M. 2010a, *MNRAS*, 408, L16
- Gieles, M., Heggie, D. C., & Zhao, H. 2011, *MNRAS*, 413, 2509
- Gieles, M., Sana, H., & Portegies Zwart, S. F. 2010b, *MNRAS*, 402, 1750

- Gouliermis, D. A., Bestenlehner, J. M., Brandner, W., & Henning, T. 2010, *A&A*, 515, A56
- Grevesse, N., & Sauval, A. J. 1998, *Space Sci. Rev.*, 85, 161
- Gürkan, M. A., Freitag, M., & Rasio, F. A. 2004, *ApJ*, 604, 632
- Gutermuth, R. A., Megeath, S. T., Pipher, J. L., Williams, J. P., Allen, L. E., Myers, P. C., & Raines, S. N. 2005, *ApJ*, 632, 397
- Habibi, M., Stolte, A., Brandner, W., & Hußmann, B. 2011, The extinction map of the Arches starburst cluster in the Galactic Center. Presented at the conference: Stellar clusters and associations - A RIA workshop on Gaia, Granada, Spain. In press.
- Hanson, M. M., Kudritzki, R.-P., Kenworthy, M. A., Puls, J., & Tokunaga, A. T. 2005, *ApJS*, 161, 154
- Hanson, M. M., Luhman, K. L., & Rieke, G. H. 2002, *ApJS*, 138, 35
- Harayama, Y., Eisenhauer, F., & Martins, F. 2008, *ApJ*, 675, 1319
- Hastie, T., Tibshirani, R., & Friedman, J. 2009, *The Elements of Statistical Learning: Data Mining, Inference, and Prediction*, Springer Science+Business Media, New York
- Hayashi, C., & Nakano, T. 1965, *Progress of Theoretical Physics*, 34, 754
- Henning, T., Feldt, M., Stecklum, B., & Klein, R. 2001, *A&A*, 370, 100
- Hillenbrand, L., Mamajek, E., Stauffer, J., Soderblom, D., Carpenter, J., & Meyer, M. 2009, in *American Institute of Physics Conference Series*, Vol. 1094, American Institute of Physics Conference Series, ed. E. Stempels, 800–803
- Hillenbrand, L. A., & Hartmann, L. W. 1998, *ApJ*, 492, 540
- Hillenbrand, L. A., & White, R. J. 2004, *ApJ*, 604, 741
- Holmberg, J., Nordström, B., & Andersen, J. 2007, *A&A*, 475, 519
- . 2009, *A&A*, 501, 941
- Horne, K. 1986, *PASP*, 98, 609
- Hosokawa, T., Offner, S. S. R., & Krumholz, M. R. 2011, *ApJ*, 738, 140
- Hußmann, B., Stolte, A., Brandner, W., & Gennaro, M. 2011, *ArXiv:1108.4331*
- Iglesias, C. A., & Rogers, F. J. 1996, *ApJ*, 464, 943
- Imbriani, G., et al. 2005, *European Physical Journal A*, 25, 455
- Ivanov, V. D., Borissova, J., Pessev, P., Ivanov, G. R., & Kurtev, R. 2002, *A&A*, 394, L1
- Izotov, Y. I., Thuan, T. X., & Stasińska, G. 2007, *ApJ*, 662, 15
- Jappsen, A.-K., Mac Low, M.-M., Glover, S. C. O., Klessen, R. S., & Kitsionas, S. 2009, *ApJ*, 694, 1161
- Jimenez, R., Flynn, C., MacDonald, J., & Gibson, B. K. 2003, *Science*, 299, 1552
- Johns-Krull, C. M., Valenti, J. A., & Koresko, C. 1999, *ApJ*, 516, 900
- Jones, D. H. P. 1969, *MNSSA*, 28, 5

- Jørgensen, B. R., & Lindegren, L. 2005, *A&A*, 436, 127
- Kass, R., & Raftery, A. 1995, *Journal of the American Statistical Association*, 90, 773
- Kenyon, S. J., & Hartmann, L. 1995, *ApJS*, 101, 117
- Kim, S. S., Figer, D. F., Kudritzki, R. P., & Najarro, F. 2006, *ApJ*, 653, L113
- Koposov, S. E., Glushkova, E. V., & Zolotukhin, I. Y. 2008, *A&A*, 486, 771
- Kothes, R., & Dougherty, S. M. 2007, *A&A*, 468, 993
- Kouwenhoven, M. B. N., & de Grijs, R. 2008, *A&A*, 480, 103
- Kraus, A. L., & Hillenbrand, L. A. 2009, *ApJ*, 704, 531
- Kroupa, P. 2001, *MNRAS*, 322, 231
- Kuchar, T. A., & Clark, F. O. 1997, *ApJ*, 488, 224
- Kurtz, S., Churchwell, E., & Wood, D. O. S. 1994, *ApJS*, 91, 659
- Lada, C. J., & Lada, E. A. 2003, *ARA&A*, 41, 57
- Larson, R. B. 1995, *MNRAS*, 272, 213
- Larson, R. B. 2003, in *Astronomical Society of the Pacific Conference Series*, Vol. 287, *Galactic Star Formation Across the Stellar Mass Spectrum*, ed. J. M. De Buizer & N. S. van der Bliek, 65–80
- Laskar, T., Soderblom, D. R., Valenti, J. A., & Stauffer, J. R. 2009, *ApJ*, 698, 660
- Lejeune, T., & Schaerer, D. 2001, *A&A*, 366, 538
- Lequeux, J., Peimbert, M., Rayo, J. F., Serrano, A., & Torres-Peimbert, S. 1979, *A&A*, 80, 155
- Linsky, J. L., et al. 2006, *ApJ*, 647, 1106
- Lucas, P. W., et al. 2008, *MNRAS*, 391, 136
- Luhman, K. L., Liebert, J., & Rieke, G. H. 1997, *ApJ*, 489, L165
- Luhman, K. L., & Steeghs, D. 2004, *ApJ*, 609, 917
- Mac Low, M.-M., & Klessen, R. S. 2004, *Reviews of Modern Physics*, 76, 125
- Mac Low, M.-M., Li, Y., & Klessen, R. S. 2005, in *Protostars and Planets V*, 8434
- Maíz Apellániz, J. 2009, *Ap&SS*, 324, 95
- Mamajek, E. E., Lawson, W. A., & Feigelson, E. D. 1999, *ApJ*, 516, L77
- . 2000, *ApJ*, 544, 356
- Marengo, M., Reiter, M., & Fazio, G. G. 2008, in *American Institute of Physics Conference Series*, Vol. 1001, *Evolution and Nucleosynthesis in AGB Stars*, ed. R. Guandalini, S. Palmerini, & M. Busso, 331–338
- Marigo, P., Girardi, L., Bressan, A., Groenewegen, M. A. T., Silva, L., & Granato, G. L. 2008, *A&A*, 482, 883
- Martin, E. L., & Rebolo, R. 1993, *A&A*, 274, 274
- Martins, F., & Plez, B. 2006, *A&A*, 457, 637

- Martins, F., Schaerer, D., & Hillier, D. J. 2005, *A&A*, 436, 1049
- Mathieu, R. D., Baraffe, I., Simon, M., Stassun, K. G., & White, R. 2007, *Protostars and Planets V*, 411
- Mathis, J. S. 1990, *ARA&A*, 28, 37
- McMillan, S. L. W., Vesperini, E., & Portegies Zwart, S. F. 2007, *ApJ*, 655, L45
- Megeath, S. T., et al. 2004, *ApJS*, 154, 367
- Mengel, S., & Tacconi-Garman, L. E. 2009, *Ap&SS*, 324, 321
- Meynet, G., & Maeder, A. 2000, *A&A*, 361, 101
- Minniti, D., et al. 2010, *New Astronomy*, 15, 433
- Moeckel, N., & Bonnell, I. A. 2009, *MNRAS*, 400, 657
- Montalbán, J., D'Antona, F., Kupka, F., & Heiter, U. 2004, *A&A*, 416, 1081
- Morris, M. 1993, *ApJ*, 408, 496
- Morris, M., & Serabyn, E. 1996, *ARA&A*, 34, 645
- Muno, M. P., Law, C., Clark, J. S., Dougherty, S. M., de Grijs, R., Portegies Zwart, S., & Yusef-Zadeh, F. 2006, *ApJ*, 650, 203
- Negueruela, I., & Clark, J. S. 2005, *A&A*, 436, 541
- Negueruela, I., Clark, J. S., & Ritchie, B. W. 2010a, *A&A*, 516, A78
- Negueruela, I., González-Fernández, C., Marco, A., Clark, J. S., & Martínez-Núñez, S. 2010b, *A&A*, 513, A74
- Nishiyama, S., Tamura, M., Hatano, H., Kato, D., Tanabé, T., Sugitani, K., & Nagata, T. 2009, *ApJ*, 696, 1407
- Nishiyama, S., et al. 2006, *ApJ*, 638, 839
- Nordström, B., et al. 2004, *A&A*, 418, 989
- Olczak, C., Spurzem, R., & Henning, T. 2011, *A&A*, 532, A119
- Olive, K. A., Steigman, G., & Walker, T. P. 1991, *ApJ*, 380, L1
- Pagel, B. E. J., & Portinari, L. 1998, *MNRAS*, 298, 747
- Pagel, B. E. J., & Simonson, E. A. 1989, *Revista Mexicana de Astronomia y Astrofisica*, vol. 18, 18, 153
- Palla, F., & Stahler, S. W. 2001, *ApJ*, 553, 299
- Paulson, D. B., & Yelda, S. 2006, *PASP*, 118, 706
- Paumard, T., et al. 2006, *ApJ*, 643, 1011
- Peimbert, M., Luridiana, V., Peimbert, A., & Carigi, L. 2007, in *Astronomical Society of the Pacific Conference Series*, Vol. 374, *From Stars to Galaxies: Building the Pieces to Build Up the Universe*, ed. A. Vallenari, R. Tantalo, L. Portinari, & A. Moretti, 81
- Peters, T., Banerjee, R., Klessen, R. S., & Mac Low, M.-M. 2011, *ApJ*, 729, 72

- Piatti, A. E., Bica, E., & Claria, J. J. 1998, *A&AS*, 127, 423
- Pietrzyński, G., et al. 2010, *Nature*, 468, 542
- Plummer, H. C. 1911, *MNRAS*, 71, 460
- Popper, D. M. 1987, *ApJ*, 313, L81
- Portegies Zwart, S. F., Baumgardt, H., Hut, P., Makino, J., & McMillan, S. L. W. 2004, *Nature*, 428, 724
- Portegies Zwart, S. F., & Rusli, S. P. 2007, *MNRAS*, 374, 931
- Prato, L., Simon, M., Mazeh, T., Zucker, S., & McLean, I. S. 2002, *ApJ*, 579, L99
- Rayner, J. T., Cushing, M. C., & Vacca, W. D. 2009, *ApJS*, 185, 289
- Reipurth, B. 2008a, *Handbook of Star Forming Regions, Volume I: The Northern Sky*, ed. Reipurth, B.
- . 2008b, *Handbook of Star Forming Regions, Volume II: The Southern Sky*, ed. Reipurth, B.
- Ribas, I., Jordi, C., & Giménez, Á. 2000, *MNRAS*, 318, L55
- Rieke, G. H., & Lebofsky, M. J. 1985, *ApJ*, 288, 618
- Ritchie, B. W., Clark, J. S., Negueruela, I., & Langer, N. 2010, *A&A*, 520, A48
- Ritchie, B. W., Clark, J. S., Negueruela, I., & Najarro, F. 2009, *A&A*, 507, 1597
- Rochau, B., Brandner, W., Stolte, A., Gennaro, M., Gouliermis, D., Da Rio, N., Dzyurkevich, N., & Henning, T. 2010, *ApJ*, 716, L90
- Rogers, F. J., & Nayfonov, A. 2002, *ApJ*, 576, 1064
- Romano, D., Chiappini, C., Matteucci, F., & Tosi, M. 2005, *A&A*, 430, 491
- Salpeter, E. E. 1955, *ApJ*, 121, 161
- Schuller, F., et al. 2009, *A&A*, 504, 415
- Serenelli, A. M., Basu, S., Ferguson, J. W., & Asplund, M. 2009, *ApJ*, 705, L123
- Sherry, W. H., Walter, F. M., & Wolk, S. J. 2004, *AJ*, 128, 2316
- Siess, L., Dufour, E., & Forestini, M. 2000, *A&A*, 358, 593
- Simon, M., Dutrey, A., & Guilloteau, S. 2000, *ApJ*, 545, 1034
- Skrutskie, M. F., et al. 2006, *AJ*, 131, 1163
- Spitzer, L. 1987, *Dynamical evolution of globular clusters*, Princeton University Press, Princeton
- Stassun, K. G. 2008, in *Astronomical Society of the Pacific Conference Series, Vol. 384, 14th Cambridge Workshop on Cool Stars, Stellar Systems, and the Sun*, ed. G. van Belle, 214
- Stassun, K. G., Mathieu, R. D., & Valenti, J. A. 2006, *Nature*, 440, 311
- Stassun, K. G., Mathieu, R. D., Vaz, L. P. R., Stroud, N., & Vrba, F. J. 2004, *ApJS*, 151, 357
- Steffen, A. T., et al. 2001, *AJ*, 122, 997
- Steigman, G. 2006, *International Journal of Modern Physics E*, 15, 1
- . 2010, *JCAP*, 4, 29

- Steigman, G., Romano, D., & Tosi, M. 2007, *MNRAS*, 378, 576
- Stempels, H. C., Hebb, L., Stassun, K. G., Holtzman, J., Dunstone, N., Glowienka, L., & Frandsen, S. 2008, *A&A*, 481, 747
- Stetson, P. B. 1987, *PASP*, 99, 191
- Stolte, A., Brandner, W., Brandl, B., & Zinnecker, H. 2006, *AJ*, 132, 253
- Stolte, A., Brandner, W., Brandl, B., Zinnecker, H., & Grebel, E. K. 2004, *AJ*, 128, 765
- Stolte, A., Brandner, W., Grebel, E. K., Lenzen, R., & Lagrange, A. 2005a, *ApJ*, 628, L113
- Stolte, A., Brandner, W., Grebel, E. K., Lenzen, R., & Lagrange, A.-M. 2005b, *ApJ*, 628, L113
- Strohmeier, W. 1959, *Neue Veranderliche: BV 223-254*
- Testi, L., Sargent, A. I., Olmi, L., & Onello, J. S. 2000, *ApJ*, 540, L53
- Tognelli, E., Prada Moroni, P. G., & Degl'Innocenti, S. 2011, *ArXiv:1107.2318*
- Torres, R. M., Loinard, L., Mioduszewski, A. J., & Rodríguez, L. F. 2009, *ApJ*, 698, 242
- Ventura, P., Zeppieri, A., Mazzitelli, I., & D'Antona, F. 1998, *A&A*, 331, 1011
- Vidal-Madjar, A., Ferlet, R., & Lemoine, M. 1998, *Space Science Reviews*, 84, 297
- Walsh, A. J., Burton, M. G., Hyland, A. R., & Robinson, G. 1998, *MNRAS*, 301, 640
- Watson, C., et al. 2008, *ApJ*, 681, 1341
- Westerlund, B. 1961, *PASP*, 73, 51
- Whitmore, B. C., et al. 2010, *AJ*, 140, 75
- Williams, J. 1999, in *Interstellar Turbulence*, ed. J. Franco & A. Carraminana, 190
- Williams, J. P., Blitz, L., & McKee, C. F. 2000, V. Mannings, A. P. Boss, S. S. Russell, eds., *Protostars and Planets IV*, University of Arizona Press, Tucson, 97